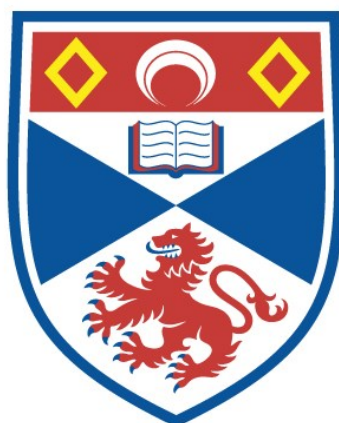


NOVEL LITHIUM-ION HOST MATERIALS FOR ELECTRODE APPLICATIONS

Christopher Lyness

A Thesis Submitted for the Degree of PhD
at the
University of St Andrews



2011

Full metadata for this item is available in
St Andrews Research Repository
at:
<http://research-repository.st-andrews.ac.uk/>

Please use this identifier to cite or link to this item:
<http://hdl.handle.net/10023/1921>

This item is protected by original copyright



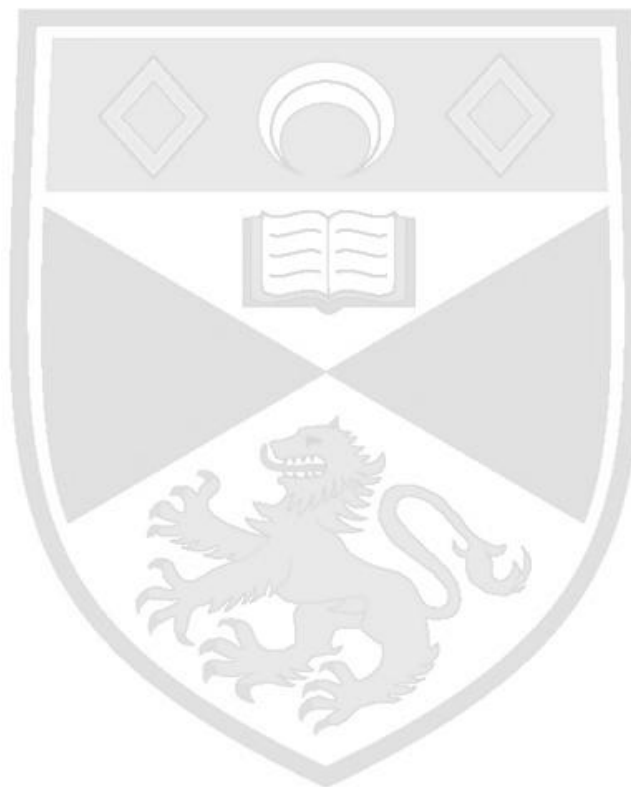
University
of
St Andrews



*A thesis presented for the degree of Doctor of Philosophy
in the Faculty of Science of the University of St Andrews*

Novel Lithium-ion Host Materials for Electrode Applications

Christopher Lyness, *M.Chem.*



May 2011

School of Chemistry
University of St. Andrews

1. Candidate's declarations:

I, Christopher Lyness, hereby certify that this thesis, which is approximately 48,000 words in length, has been written by me, that it is the record of work carried out by me and that it has not been submitted in any previous application for a higher degree.

I was admitted as a research student in September 2006 and as a candidate for the degree of Ph.D. in September 2007; the higher study for which this is a record was carried out in the University of St Andrews between 2006 and 2010.

Date

Signature of candidate

2. Supervisor's declaration:

I hereby certify that the candidate has fulfilled the conditions of the Resolution and Regulations appropriate for the degree of Ph.D. in the University of St Andrews and that the candidate is qualified to submit this thesis in application for that degree.

Date

Signature of supervisor

3. Permission for electronic publication:

In submitting this thesis to the University of St Andrews I understand that I am giving permission for it to be made available for use in accordance with the regulations of the University Library for the time being in force, subject to any copyright vested in the work not being affected thereby. I also understand that the title and the abstract will be published, and that a copy of the work may be made and supplied to any bona fide library or research worker, that my thesis will be electronically accessible for personal or research use unless exempt by award of an embargo as requested below, and that the library has the right to migrate my thesis into new electronic forms as required to ensure continued access to the thesis. I have obtained any third-party copyright permissions that may be required in order to allow such access and migration, or have requested the appropriate embargo below.

The following is an agreed request by candidate and supervisor regarding the electronic publication of this thesis:

Embargo on both all of printed copy and electronic copy for the same fixed period of 2 years on the following ground:

Publication would preclude future publication

Date Signature of candidate

Signature of supervisor

Acknowledgements

This thesis could not have happened without the help and advice of many people. While it is my name on the cover, it is only through the support of others that this work was possible.

Foremost, I would like to thank my supervisor Professor Peter Bruce for his guidance. His knowledge, enthusiasm, and, perhaps most importantly, his patience were crucial in helping me bring this project to fruition. A special mention must go to Dr. Rob Armstrong, who has endeavoured to impart his expansive knowledge of lithium-ion materials to me, an effort which, at times, may have seemed in vain, but hopefully now I have finally established the difference between the Mimms and the Maccor machines, he will deem it a success. Thanks are also due to Peter and Rob for taking on the task of proof reading.

I am grateful to both Dr. Yuri Andreev, and Dr. Armstrong, for their efforts to explain powder x-ray structural refinement to me. I promise one day to try to reach their level of understanding of the dark art. Perhaps then I may gain as much entertainment from looking at their refinement results as they seemed to do from witnessing some of mine.

My time here at St. Andrews would have been significantly diminished were it not for the other members and fellow students of the Bruce group, past and present, whose input was always valuable, support always dependable and advice generally questionable.

I would like to thank my friends, who made my time in St. Andrews so enjoyable, without them, this thesis may have been finished a lot sooner, but I would have a far fewer tales to tell.

Finally I would like to thank my family and beautiful girlfriend, Gemma, whose love and support have been unwavering from the beginning, especially Gem, who despite proof reading this work still attempts to maintain an interest in lithium-ion materials.

ABSTRACT

Two novel lithium host materials were investigated using structural and electrochemical analysis; the cathode material $\text{Li}_2\text{CoSiO}_4$ and the LiMO_2 class of anodes (where M is a transition metal ion).

$\text{Li}_2\text{CoSiO}_4$ materials were produced utilising a combination of solid state and hydrothermal synthesis conditions. Three $\text{Li}_2\text{CoSiO}_4$ polymorphs were synthesised; β_I , β_{II} and γ_0 . The $\text{Li}_2\text{CoSiO}_4$ polymorphs formed structures based around a distorted Li_3PO_4 structure. The β_{II} material was indexed to a $Pmn2_1$ space group, the β_I polymorph to $Pbn2_1$ and the γ_0 material was indexed to the $P2_1/n$ space group. A varying degree of cation mixing between lithium and cobalt sites was observed across the polymorphs.

The β_{II} polymorph produced 210mAh/g of capacity on first charge, with a first discharge capacity of 67mAh/g. It was found that the β_I material converted to the β_{II} polymorph during first charge. The γ_0 polymorph showed almost negligible electrochemical performance. Capacity retention of all polymorphs was poor, diminishing significantly by the tenth cycle. The effect of mechanical milling and carbon coating upon β_{II} , β_I and γ_0 materials was also investigated.

Various $\text{Li}_{1+x}\text{V}_{1-x}\text{O}_2$ materials (where $0 \leq x \leq 0.2$) were produced through solid state synthesis. LiVO_2 was found to convert to Li_2VO_2 on discharge, this process was found to be strongly dependent on the amount of excess lithium in the system. The $\text{Li}_{1.08}\text{V}_{0.92}\text{O}_2$ material had the highest first discharge capacity at 310mAh/g. It was found that the initial discharge consisted of several distinct electrochemical processes, connected by a complicated relationship, with significant irreversible capacity on first discharge.

Several other LiMO_2 systems were investigated for their ability to convert to layered Li_2MO_2 structures on low voltage discharge. While LiCoO_2 failed to convert to a Li_2CoO_2 structure, $\text{LiMn}_{0.5}\text{Ni}_{0.5}\text{O}_2$ underwent an addition type reaction to form $\text{Li}_2\text{Mn}_{0.5}\text{Ni}_{0.5}\text{O}_2$. A previously unknown $\text{Li}_2\text{Ni}_x\text{Co}_{1-x}\text{O}_2$ structure was observed, identified during the discharge of $\text{LiNi}_{0.33}\text{Co}_{0.66}\text{O}_2$.

Chapter 1: Introduction.....	1
1.1. Thesis Introduction.....	2
1.2. References.....	4
Chapter 2: Current Battery Technology.....	5
2.1. Battery Overview.....	7
2.2. Intercalation Materials.....	11
2.3. References.....	27
Chapter 3. Experimental Methodology and Theory.....	31
3.1. Chemicals.....	33
3.2. Electrochemical Techniques.....	37
3.3. Structural Analysis.....	51
3.4. Reference.....	64
Chapter 4. $\text{Li}_2\text{CoSiO}_4$.....	65
4.1. Introduction.....	67
4.2. Results and Discussion.....	73
4.3. Conclusions and Further Work.....	114
4.4. References.....	116

Chapter 5. $\text{Li}_2\text{CoSiO}_4$ Electrode Optimisation..... 118

5.1. Introduction..... 120

5.2. Results and Discussion..... 121

5.3. Conclusions and Further Work..... 150

5.4. References..... 152

Chapter 6. LiVO_2 as a lithium intercalation anode..... 153

6.1. Introduction..... 155

6.2. Results and Discussion..... 157

6.3. Conclusions and Further Work..... 185

6.4. References..... 187

Chapter 7: Preliminary Investigation into Layered Metal Oxide

Anodes..... 189

7.1. Introduction..... 191

7.2. Results and Discussion..... 193

7.3. Conclusions and Further Work..... 211

7.4. References..... 213

Chapter 8: Conclusions and Further Work.....	215
8.1. Conclusions	217
8.2. $\text{Li}_2\text{CoSiO}_4$	217
8.3. LiVO_2	223
8.4. LiMO_2	225
8.5 Summary.....	228
8.6 References	229
Appendices	230

Chapter 1: Introduction

1.1. Thesis Introduction

The ability to store electrical energy has become a fundamental necessity for modern society, from the small scale, powering our portable technology, to the large scale, as a crucial component of our burgeoning renewable energy infra-structure. We are now able to store more energy at greater density with more efficiency than ever before. Our understanding of the techniques and mechanisms for storing energy and converting it into useful power is ever expanding, constantly providing innovative and elegant means to produce electricity as and when we need it.

The ability to store energy chemically and convert it, when needed, to electrical power has been known in modern times since the Italian physicist Alessandro Volta first described the electrochemical storage device the ‘Volta pile’ in 1800¹. Since then several battery systems have been developed and intensely researched, each improving on an aspect of battery function (be it safety, energy density or any of the many factors affecting battery performance). Today much attention is focussed on the ubiquitous Li-ion battery, first theorised by Whittingham in the late 70’s²; its high energy density and convenient discharge voltage have allowed it to dominate in an ever expanding number of applications.

While the concept of lithium ions moving between host electrodes has remained relatively unchanged for twenty years since the rechargeable Li-ion battery was first commercialised³, the individual components have undergone a constant evolution. Today, the once widespread LiCoO_2 cathode is being replaced by the cheaper and safer LiFePO_4 , first proposed by Goodenough *et al.*⁴. However the amount of chemical energy that the battery can store has not grown significantly over the two

decades, with the storage ability of the cathode still lagging significantly behind the anode. As the fledgling field of partially and fully electric vehicles makes ever increasing demands on battery lifetime and cell kinetics, the search for new cathode materials is intensifying. Graphite still maintains its dominance of anode materials but its low volumetric capacity and near-lithium intercalation voltage are less than ideal and the search into replacement anode materials is gaining momentum.

Li-ion batteries span the fields of electrochemistry and solid state chemistry and as such, the investigation of any new battery materials relies on analytical techniques from both disciplines. Utilising structural characterisation and electrochemical analysis, this work comprises an investigation into a promising cathode material and a novel class of anodes. The aim of this research is to understand the mechanisms and processes occurring within these electrode materials in order to further inform our understanding of lithium ion host materials.

1.2. References

1. A. Volta, *Phil. Mag.*, 1800, **7**, 31.
2. M. S. Whittingham, *Science*, 1976, **192**, 1126-1127.
3. K. Sekai, H. Azuma, A. Omaru, S. Fujita, H. Imoto, T. Endo, K. Yamaura, Y. Nishi, S. Mashiko, and M. Yokogawa, *Journal of Power Sources*, 1993, **43**, 241-244.
4. K. S. Nanjundaswamy, A. K. Padhi, J. B. Goodenough, S. Okada, H. Ohtsuka, H. Arai, and J. Yamaki, *Solid State Ionics*, 1996, **92**, 1-10.

Chapter 2. Current Battery Technology

Chapter 2: Current Battery Technology

Chapter Contents:

2.1. Battery Overview	7
2.1.1. Basic Theory	7
2.1.2. Battery Components	9
2.2. Intercalation materials	11
2.2.1. Cathode	11
2.2.1.1. LiFePO_4	13
2.2.1.2. Li_2MSiO_4	15
2.2.2. Current Research	18
2.2.2.1. Li_2MSiO_4	18
2.2.2.2. $\text{Li}_2\text{FeSiO}_4$	19
2.2.2.3. $\text{Li}_2\text{MnSiO}_4$	20
2.2.2.4. $\text{Li}_2\text{CoSiO}_4$	21
2.2.3. Anode	21
2.3. References	27

2.1. Battery Overview

2.1.1. Basic Theory

At its heart, the lithium intercalation battery system is a simple thermodynamic pump. Within the battery are two, thermodynamically distinct, reservoirs of charge; the cathode and the anode. On discharge the charge carriers are forced from anode to the cathode due to the electrode's thermodynamic difference. The charge is drawn by the lower Gibbs free energy position of the cathode. Upon charging an external force has to be applied to drive the charge carriers back to the higher Gibbs energy position of the anode. The thermodynamic difference between the anode and cathode free energy gives the cell voltage, one of the fundamental properties of the cell, highlighted in the schematic in Figure 2.1.1

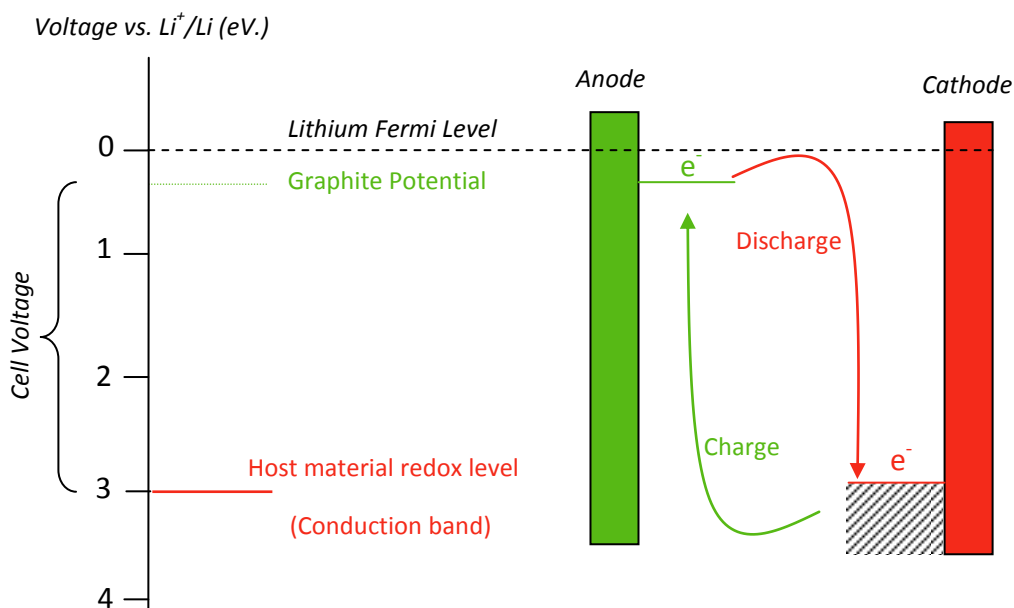
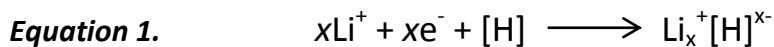


Figure 2.1.1. Schematic of the thermodynamic properties of a lithium intercalation galvanic cell (generic example voltages given, not to scale).

From an electrochemical perspective a lithium intercalation battery revolves around a reversible ion/electron reaction at each electrode. The anode, traditionally, consists of a material (such as graphite) which can intercalate Li^+ ions at a voltage near to the lithium equilibrium potential. The cathode reaction also involves insertion of

lithium into a host material with a transition metal redox couple allowing for charge compensation on insertion and removal of lithium. A typical half equation is given in equation 1.



[H] is the host material, x is the intercalation fraction (i.e. the number of lithium ions intercalated per unit cell).

An intercalation battery consists of 3 parts, the cathode, electrolyte and the anode. Upon charging, lithium ions are removed from the cathode, migrate through the electrolyte and are inserted within the graphite layers of the anode. Meanwhile the electrons travel through the external circuit from the cathode to the anode. Whilst discharging the lithium ions travel in the reverse direction from anode to cathode, as do the electrons through the external circuit. A schematic of this process is shown in Figure 2.1.2.

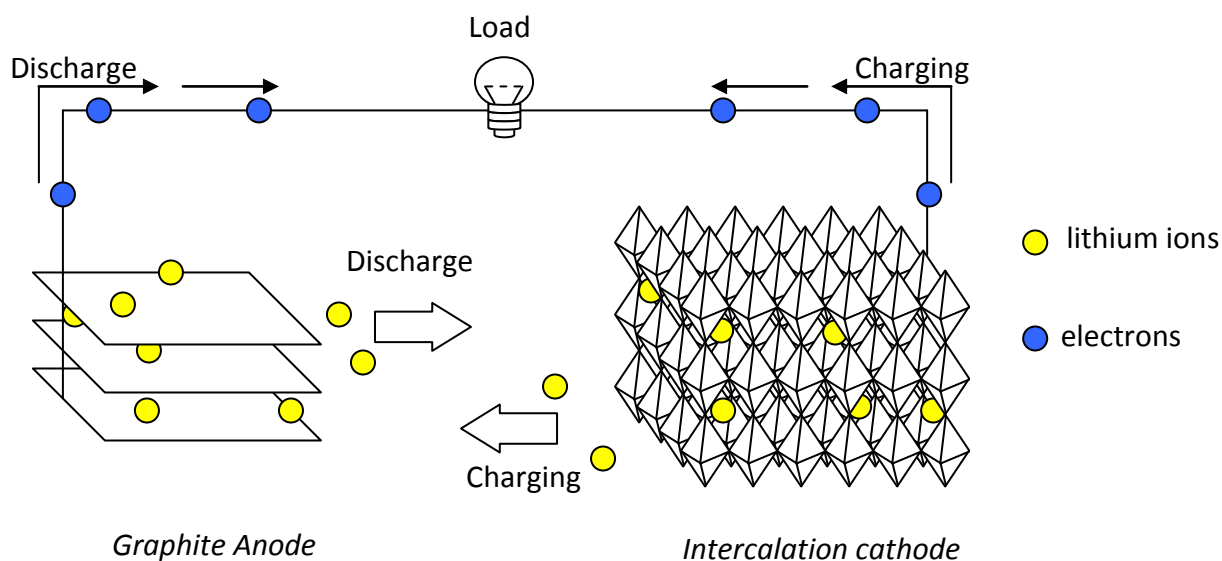


Figure 2.1.2. Schematic representation of a lithium intercalation battery operation.

2.1.2. Battery Components

Fundamentally the Li-ion battery consists of 3 components:

The anode: Traditionally graphite, this incorporates lithium ions within its layered structure and has a similar Li^+ ion deintercalation potential to lithium metal. Graphite is most widely used because it exhibits good cycling stability, good volumetric capacity whilst also being low cost. Other cathode materials have been suggested, mainly lithium metal alloys Li_xM ($\text{M} = \text{Al}, \text{Sn}, \text{Si}, \text{Sb}$ etc.)¹⁻⁵. Though these materials generally display large volumetric capacities they have problems with large volume expansion/contractions upon cycling that can cause poor structural stability over large numbers of cycles.

The electrolyte: This conducts lithium ions between the two electrodes and comprises of a lithium salt (LiPF_6 and lithium bis (trifluoromethane sulfonyl) imide are some of the more ubiquitous salts) usually dissolved within a liquid organic carbonate (common commercial electrolytes use, both on their own and as binary mixtures, ethylene carbonate (EC), diethyl carbonate (DEC), dimethyl carbonate (DMC) amongst others). The electrolyte must have high stability within the electrochemical 'window' between anode and cathode potentials and have low volatility whilst still ensuring good ion migration between the electrodes.

The cathode: This provides the source of the lithium ions and usually is based on either a transition metal dichalcogenide or a transition metal oxide (such as LiMO_2 ($\text{M} = \text{Co}, \text{Ni}, \text{Mn}^{6-8}$) or spinel LiMnO_2 ⁹). More recently LiFePO_4 ¹⁰ has been implemented in some applications. Intercalation is driven by a charge transfer (see Figure 2.1.1) from the intercalant to the host in what can be thought of as charge transfer on a discrete

atomic level, on the molecular level of a polyatomic moiety or as part of the material conduction band, depending on the nature of the process.

2.2. Intercalation materials

2.2.1. Cathode

Cathode materials form an integral part of the Li-ion battery and currently stand as the limiting factor for the amount of charge that can be stored in a battery (graphite can host one lithium per six carbons giving a capacity of 370 mAh/g). Often the stability of the cathode can determine the lifetime of the cell as a whole.

A desirable cathode material would have a relatively flat open circuit voltage over a range of lithium content, ensuring a constant voltage is supplied upon discharge. A critical property for lithium intercalation is the potential at which lithium can be extracted and inserted. If the potential is too high then side reactions such as electrolyte oxidation may occur, if the potential is too low it risks diminishing the gravimetric and volume energy density of the material. The optimum cathode would have an extraction/insertion potential residing within the voltage range of 2.5 - 4.0V vs. Li^+/Li (Voltages in excess of 4.5V generally are not used because of limits imposed by commercial electrolyte stability windows) though with the introduction of more exotic electrolytes, such as those based on dry polymers or ionic liquids, this voltage 'ceiling' may be increased¹¹). The material should also be inexpensive, easy to fabricate, environmentally benign as well as being electrochemically and mechanically stable.

Reversible intercalation has been achieved by a number of different compounds, namely transition metal dichalcogenides and transition metal oxides, the latter being far more widely implemented in commercial applications. The metal

oxides generally have a layered structure in which lithium ions sit between the layers, the most widely used compound being LiMO_2 ($M=\text{Co}$, Ni or solid solutions of the two).

LiCoO_2 is utilised in many commercial batteries as it does not suffer from the same instabilities as its nickel counterpart. The voltage for complete lithium intercalation/ deintercalation is around 4.7 V vs. Li^+/Li^0 ensuring the material has a suitably high gravimetric energy density. Unfortunately LiCoO_2 is unable to facilitate complete lithium extraction at such high voltages without suffering structural changes (this probably occurs via an exothermic reaction between the cobalt rich phase and the electrolyte). Thus for commercial applications only 0.5 Li is removed at a cut off voltage of 4.2V vs. Li^+/Li giving a maximum practical capacity of 130 mAh/g¹².

Both cobalt and cobalt nickel solid solution cathode materials have inherent safety issues. In the delithiated state both are strong oxidisers which is problematic when in contact with an organic electrolyte. There are also some long-term stability problems with the commercially available oxides, for example durability when exposed to extremes of temperature, such as the fully charged phase of $\text{Li}_{1-x}\text{CoO}_2$ which loses oxygen at elevated temperatures ($>180^\circ\text{C}$)¹³.

These factors in conjunction with the rarity and expense of pure cobalt mean the usage of such materials in large battery applications, such as transportation, is questionable and other more stable options have to be explored; one of the more promising materials is LiFePO_4

2.2.1.1. **LiFePO₄**

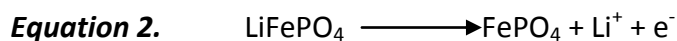
Iron based cathodes offer an excellent alternative to the aforementioned metal oxides as the iron compounds are generally cheap, the starting materials prolific and compounds tend to be both environmentally and physiologically benign. Unfortunately iron oxides in the form of LiFeO_2 are ill suited to cathode applications as the $\text{Fe}^{4+}/\text{Fe}^{3+}$ redox couple lies too far below the Li anode Fermi level and the $\text{Fe}^{3+}/\text{Fe}^{2+}$ redox level is too close to be exploited. To avoid this problem polyanions, such as $(\text{SO}_4)^{2-}$, $(\text{PO}_4)^{3-}$ and $(\text{AsO}_4)^{3-}$ amongst others¹⁴, can be employed to lower the $\text{Fe}^{3+}/\text{Fe}^{2+}$ redox energy to a point far enough below the lithium Fermi level to provide a useful voltage.

Phosphate based intercalation compounds were first described in the research of Delmas *et al.* into the NASICON based phase of $\text{NaTi}_2(\text{PO}_4)$ -which upon intercalation gives $\text{Na}_3\text{Ti}_2(\text{PO}_4)^{15}$. At the same time lithium intercalation of NASICON type materials was also researched, e.g. $\text{Li}_3\text{Fe}(\text{PO}_4)^{16}$ (with LiFePO_4 being described as an impurity!).

LiMPO_4 ($M=\text{Fe}$, Mn , Co and Ni . known as phospho-olivines) as a lithium intercalation material was first described by Goodenough *et al.*¹⁰. Attempts to delithiate LiNiPO_4 , LiMnPO_4 and LiCoPO_4 all failed¹⁷ and so research centred on LiFePO_4 . It was found that the $\text{Fe}^{3+}/\text{Fe}^{2+}$ redox level is around 3.5eV below the Li Fermi level in $\text{Li}_{1-x}\text{Fe}(\text{PO}_4)$ which compares favourably with $\text{Li}_{3+x}\text{Fe}(\text{PO}_4)_3$ (2.8eV)^{12,13} and surpassed other polyanions such as $\text{Li}_2\text{FeTi}(\text{PO}_4)_3$ (2.75 eV)¹⁵.

The nature of the LiFePO_4 structure involves a Fe-O-P linkage. The oxygen becoming electron deficient by its proximity to the electrophilic phosphorus ion. In turn the Fe ion feels an inductive effect from the electron deficient oxygen, removing electron density from a 3d antibonding orbital (Fe HOMO). This decreases the Fermi

level of the $\text{Fe}^{3+}/\text{Fe}^{2+}$ couple, which, in turn, causes an increased cell voltage (via increasing the gap between the cathode and anode redox levels). Its counterpart oxide LiFeO_2 has no such polarised oxygen.



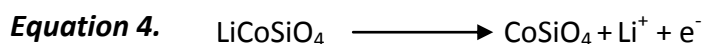
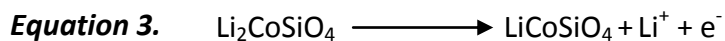
The reaction scheme in equation 2 displays the intercalation behaviour of LiFePO_4 which has a theoretical capacity of around 170 mAh/g. Upon cycling the compound shows a voltage plateau at 3.45V vs. Li^+/Li^0 . Though initially the intercalation process was assumed to be a two phase process it now appears more complicated, involving multiple phases, the type of which depends on the lithium content¹⁷. The morphology and stoichiometry of the pristine materials also plays a crucial role of the phase behaviour during cycling¹⁸ with evidence that single phase behaviour is possible with delicate control of the particle size.

A major drawback to the large-scale implementation of this material has been its inherent poor electronic conductivity (10^{-9} S/cm at room temperature)¹⁹. Because of the low electronic conductivity of the compound various mechanical and synthetic processes have been proposed to improve electrochemical performance. It would seem the best performance is offered from two simple processes, by reducing the length of the lithium transport paths, via producing nano-sized or highly porous particles^{20,21} and coating the particles in a thin layer of conducting material (usually graphite²¹⁻²³). Heating the mixture of active material and carbon precursor coats the material in the carbon, at the same time sp^2 linkages within the carbon material itself are increased. When both processes are used in conjunction, near theoretical capacities have been reported²⁴ (though it has been suggested that the limiting factor

is primarily the ionic conductivity²⁵). Another optimisation approach is to partially replace the iron with a similar transition metal. Studies have shown that when low levels of Co are introduced to the LiFePO₄ system (such as in LiCo_{0.2}Fe_{0.8}PO₄) an increase in capacity compared to the iron only olivine is observed²⁶. Pure LiCoPO₄ shows irreversible cycling behaviour, possibly caused by the high Co²⁺/Co³⁺ redox level (4.8V vs. Li⁺/Li) and subsequent electrolyte-salt decomposition²¹(though limited progress has been made recently^{27,28}).

2.2.1.2. Li₂MSiO₄

A logical extension of research into the phospho-olivine type materials is the similar silicate polyanion family which has the generic formula of Li₂MSiO₄. This material displays similar structural properties to Li₃MPO₄²⁹. The silicates again exploit the M³⁺/M²⁺ transition during lithium extraction/insertion but with the added possibility of more than one lithium extraction, through utilisation of the M⁴⁺/M³⁺ couple of the transition metals to extract two lithiums per formula weight. For example the complete oxidation of Li₂CoSiO₄ would probably result in a two step process with two corresponding voltage plateaus (seen in equation 3 and 4).



The specific capacity of Li₂CoSiO₄, and the related Fe and Mn analogues, is a contentious issue as it depends whether the capacity is defined with respect to one or two lithium ion extractions per unit cell. While some of the literature suggests that more than one lithium extraction is possible³⁰ it has never been shown that >1 Li⁺

capacity exists past the first cycle and thus spurious side reactions can't be ruled out as a cause of these high initial capacities. In light of this, the more conservative estimate of one lithium extraction per unit cell is adopted for $\text{Li}_2\text{CoSiO}_4$, giving a specific capacity of 162 mAh/g (rather than 325 mAh/g)

2.2.1.2.1. **Structural considerations**

The Li_2MXO_4 group can be thought of as a slightly distorted form of oxide hexagonal close packing. Half the tetrahedral sites are occupied by cations such that face sharing between the pairs of tetrahedral sites is avoided³¹. The structures show polymorphism and can be divided into 2 families β and γ (seen in Figure 2.2.1.), which are based on the Li_3PO_4 nomenclature³². Within the β form all the tetrahedra point in the same direction, perpendicular to the close packed oxygen plane, and share only corners with each other.

The γ polymorphs contain tetrahedra arranged in groups of 3 with the central tetrahedra pointing in the opposite direction to the outer 2, with which it shares edges³³. At low temperatures β is stable and at high temperature γ is the equilibrium phase. Cooling the γ form at high temperatures causes a sluggish conversion to the β phase, thus γ can be conserved at low temperatures by rapid cooling suppressing the transition of phases and producing a material that is kinetically stable but only meta-stable thermodynamically. During polymorph transition the oxide layer remains unmoved, with migration between sites only thought to occur amongst the transition metal cations³².

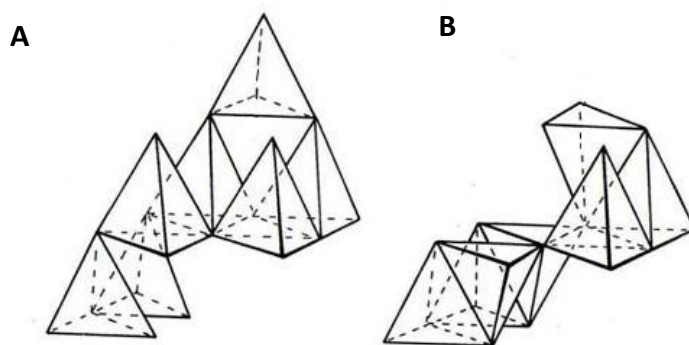


Figure 2.2.1. Schematic representations of the Li_3PO_4 structure. A) The β type structure, B) The γ type structure.

Several variants of both β and γ exist involving either ordering or distortions of the parent structures, they are denoted β_I , γ_0 , γ_{II} etc. It has been suggested previously that transition to the sub-polymorphs would not involve a cation migration, instead requiring a minor step that only distorts the lattice of the patriarch phase perhaps through rotation of MO_4 tetrahedra³⁴, though this has yet to be experimentally observed. Previous work on Li_2MSiO_4 has been limited, with the majority occurring in the early 70's on $\text{Li}_2\text{CoSiO}_4$ and latterly around $\text{Li}_2\text{FeSiO}_4$ as an intercalation material.

Two crystallographic distinct cation sites exist, M1 and M2, these introduce selectivity into the structure which becomes an important feature when more than one transition metal ion is present, such as in solid solutions. The M2 site is always larger than the M1 site in olivines³⁵. This implies that larger cations are favoured for this site. It has also been suggested that another predominant factor is the electronegativity of the ions. It is thought that the M2 sites in olivine structures are more ionic than the M1 site³⁶ suggesting that less electronegative ions prefer the M1 site. Though it has been shown that neither ionic radii nor electronegativity has a systematic effect on the choice of cation site, when both are combined a more

consistent picture emerges. This may not affect the site selectivity in Li_2MSiO_4 because of the radii and electronegativity disparity between Li^+ and M but may become a deciding factor if considering $\text{Li}_2M'\text{MSiO}_4$ selectivity for solid solutions.

Like LiFePO_4 , the silicates have a structure that contains a Si-O- M system, where $M=\text{Fe, Co or Mn}$. The Si-O acts in a similar manner to the P-O bond component in LiFePO_4 , causing an electronic polarisation towards the silicon atom. The lower electrophilicity of silicon vs. phosphorus should reduce the inductive effect of the oxygen in the M -O bond and in turn reduce the voltage difference between the M^{3+}/M^{2+} couple and the graphite lithium intercalation level. This may be useful for the transition metal ions with higher redox levels-like Co. Again a silicate battery material would have the safety and cost benefits of the phospho-olivine.

2.2.2. Current Research

2.2.2.1. Li_2MSiO_4

By fine-tuning the M -O-X linkage the redox level (and thus the lithium intercalation voltage) can be affected. This notion has been further examined by computation, the study³⁷ looked at different compositions of Li_2MXO_4 (where $M=\text{Fe, Co and Mn}$ and $X=\text{P, Si, Ge, As and Se}$) and centred around the ion-covalent character of the M -O bond. The nature of this bond is known to be influenced through the inductive effect, felt from the polarising X atom (in the M -O-X bond) thus by careful selection of X, the transition-metal redox level can be systematically altered.

In all cases the insertion voltage increased with the electronegativity of the X counter ion. This relationship displayed almost linear dependence, the explanation

being that by increasing the polarisation of the X-O bond (and hence the inductive effect felt by the transition-metal ion) less electron density remained upon the transition-metal ion, this in turn increased the voltage of insertion. To fully optimise the potential of lithium intercalation it was suggested that the redox level could be more intimately tuned by introducing a second polyanion metal to give the material formula $\text{Li}_2\text{MSi}_{1-y}\text{X}_y\text{O}_4$

Though in theory it is possible to remove two lithiums through utilisation of both M^{3+}/M^{2+} and M^{4+}/M^{3+} 3d metal couples, several problems may arise with the extraction of a second lithium.

It is unlikely that in $\text{Li}_2\text{FeSiO}_4$ extraction above 1 Li ion is useful because of the highly stable Fe^{3+} oxidation state occurring when one lithium is removed and a high energy barrier exists for further oxidising it. A second lithium extraction from $\text{Li}_2\text{CoSiO}_4$ is thought to be possible but this would occur at a voltage outside of commercial electrolyte windows. $\text{Li}_2\text{MnSiO}_4$ has the lowest theoretical second lithium extraction potential (4.4V vs. Li^+/Li) but poor conductivity may make even extraction of the first lithium difficult and thus preclude a second lithium extraction.

2.2.2.2. **$\text{Li}_2\text{FeSiO}_4$**

Initial attempts to synthesise LiFe(III)SiO_4 resulted in mixed phase products (primarily spodumene $\text{LiFeSi}_2\text{O}_6$) and it wasn't until 2003 when $\text{Li}_2\text{FeSiO}_4$ was produced as the sole product of a reaction³⁸. The material $\text{Li}_2\text{FeSiO}_4$ is by far the most developed of the polyanion silicates because of the benign nature of iron compared to other first row transition metals (and its favourable electrochemistry) making it a particularly attractive cathode material.

Two crystal structures have been proposed for $\text{Li}_2\text{FeSiO}_4$; Nyten *et al.*^{39,40} suggest (in agreement with Tarte and Cahay²⁹) that the structure takes the form of a $\text{Pmn}2_1$ space group with lattice parameters of $a=6.266(5)\text{\AA}$ $b=5.3295(5)\text{\AA}$ and $c=5.0148(4)\text{\AA}$ and is isostructural with Li_3PO_4 . The differences between the structures is discussed by Nishimura *et al.*⁴¹.

Studies of the electrochemistry of the compound have been ambiguous, Nyten *et al.* reported a shift in the $\text{Li}_2\text{FeSiO}_4$ voltage plateau from 3.1 to 2.8V vs. Li^+/Li after the first cycle; this was attributed to a possible transition to a more stable $\text{Li}_2\text{FeSiO}_4$ phase. Other work where the purity of $\text{Li}_2\text{FeSiO}_4$ was confirmed by magnetic measurements¹⁴ disagreed with previous studies and found an absence of the 3.1V oxidation plateau reported in the Nyten papers (though this does go against the grain of most reports). It was suggested that the high quality of the material is responsible for the lack of change in the plateau voltage when cycling the material. Stable charging capacities of around 140 mAh/g and discharge capacities of around 130 mAh/g have been reported for $\text{Li}_2\text{FeSiO}_4$ ^{38-40,42,43}.

2.2.2.3. $\text{Li}_2\text{MnSiO}_4$

Work on $\text{Li}_2\text{MnSiO}_4$ has thus far shown Mn based materials to be an inferior cathode material to $\text{Li}_2\text{FeSiO}_4$, Dominko *et al.* achieved a first charge removal of 0.6 Li which subsequently dropped to 0.3 Li by the 5th cycle⁴². This is thought to be due to the relatively poor electronic conductivity compared to $\text{Li}_2\text{FeSiO}_4$, as theorised by Arroyo-de Dampablo *et al.*³⁷ Structural studies have concluded that $\text{Li}_2\text{MnSiO}_4$ crystallises isostructurally to $\text{Li}_2\text{FeSiO}_4$ ⁴².

2.2.2.4. $\text{Li}_2\text{CoSiO}_4$

The first work on $\text{Li}_2\text{CoSiO}_4$ was carried out by West and Glasser in the early 1970s³² (though not motivated by interest in intercalation compounds). The polymorphs (of which four were found, denoted β_I , β_{II} or γ_O , γ_{II}) and their transition temperatures were identified. Access to the four polymorphs was achieved by exploiting the slow rates of inversions of the high temperature γ polymorphs to the low temperature β structures, rapid quenching was employed to overcome such temperature dependencies. The β_{II} phase was researched most intensively (mainly because of the ability to isolate single crystals of the polymorph⁴⁴). It was found that β_{II} exhibited disorder in Co^{2+} and Li^+ positions⁴⁵ that were absent in the other polymorphs

2.2.3. Anode

The anode for the lithium ion battery serves as the counter-electrode to the cathode, traditionally intercalating ions close to the lithium equilibrium potential, the anode acts as a store of lithium ions which, upon discharge, are released to intercalate into the cathode.

Historically it was the introduction of the carbon anode^{46,47} that freed the lithium ion battery from many of its inherent safety issues (such as dendritic growth upon cycling) and allowed its wide-spread commercialisation.

Many properties required of anode materials are similar to those for the cathode (such as high theoretical capacity, and mechanical and chemical stability on multiple cycles). A significant number of these demands are met in the layered carbon

material graphite, it being cheap, ubiquitous, benign and having a high specific capacity ($\sim 370\text{mAh/g}$) (the drawbacks of low volumetric capacity and safety concerns forcing lower rate capability on cycling being outweighed by the benefits).

It was found that graphite could accommodate Li^+ ions in-between the layers of sp^2 carbon ring systems to a stoichiometry of LiC_6 ⁴⁸. It does so at a voltage of $\sim 0.1\text{ V}$ versus the lithium couple making it an ideal lithium metal replacement. While graphite provides a convenient anode material it is not without its faults. A low volumetric power density (800 Ah/l) combined with its inability to handle the higher rate capabilities⁴⁹ needed to satisfy future applications (i.e. electric vehicles) have caused alternatives to be sought.

The success of the graphite anode has meant that anodes have received less attention than their cathode counterpart due to the cathode contributing the limiting capacity to the battery system and the convenience of the graphite anode which diminished the need for an alternative. Recent advances in cathode design have instigated a search for more versatile anode materials which are able to offer greater volumetric stability on cycling or present alternative intercalation voltages to match the high voltage spinel cathodes or avoid any lithium metal plating issues during, for example, a fast recharge.

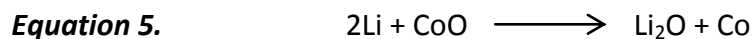
Much research has focused upon lithium metal alloys, most popularly tin alloys^{1-3,50-52}. Some of the alloys show packing Li densities similar or above Li metal itself, obviously an advantage compared to graphite. The primary problem with alloys is they show up to 4-fold volume change between lithiated and delithiated forms, this can cause large mechanical stresses through the alloy material and battery as a whole

causing cracking and crumbling of the alloy anode; subsequently the conductivity of the electrode is reduced and the internal resistance of the cell increases. Thus far a serious commercially viable alloy anode hasn't been developed (Fuji's STALION battery being the only serious contender, though development is in progress, utilising recent advancement in high surface area silicon anodes, by companies such as Nexeon) but interest continues due to the impressive volumetric and gravimetric capacities, with research now focusing on materials utilising two different active phases which operate at different voltages⁵³, each material being used to stabilise the other while electrochemically inactive (so called buffer matrices).

A recently developed class of anodes is the 'zero strain' series of materials which show no volume change upon lithiation and de-lithiation⁵⁴⁻⁵⁹, the most prominent being $\text{Li}_4\text{Ti}_5\text{O}_{12}$. Lithium titanates have high cycling stability due, in part, to their negligible crystallographic volume change during cycling, a flat voltage response at 1.5V and excellent lithium diffusivity, but they suffer from low gravimetric capacity and so far have only been applied to specialist applications which utilise a high voltage cathode (to maintain power density).

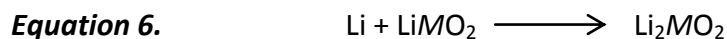
After the work of Fuji Co. on metal vanadates which found the materials to be low potential/large capacity compounds⁶⁰, various layered Li-metal oxide systems were investigated⁶¹. It was determined that at low potentials these systems behaved in a different manner to the classic intercalation process, instead of inserting lithium into the host structure an electrochemical formation of metal nanoparticles is believed to occur during first discharge and is accompanied by production of Li_2O ⁶²⁻⁶⁴. Various layered oxide systems have been explored⁶⁵⁻⁷⁰ a typical example is the CoO system

which revolves around the reaction in equation 5. This is thought to have a capacity >1000mAh/g (compared to the 370mAh/g capacity offered by graphite).



On charging to 3V the lithia is reduced via the catalytic activity of the nanoscale metal which then regenerates the metal oxide.

Recently Thackeray *et al.*⁷¹⁻⁷⁵ have explored a different type of anodic reaction involving layered oxides. It was found for certain oxides (i.e. $\text{LiMn}_{0.5}\text{Ni}_{0.5}\text{O}_2$) with the classic $\alpha\text{-NaFeO}_2$ $R\bar{3}m$ structure, an alternative reaction took place at low voltages. Instead of the so called dissociation reaction (eq. 5) an addition of lithium to the $\text{LiMn}_{0.5}\text{Ni}_{0.5}\text{O}_2$ system was seen to cause a phase change to $\text{Li}_2\text{Mn}_{0.5}\text{Ni}_{0.5}\text{O}_2$ $P\bar{3}m1$ rhombohedral structure, as per eq. 6 (both structures can be seen in Figure 2.3.1.)



Similar to the $\alpha\text{-NaFeO}_2$ structure, the transition metal layer has all the octahedral holes filled but the lithium ions occupy all of the tetrahedral holes in the lithium layer. This structure had been chemically synthesised in Li_2NiO_2 ^{76,77} and Li_2MnO_2 ⁷⁸ but never seen as a consequence of electrochemical lithiation until the work of Thackeray *et al.*

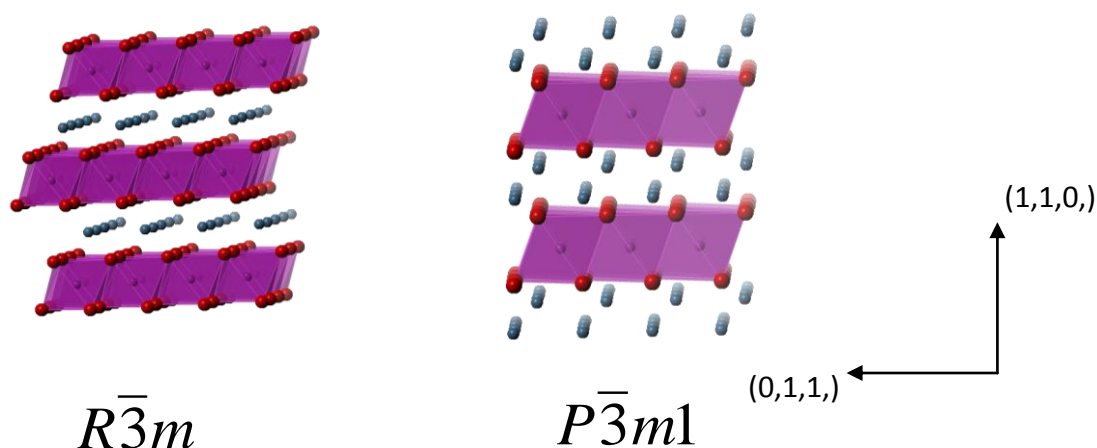


Figure 2.3.1 Schematic of $R\bar{3}m$ (LiMO_2) and $P\bar{3}m1$ (Li_2MO_2) type structures, Purple polyhedra VO_6 , Red spheres oxygen, blue spheres lithium.

Both LiCoO_2 and LiNiO_2 materials have also been tested to determine their low voltage behaviour, but unlike $\text{LiMn}_{0.5}\text{Ni}_{0.5}\text{O}_2$ it was found that they are predisposed to the dissociation type reactions⁷³. It was concluded that the reaction path of anodic insertion of LiMO_2 depends on kinetic factors such as the lithium diffusion and the cell current rates in addition to the thermodynamic factors and thus the true reaction path is difficult to predict easily. Work by Thackeray *et al.*^{75,73} suggested that three types of reaction can occur; (1) the addition reaction to form Li_2MO_2 (2) the decomposition reaction in which the metal oxide and Li_2O are formed and (3) the displacement reaction in which the metal and Li_2O are formed (probably a sequential reaction involving both 2 and 3 reaction pathways). In work on layered oxide anodes (both MO and LiMO_2 type materials) it has been noted that there is a considerable irreversible capacity on first discharge, this has been ascribed to significant SEI formation by Tarascon^{62,79} due to displacement of metallic transition metal ions during the first discharge. This theory has yet to be explored fully, due in part to the amorphous and possibly nano-scopic nature of the products of this process.

Lithium vanadate is a relatively neglected material with the majority of studies of layered LiVO_2 focussing upon the novel thermal behaviour of the V-V distance and unusual orbital degeneracy formed by the V^{3+} triangular lattice in LiVO_2 ⁸⁰⁻⁸⁴. Some cathodic studies have been carried out, with the material characterised in various delithiated phases^{82,85-87} where it was found to undergo a spinel transformation at low lithium concentrations. It was found that just as there is a 'high temperature' and 'low temperature' structure for LiCoO_2 ⁸⁸ there also exist two structurally similar LiVO_2 phases which have different electrochemical properties⁸⁹. It was not until very recently that LiVO_2 was seen as a viable anode⁹⁰⁻⁹². Samsung initially established the ability of LiVO_2 to intercalate one lithium and form Li_2VO_2 , but little is currently known about the processes which occur within the electrode as lithium is inserted and a phase change occurs. LiVO_2 exhibits rather poor capacity retention on cycling, the cause of this is yet to be explored, but it may have some correlation with the unexplained large irreversible capacity seen on the first cycle.

Currently there are more questions than answers with the layered oxide anode systems, given the ambiguous preference for dissociation vs. addition reactions especially in materials where both LiMO_2 and Li_2MO_2 phases are known to exist but (presumably due to kinetic factors) do not undergo this transformation. To improve matters more systems must be identified which can form Li_2MO_2 phases under low voltage cycling and further investigation is needed into the structural changes that occur throughout cycling to better understand the nature of reaction pathway selection.

2.3. References.

1. H. Li, X. Huang, and L. Chen, *Journal of Power Sources*, 1999, **81-82**, 340-345.
2. J. Yang, M. Winter, and J. O. Besenhard, *Solid State Ionics*, 1996, **90**, 281-287.
3. J. O. Besenhard, M. Wachtler, M. Winter, R. Andreaus, I. Rom, and W. Sitte, *Journal of Power Sources*, 1999, **81-82**, 268-272.
4. A. N. Dey, *J. Electrochem. Soc.*, 1971, **118**, 1547-1549.
5. J. O. Besenhard, *Handbook of Battery Materials*, Wiley-VCH, 1999.
6. K. Mizushima, P. Jones, P. Wiseman, and J. Goodenough, *Materials Research Bulletin*, 1980, **15**, 783-789.
7. J. R. Dahn, U. von Sacken, M. W. Juzkow, and H. Al-Janaby, *J. Electrochem. Soc.*, 1991, **138**, 2207-2211.
8. A. R. Armstrong and P. G. Bruce, *Nature*, 1996, **381**, 499-500.
9. M. Thackeray, W. David, P. Bruce, and J. Goodenough, *Materials Research Bulletin*, 1983, **18**, 461-472.
10. A. K. Padhi, *J. Electrochem. Soc.*, 1997, **144**, 1188.
11. C. Austen Angell, J. Fan, C. Liu, Q. Lu, E. Sanchez, and K. Xu, *Solid State Ionics*, 1994, **69**, 343-353.
12. R. V. Chebiam, F. Prado, and A. Manthiram, *Chemistry of Materials*, 2001, **13**, 2951-2957.
13. A. K. Padhi, *J. Electrochem. Soc.*, 1997, **144**, 2581.
14. K. Zaghib, A. Ait Salah, N. Ravet, A. Mauger, F. Gendron, and C. Julien, *Journal of Power Sources*, 2006, **160**, 1381-1386.
15. C. Delmas, F. Cherkaoui, A. Nadiri, and P. Hagenmuller, *Materials Research Bulletin*, 1987, **22**, 631-639.
16. K. S. Nanjundaswamy, A. K. Padhi, J. B. Goodenough, S. Okada, H. Ohtsuka, H. Arai, and J. Yamaki, *Solid State Ionics*, 1996, **92**, 1-10.
17. A. Yamada, H. Koiumi, N. Sonoyama, and R. Kanno, *Abstract IBA-HBC, Hawaii*, 2006.
18. P. Gibot, M. Casas-Cabanas, L. Laffont, S. Levasseur, P. Carlach, S. Hamelet, J. Tarascon, and C. Masquelier, *Nat Mater*, 2008, **7**, 741-747.
19. S. Chung, J. T. Bloking, and Y. Chiang, *Nat Mater*, 2002, **1**, 123-128.
20. H. Huang, S. Yin, and L. F. Nazar, *Electrochem. Solid-State Lett.*, 2001, **4**, A170-A172.
21. Z. Chen and J. R. Dahn, *J. Electrochem. Soc.*, 2002, **149**, A1184-A1189.
22. C. Li, H. Zhang, L. Fu, H. Liu, Y. Wu, E. Rahm, R. Holze, and H. Wu, *Electrochimica Acta*, 2006, **51**, 3872-3883.
23. I. Belharouak, C. Johnson, and K. Amine, *Electrochemistry Communications*, 2005, **7**, 983-988.
24. K. Striebel, J. Shim, V. Srinivasan, and J. Newman, *J. Electrochem. Soc.*, 2005, **152**, A664-A670.
25. M. Gaberscek, R. Dominko, and J. Jamnik, *Electrochemistry Communications*, 2007, **9**, 2778-2783.
26. N. Penazzi, M. Arrabito, M. Piana, S. Bodoardo, S. Panero, and I. Amadei, *Journal of the European Ceramic Society*, 2004, **24**, 1381-1384.
27. I. Jang, H. Lim, S. Lee, K. Karthikeyan, V. Aravindan, K. Kang, W. Yoon, W. Cho, and Y. Lee, *Journal of Alloys and Compounds*, 2010, **497**, 321-324.
28. M. Rabanal, M. Gutierrez, F. Garcia-Alvarado, E. Gonzalo, and M. Arroyo-de Dompablo, *Journal of Power Sources*, 2006, **160**, 523-528.
29. P. Tarte and R. Cahay, *C.R. Acad. Sc. Paris*, 1970, 139C.
30. Z. Gong, Y. Li, and Y. Yang, *Journal of Power Sources*, 2007, **174**, 524-527.

31. A. R. West and P. G. Bruce, *Acta Crystallogr B Struct Crystallogr Cryst Chem*, 1982, **38**, 1891-1896.
32. A. R. West and F. P. Glasser, *Journal of Solid State Chemistry*, 1972, **4**, 20-28.
33. M. E. Villafuerte-Castrejon and A. R. West, *J. Chem. Soc., Faraday Trans. 1:*, 1979, **75**, 374-384.
34. M. E. Villafuerte-Castrejon and A. R. West, *J. Chem. Soc., Faraday Trans. 1:*, 1981, **77**, 2297-2307.
35. K. Tsukimura and S. Sasaki, *Physics and Chemistry of Minerals*, 2000, **27**, 234-241.
36. O. Tamada, *Mineralogical Journal*, 1984, **12**, 137.
37. M. Arroyo-de Dompablo, M. Armand, J. Tarascon, and U. Amador, *Electrochemistry Communications*, 2006, **8**, 1292-1298.
1. A. Abouimrane, N. Ravet, M. Armand, A. Nyten, and J. Thomas, *IMLB 12 japan*, 2004.
39. A. Nytén, A. Abouimrane, M. Armand, T. Gustafsson, and J. O. Thomas, *Electrochemistry Communications*, 2005, **7**, 156-160.
1. A. Nyten, M. Stjerndahl, H. Rensmo, H. Siegbahn, M. Armand, T. Gustafsson, K. Edstrom, and J. O. Thomas, *J. Mater. Chem.*, 2006, **16**, 3483-3488.
41. S. Nishimura, S. Hayase, R. Kanno, M. Yashima, N. Nakayama, and A. Yamada, *Journal of the American Chemical Society*, 2008, **130**, 13212-13213.
42. R. Dominko, M. Bele, M. Gaberscek, A. Meden, M. Remskar, and J. Jamnik, *Electrochemistry Communications*, 2006, **8**, 217-222.
43. M. Herstedt, M. Stjerndahl, A. Nyten, T. Gustafsson, H. Rensmo, H. Siegbahn, N. Ravet, M. Armand, J. O. Thomas, and K. Edstrom, *Electrochem. Solid-State Lett.*, 2003, **6**, A202-A206.
44. J. Setoguchi, S. Kobayashi, H. Yamaguchi, C. Sakamoto, and K. Akatsuka, *Mem. Osaka Kyioko Univer.*, 1979, 27.
45. Y. Takaki and H. Yamaguchi, *Acta Crystallogr B Struct Crystallogr Cryst Chem*, 1980, **36**, 234-237.
46. M. Mohri, N. Yanagisawa, Y. Tajima, H. Tanaka, T. Mitate, S. Nakajima, M. Yoshida, Y. Yoshimoto, T. Suzuki, and H. Wada, *Journal of Power Sources*, 1989, **26**, 545-551.
47. K. Ozawa, *Solid State Ionics*, 1994, **69**, 212-221.
48. N. Kambe, M. Dresselhaus, G. Dresselhaus, S. Basu, A. McGhie, and J. Fischer, *Materials Science and Engineering*, 1979, **40**, 1-4.
49. D. Aurbach, E. Zinigrad, Y. Cohen, and H. Teller, *Solid State Ionics*, 2002, **148**, 405-416.
50. A. Anani and R. Huggins, *Journal of Power Sources*, 1992, **38**, 363-372.
51. J. Besenhard, M. Hess, and P. Komenda, *Solid State Ionics*, 1990, **40-41**, 525-529.
52. S. Matsuno, M. Nakayama, and M. Wakihara, *J. Electrochem. Soc.*, 2008, **155**, A61-A65.
53. A. Anani, S. Crouch-Baker, and R. A. Huggins, *J. Electrochem. Soc.*, 1987, **134**, 3098-3102.
54. J. Li, Z. Tang, and Z. Zhang, *Electrochemistry Communications*, 2005, **7**, 894-899.
55. J. Gao, C. Jiang, J. Ying, and C. Wan, *Journal of Power Sources*, 2006, **155**, 364-367.
56. K. Nakahara, R. Nakajima, T. Matsushima, and H. Majima, *Journal of Power Sources*, 2003, **117**, 131-136.
57. A. Y. Shenouda and K. Murali, *Journal of Power Sources*, 2008, **176**, 332-339.
58. P. P. Prosini, R. Mancini, L. Petrucci, V. Contini, and P. Villano, *Solid State Ionics*, 2001, **144**, 185-192.
59. X. Yao, S. Xie, C. Chen, Q. Wang, J. Sun, Y. Li, and S. Lu, *Electrochimica Acta*, 2005, **50**, 4076-4081.
60. Idota, U.S. Patent Number: 5478671, 1995.

61. P. Poizot, S. Laruelle, S. Grugeon, L. Dupont, and J. Tarascon, *Nature*, 2000, **407**, 496-499.
62. P. Poizot, S. Laruelle, S. Grugeon, and J. Tarascon, *J. Electrochem. Soc.*, 2002, **149**, A1212-A1217.
63. S. A. Needham, G. X. Wang, K. Konstantinov, Y. Tournayre, Z. Lao, and H. K. Liu, *Electrochem. Solid-State Lett.*, 2006, **9**, A315-A319.
64. C. Delacourt, L. Laffont, R. Bouchet, C. Wurm, J. Leriche, M. Morcrette, J. Tarascon, and C. Masquelier, *J. Electrochem. Soc.*, 2005, **152**, A913-A921.
65. P. Balaya, H. Li, L. Kienle, and J. Maier, *Advanced Functional Materials*, 2003, **13**, 621-625.
66. D. C. S. Souza, V. Pralong, A. J. Jacobson, and L. F. Nazar, *Science*, 2002, **296**, 2012-2015.
67. J. Meier, J. Schiøtz, P. Liu, J. Nørskov, and U. Stimming, *Chemical Physics Letters*, 2004, **390**, 440-444.
68. C. Jiang, E. Hosono, and H. Zhou, *Nano Today*, 2006, **1**, 28-33.
69. J. Maier, *Nat Mater*, 2005, **4**, 805-815.
70. F. Jiao, J. Bao, and P. G. Bruce, *Electrochem. Solid-State Lett.*, 2007, **10**, A264-A266.
71. J. Kim, C. S. Johnson, J. T. Vaughey, M. M. Thackeray, S. A. Hackney, W. Yoon, and C. P. Grey, *Chemistry of Materials*, 2004, **16**, 1996-2006.
72. C. S. Johnson, J. Kim, A. J. Kropf, A. J. Kahaian, J. T. Vaughey, L. M. L. Fransson, K. Edstrom, and M. M. Thackeray, *Chemistry of Materials*, 2003, **15**, 2313-2322.
73. J. Vaughey, A. M. Geyer, N. Fackler, C. S. Johnson, K. Edstrom, H. Bryngelsson, R. Benedek, and M. M. Thackeray, *Journal of Power Sources*, 2007, **174**, 1052-1056.
74. C. S. Johnson, J. Kim, A. Jeremy Kropf, A. J. Kahaian, J. T. Vaughey, and M. M. Thackeray, *Electrochemistry Communications*, 2002, **4**, 492-498.
75. R. Benedek, J. Vaughey, and M. M. Thackeray, *Chemistry of Materials*, 2006, **18**, 1296-1302.
76. J. R. Dahn, U. von Sacken, and C. A. Michal, *Solid State Ionics*, 1990, **44**, 87-97.
77. I. Davidson, J. Greedan, U. von Sacken, C. Michal, and J. Dahn, *Solid State Ionics*, 1991, **46**, 243-247.
78. W. David, M. Goodenough, M. Thackeray, and J. Thomas, 1983, **20**.
79. P. Poizot, S. Laruelle, S. Grugeon, L. Dupont, and J. Tarascon, *Nature*, 2000, **407**, 496-499.
80. T. A. Hewston and B. L. Chamberland, *Journal of Solid State Chemistry*, 1986, **65**, 100-110.
81. W. Tian, M. Stone, D. Mandrus, B. Sales, R. Jin, D. Adroja, and S. Nagler, *Physica B: Condensed Matter*, 2006, **385-386**, 50-52.
82. W. Tian, M. F. Chisholm, P. G. Khalifah, R. Jin, B. C. Sales, S. E. Nagler, and D. Mandrus, *Materials Research Bulletin*, 2004, **39**, 1319-1328.
83. L. P. Cardoso, D. E. Cox, T. A. Hewston, and B. L. Chamberland, *Journal of Solid State Chemistry*, 1988, **72**, 234-243.
84. H. F. Pen, J. van den Brink, D. I. Khomskii, and G. A. Sawatzky, *Phys. Rev. Lett.*, 1997, **78**, 1323.
85. M. M. Thackeray, L. A. de Picciotto, W. I. F. David, P. G. Bruce, and J. B. Goodenough, *Journal of Solid State Chemistry*, 1987, **67**, 285-290.
86. L. de Picciotto, M. Thackeray, W. David, P. Bruce, and J. Goodenough, *Materials Research Bulletin*, 1984, **19**, 1497-1506.
87. L. de Picciotto and M. Thackeray, *Materials Research Bulletin*, 1985, **20**, 187-195.
88. S. G. Kang, S. Y. Kang, K. S. Ryu, and S. H. Chang, *Solid State Ionics*, 1999, **120**, 155-161.

89. K. Ozawa, Y. Nakao, L. Wang, Z. Cheng, H. Fujii, M. Hase, and M. Eguchi, *Journal of Power Sources*, 2007, **174**, 469-472.
90. S. Kim, Y. Nitta, N. Tatiana, and J. Lee, .
91. N. Choi, J. Kim, R. Yin, and S. Kim, *Materials Chemistry and Physics*, 2009, **116**, 603-606.
92. J. H. Song, H. J. Park, K. J. Kim, Y. N. Jo, J. Kim, Y. U. Jeong, and Y. J. Kim, *Journal of Power Sources*, 2010, **195**, 6157-6161.

Chapter 3. Experimental Methodology and Theory

Chapter 3: Experimental Methodology and Theory.

Chapter Contents:

3.1. Chemicals	33
3.1.1. $\text{Li}_2\text{CoSiO}_4$	33
3.1.1.1. Solid State Preparation.....	33
3.1.1.2. Hydrothermal Preparation.	33
3.1.1.3. Mechanical (ball) Milling	34
3.1.1.4. Carbon coating	34
3.1.2. LiMO_2 Anode materials	35
3.1.2.1. LiVO_2	35
3.1.2.2. LiMO_2 (M=Co,Ni,Mn or a combination thereof).....	35
3.2. Electrochemical Techniques	37
3.2.1. Composite Electrode	37
3.2.2. Coin Cells	38
3.2.3. Galvanostatic cycling	39
3.2.4. Potentiostatic cycling.....	42
3.2.5. AC Impedance and DC conductivity	45
3.3. Structural Analysis	51
3.3.1. Transmission Electron Microscopy(TEM).....	51
3.3.2. X-ray Diffraction and Rietveld Refinement	52
3.3.2.1. Diffraction theory	52
3.3.2.2. Structural Refinement.	59
3.4. References:	64

3.1. Chemicals

3.1.1. $\text{Li}_2\text{CoSiO}_4$

3.1.1.1. Solid State Preparation

Lithium acetate (0.02M, Aldrich) was dispersed with cobalt acetate (0.01M, Aldrich) and tetraethylorthosilicate (TEOS)(0.01M, Aldrich) in a 50:50 mixture of distilled water and ethanol. The solution was stirred for two days and the resulting solid filtered and dried overnight at 60°C. The solid was then calcinated at 350°C for 4hrs before being pressed into a pellet for two seconds at a pressure of $13 \times 10^3 \text{ KN/m}^2$ (2 ton/inch²) and heated to 700°C for 3 hours in a reducing gas flow (Ar:H₂ 95:5 V:V, BOC Gas) to suppress any oxidation of the transition metal that may occur.

3.1.1.2. Hydrothermal Preparation.

LiOH.H₂O (0.05moles, Aldrich) was added to fumed SiO₂ powder (0.0125M, Aldrich) in 20ml of distilled water and the mixture was stirred till homogeneous. At the same time CoCl₂ (0.0125M, Aldrich) was added to 10ml of ethylene glycol and stirred under gentle heat until it was seen to dissolve. The two solutions were then mixed and further stirred till homogeneous. This slurry was decanted to a 40ml Teflon lined autoclave and the remaining volume topped up with de-oxygenated distilled water. The autoclave was sealed and placed in an oven for 72 hours at 150°C. The resulting material was filtered and placed in an oven at 60°C overnight to dry.

Not all polymorphs could be achieved directly. To realise the β_I phase the hydrothermally produced β_{II} polymorph was placed in an oven (in air) and quickly heated, at a rate of 300°C/h to 700°C for two hours and allowed to cool with the oven.

To form the γ_0 phase the hydrothermal material was quickly heated at a rate of 300°C/h in an oven to 1100°C for two hours. The oven was cooled to 850°C where the material was removed and allowed to cool to room temperature (the heating regimes were based on the work of West and Glasser¹).

3.1.1.3. Mechanical (ball) Milling

The active material was sealed inside a tungsten carbide milling vessel with two tungsten carbide (\varnothing 10mm) ball bearings. The whole container was then mechanically shaken (SPEX Centri-Prep 8000 M mixer/mill) for 30 minutes and the milled material was recovered.

3.1.1.4. Carbon coating

The as-prepared material was ground with the carbon xerogel precursor (0-20% wt.) in a pestle and mortar in acetone for 10 minutes. The acetone was allowed to evaporate, then the material was placed in a furnace under flowing argon and heated from 500 - 1000°C for 8-24hrs and allowed to cool with the oven.

To make the Xerogel; resorcinol, $\text{C}_6\text{H}_4(\text{OH})_2$ (Aldrich) and formaldehyde, CH_2O (35% wt. aq.) (Aldrich) were mixed in a molar ratio of 1:2. sodium carbonate, Na_2CO_3 (Aldrich) was added as a catalyst at a molar ratio of 50:1 resorcinol: Na_2CO_3 . The pH of the solution was initially set at 6 by addition of dilute nitric acid, HNO_3 (1M, Aldrich). The solution was sealed in a TeflonTM (Dupont) lined autoclave and stirred magnetically for thirty minutes. The mixture was then cured for one week in an oven at 85°C . The resulting gel was washed with acetone for three days, fresh solvent was added daily after vacuum filtration. The washed gel was heated under nitrogen gas in a tube furnace at 65°C for 5hrs, where upon the temperature was increased to 110°C and

held for a further 5hrs. The pyrolysis stage of the dried gel occurred at a chosen temperature (700°C - 1000°C , depending on desired properties for the gel) for three hours under nitrogen.

3.1.2. **LiMO₂ Anode materials**

3.1.2.1. **LiVO₂**

$\text{Li}_{1+x}\text{V}_{1-x}\text{O}_2$ was synthesised from lithium carbonate and vanadium oxide using a solid state method. Appropriate ratios of dried V_2O_3 (Aldrich, 99%) and Li_2CO_3 (Aldrich, 99+%) powders were mixed together in an argon atmosphere, placed in a gas-tight container and subsequently ball-milled for sixty minutes (SPEX Centri-Prep 8000 M mixer/mill). The mixture was then placed in an alumina crucible, covered with a lid (to reduce lithia vaporisation) and heated at 800°C for ten hours under flowing argon. The compound was allowed to cool to room temperature then heated to 850°C for twelve hours under a flowing gas mixture of 95% argon/5% hydrogen (to suppress the conversion of V^{3+} to V^{4+}).

3.1.2.2. **LiMO₂ (M=Co,Ni,Mn or a combination thereof)**

Layered transition metal compounds LiCoO_2 (Aldrich), $\text{LiNi}_{0.5}\text{Mn}_{0.5}\text{O}_2$ (Fluka), and LiMnO_2 (made in house²) were checked for purity by X-ray diffraction and used as received from the supplier. $\text{LiMn}_{0.33}\text{Ni}_{0.33}\text{Co}_{0.33}\text{O}_2$, $\text{LiNi}_x\text{Co}_{1-x}\text{O}_2$ (where $x=0.33, 0.5$ & 0.66) & $\text{LiMn}_{0.5}\text{Co}_{0.5}\text{O}_2$ were synthesised by the resorcinol/formaldehyde gelation method³. Resorcinol (0.1 mol, Fluka; 99%), formaldehyde (0.15 mol, Fluka; 36.5 % in aq.) and lithium carbonate (0.5 mmol, Aldrich) were added to a given amount of

distilled water and the mixture was stirred until the resorcinol was seen to dissolve. Stoichiometric quantities of the lithium and transition metal acetates were added to the stirring mixture until all had dissolved. The resulting solution was then heated in a sealed moist atmosphere for 10hrs at 90⁰C. The resultant mixture was placed in an alumina crucible and calcined in a furnace at 900⁰C for 12hrs in air.

3.2. Electrochemical Techniques

Electrochemical analysis is a broad subject, encompassing many useful techniques, the procedures and theory discussed below represent just a fraction of the many different methods that exist that can be used to inform and illuminate the inner processes occurring inside batteries. For a more in-depth discussion surrounding electrochemistry and the techniques that can be used, a good starting point for general electrochemistry is; *Electrochemical Methods: fundamentals and applications*⁴, more specific to ionic host materials is *Solid State Electrochemistry*⁵ amongst others^{6,7} as well as useful review articles⁸. For AC impedance, *Impedance Spectroscopy*⁹ by Barsoukov and Macdonald and *Electrochemical Impedance Spectroscopy*¹⁰ are useful references.

3.2.1. Composite Electrode

To make a composite electrode for testing, the active material is mixed with a high surface-area carbon to improve conductivity (a binder is also used to improve electrode homogeneity and texture).

The active-material is ground (either in a pestle and mortar or through mechanical milling) with Super P carbon (TIMCAL Graphite and Carbon). A polymer binder (Kynar Flex™ 2801 binder) is then mixed with the material resulting in a composite material with a final composition of active material: carbon: kynar at a ratio of 80:10:10 respectively (this composition is dependent on the conductivity of the active material, better conductivity = less carbon etc.). All capacities are calculated with this in mind and are quoted for the active material only.

3.2.2. Coin Cells

Coin cells offer a convenient method to prepare and test laboratory battery systems. Unlike their commercial counter-parts, coin cells pack a very low density of materials (compared to the rolled cylindrical or prismatic cells for example¹¹) but because of their convenient preparation and durable nature make for an excellent and accessible way to characterise battery systems.

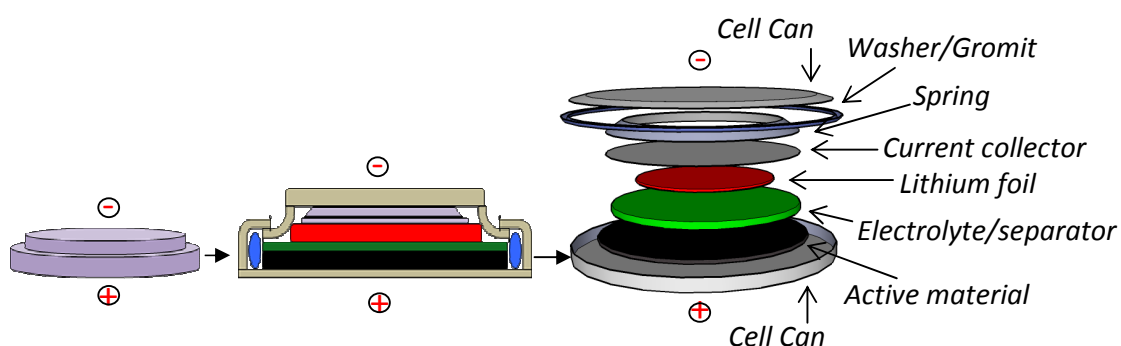


Figure 3.2.1. Schematic of the CR2025 battery coin cell system.

The CR2025 coin cell comprises several individual bespoke components that fit together to form a gas tight seal. Inside the coin cell an electrolyte soaked fibreglass disc separates the cathode from the lithium foil anode. The two electrodes are in turn contacted to a sprung steel current collector, thus ensuring a good contact with the coin cell can. The exterior cell can is made of high quality stainless steel (electrochemically inert in the voltage region under investigation) with a top cap and a bottom cap that fit together utilising a plastic washer/gromit to ensure the internal atmosphere is maintained. When the cell is assembled it is compressed using a pneumatic press to ensure a good gastight seal and contact between various components (as seen in Figure 3.2.1). All cells were constructed and handled in an Ar

filled MBraun glovebox. Electrochemical measurements were carried out using a Maccor Series 4200 battery cycler in a temperature controlled oven.

3.2.3. Galvanostatic cycling

The most widely used battery testing technique is galvanostatic cycling. By the application of a constant current to a cell, the change in voltage as a function of time can be measured. By forcing charge into, or removing charge from a cell the cathode and/or anode undergo reactions to accept or extrude the electrons (and charge carriers). Each reaction has a distinct thermodynamic free energy which corresponds to the voltage observed at the electrode. The length of time a certain voltage is maintained corresponds to the length of time the system is receiving or extruding charge at that voltage. Thus, the amount of charge at a known rate for a given length of time can be used to determine the capacity for each voltage step

The capacity generated by each voltage step (and the reaction associated with it) can then be calculated by the charge passed multiplied by time (t) and is normally quoted as mA.h (milli-amps (mA) multiplied by hours(h)). More commonly used is the gravimetric capacity, which is calculated from the total amount of charge passed per unit mass of the active electrode material (g) for a complete charge (or discharge) given by the equation below.

Equation 1

$$\text{Gravimetric capacity} = Q.t / m$$

Where Q is the constant charge applied (mA) t is the time passed (h) and m is the mass (g)

If we assume all (or nearly all) of the capacity generated from a galvanostatic cycle is generated from the intercalation process, then by dividing the gravimetric capacity by the theoretical gravimetric capacity (given in equation 2) we can match each voltage step to a different composition of lithium in the compound (so after 50mAh/g of capacity passing in a material of the formula LiMO_2 which has a theoretical capacity of 100mAh/g we can say 0.5 Li have been removed, or the materials composition is now $\text{Li}_{0.5}\text{MO}_2$)

Equation 2

For the half reaction; $\text{Li}_n\text{A} \longrightarrow n\text{Li}^+ + n\text{e}^- + \text{A}$

$$\text{Theoretical capacity (mAh/g)} = [(1/m) \times nF]/3.6$$

Where m is the molar mass of A , n is the moles of Li^+ ions exchanged, F is the Faraday constant (3.6 is the conversion factor encompassing the change from seconds into hours and amps to milli-amps).

This allows us to plot how the voltage changes with lithium composition, which is similar to an 'equation of state'. If the electrode undergoes reversible changes from cycle to cycle then the plot should not change between cycles, and hence the plot must not change as a function of cycle number.

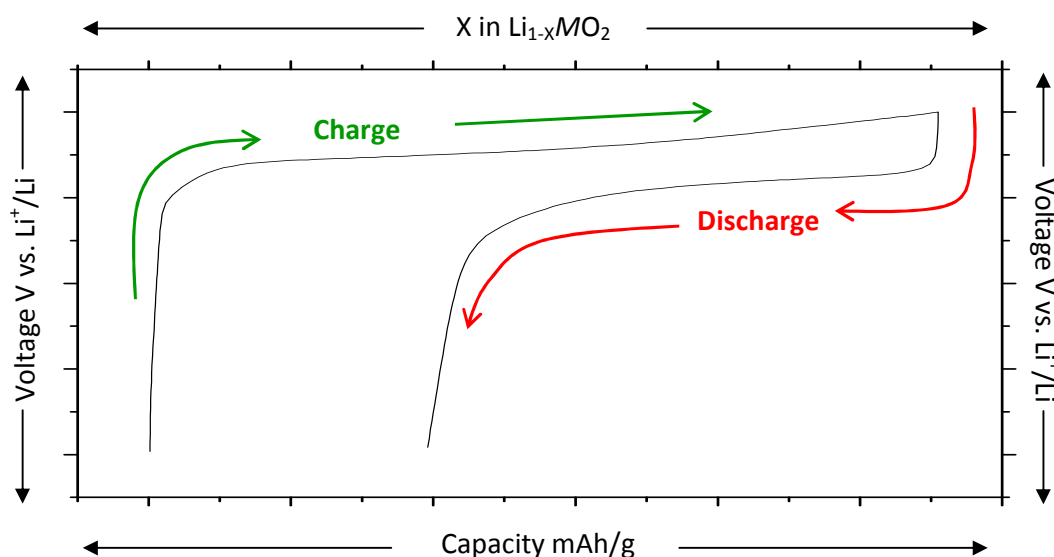


Figure 3.2.2 Schematic of a galvanostatic charge and discharge profile.

Figure 3.2.2 shows a typical galvanostatic profile of a cathode material with a lithium counter electrode. The initial steep voltage increase on charging suggests no electrochemical activity at those voltages due to the minimal capacity generated. The voltage plateau is the first hint of a sustained electrochemical process. The existence of a flat plateau is due to a two phase transformation process caused by the co-existence of two phases, a Li^+ dilute and a lithium concentrated phase with a distinctive voltage associated with the transformation from one to the other. The movement of lithium ions is dominated by a phase boundary movement rather than Li diffusion through particles (characterised by a sloping galvanostatic profile). After the charging section of the cycle has reached the designated voltage cut off the current is reversed and discharge begins. Discharge is characterised by an inflow of current to the cathode, in Figure 3.2.2 this is displayed as reduction of capacity. In a fully reversible system the charge and discharge sections of the galvanostatic profile should be almost equal-ideally with similar length plateaus (the profile in Figure 3.2.2 generates more capacity on charging than discharging).

An extension of this technique is the incremental capacity plot (or differential capacity plot) where the differential product of the galvanostatic plot is plotted against voltage (E vs. dQ/dE). This is calculated from adjacent points in the voltage time data using the known value for the current I and the active electrode mass m . The resulting plot is roughly analogous to the potential sweep voltammetry technique with some important differences. The plot shows the rate of change of capacity versus the voltage, thus plateaus are equivalent to a constant rate of change and peaks equate to a local maxima or minima (i.e. a plateau in the galvanostatic plot). Unlike with potential sweep techniques, there is little or no sweep rate dependence

and hence the exact voltage position of the peaks is less likely to be masked by overcharge issues. This technique has the advantage of easily identifying individual processes within the electrochemical cycle because each peak represents a plateau from the galvanostatic load curve, with the voltage of the peak representing the mid-plateau voltage. Thus even minor galvanostatic plateaus can be identified by the peaks in an incremental capacity plot. By integration of the area under the peak we are also able to calculate the exact capacity of each peak (and hence the capacity of the associated electrochemical process).

A special case of galvanostatic cycling is Galvanostatic Intermittent Titration (GITT). It is a method to establish the equilibrium (or near equilibrium) voltage of the material, versus lithium composition of an electrode. To achieve this, a pulse of current is applied to a cell for a discrete time period (thus inserting or removing a known amount of lithium and hence causing a voltage response from the electrode). The cell is then allowed to relax to an open circuit voltage which can be linked with the current lithium composition of the cell. The time taken to reach open circuit voltage upon relaxation can provide information on the kinetics of electrode processes.

3.2.4. Potentiostatic cycling

Potentiostatic cycling (including voltammetry and cyclic voltammetry) utilises a different method to galvanostatic cycling. Instead of current being applied and the voltage measured, a uniformly changing voltage is used to generate a current, which is then measured and thus, the relative amount of current generated at a certain voltage can be plotted. Since the thermodynamic free energy of an electrochemical reaction

can be linked to the voltage, the amount of charge developed at a voltage is indicative of the amount of charge developed by a reaction linked with that voltage (once the number of electrons involved with the reaction are known, the amount of current generated can be used to inform on matters such as kinetics of the reaction).

Due to the constantly changing nature of the voltage, the amount of current generated is dependent on internal and external kinetics of the material and the system at large (e.g. if the sweep rate is on a considerably faster kinetic scale to lithium diffusion through the particle, only a small amount of generated current will be observed at the voltage usually associated with lithium removal/insertion, i.e. equilibrium voltage). So by altering the speed at which the voltage changes (the so called 'sweep rate') various kinetic parameters of the system can be determined and the various rate dependencies of electrochemically distinct processes can be determined.

A key factor in voltammetry is the over-potential, at high sweep rates or when the reaction is kinetically hindered the potential at which charge is developed may be different from the equilibrium potential for the reaction; this must be taken into account when looking at the absolute voltage. The over-potential is governed by the relationship described in the Nernst equation (given as for the reduction half reaction in equation 3)

$$\textbf{Equation 3} \quad \varepsilon = \varepsilon^0 - (RT/nF) \cdot \ln(C_{\text{oxidised}}/C_{\text{reduced}})$$

Equation 3. Nernst equation. ε is the observed reduction potential, ε^0 equilibrium potential, R is the universal gas constant, T is the temperature, n is the number of electrons being transferred, F is the Faraday constant, C_{oxidised} is the concentration of oxidised species present and C_{reduced} is the concentration of reduced species present- to convert the equation for the oxidised half reaction invert the concentration term

A cyclic voltammetry plot is shown in Figure 3.2.1 for the common electrolyte LP30. The profile shows very little current generated across the 1-5V region selected (note for slower scan rates more current would be expected as the system is less kinetically hindered) the rise at the end of oxidation near 5V is the electrolyte disassociating suggesting that above $\sim 4.6\text{V}$ the electrolyte may become unstable and side reactions may become prevalent. On reduction, near 1V we see a slight increase in current suggesting the start of an electrochemical process and may define the low voltage stability of the electrolyte. It can be observed that this reaction is seemingly a reversible process (at least in the non-technical sense of the word) due to the presence of a corresponding peak at 1.5V with oxidation (slightly offset due to over-potential effects) and, alternatively, may represent impurities in the sample.

From a battery electrode point of view when testing with cyclic voltammetry, mildly offset, symmetric peaks in both oxidation and reduction sections which do not change with repeated cycling show a stable lithium insertion and removal process.

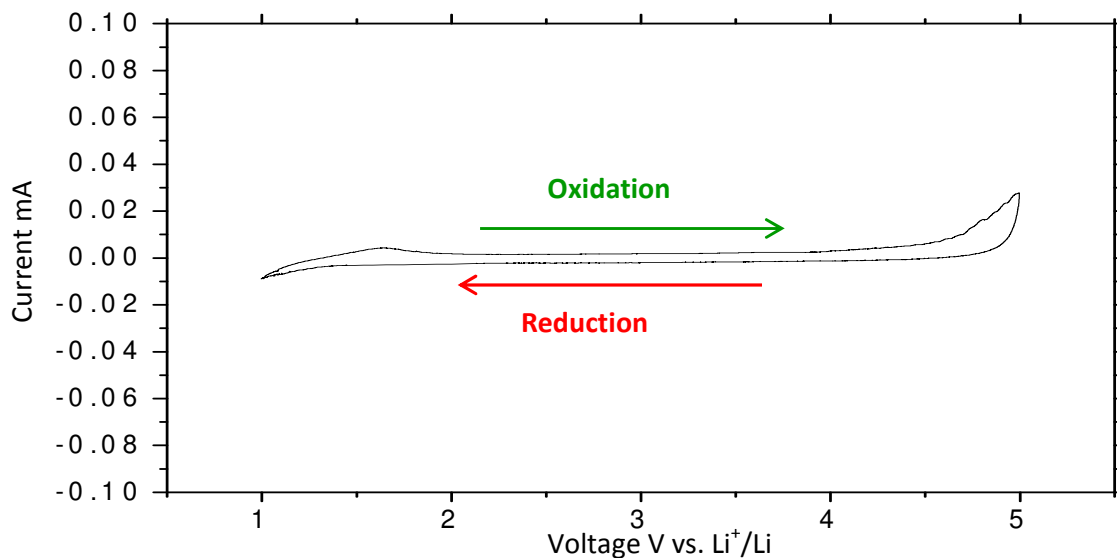


Figure 3.2.3. Cyclic voltammetry plot for the electrolyte LP30 (1:1 by weight mixture of dimethyl carbonate(DMC) and ethylene carbonate(EC) with 1M LiPF_6 as the conductive salt) at a (slow) scan rate of 0.05mV/s at 30°C.

Potentiostatic measurements were carried out on a Biologic VMP3 multichannel potentiostat, using the ECLab program to record data.

3.2.5. AC Impedance and DC Conductivity

Much of electrochemistry is dominated by the interactions that occur at interfaces; various physical factors (electrical, morphological, crystallographic etc.) affect the conductivity of the system as a whole due to the inhomogeneous distribution of charge (polarisations) at the interface. Each interfacial interaction will have distinct polarisation behaviour when a potential difference or current is applied. The rate of change of polarisation when the potential (or charge) is applied or reversed will also be individual to the specific interface, allowing further characterisation of the interface.

Qualitatively the polarisation change is slow for chemical reactions and significantly faster across grain boundaries. Double layers and their capacitances, ubiquitous throughout many 'wet' electrochemical systems, can be determined by their (distribution of) relaxation times. While individual materials may produce a simple polarisation relaxation signature. The many interactions of individual components within an electrochemical system combine to form a cumulative signal which may contain overlapping contributions from various sources making determining individual contributions a distinctly non-trivial task.

Within the context of battery systems Impedance spectroscopy can be used to characterise the properties such as the dynamics of mobile charge carriers in the bulk or in boundary regions of materials, as well as the charge associated with electron transfer at the solid-electrolyte or solid-solid interface.

The basic impedance experiment consists of applying a known voltage or current and observing the resulting current or voltage response. The voltage (or current) is applied as an oscillating single frequency and the phase shift and amplitude (the real and imaginary parts, respectively) of the response of the current (or voltage) is recorded and analysed using Fast Fourier Transforms (FFT); this is normally repeated for frequencies in the range from mHz to MHz. The frequency signal can be described as a wave using $v(t) = V_m \sin(\omega t)$ where $v = \omega/2\pi$ (and ω is the angular frequency), the resulting current response can be characterised by $i(t) = I_m \sin(\omega t + \Theta)$ where Θ describes the phase difference between the voltage and current (DC measurements are a special case of this, as there is no oscillation in the current there is no lag in the voltage response hence $\Theta = 0$, and the simple ohmic relationship can be used).

Response from the capacitance and inductive elements can be divined from differential equations but the picture becomes increasingly complicated: a situation that is remedied through Fourier transforms. For simplicity, the frequency domain voltage/current relationship can then be expressed using the ohmic relationship of $I(j\omega) = V(j\omega)/Z(j\omega)$ where the resistance has been replaced by the complex impedance (Z), (for capacitance $Z(j\omega) = 1/C \cdot j\omega$ and for inductance $Z(j\omega) = L \cdot j\omega$) using the ohmic relationship a circuit with multiple elements can be modelled in a similar way to multiple resistors.

The real and imaginary elements of Z can be separated by expressing Z as a vector sum of the components a and b along the X and Y axis of a right hand orthogonal axis ($Z = a + jb$ with $j = \sqrt{-1} = \exp(j\pi/2)$) indicating (by counter clockwise rotation) that the real component, a , is along the x axis and b , the imaginary component, along the y axis hence the impedance $Z(\omega)$ is equal to $Z' + Z''j$ with Z' = the real component and Z'' the imaginary (or expressed as rectangular coordinate $Z' = |Z| \cos\theta$ and $Z'' = |Z| \sin\theta$ respectively).

For real world systems (i.e. non ideal) impedance is normally constricted to the time or frequency domain and analytical techniques have grown up both empirically and theoretically, to support these functions. One of the most common ways of analysing impedance data is through a Nyquist plot. It involves a polar coordinate plot with the negative imaginary component ($-Z''$) plotted against the real component (Z'), an example is shown in Figure 3.2.4.

One of the most prevalent techniques to analyse electrochemical Nyquist plots is equivalent circuit modelling. Equivalent circuit model attempts to replicate the

internal ‘wiring’ of the electrochemical systems using common electrical components, by pseudo-empirically producing a circuit model that is equivalent to the internal electrochemical behaviour. The model produces a theoretical Nyquist impedance spectrum and this is compared to the observed experimental spectrum using least squares fitting to determine the appropriate values of the circuitry components. How well the model fits (usually given a χ^2 value) can then be used to analyse if the equivalent circuit model needs refinement. The ability of fitting an equivalent circuit is considerably easier with a greater number of elements. This is problematic as this may not represent the true nature of the processes occurring within the system, thus Occam’s razor dominates circuit selection, with the general rule that if a new element does not reduce the χ^2 value by an order of magnitude then it can be ignored.

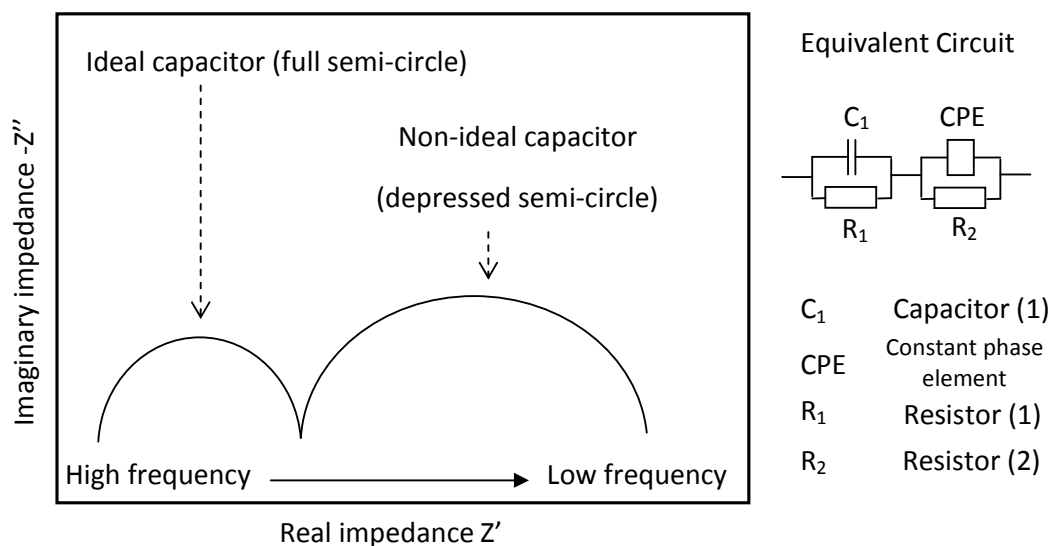


Figure 3.2.4 Example Nyquist plot.

To model the equivalent circuit a dipole couple of a capacitor and resistor in parallel is used. This is thought to model an individual time domain component, this describes the left hand, high frequency, semi circle. This is set in series with a constant

phase element and another resistor. The constant phase element accounts for the non-ideal nature of the capacitor (and hence, the semi-circle). Many explanations exist why some real-world systems do not display ideal capacitor behaviour, but it is generally thought that it is a consequence of inhomogeneous nature of the physical properties in the corresponding element in the real system)¹⁰. The constant phase element is described by the equation below (eq. 4):

$$\textbf{Equation 4} \quad Z_{CPE} = 1/(Q_o \omega i)^n = 1/(Q_o \omega^n) \cdot e^{-\pi/2 \cdot n i}$$

Where $Q_o = 1/|Z|$ at $\omega = 1$ rad/s, n then describes the 'ideality' of the CPE, $n=1$ is an ideal capacitor, $n=0$ is a pure resistor.

The equivalent circuit, shown adjacent to the Nyquist plot in Figure 3.2.4 displays a typical equivalent circuit that could be used to model the plot. It suggests that the plot was generated by a material (or system) with 2 different polarisation behaviours connected in series. This is typical of a polycrystalline material where the electrical interactions are dominated by bulk interactions (the high frequency semi-circle) and grain-boundary interactions (low frequency semi-circles), thus the individual capacity and resistance contributions from different physical regions in the material can be separated out and analysed individually (though care is needed to ensure only contributions from the active materials are present). Obviously, with more complex systems (such as a complete battery system) the picture becomes notably more complicated as more systems interact and overlap and care must be taken with analysis.

AC impedance and DC conductivity measurements were produced using Solatron Analytical Modulab equipment and the Modulab program, in conjunction with 2 stainless steel blocking electrodes. Equivalent circuit fitting was undertaken

using the ECLab Zfit program. All measurements were taken in a temperature controlled oven (Room temperature was set at 22⁰C).

3.3. Structural Analysis

3.3.1. Transmission Electron Microscopy(TEM)

Transmission electron microscopy (TEM) acts in a similar manner to other forms of microscopy in that a beam of light (or electrons) is incident on a material/substrate and the following scattering of the beam allows observation of physical properties of the material/substrate. In the case of TEM, electrons are the used as the incident beam. They are chosen specifically for their smaller de Broglie wavelength, allowing them to probe at a higher resolution and finer detail than visible light microscopy, this allows studying of materials on a micro (crystallite) to nano (molecular and even atomic) meter scale. Transmission electron microscopy uses a beam of electrons incident on a substrate, after passing through the substrate the scattered electron beam is incident upon a CCD detector and an image is developed. Under vacuum the TEM uses an electron gun to generate a beam of electrons which is focussed by a series of magnetic lenses, this is then incident on the sample and the transmitted electrons are picked up by the CCD detector.

All TEM images were taken by Mr Yu Ren, using a Jeol JEM-2011 HRTEM.

3.3.2. X-ray Diffraction and Rietveld Refinement

The following discussion is just a brief overview of the theory behind X-ray diffraction and structural refinement, more authoritative and definitive descriptions can be found in many text books, some good examples are the relevant chapters in Kittel's solid state physics text book¹², similarly the textbook of Ashcroft and Mermin¹³ and the work of Woolfson¹⁴

3.3.2.1. Diffraction theory

When X-rays are incident upon electrons they are scattered, upon interacting with planes of electron density of similar scale to the X-ray wavelengths, constructive and destructive interference is set up within the scattered beams. This gives rise to the 'peaks' of a diffraction pattern, occurring where the scattered X-rays constructively interfere with so called 'crystal planes' and give areas of varying photon intensities on the detector. The angle from the incident beam can be used as a dimension to describe the position of photon intensity peaks within the scattered beam. The condition for interference of radiation scattered from crystalline materials was first described by Laue¹⁵⁻¹⁷ (for which he subsequently won the Nobel prize in physics) and later expanded by the Braggs¹⁸ (who were awarded the Nobel prize in physics the following year). By visualising a crystal as formed by infinite, uniformly spaced, parallel planes Bragg was able to theorise how X-rays would scatter from a crystal. Bragg the younger suggested that the angle of incident would be equal to the angle of reflection (θ). Under this condition the radiation reflected from successive planes interfere constructively whenever their path difference is an integral multiple of the incident

wavelength (i.e. when the phase difference of the scattered wavelengths equals $n2\pi$) giving the famous Bragg condition.

Equation 5.
$$n\lambda = 2d\sin\theta$$

Where n is the n is the integral, λ is the wavelengths of incident radiation, d is the distance between planes of uniform electron density, θ is the angle between planes and the incident/reflected radiation.

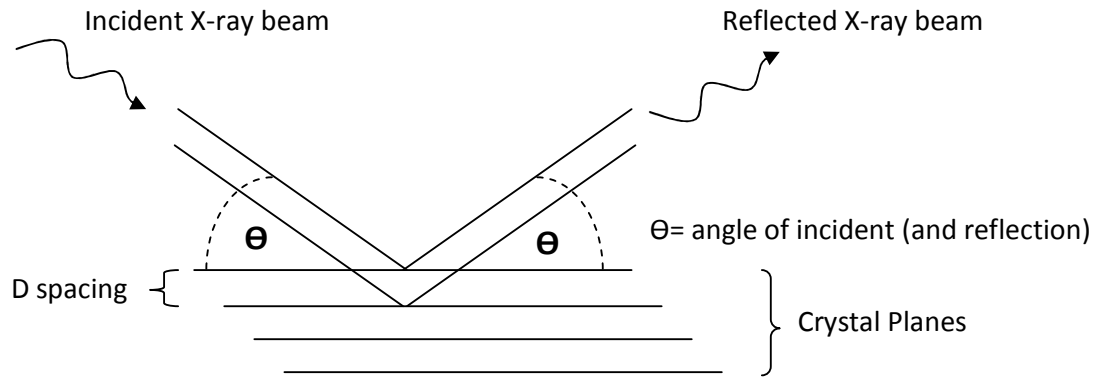


Figure 3.3.1. Schematic of X-ray beam scattered from crystal planes.

For powder diffraction the samples consist of very small crystallites which are randomly orientated with respect to the incident beam. The random particle orientation will cause planes correctly orientated to the beam within the crystallites to scatter the beam constructively. As there is effectively an infinite number of crystallites within the powder (and hence an infinite number of orientations) all planes will be represented and hence all reflections can be observed.

A three dimensional repeating unit (unit cell) motif can be identified within the crystal structure which can be used to describe the atomic positioning throughout the entire crystal. The vast majority of materials have a unit cell that can be described by a Bravais lattice; these are a collection of 14 different crystal systems defined through

the ratio of the dimensions of the unit cell, the angles between the sides and the symmetry of the lattice.

To relate the Bravais lattice to the diffraction pattern we can use Miller indices. By labelling the sides of a unit cell h, k and l (along the X, Y , and Z axes, respectively) and equating the full length of the unit cell to one, we can then describe how a lattice plane intersects through a unit cell, by describing the point at which all three axis of the unit cell are intersected by a crystal plane (as a fraction of one). Each crystal plane that bisects the unit cell can be assigned an h, k, l value that corresponds to position of the intersecting crystal plane with respect to the unit cell. As each suitable crystal plane will generate its own constructive interference peak (i.e. peak in the diffraction pattern) these peaks can be assigned h, k, l values and be used to identify the unit cell from the diffraction pattern.

To determine the individual ionic or atomic positions in a unit cell (or crystal plane) a more intricate method has to be invoked. It helps if we look at the Laue approach in closer detail (Von Laue developed his work before the two Bragg's work, and connects the scattering angles and the size and orientation of the unit-cell spacing in the crystal. Bragg built on this to produce the Bragg law which connects the observed scattering with reflections from evenly spaced crystal planes within the crystal).

Similarly to Bragg's description, Von Laue considered a beam incident upon a lattice. Von Laue defined the conditions that two atoms/ions described by a vector would have to satisfy in order for there to be constructive interference. The scattered

rays will constructively interfere when the difference between the periods of the incident and scattered beam is an integer multiplied by 2π .

In the case of a Bravais lattice, all atomic positions can be described by the vectors separating them i.e. the lattice is made up of an infinite set of points generated through discrete translation operations, so that the lattice can be expressed by a single term (\mathbf{R}) formed by the sum of vectors that span the lattice. The requirement for constructive interference then becomes that the difference between the incident and scattered beam wave vectors, after diffraction through atomic positions(\mathbf{R}), is equal to an integer multiple of 2π . This is similar to saying any momentum transfer (i.e. change in wave vector) must have a periodicity of the Bravais lattice.

The set of wavevectors that are able to meet this condition are called the reciprocal lattice. As this is just an inverse of the 'real space' lattice, this is itself a Bravais lattice and can be described using the primitive vectors related to the real space lattice vectors by a geometric relationship. This reciprocal lattice vector (\mathbf{G}) can then be used to describe planes in the real lattice (as each crystal plane will have a reciprocal lattice vector that is normal to it) and so a plane with Miller indices of h,k,l , can be related to a reciprocal lattice vector.

It is then possible to relate the Von Laue conditions to the Bragg equation by stating if the difference in incident and scattered beam periodicity equals the reciprocal lattice vector(\mathbf{G}) the scattering must be elastic (i.e. the incident and scattered beams have the same magnitude) thus, the incident and scattering angle must be the same. By being able to describe the Miller indices of the real lattice in

terms of reciprocal space, Bragg was able to build on Von Laue's work and develop his famous equation relating the spaces between crystal planes to the scattering angle of the incident beams.

From the Bragg equation (and Von Laue conditions) it can be seen that the diffraction peaks give the spacing between different crystal planes within the material, with each peak being assigned its own set of Miller indices to describe how it bisects the unit cell. These inter-planar distances can be used to assign the crystal to a crystal system and develop approximate values of the lattice parameters.

While it is possible to employ a computational method to search crystal systems for a reasonable d spacing match, a large number of peaks are required and the method is not fool-proof. In the vast majority of cases a prediction is made about the expected crystal system based on the materials and synthetic procedure used to form the materials, as well as any other methods of chemical analysis used in conjunction with the X-ray diffraction.

Bravais showed that there are only 14 types of space lattice when defined by their point symmetry, which is the symmetry taken from a central point in the lattice. This can define the repeating unit of the crystal without needing to directly reference the atoms/ions present. Finally an additional descriptor is added to fully describe the translational symmetry of the lattice. This involves describing spatial shifts in the symmetry in addition to point symmetry, when this is taken into account there are two hundred and thirty combinations which can describe any crystal symmetry, these are called the space groups.

After the lattice parameters of the unit cell have been determined and the reflection peaks have been assigned Miller indices, a study of the missing reflections can reveal the lattice type (face centred, body-centred, primitive) and the transitional symmetry elements can be found. While the positions of the peaks are able to inform about the type of lattice, their relative intensities (peak height) can give information about the atomic arrangement inside the cell with reference to any lattice point.

Revisiting the conditions for constructive interference; if an incoming wave is scattered from two points r_i and r_j the path difference between the scattered rays will be differ by a factor of $e^{i\Delta\mathbf{k} \cdot (\bar{r}_i - \bar{r}_j)}$ (where $\Delta\mathbf{k}$ is the difference between the incident and scattered wavevectors). Similarly the rays scattered from $\bar{r}_1 \rightarrow \bar{r}_n$ will have phases in the ratio of $e^{i\Delta\mathbf{k} \cdot (\bar{r}_1)} \rightarrow e^{i\Delta\mathbf{k} \cdot (\bar{r}_n)}$ and so, to describe rays from the entire cell the expression $S_{\Delta\mathbf{k}} = \sum_{j=1}^n e^{i\Delta\mathbf{k} \cdot \bar{r}_j}$ can be used.

The condition for constructive interference requires $\Delta\mathbf{k}$ be a reciprocal lattice vector (\mathbf{G}), so the factor associated with a particular Bragg reflection can be expressed in terms of \mathbf{G} as $S_{\mathbf{G}} = \sum_{j=1}^n e^{i\mathbf{G} \cdot \bar{r}_j}$. This is called the structure factor. The structure factor indicates to what extent a particular Bragg reflection is diminished by interference effects between identical ions. As the X-rays scatter from areas of electron density the total scattering from a distinct volume will be dependent on the concentration of electrons in that volume which can be expressed as a volume element dV which is proportional to the electron concentration. Expanding this idea to encompass atoms with different electron densities, a Fourier Transform can be applied to the structure

factor for an electron density of n_j for each atom j . This modulating factor is called the atomic scattering factor. The atomic scattering factor is an integral over all space associated with electron concentration of the j^{th} atom multiplied by the phase factor.

The phase factor depends on the position of the electron density with respect to the centre of the atom. If the corner of a unit cell is defined as $\vec{r} = 0$ and \vec{r}_j is the centre of an atomic position then the atomic scattering factor can be written as:

$$f_j = \int dV n_j(\vec{r} - \vec{r}_j) e^{i\vec{G} \cdot (\vec{r} - \vec{r}_j)}$$

Adding this to the x-ray structure factor, this achieves:

$$S_G = \sum_{j=1}^n e^{i\vec{G} \cdot \vec{r}_j} \int dV n_j(\vec{r} - \vec{r}_j) e^{i\vec{G} \cdot (\vec{r} - \vec{r}_j)} \text{ or } S_G = \sum_{j=1}^n f_j e^{i\vec{G} \cdot \vec{r}_j}$$

The structural factor, can of course, be written in terms of the miller indices:

$$S_G = \sum_{j=1}^n f_j \exp[2\pi i(hx_j + ky_j + lz_j)]$$

Thus over a large enough number of reflections the structure factor can be used to calculate all the positions of the atoms in the cell.

One final addition to the structure factor is the effect of temperature on the atomic positions in the unit cell and hence the structure factor. Depending upon the temperature, the atoms/ions in the unit cell will deviate from their equilibrium positions through thermal motion (depending on factors such as how tightly bound in place they are etc.). With large deviations of atomic positions there is an effect of diminishing the amplitude of coherent scattering in the cell (by a factor of $\exp(-2B_j \sin^2 \theta / \lambda^2)$ where B_j is the average displacement of an atom J , and is called the

temperature factor in the intensity of the peaks). This temperature factor is called the Debye-Waller factor.

Resolving atomic positions using the structural factor is hampered by one of the most famous problems in powder diffraction structural refinement; the structure factor cannot be measured directly. This is due to the X-ray detector is only able to measure the intensity of the photons hitting the detector (i.e. the number of x-rays hitting the detector as a function of 2θ) but the scattered x-rays not only have amplitude but phase information as well (vital for determining the structure factor). Due to this discrepancy, a method had to be evolved to solve the 'phase problem'. This was done by assuming the structure factor is proportional to the amplitude of the scattered rays, and because the intensity is proportional to the square of the absolute value of the amplitude, the relative intensities of the Bragg peaks can, by proxy be used to determine information about the structure factor.

Thus the final structure factor can be written as:

Equation 6.
$$S_G = \sum_{j=1}^n f_j \exp[2\pi i(hx_j + ky_j + lz_j)] \exp(-B_j \sin^2 \theta / \lambda^2)$$

The full structure factor is equivalent to the Fourier transform of the electronic charge distribution of an atom and depends upon the reciprocal lattice vector. It shows the relationship between a single electron acting as a single point in lieu of an atom and the amplitude of scattered coherent radiation.

3.3.2.2. Structural Refinement.

Structural refinement is a technique employed to model the structural nature of the unit cell. The Rietveld refinement method¹⁹, developed in 1969, introduced an

easy method of structural refinement from powder data. The method relies on a stepwise collection of data such that intensity is measured against a discrete finite 2θ scale. A calculated profile is then measured against the collected data. The calculated profile is built from the unit cell parameters, along with a zero point correction to determine the position of the Bragg peaks on the 2θ scale. The intensities of the peaks are then determined by atomic positions and displacement parameters (i.e. the calculated structure factor).

The individual peak profile is described by a peak function which is generally made up of a linear combination of Gaussian and Lorentzian terms, called the pseudo-Voigt function and defined by $G_{ik} = \eta L + (1-\eta)G$ where η is the mixing coefficient determining the size of contribution from the Lorentzian (L) and Gaussian (G) contribution. Generally an extra term is needed to fully describe a peak shape, accounting for any peak asymmetry due to instrumental and sample defects.

Another parameter that is commonly used considers the preferred orientation of the crystallites. If the powder particles have a common asymmetry to their shape (i.e. a cylinder where length \gg breadth) then it is likely that many of the crystallites will be lying in a similar way. This can cause a bias of certain crystal planes due to the unnatural prevalence of the crystal planes in the particles' orientation. In this work preferred orientation has not been considered, as the particles are generally homogenous in dimensions, confirmed by TEM. Finally a background function is used to describe any non-peak intensity (i.e. background intensity).

The intensity of any calculated point $Y_i(\text{calc})$ is then compared to its observed counter-part $Y_i(\text{obs})$ across all i steps of the pattern. This enables a refinement to take

place by comparing the calculated to the observed pattern and minimising the difference between them.

The so called 'goodness' of fit can be written as $S = \sum W_i |Y_i(\text{calc}) - Y_i(\text{obs})|^2$ where W_i is the weighted factor determined by the standard deviations of intensity of the i^{th} profile point .

Prior to starting refinement it is usual to have already established the nominal composition of the material (usually through knowledge of similar synthesis), the shape and approximate dimensions of the unit cell (from fitting of the d spacings or *a priori* knowledge). It is usual that the most probable space group would have also been established (through previous knowledge and identifying any systematic absences in the diffraction pattern).

Structural refinement employs a computer program (in the case of this work GSAS²⁰ was used) to perform least squares comparison of the calculated pattern to the observed diffraction pattern, attempting to minimise the difference between the experimental data and the model; this is expressed as the weighted R-factor, R_{wp} . The R_{wp} represents the normalised weighted sum of the differences between the observed

profile and the model and can be expressed as:
$$R_{wp} = \left[\frac{\sum_i W_i (Y_i(\text{obs}) - Y_i(\text{cal}))^2}{\sum_i W_i (Y_i(\text{obs}))^2} \right]^{1/2} \times 100$$

Where the sums are taken over all the data points, $Y_i(\text{obs})$ and $Y_i(\text{cal})$ are the observed and calculated profile points, and $w_i = (Y_i(\text{obs}))^{-1}$ is the weighting factor. The parameters, with respect to R_{wp} are minimised, include the scale factor, the fractional coordinates and the temperature factors of individual ions/atoms.

As well as R_{wp} (and R_p , the unweighted R-factor) χ^2 is also quoted. χ^2 is a measure of the 'goodness' of fit. χ^2 is derived from the formula $\chi^2 = S/(N-P)$ where S is the term being minimised, N is the number of profile points and P is the number of parameters, generally the lower the χ^2 value the better, though very low χ^2 values can indicate the number of refinement parameters being employed possible exceeds the resolution of the profile.

The actual refinement involves the minimisation of χ^2 , through variation of the factors that contribute to the model pattern (atomic co-ordinates, displacement factors, peak profile parameters, background function, peak asymmetry, extinction coefficients and scale factors). The least squares process itself focuses on calculating the gradient of the χ^2 function and trying to solve for the gradient equalling zero, i.e. a minima of χ^2 . There are several different methods which can be used (Newton-Raphson, Gauss-Newton etc.) but they all revolve around the above methodology.

Using these calculations, precise information about the crystal structure of novel and well established materials alike can be found. This in turn allows information about the bond length, bond angles and atomic coordination to be determined, which is of great importance when trying to establish the mechanisms and processes involved with cycling anodic and cathodic battery materials.

X-ray refinements were taken on several machines. The choice of machine was determined by the elements present in the materials and the radiation source offered by the machine in order to avoid fluorescence. Measurements of $\text{Li}_2\text{CoSiO}_4$, LiCoO_2 materials were undertaken on Stoe STADI-P powder diffractometer with $\text{Fe-K}\alpha 1$ radiation, operating in flat plate (pristine materials) or silicon sealed 0.5mm \varnothing quartz

capillaries (*ex situ materials*) transmission mode. LiVO_2 and all other LiMO_2 material's diffraction patterns were achieved on a Stoe STADI-P powder X-ray diffractometers with $\text{Cu K}\alpha$ radiation, again operating in flat plate (pristine materials) or silicon sealed 0.5mm \varnothing quartz capillaries (*ex situ materials*) transmission mode.

Rietveld refinements were undertaken using the GSAS program²⁰, utilising the EXPGUI graphical interface²¹.

While this chapter seeks to provide basic explanations of the experimental techniques employed in this thesis, these are just brief overviews of the topics and only hint at the insights these analytical techniques offer. Far more authoritative descriptions exist to enable a more complete use of these powerful methods of analysis. There are also many other techniques which could be employed to provide a different perspective on the internal processes of lithium intercalation, not to mention the many novel analysis methods currently being developed which may provide useful insights in the future.

3.4. References

1. A. R. West and F. P. Glasser, *J. Solid State Chem.*, 1972, **4**, 20-28.
2. A. R. Armstrong and P. G. Bruce, *Nature*, 1996, **381**, 499-500.
3. K. Shaju and P. G. Bruce, *J. Power Sources*, 2007, **174**, 1201-1205.
4. A. J. Bard and L. Faulkner, *Electrochemical Methods: Fundamentals and Applications*, John Wiley & Sons, 2nd edn., 2001.
5. P. G. Bruce, *Solid State Electrochemistry*, Cambridge University Press, New Ed., 1997.
6. R. A. Huggins, *Energy Storage*, Springer, 1st edn., 2010.
7. P. J. Gellings and H. J. Bouwmeester, *Handbook of Solid State Electrochemistry*, CRC Press, 1st edn., 1997.
8. C. M. Julien, *Materials Science and Engineering: R: Reports*, 2003, **40**, 47-102.
9. E. Barsoukov and J. R. Macdonald, *Impedance Spectroscopy: Theory, Experiment, and Applications*, Wiley-Blackwell, 2nd edn., 2005.
10. M. E. Orazem and B. Tribollet, *Electrochemical Impedance Spectroscopy*, Wiley-Interscience, 2008.
11. J. Tarascon and M. Armand, *Nature*, 2001, **414**, 359-367.
12. C. Kittel, *Introduction to Solid State Physics*, John Wiley & Sons, 8th edn., 2004.
13. N. W. Ashcroft and N. D. Mermin, *Solid State Physics*, Brooks/Cole, 1976.
14. M. M. Woolfson, *An Introduction to X-ray Crystallography*, Cambridge University Press, 2nd edn., 1997.
15. M. Laue, *Ann. Phys.*, 1913, **346**, 989-1002.
16. W. Friedrich, P. Knipping, and M. Laue, *Ann. Phys.*, 1913, **346**, 971-988.
17. M. Von Laue, *Annalen der physik*, 1913, **41**, 998-1002.
18. W. Bragg, *Proceedings of the Cambridge Philosophical Society*, 1913, **17**, 43-57.
19. H. M. Rietveld, *J. Appl. Crystallogr.*, 1969, **2**, 65-71.
20. A. Larson and R. Von Dreele, *Los Alamos National Laboratory Report LAUR*, 2000, 86-748.
21. B. Toby, *J. Appl. Crystallogr.*, 2010, **34**, 210.

Chapter 4. $\text{Li}_2\text{CoSiO}_4$

Chapter 4: $\text{Li}_2\text{CoSiO}_4$

Chapter Contents:

4.1. Introduction.....	67
4.2. Results and Discussion	73
4.2.1. Structural Studies of Lithium Cobalt Silicates	73
4.2.1.1. $\text{Li}_2\text{CoSiO}_4$ β_{II} polymorph	74
4.2.1.2. $\text{Li}_2\text{CoSiO}_4$ β_{I} polymorph (hydrothermal)	78
4.2.1.3. $\text{Li}_2\text{CoSiO}_4$ γ_0 polymorph	83
4.2.1.4. $\text{Li}_2\text{CoSiO}_4$ β_{I} (solid state) material	87
4.2.2. Morphological considerations	89
4.2.2.1. $\text{Li}_2\text{CoSiO}_4$ β_{II} material	90
4.2.2.2. $\text{Li}_2\text{CoSiO}_4$ β_{I} (hydrothermal) material	91
4.2.2.3. $\text{Li}_2\text{CoSiO}_4$ γ_0 material	92
4.2.2.4. $\text{Li}_2\text{CoSiO}_4$ β_{I} (solid state) material	93
4.2.3. Electrochemical Performance of as Prepared Materials	94
4.2.3.1. $\text{Li}_2\text{CoSiO}_4$ β_{II} polymorph	95
4.2.3.2. $\text{Li}_2\text{CoSiO}_4$ β_{I} (hydrothermal) material	101
4.2.3.3. $\text{Li}_2\text{CoSiO}_4$ β_{I} (solid state) material	107
4.2.3.4. $\text{Li}_2\text{CoSiO}_4$ γ_0 material	110
4.3. Conclusions and Further work	114
4.4. References.	116

4.1. Introduction

This chapter explores the structural and electrochemical properties of $\text{Li}_2\text{CoSiO}_4$ and three of its polymorphs. *(A summary of some of the results presented in this chapter can be found in two published papers, attached as appendix i and ii).*

While silicate polyanion materials are a well understood class of minerals and have been investigated for a considerable time, their properties as cathode material have only recently been explored. The investigation of the silicate three dimensional polyanion class of compounds is a logical extension of the recent research, and the subsequent commercialisation of LiFePO_4 ¹⁻³. While the Li_2MSiO_4 materials typically offer slightly lower specific capacities than their LiMFePO_4 cousins ($\text{Li}_2\text{CoSiO}_4 = 162.5$ mAh/g, $\text{LiCoPO}_4 = 166.6$ mAh/g) olivine type silicates may offer a cheaper and potentially, more readily available alternative to LiMPO_4 materials. The subtleties in the different chemistries contained within the structures of Li_2MSiO_4 ($M = \text{Fe}, \text{Co}, \text{Mn} \dots$) potentially enables a great degree of engineering available on the molecular scale compared to the LiMPO_4 counter-parts.

While the low toxicity and potentially low price of $\text{Li}_2\text{FeSiO}_4$ and $\text{Li}_2\text{MnSiO}_4$ make these particularly attractive battery materials, it has been suggested that inherent conductivity problems may arise in the manganese and iron analogues which would not be present in the cobalt Li_2MSiO_4 system⁴, making $\text{Li}_2\text{CoSiO}_4$ an obvious material to investigate. Furthermore in $\text{Li}_2\text{CoSiO}_4$ the cobalt ion is positioned in a three dimensional oxide lattice negating many of the safety problems associated with $\text{Co}^{3+/4+}$ electrolyte reactions seen in LiCoO_2 ⁵. $\text{Li}_2\text{CoSiO}_4$ also may provide important

insight into the mechanism of lithium insertion and removal of the Li_3PO_4 type materials.

The first work on $\text{Li}_2\text{CoSiO}_4$ was carried out by West and Glasser^{6,7} in the early 1970s. Several polymorphic structures (derivatives of the Li_3PO_4 structure) were investigated and rudimentary phase diagrams were established. It was found that the Li_2MSiO_4 group may be thought of as based around a slightly distorted oxide hexagonal close packing with half the tetrahedral sites occupied by cations such that face sharing between the pairs of tetrahedral sites is avoided¹. It was found that the structures show polymorphism and can be divided into 2 families, β and γ . Within the β form all the MO_4 (M= Li, Si, Co) tetrahedra point in the same direction, perpendicular to the close packed oxygen plane, sharing only corners with each other. The γ polymorphs contain tetrahedra arranged in groups of 3 with the central tetrahedra pointing in the opposite direction to the outer 2, with which it shares edges, examples of the β and γ polymorphs are shown in figure 4.1.1.

Variants of both β and γ polymorph exist, involving distortions of the parent structures; they are denoted β_{I} , β_{II} , γ_0 and γ_{II} . At low temperatures β is the stable structure and at high temperature γ is the stable equilibrium phase. Cooling the γ form at high temperatures causes a sluggish conversion to the β phase, thus γ can be conserved at low temperatures by rapid cooling. This fast 'quench' suppresses the transition of phases and produces a material that is kinetically stable but only meta-stable thermodynamically. During polymorph transition the oxide layer remains unmoved, with migration between sites only thought to occur amongst the transition metal cations⁶. It is suspected that transition to the sub-polymorphs doesn't involve a

cation migration, instead involving a minor step that only distorts the lattice of the patriarch phase, perhaps through rotation of MO_4 tetrahedra⁷. By re-visiting the polymorphic structures of $\text{Li}_2\text{CoSiO}_4$ materials with modern techniques it should be possible to elucidate a more thorough picture of the differences between the polymorphs and how these structural differences affect the electrochemical behaviour of the polymorphs.

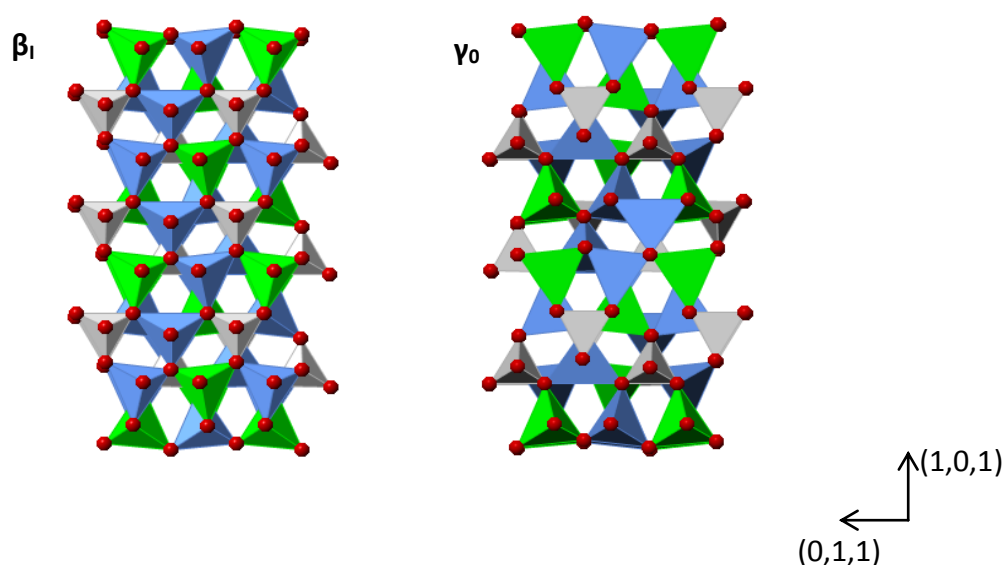


Figure 4.1.1. Polyhedra schematic of β_I and γ_0 $\text{Li}_2\text{CoSiO}_4$ polymorphs: Blue Polyhedra LiO_4 , Grey polyhedra SiO_4 , Green Polyhedra $(\text{Co/Li})\text{O}_4$, Red spheres Oxygen atoms.

Previous work upon the Li_2MSiO_4 structures has been brief and focussed on structural determination, with Glasser *et al.* establishing some basic structures of various Li_xMO_4 and Li_2MXO_4 compounds and investigating the phase boundaries of many of the polymorphs contained within these systems⁶⁻⁹. Subsequent work on Li_2MSiO_4 solved the full structure for some of the polymorphs¹⁰. The Bruce group has recently published two papers covering the preliminary investigation of $\text{Li}_2\text{CoSiO}_4$ materials^{11,12} which has sparked some interest in the topic¹³⁻¹⁶.

From recent first principle work it has been established that insertion voltage (and band gaps) of Li_2MSiO_4 materials roughly correlate to the electronegativity of their late 3rd period metal, e.g. silicon^{1,4}. This behaviour revolves around the M-O-Si

relationship, which is ubiquitous throughout the Li_2MSiO_4 structure. This can be seen in Figure 4.1.1. as the corrugated layers of $\text{Li}_2\text{CoSiO}_4$ where a SiO_4 tetrahedra shares all 4 of the corner oxygen atoms with 4 different CoO_4 tetrahedra and so on through the 3D mosaic. It has been established in LiMO_2 systems that the lithium insertion voltage can be linked to the $M^{n+1/n}$ redox level². It has been suggested that this theory can be extended to the Li_2MSiO_4 system with the addition of the M -O-Si relationship exhibiting a strong influence upon the $M^{n+1/n}$ redox level.

In Li_yMXO_4 materials the precise nature of the transition metal redox level (or bonding to anti-bonding orbital band gap of the M ion) is thought to be intricately linked to the P-block ion (for example, silicon) through the inductive effect across the M -O-X triplet (where M is the transition metal, O is the oxygen and X is the P-block ion, in this case silicon). The inductive effect is manifested by the polarisation of the metal-oxygen bond due to the adjacent Si-O bond. This effect is thought to control the ionic-covalent nature of the M -O bond, and subsequently the redox level of the transition metal ion.

First principles investigations into the factors that affect the transition metal redox level have suggested that, given the nature of the M -O-X group a weak correlation between the electronegativity of the P-block element and the redox level of the transition metal exists⁴. The reasons for this have yet to be experimentally investigated but it has been suggested that by lowering the electronegativity of the X ion in the M -O-X couple, the polarisation of the O-X bond is decreased and the M -O bond subsequently shortens. By shortening the M -O bond the electron density on the transition metal ion is increased and hence affects the $M^{n+1/n}$ redox couple and the

lithium insertion voltage. From an atomic orbital perspective, by shortening the $M\text{-O}$ bond length, the orbital overlap between the O_{2p} and M_{3d} orbital is increased. This pushes 'bonding' O_p orbitals lower and the anti-bonding d-orbitals of the transition metal ion higher, increasing the band gap (the electron that is introduced with Li^+ insertion fills the transition metal anti-bonding d-orbital).

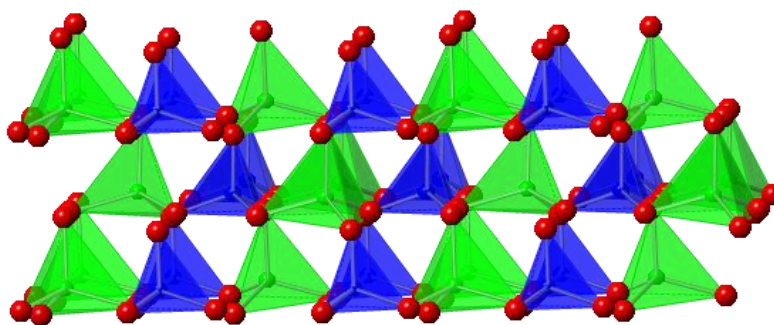


Figure 4.1.2. A schematic representation of the Cobalt(green) to Oxygen(red) to Silicon(blue) connectivity in the β_1 polymorph.

One of the more promising aspects of Li_2MSiO_4 as a battery material is the possibility to insert/remove 2 lithia per formula weight. Recent studies on $\text{Li}_2\text{MnSiO}_4$ and $\text{Li}_2\text{FeSiO}_4$ materials have given mixed results as to their ability to remove more than one electron. The manganese based cathode has been shown to have the ability to remove more than 1 Li^+ ion per cycle^{4,3}. This performance has yet to be well established and attempts to extract more than one lithium from the iron silicate have so far been unsuccessful¹⁷. It is thought the poor conductivity of the manganese sample in its native (un-doped) state and the iron silicate upon removal of 1 Li^+ may be the cause of the lithium extraction limit. By using crystal field theory a consistent picture emerges which explains why the conductivity may have an important role to play in the removal of lithium from the structure.

The nature of the band-gap and orbital into which the electron is inserted dictates the ability of the material to accept or expel an electron during lithium removal or insertion. In the case of silicate materials this orbital is thought to be the LUMO of the transition metal. For example both Mn^{2+} (the reduced state) and Fe^{3+} have half filled orbital states (d^5) according to crystal field theory. When the metals occupy these oxidation states they are particularly stable (or in crystal field terms, the tetrahedral geometry causes a large (hence stable) gap between the filled e to unfilled t_2 level giving transitions between the two a lower probability). This infers a reluctance to accept or lose an electron (the effect will, of course, vary with differing orbital states, degeneracy and bonding/anti-bonding interactions).

The ability of cobalt silicate material to insert or remove more than one lithium is currently unknown, if the crystal field theory is consistent then neither of the cobalt oxidation states should yield a d^5 state and thus should not meet the conductivity problem when removing or inserting more than one lithium. As the electronic conductivity is also intimately linked to the ability of the material to accept or impart electrons, resistivity measurements in conjunction with the galvanostatic performance will be used to assess the affect the transition metal state has upon the lithium insertion process.

There are several structural factors that could affect the lithium insertion/removal efficiency of $\text{Li}_2\text{CoSiO}_4$ materials, and with close analysis of the physical and electrochemical properties of the materials it is hoped that a clear picture of the $\text{Li}_2\text{CoSiO}_4$ lithium insertion and removal mechanisms can be elucidated.

4.2. Results and Discussion

4.2.1. Structural Studies of Lithium Cobalt Silicates

Both solid state and hydrothermal production methods were investigated to determine the most convenient method of $\text{Li}_2\text{CoSiO}_4$ synthesis. Due to the energetic nature of the hydrothermal conditions, the synthesis was expected to produce one of the more thermodynamically stable phases (i.e. closer to equilibrium). If, as suggested in previous work, the $\text{Li}_2\text{CoSiO}_4$ structure is analogous to Li_3PO_4 and its associated β and γ polymorphs⁷, it is most likely that the low temperature Li_3PO_4 variant (β) would be the most thermodynamically stable (given the room temperature existence of γ Li_3PO_4 phase is dependent upon its very slow kinetic transformation to the β phase) and so one of the β $\text{Li}_2\text{CoSiO}_4$ polymorphs would be expected to be produced. According to the work of West and Glasser⁶ the solid state preparation should produce the β_1 phase due to the heating regime involved in the final phase of the preparation method.

4.2.1.1. $\text{Li}_2\text{CoSiO}_4$ β_{II} polymorph

The hydrothermal synthesis method natively produced the phase identified by West *et al.* as β_{II} and the x-ray diffraction pattern (and subsequent Rietveld fitting) can be observed in Figure 4.3.1. The Rietveld fit was made using the $Pmn2_1$ space group and gave a reasonable fit of $R_{\text{wp}} = 8\%$. With suitably similar lattice parameters to those reported previously⁶ (this was further confirmed through subsequent neutron diffraction work carried out by Dr A. Armstrong within the Bruce group, which has since been published^{11,12})

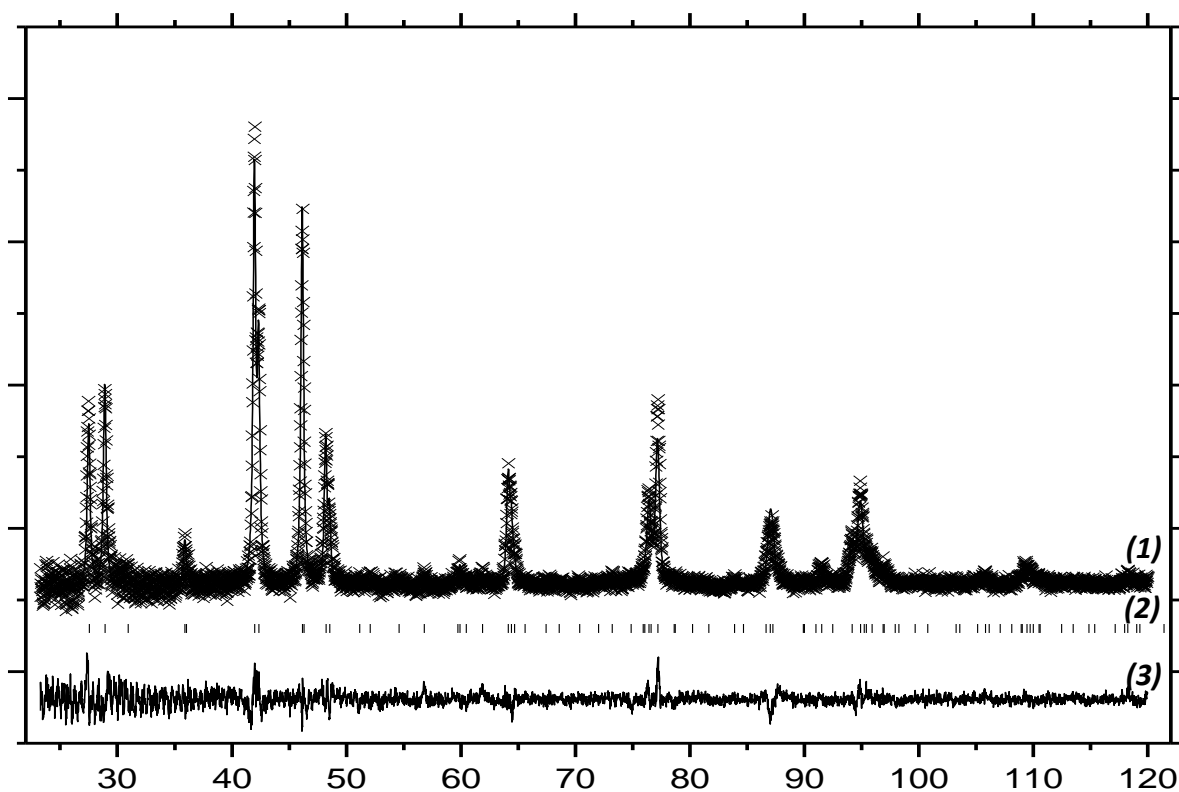


Figure 4.3.1 X-ray diffraction pattern and Rietveld refinement fit of β_{II} of $\text{Li}_2\text{CoSiO}_4$: (1) X diffraction data, - Rietveld fit; (2) Peak marks generated from the $Pmn2_1$ space group; (3) data and fit difference

The material was assumed to be phase pure and free of other impurities. As is shown in Table 4.3.1 the material deviates slightly from an ideal β_{II} model as it contains both lithium and cobalt within the 4b site at approximately equal ratios. This leaves

the 2a site exclusively for lithium occupation, giving the material an overall composition of Li_{2.06}Co_{0.94}SiO₄. (This disorder was also confirmed by a ⁷Li NMR study¹¹)

Atom	Wyckoff Symbol	x/a	y/b	z/c	B _{iso}	Occupancy
Li1	2a	0.0000	0.178(1)	0.760(2)	0.1(7)	1
Si1	2a	0.5000	0.180(2)	0.842(2)	0.10(2)	1
Li2/Co1	4b	0.2529(9)	0.337(2)	0.339(2)	0.13(5)	0.53/0.47(1)
O1	4b	0.270(1)	0.328(2)	0.761(1)	0.02(2)	1
O2	2a	0.0000	0.146(2)	0.247(3)	0.010(1)	1
O3	2a	0.5000	0.181(2)	0.339(2)	0.015(4)	1

$$a = 6.2606(7) \text{ } b = 5.3264(6) \text{ } c = 4.9401(6) \text{ } \text{Space Group: } Pmn2_1$$

$$\text{Cell Volume} = 164.74(5) \text{ } \text{\AA}^3, R_p = 6.22\%, R_{wp} = 8.03\%, \chi^2 = 1.654$$

Table 4.3.1 Refined parameters Li₂CoSiO₄ β_{II} polymorph from the hydrothermal preparation

	Li1-O	Li2-O	Co1-O	Si1-O
O1	2.037(8)	2.189(7)	2.189(1)	1.625(9)
O1	2.037(8)	1.940(8)	1.94(1)	1.644(9)
O2	1.93(1)	1.940(6)	1.94(1)	1.67(1)
O3	2.020(6)	1.893(7)	1.893(8)	1.754(4)
Average Bond Length Å	2.006	1.9905	1.9905	1.6732
Tetrahedra volume Å³	5.41(1)	5.19(2)	5.19(2)	2.62(2)

Table 4.3.2 Selected polyhedra bond lengths and volumes for β_{II} Li₂CoSiO₄ material.

The disorder amongst the cation sites could be due to the hydrothermal synthesis method, where the possibility exists for the nucleation of small crystallites to occur under fairly energetic atomic/ionic movement allowing for significant cation mixing^{18,19}.

Table 4.3.2 displays selected bond distances of the metal tetrahedra within the material and may hint towards some of the electrochemical behaviour of the material. It can be expected that, as the β_{II} phase displays 2 structurally distinct Li^+ sites, removal/insertion of lithium will favour one over the other. There is a chance that the lithium-only 2a site (Li1-O) will be chosen, given that the 4b lithium site shares occupancies with cobalt, possibly occluding the free lithium movement (the 2a lithium site also has the larger of the 2 LiO_4 polyhedra volumes, reducing the thermodynamic burden of lithium movement^{20,21}).

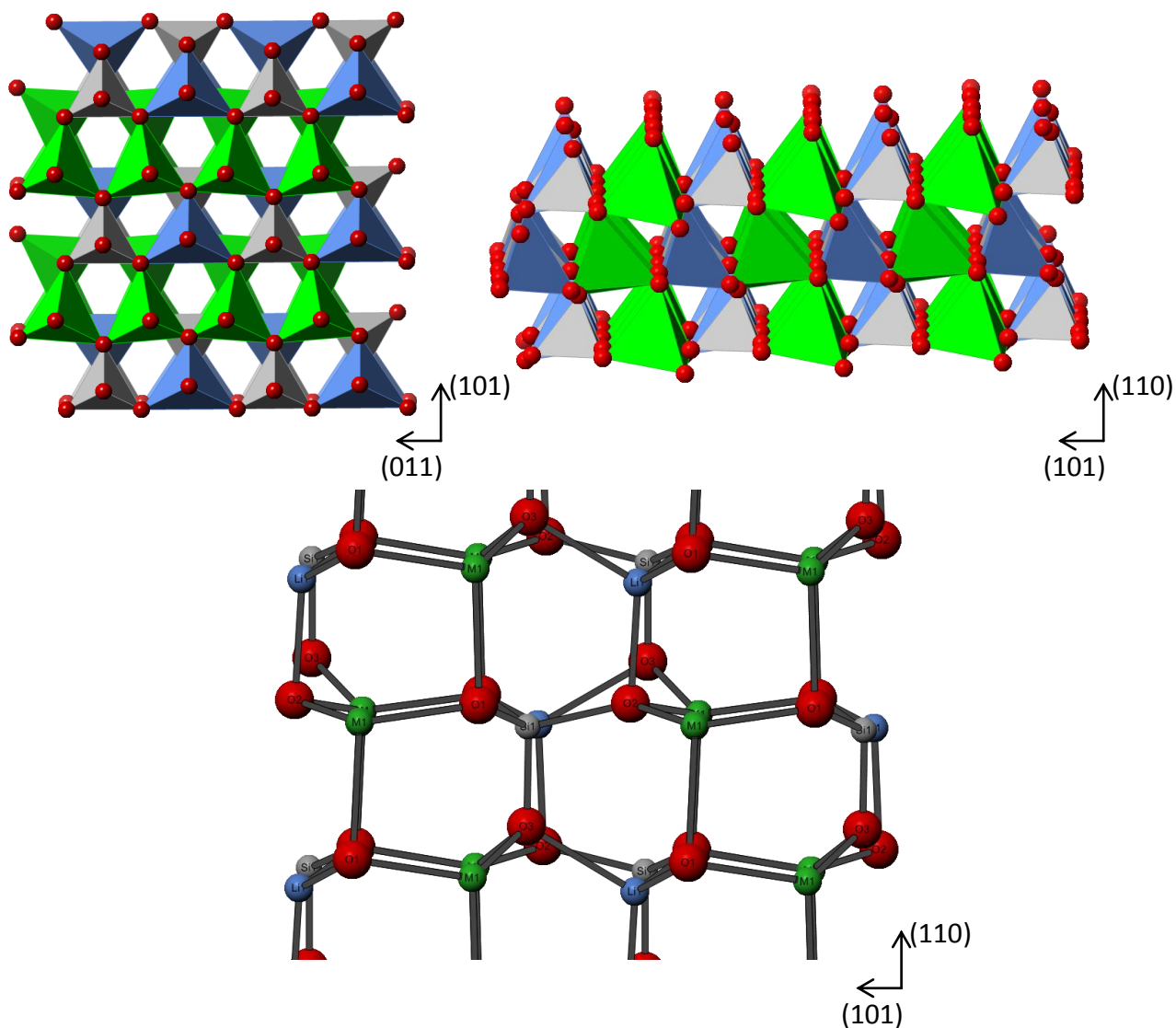


Figure 4.3.2. Schematic representations of β_{II} $\text{Li}_2\text{CoSiO}_4$ structures, obtained from Rietveld refinement. Blue Polyhedra LiO_4 , Grey polyhedra SiO_4 , Green Polyhedra $(\text{Co/Li})\text{O}_4$, Red spheres Oxygen atoms.

Figure 4.3.2. displays structural projections of the β_{II} phase. All polyhedra within β_{II} are arranged so that the vertices of the corner sharing tetrahedra point along the c axis, with the disordered lithium/cobalt tetrahedra translating along the a axis and alternating chains of LiO_4 and SiO_4 tetrahedra running in parallel.

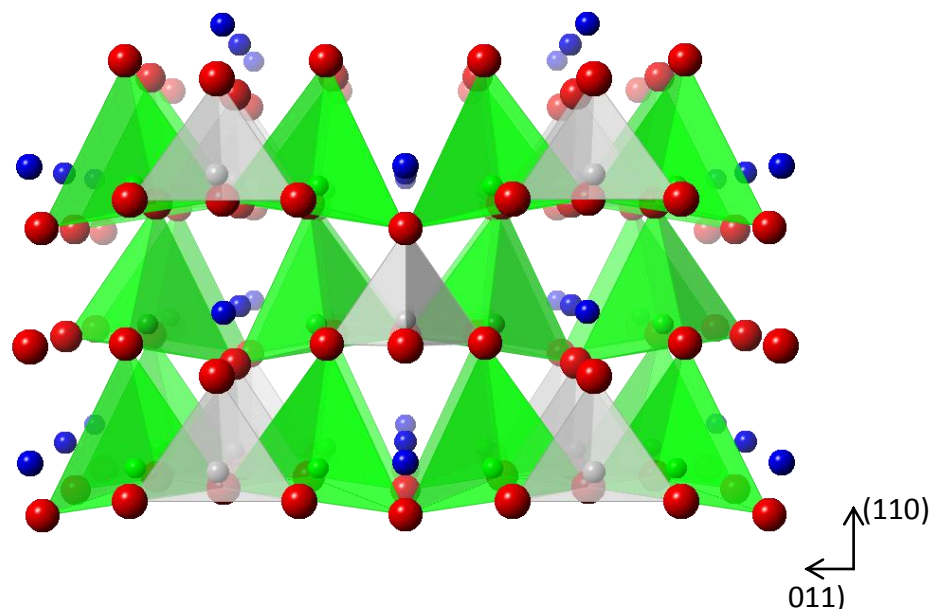


Figure 4.3.3. Schematic representation of a potential lithium insertion/removal pathway in β_{II} $\text{Li}_2\text{CoSiO}_4$; Grey polyhedra SiO_4 , Green polyhedra $(\text{Co/Li})\text{O}_4$, Blue spheres lithium (in 2a site), Red spheres Oxygen).

Figure 4.3.3 shows one of the potential lithium removal/insertion pathways present within the β_{II} phase. The 2a lithium sites are aligned in a linear arrangement along the b axis. Though not placed ideally within this 'tunnel' the lithium ions could easily propagate along the channel, possibly improving the favourability of removing lithium from this site (compared to the 4b shared site, shown as green polyhedra).

The hydrothermal synthesis presents several advantages over the solid state method, such as cost (especially with respect to up-scaling) and exploitation of ‘wet’ chemistry environment to manipulate chemical conditions of production. These factors make accessing the polymorphs from the natively produced β_{II} phase a very attractive proposition. To this end (as suggested by the work of West⁶) the synthesis of the β_{I} , γ_{II} , and γ_0 phases was pursued through reheating the hydrothermal product and using an appropriate temperature/cooling regime to access the other polymorphs.

4.2.1.2. $\text{Li}_2\text{CoSiO}_4$ β_{I} polymorph (hydrothermal)

It was found that the β_{I} phase could be easily achieved by heating the hydrothermally produced β_{II} material to 700°C for 2hrs, in air, and allowing the material to cool with the oven (at a rate of approximately $1.6^\circ\text{C}/\text{min}$).

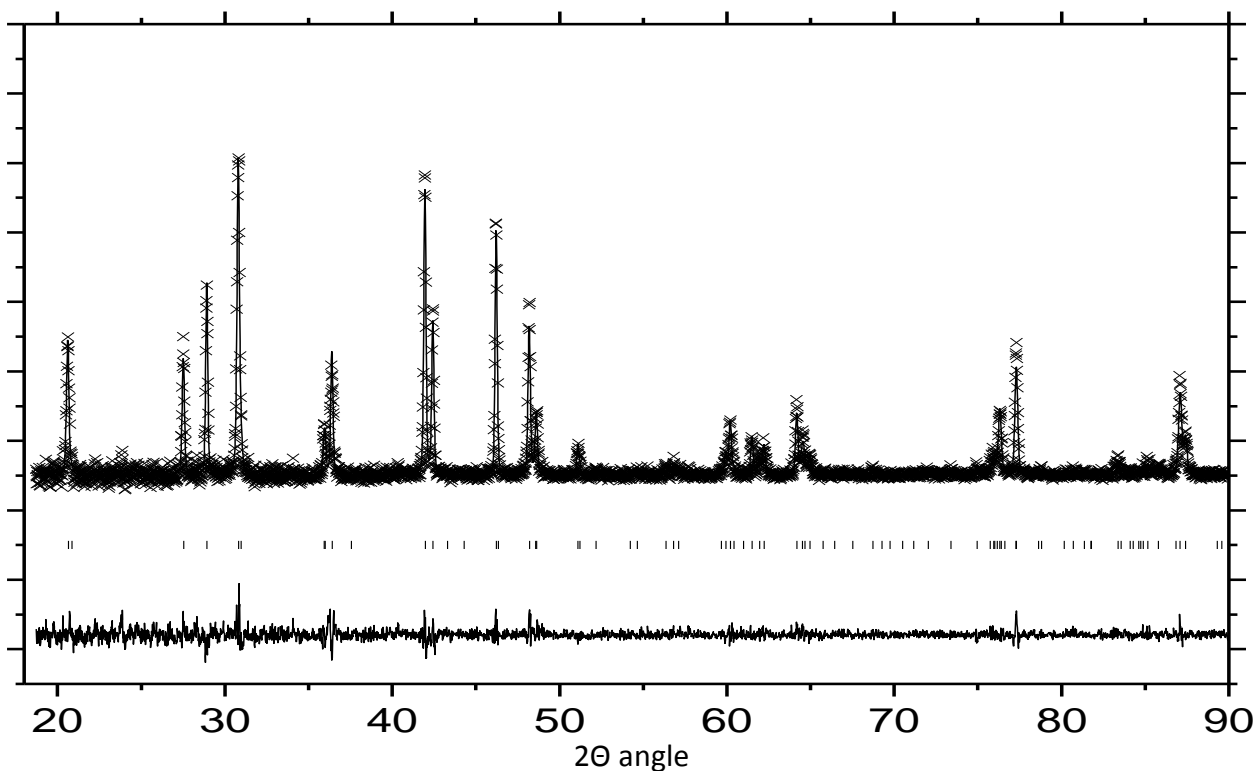


Figure 4.3.4. X-ray diffraction pattern and Rietveld refinement fit of β_{I} of $\text{Li}_2\text{CoSiO}_4$.

The Rietveld fit of β_I was based on the data obtained from a single crystal refinement by Yamuguchi¹⁰ of $\text{Li}_2\text{ZnSiO}_4$, who indexed the structure to an orthorhombic $Pbn2_1$ space group (Yamaguchi reports this material as β_{II} using different notation to West). The β_I (hydrothermal) material gave a fit of $R_{wp}=17.67\%$, which is not ideal though the low $\chi^2(1.157)$ suggests this could be improved by improved diffraction statistics. (The nature of the β_I structure and its structural parameters have subsequently been confirmed through neutron diffraction and the nature of the lithium environments in the structure corroborated with ^7Li NMR¹¹). The β_I material has lower symmetry than its parent β_{II} phase, indicated by the approximate doubling of the unit cell along the b axis. From Table 4.3.3 we can see that cation mixing occurs within both the cobalt site (0.93% Co/ 0.07% Li) and one of the lithium sites (0.95% Li/ 0.05% Co) giving the material an overall stoichiometry of $\text{Li}_{2.02}\text{Co}_{0.98}\text{SiO}_4$. The disorder did not vary greatly when different heating (or grinding and reheating) times were employed and thus, may be a consequence of the disorder in the β_{II} starting material and subsequent formation.

Atom	Wyckoff Symbol	x/a	y/b	z/c	B _{iso}	Occupancy
Co1	4a	0.498(2)	0.1647(7)	0.273(1)	0.054(3)	Co 0.930/Li 0.070(7)
Si1	4a	0.248(3)	0.413(1)	0.265(9)	0.079(6)	1
Li1	4a	0.02(1)	0.160(8)	0.22(2)	0.18(2)	Li 0.95(1)/Co 0.05(1)
Li2	4a	0.69(3)	0.41(1)	0.23(2)	0.12(7)	1
O1	4a	0.033(3)	0.344(2)	0.159(5)	0.01(1)	1
O2	4a	0.240(3)	0.560(2)	0.165(5)	0.017(4)	1
O3	4a	0.251(4)	0.409(2)	0.605(4)	0.009(3)	1
O4	4a	0.475(4)	0.332(2)	0.156(5)	0.012(6)	1

$$a = 6.2826(4) \text{ \AA} \quad b = 10.7029(7) \text{ \AA} \quad c = 4.93465(3) \text{ \AA} \quad \text{Space Group: } Pbn2_1$$

$$\text{Cell Volume} = 331.017(2) \text{ \AA}^3, \quad R_p = 13.02\% \quad R_{wp} = 17.69\%, \quad \chi^2 = 1.157$$

Table 4.3.3. Refined parameters for β_I polymorph obtained via reheating hydrothermal product to 700°C for 2hr.

	Li1-O	Li2-O	Co1-O	Si1-O
O1	1.99(1)	2.29(1)	1.919(8)	1.622(9)
O2	1.843(8)	2.194(6)	1.94(2)	1.64(1)
O3	1.956(5)	1.971(7)	1.962(7)	1.678(1)
O4	2.152(7)	1.69(1)	1.89(1)	1.754(9)
Average Bond Length \AA	1.9852	2.0363	1.9277	1.6735
Tetrahedra volume \AA³	5.166(7)	5.599(7)	4.6(3)	2.62(2)

Table 4.3.4 Selected polyhedra bond lengths and volumes for β_I Li₂CoSiO₄ material.

Table 4.3.4 indicates that there is considerable difference within the MO₄ polyhedra environments present in β_I material compared to the β_{II} phase, with the average Co-O bonds significantly shorter in the former (1.9277 Å vs. 1.9905 Å for β_I

compared to β_{II}). Given the theory presented by Arroyo-de Dompablo *et al*⁴ concerning the Si-O-Co influence upon the $\text{Co}^{3+/2+}$ redox couple, the difference in bond length would qualitatively suggest a higher voltage for the β_{I} material, though due to the many other contributing factors, others may be more dominant. Two distinct LiO_4 polyhedra are present in β_{I} material, both of different volumes suggesting one site will be favoured for lithium removal.

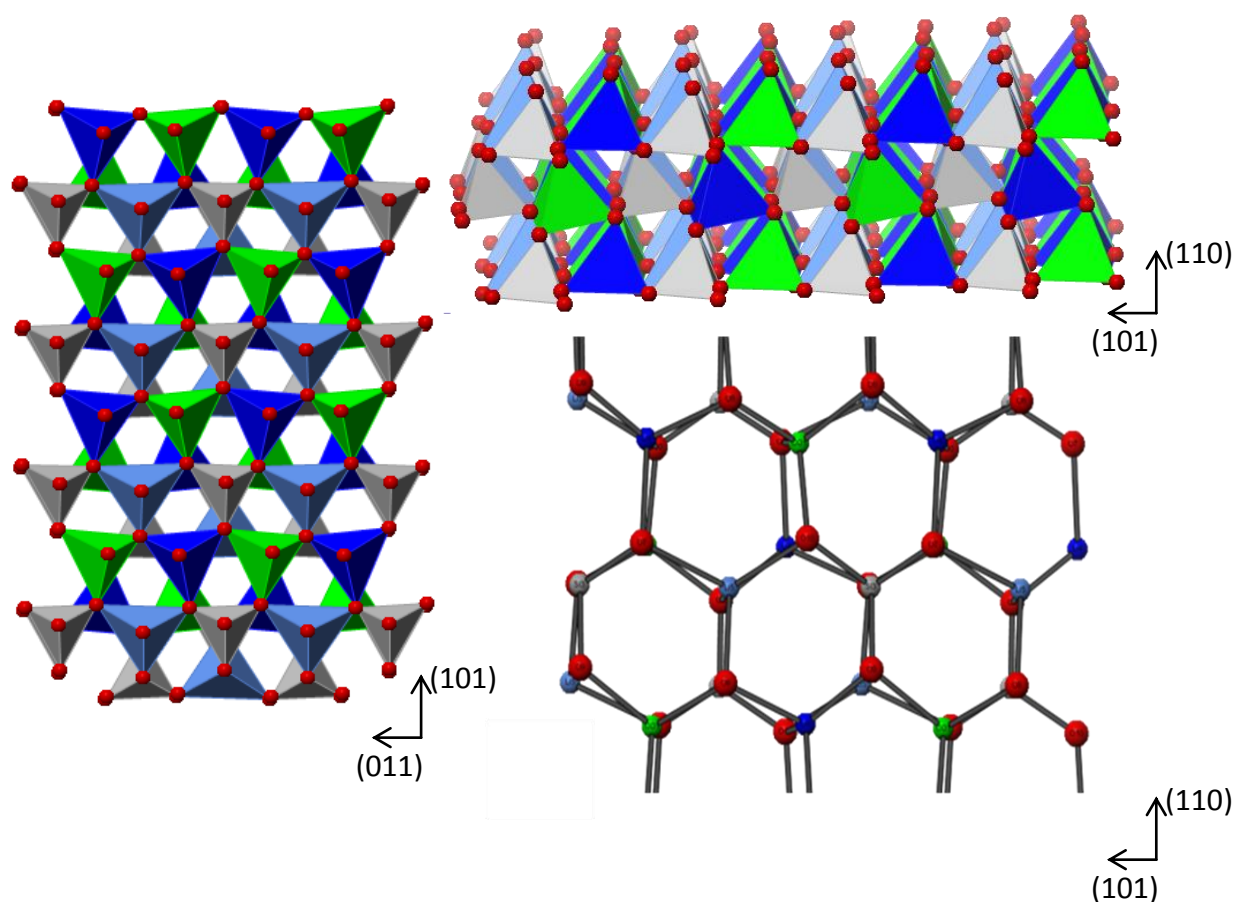


Figure 4.3.5 Schematic representations of β_{I} $\text{Li}_2\text{CoSiO}_4$ (hydrothermal) structure, obtained from Rietveld refinement. Light blue Polyhedra LiO_4 , Dark Blue (Li 95%/Co 5%) O_4 , Grey polyhedra SiO_4 , Green Polyhedra (Co 93%/Li 7%) O_4 , Red spheres Oxygen atoms.

The β_{I} structure consists of alternating layers of polyhedra with their vertices aligned along the c axis. Each layer consists of lines of alternating LiO_4 and SiO_4 ,

interspaced with lines of the two mixed metal oxide tetrahedra propagating along the a axis. The above/below layer consists of similarly alternating polyhedra lines but their polyhedra facing in the opposite direction along the b axis, as the $(1,1,0),(1,0,1)$ projection shows in Figure 4.3.5.

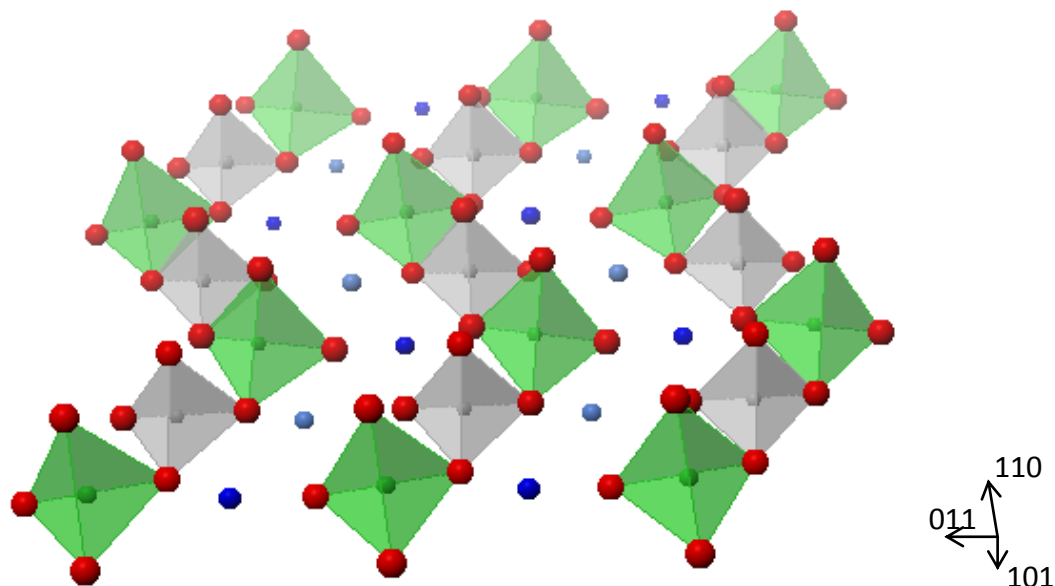


Figure 4.3.6 Schematic representation of a potential lithium insertion/removal pathway in β_I $\text{Li}_2\text{CoSiO}_4$; Grey polyhedra SiO_4 , Green polyhedra (Co 93%/Li 7%) O_4 , Light blue spheres lithium, Dark Blue spheres mixed Li(0.95%) Co(0.05%) site, Red spheres Oxygen.

As demonstrated from the schematics of the β_I material, there are distinct structural differences between the β_I and β_{II} polymorphs. Figure 4.3.6 highlights one possible lithium insertion/removal pathway (also seen as a 'zigzag' of dark/light blue polyhedra in schematic of a,b plane in Figure 4.3.5). β_I does not seem to present the direct Li^+ pathway seen in the β_{II} structure, instead consisting of 'zigzag' tunnels along the b axis. This may be indicative of distinct electrochemical behaviour between the β_I and β_{II} polymorphs.

4.2.1.3. $\text{Li}_2\text{CoSiO}_4$ γ_0 polymorph

West *et al.* noted that the phase boundary for the γ polymorphs lie above 1000°C but observed that the phase hysteresis caused by the sluggish phase conversions can be exploited to produce the γ polymorphs at room temperature. Because the material will naturally revert to the β polymorphs if allowed to slowly cool, the material must be rapidly cooled to maintain the γ structure. To this end it was found that by rapid quenching from above 850°C (removing the sample from the oven to room atmosphere) the γ_0 polymorph could be produced (diffraction pattern and refinement presented in Figure 4.3.7).

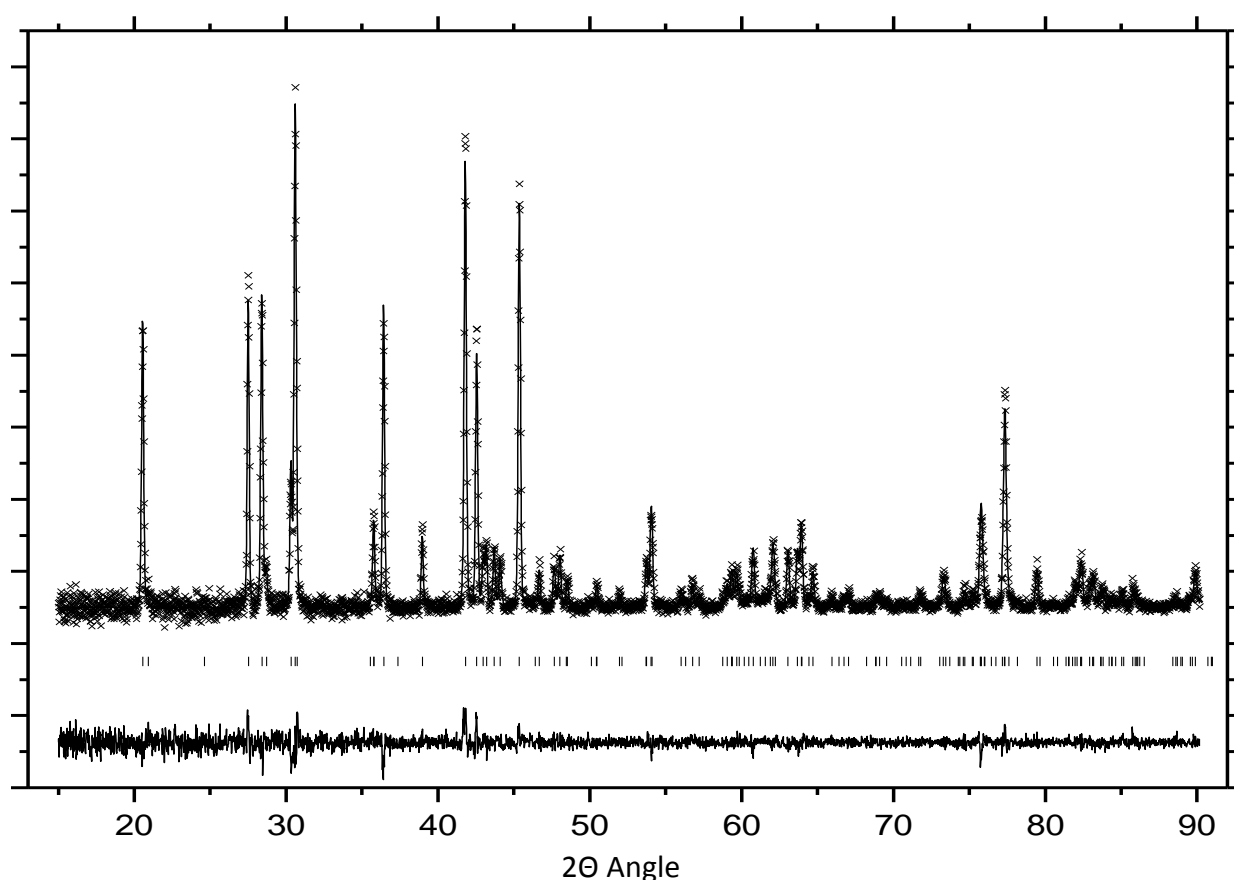


Figure 4.3.7 Xray diffraction pattern and Rietveld refinement of γ_0 $\text{Li}_2\text{CoSiO}_4$ material (produced by reheating hydrothermally lithium cobalt silicate to 1100°C and quenching to room temperature from 850°C).

The material was refined with the $P2_1/n$ space group and gave a good fit of $R_{wp}=7.55\%$. Table 3.3.7 shows that there is no observed site disorder within the cobalt and lithium sites in the material (again, confirmed by subsequent neutron diffraction work¹¹).

Atom	Wyckoff Symbol	x/a	y/b	z/c	B _{iso}	Occupancy
Co1	4a	0.4967(4)	0.1643(2)	0.3106(4)	0.038(1)	1
Si1	4a	0.245(1)	0.4124(5)	0.310(4)	0.025(2)	1
Li1	4a	0.994(3)	0.155(1)	0.309(4)	0.012(9)	1
Li2	4a	0.221(4)	0.073(2)	0.704(5)	0.02(1)	1
O1	4a	0.033(1)	0.3411(8)	0.213(2)	0.019(3)	1
O2	4a	0.247(1)	0.4126(8)	0.632(1)	0.02(3)	1
O3	4a	0.245(1)	0.4124(9)	0.342(2)	0.022(3)	1
O4	4a	0.453(1)	0.3423(7)	0.207(1)	0.013(3)2	1

$$a = 6.3064(1) \text{ } b = 10.6764(1) \text{ } c = 5.02334(7) \text{ } A = 90.0^\circ B = 90.587(2)^\circ C = 90.0^\circ$$

$$\text{Cell Volume} = 338.213(8) \text{ } \text{\AA}^3, \text{ } R_p = 5.66\%, \text{ } R_{wp} = 7.55\%, \text{ } \chi^2 = 1.085$$

Space Group: $P2_1/n$

Table 4.3.5 Refined lattice parameters of γ_0 Li₂CoSiO₄.

	Li1-O	Li2-O	Co1-O	Si1-O
O1	1.926(2)	1.919(6)	1.984(9)	1.63(1)
O2	1.91(1)	2.08(2)	1.982(9)	1.620(8)
O3	2.024(9)	2.183(8)	2.03(1)	1.60(1)
O4	2.032(7)	1.892(7)	1.938(8)	1.603(8)
Average Bond Length \AA	1.973	1.99175	1.938	1.603
Tetrahedra volume \AA^3	5.05(3)	5.51(1)	5.11(4)	2.27(1)

Table 4.3.6 Selected polyhedra bond lengths and volumes for γ_0 Li₂CoSiO₄ material.

Both the LiO_4 polyhedra present in the γ_{II} phase are a smaller volume than their β phase counterparts suggesting that if this presents a thermodynamic impediment to removing, it will require more energy to remove Li^+ from the structure.

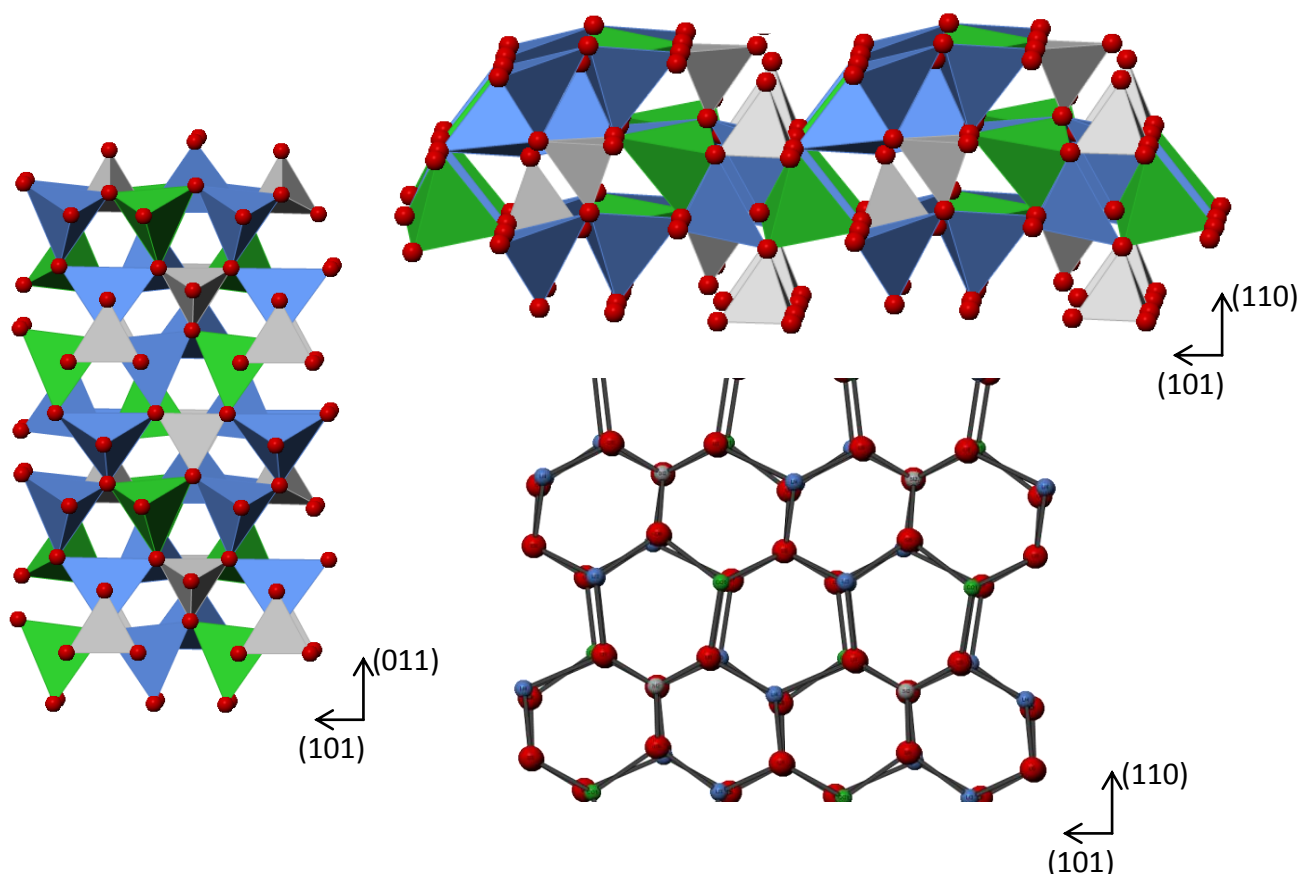


Figure 4.3.8 Schematic representations of γ_0 $\text{Li}_2\text{CoSiO}_4$ (hydrothermal) structure, obtained from Rietveld refinement. Light blue Polyhedra LiO_4 , Dark Blue (Li 95%/Co 5%) O_4 , Grey polyhedra SiO_4 , Green Polyhedra (Co 93%/Li 7%) O_4 , Red spheres Oxygen atoms.

Figure 4.3.8 shows the γ_0 phase has notably lower symmetry than either of the β polymorphs with layers in the c direction consisting of polyhedra with their vertices pointing in opposing directions (as shown in the a,b plane in Figure 4.3.8). The structure consists of clusters of 3 edge sharing tetrahedra with a central tetrahedron facing one way accompanied by two tetrahedra facing the opposite direction.

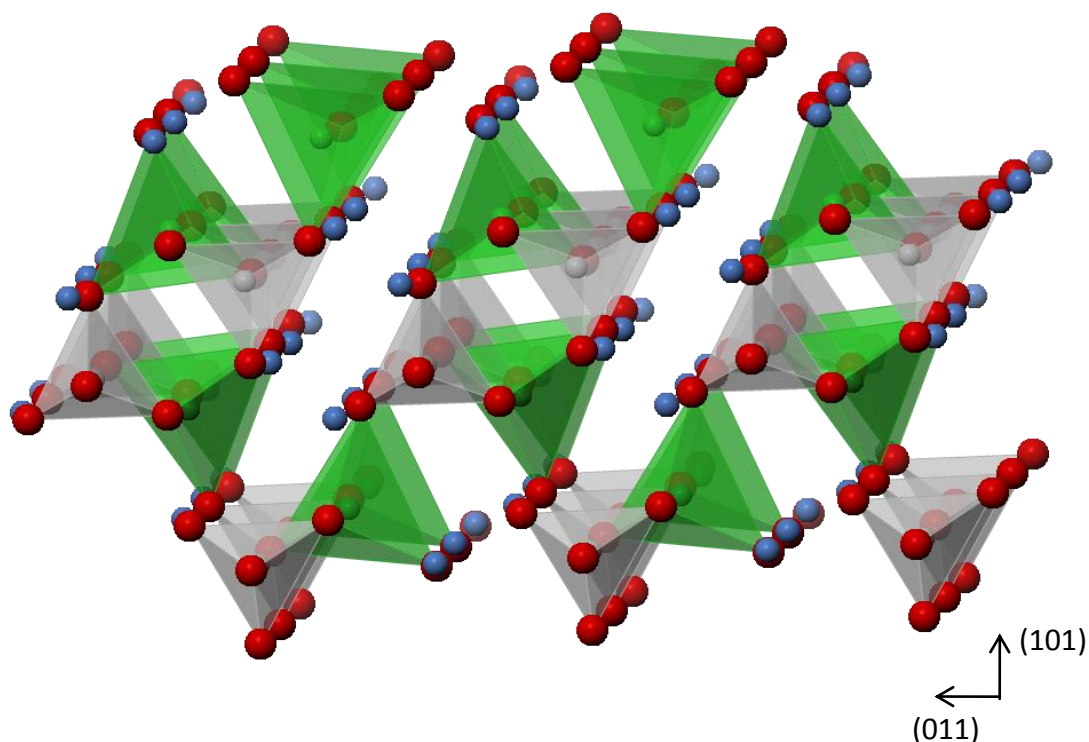


Figure 4.3.9 Schematic representation of a potential lithium insertion/removal pathway in $\beta_I \text{Li}_2\text{CoSiO}_4$; Grey polyhedra SiO_4 , Green polyhedra $(\text{Co/Li})\text{O}_4$, Blue spheres lithium, Red spheres Oxygen.

Figure 4.3.9 shows a projection of the relatively open structure of γ_0 . It does not possess the obvious lithium pathways of the β_I and β_{II} suggesting, that the electrochemical behaviour may be markedly different between the polymorphs.

West gives evidence for the existence of another polymorph, γ_{II} , produced from a fast, high temperature quench ($>1000^\circ\text{C}$) of the β_{II} phase²². Though synthesis of this phase was attempted numerous times (via quenching at 1000°C from air into liquid nitrogen and similar quenching under an argon atmosphere) the γ_{II} polymorph was never observed. The produced material was either a mixture of oxidised lithium silicates and cobalt oxides or one of the other previously observed polymorphs.

4.2.1.4. $\text{Li}_2\text{CoSiO}_4$ β_1 (solid state) material

Several attempts were made to natively produce other polymorphs through solid state synthesis, these attempts focussed primarily on the later heating regime of the solid state synthesis. It was determined that heating the precursor (a largely amorphous material, consisting of cobalt oxide/hydroxide and organic derivatives-see appendix *iii*) led to cobalt reduction and formation of lithium silicates, a possible consequence of organic components decomposing to reducing agents at higher temperatures²². At lower temperatures β_1 remained the preferred phase no matter the quenching regime. This suggests that the solid state synthesis depressed the phase change from β_1 to β_{II} . The lack of doping in the Li1 site may also influence the phase behaviour.

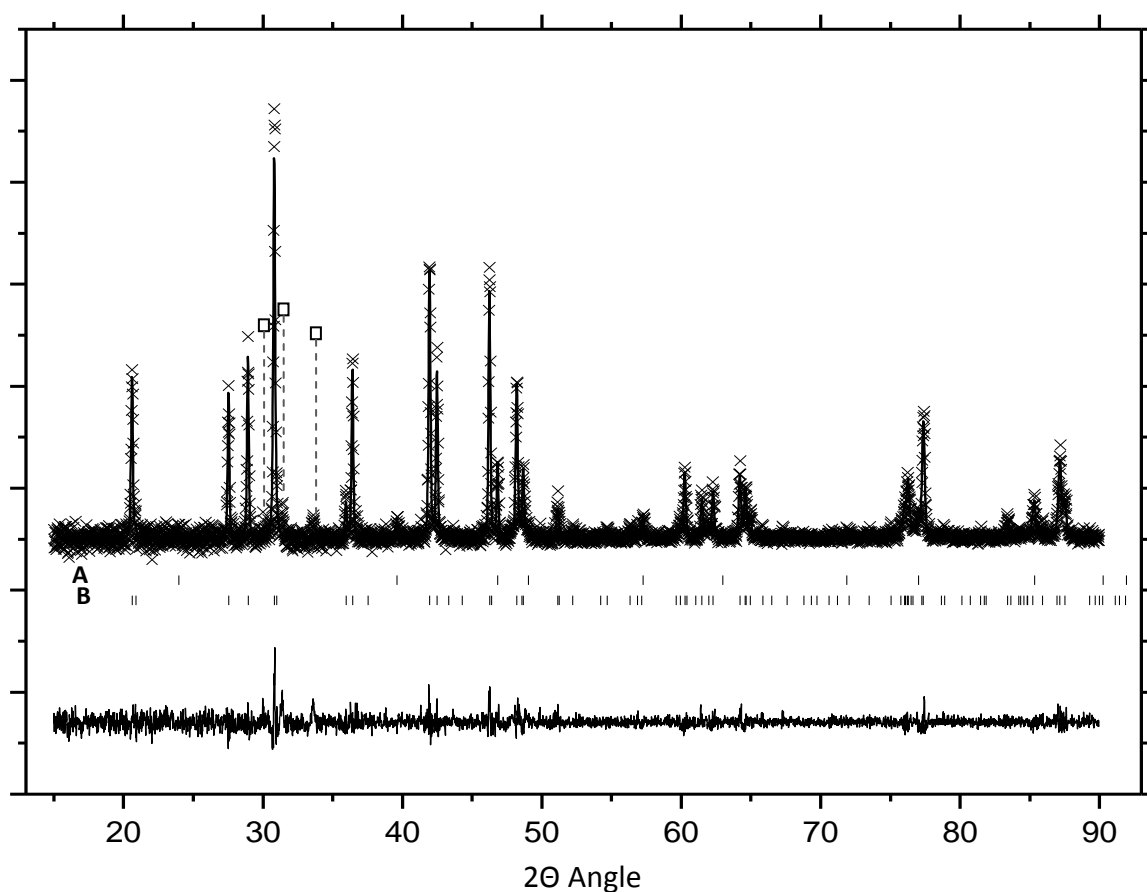


Figure 4.3.10 X-ray diffraction pattern and Rietveld refinement of β_1 $\text{Li}_2\text{CoSiO}_4$ prepared by solid state synthesis: A, Peak positions of Co_3O_4 impurity phase. B, Peak positions of β_1 $\text{Li}_2\text{CoSiO}_4$. \square Unknown impurity peaks.

As before the space group $Pbn2_1$ was used to refine the β_I structure. This produced a fit of $R_{wp}=20.33\%$ which is far from ideal. The presence of an unknown impurity (marked with an \square in Figure 4.3.10 and suspected to be a higher lithium silicate impurity $Li_xSi_yO_z$) and the known impurity of Co_3O_4 (see peak marks **A**) combined to lower the fitting factors. Even after multiple attempts no impurity free materials were produced

Atom	Wyckoff Symbol	x/a	y/b	z/c	B _{iso}	Occupancy
Co1	4a	0.491(1)	0.1647(6)	0.266(2)	0.031(3)	Co 0.93/Li 0.07(3)
Si1	4a	0.248(3)	0.410(1)	0.251(9)	0.039(5)	1
Li1	4a	0.96(1)	0.1748(6)	0.16(1)	0.02(8)	1
Li2	4a	0.69(2)	0.412(6)	0.24(2)	0.02(7)	1
O1	4a	0.031(5)	0.339(2)	0.154(5)	0.019(7)	1
O2	4a	0.254(6)	0.562(2)	0.151(5)	0.002(7)	1
O3	4a	0.239(6)	0.411(2)	0.594(5)	0.007(7)	1
O4	4a	0.465(4)	0.337(2)	0.158(7)	0.010(8)	1
<i>a</i> = 6.271(4) <i>b</i> = 10.689(7) <i>c</i> = 4.930(3) <i>Space Group</i> : $Pbn2_1$						
<i>Cell Volume</i> = 330.50(6) Å ³ <i>R_p</i> = 14.63% <i>R_{wp}</i> = 20.33%, χ^2 = 1.128						

Table 4.3.7 Refined parameters Li₂CoSiO₄ β_I polymorph from solid state preparation.

Unlike the hydrothermally based β_I , Table 4.3.7 shows that the solid state synthesis only has cation disorder on the cobalt site (in the same Co/Li ratio as seen in the hydrothermal β_I). This may infer that the disorder on the Li1 site in the hydrothermal β_I phase is possibly an artefact of the disorder seen in the parent β_{II} phase and the subsequent β_{II} to β_I transformation, or at least show that the different

synthesis conditions between the β_1 hydrothermal and solid state polymorphs have a measurable structural effect on the final material.

As can be seen through the structural refinements of the various polymorphs there is a wide range of metal ion environments across the various polymorphs and different production methods. While determining electrochemical properties from structural information is speculative at best, the different environments provided by the polymorphs do at least suggest that the lithium polymorphs that were produced should have individual behaviour when lithium is removed (and replaced)

4.2.2. Morphological considerations

As each polymorph is produced under different conditions it is expected that each would have individual morphological characteristics. In an electrochemical context, having natively smaller particle sizes improves the lithium insertion/removal kinetics, reducing the ionic diffusion length of lithium in the bulk and exposing a greater surface area of the material to the electrolyte, increasing the rate of ionic and electron transfer. This enhanced interface area effect is balanced (and occasionally negated) by the possibility that the increased surface area will increase the rate of any parasitic side-reactions between the electrolyte and electrode (an extension of this problem on the nano-scale is the lowering of surface activation energy for very small particles^{1-3,23}). To this end transmission electron microscopy was undertaken to study the nano and microscopic nature of the various natively produced polymorphs.

4.2.2.1. $\text{Li}_2\text{CoSiO}_4$ β_{II} material

The hydrothermally prepared β_{II} material can be seen in the TEM image displayed in Figure 4.3.11. The image indicates that the hydrothermally prepared β_{II} material has an approximate diameter of 30-60 nm and relatively uniform particle size with only small variations between the width and length of the particles. This can be explained given the nature of hydrothermal production, where nucleation and crystal growth tends to be a lot faster (compared to solid state synthesis) and hence produce far smaller crystallites¹⁹.

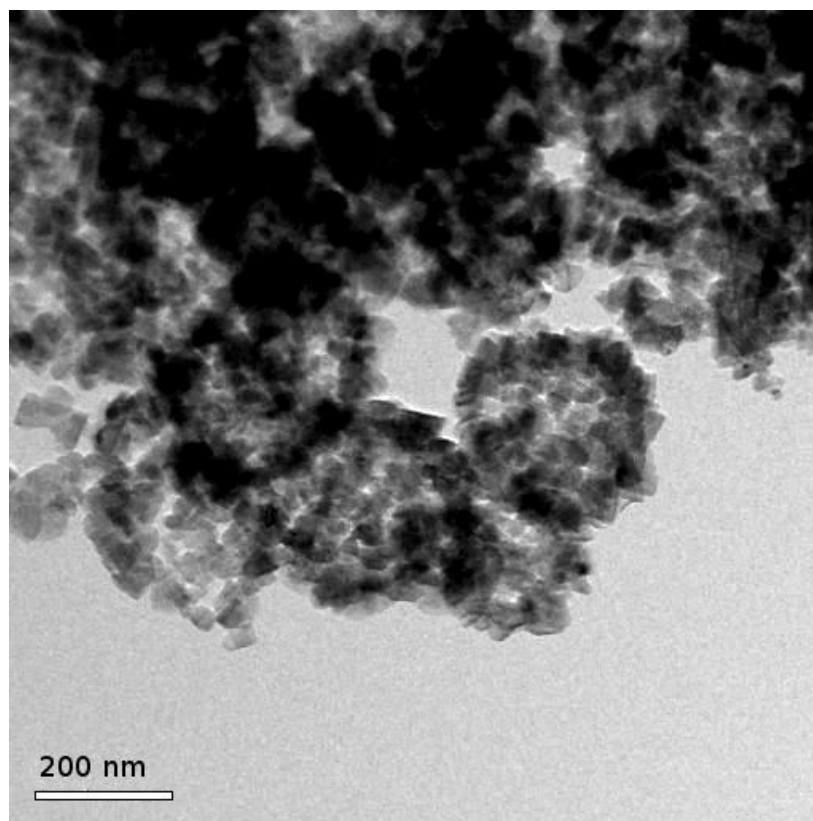


Figure 4.3.11 TEM images taken of the hydrothermally prepared β_{II} $\text{Li}_2\text{CoSiO}_4$ polymorph.

4.2.2.2. $\text{Li}_2\text{CoSiO}_4$ β_I (hydrothermal) material

It can be seen from the TEM image of the β_I (hydrothermal) polymorph, shown in Figure 4.3.12, that the reheating process creates crystallites that are larger than its parent β_{II} material, most likely due to crystallite growth during the reheating/annealing stage. The particles have a range of 380 nm to 1 μm along their long axis and a range of approximately 160 nm to 500 nm across their width. It would appear that the crystal growth is anisotropic with the shorter axis having a value of 40-50% of the long axis.

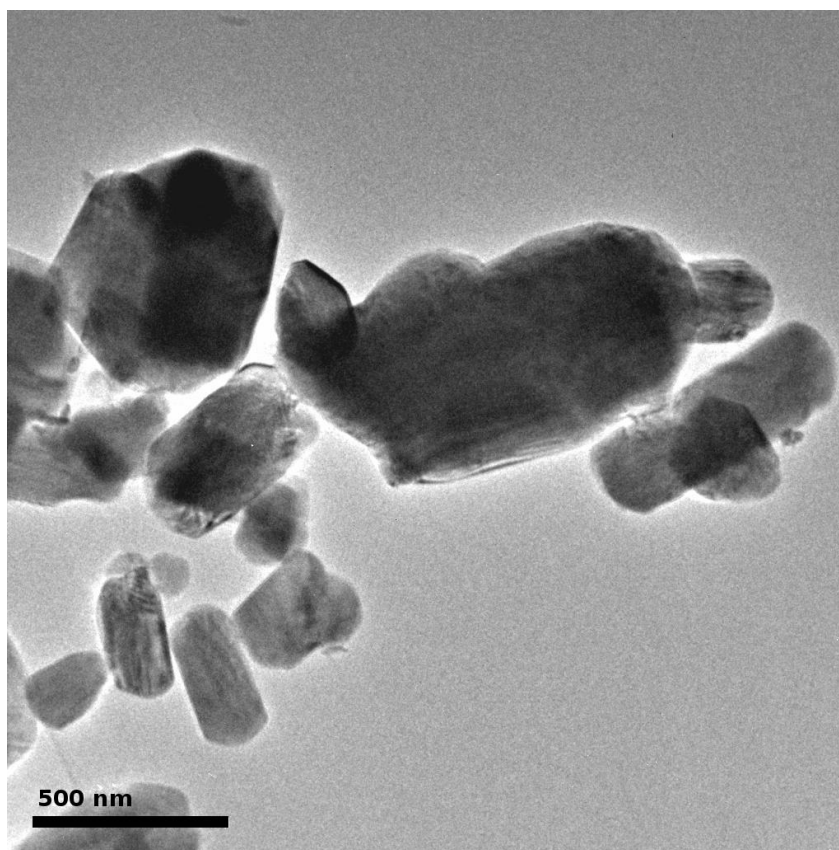


Figure 4.3.12 TEM images taken of the β_I $\text{Li}_2\text{CoSiO}_4$ polymorph prepared through reheating hydrothermally prepared β_{II} material.

4.2.2.3. $\text{Li}_2\text{CoSiO}_4$ γ_0 material

As can be expected from the evidence observed for the β_{II} to β_{I} transition, the γ_0 material which is produced from reheating the β_{II} hydrothermal product to 1100°C and rapidly quenching, also produces large crystallites. This is apparent in Figure 4.3.13. Similar to the β_{I} phase, the γ_0 material can be seen to have a large range of crystallite sizes the smallest around 200nm on its long axis, up to over $1\mu\text{m}$. The γ_0 phase looks to contain a greater range of irregular shaped particles compared to β_{I} , possibly due to the β to γ_0 transition affecting the nature of crystal growth.

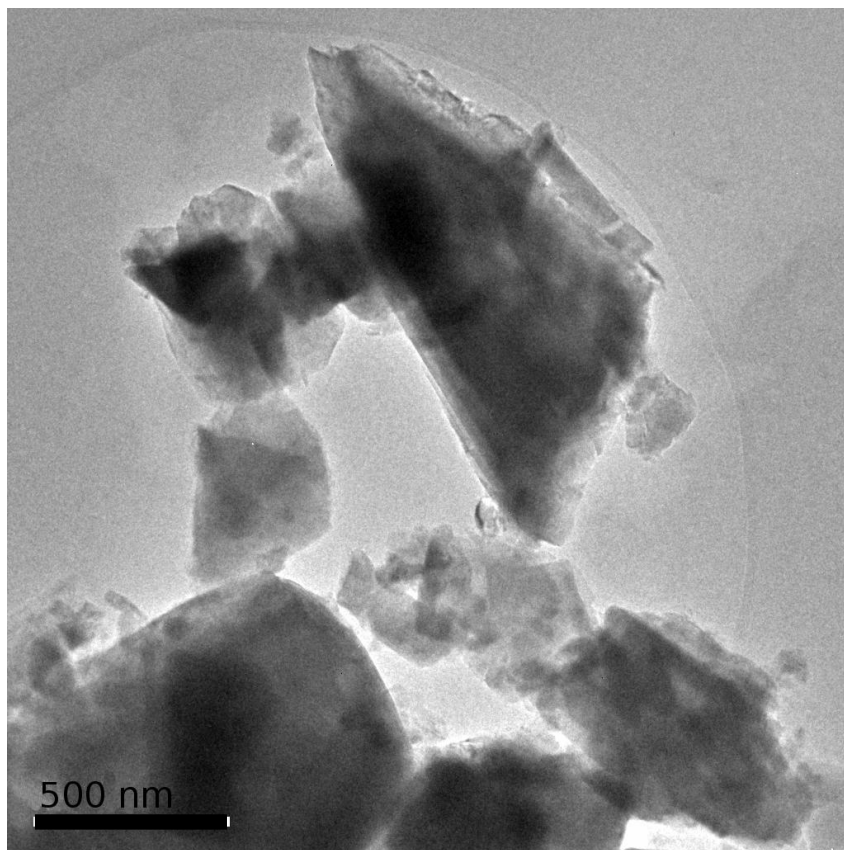


Figure 4.3.13 TEM image of γ_0 $\text{Li}_2\text{CoSiO}_4$ phase obtained via reheating the hydrothermally produced β_{II} phase.

4.2.2.4. $\text{Li}_2\text{CoSiO}_4$ β_1 (solid state) material

From the TEM image (Figure 4.3.14) of the β_1 solid state material we can see that there appears to be non uniform particles with a range of diameters from ~ 200 to 900 nm across their length. Most particles are in the range of 250 - 400 nm; the approximate dimensions roughly correlate to the β_1 hydrothermal material suggesting that the particle growth stage in both preparations may be similar irrespective of synthesis conditions.

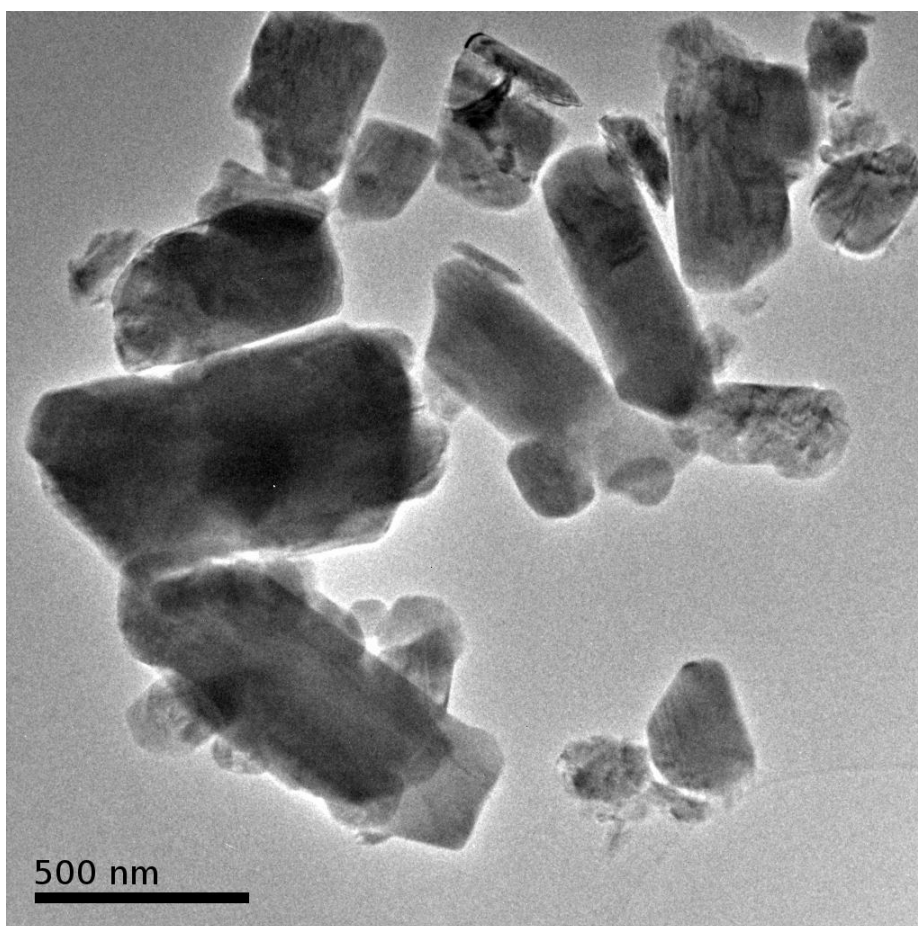


Figure 4.3.14 TEM image of pristine β_1 $\text{Li}_2\text{CoSiO}_4$ produced through solid state synthesis.

The size of the particles can not only offer an insight into the synthesis conditions but can be used to inform about the electrochemical behaviour of the crystallites. Given the important nature of surface based charge and ionic transfer reactions and diffusion lengths. With this in mind it is obvious that both β_1 and γ_0 are at a disadvantage (electrochemically) and this must be considered when investigating the electrochemical properties.

4.2.3. Electrochemical Performance of as Prepared Materials

Inherently the electrochemical behaviour of any new cathode material is of the utmost importance to its performance within the battery system. By using a variety of techniques to monitor the behaviour of a material when lithium is inserted or removed, a picture of the processes occurring within the material during battery cycling can be obtained.

To accommodate the possibility of poor electronic kinetics in the sample, as had been suggested by previous work on $\text{Li}_2\text{FeSiO}_4$ ^{17,24}, a slow cycling regime was chosen (C/16 equivalent to 10mA/g) in conjunction with elevated temperature (50°C). The electrolyte chosen is a laboratory standard (denoted as LP30) which consists of a 1:1(M) mixture of ethyl carbonate and diethyl carbonate with 1M LiPF_6 salt added. The choice of electrolyte is crucial, controlling factors such as mass transport and mitigating possible parasitic side-reactions between the electrode and electrolyte. As well as being convenient, LP30 provides fairly good stability within the voltage range predicted (see figure 3.2.3. in chapter 3) for $\text{Li}_2\text{CoSiO}_4$ materials which, with its high predicted voltage $\sim 4.3\text{V}^4$ discounts a significant number of other electrolyte systems.

Galvanostatic testing was undertaken using a 2 electrode 'coin cell' system incorporating a composite working electrode (consisting of the $\text{Li}_2\text{CoSiO}_4$ active material, a high surface area 'Super S' carbon as a conductivity enhancer and Kynar Flex 2801 binder in a 75:18:7 weight ratio respectively). The counter electrode was prepared from lithium foil, with all elements being sealed gas-tight within the coin cell under an argon atmosphere.

4.2.3.1. $\text{Li}_2\text{CoSiO}_4$ β_{II} polymorph

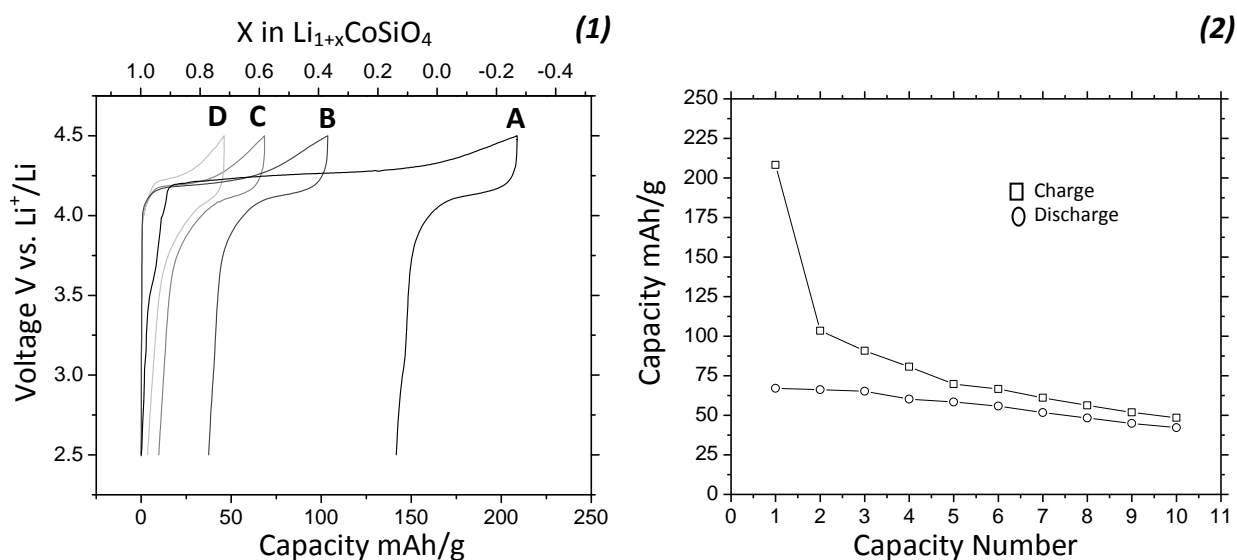


Figure 4.3.15 β_{II} material (1) Galvanostatic load curve; A) 1st cycle, B) 2nd cycle, C) 5th cycle, D) 10th cycle (2) Variation of capacity vs. Cycle number; \square Charging, \circ Discharging - Electrolyte LP30, cycling Rate 10 mA/g at 50°C.

Figure 4.3.15 shows the β_{II} material gives a first charge capacity of over 210 mAh/g, which far exceeds the $\text{Li}_2\text{CoSiO}_4$ theoretical capacity (~ 162 mAh/g) for 1 Li^+ removal. This 'over capacity' could be due to removal of more than one lithium per formula unit upon charging or perhaps, less desirable factors, such as side-reactions with the electrolyte. The voltage rapidly rises to the start of a plateau at approximately 4.2 V, the nearly flat plateau suggests a two phase reaction for Li^+ removal, a phase change from $\text{Li}_2\text{CoSiO}_4$ to LiCoSiO_4 . The plateau gently slopes at a constant gradient

until 4.35 V where the voltage begins to rise rapidly again. This most likely represents the removal of all (reversibly) accessible lithium. Given that the two Li^+ ions occupy two structurally and energetically different sites, it would be expected that, if more than one lithium was being removed the voltage would shift significantly to accommodate the energy required to remove the second. This is not the case, as above 4.35 V the voltage slowly rises, the constantly changing voltage gradient indicates that this involves a significantly different process from the plateau and may not involve lithium insertion/removal at all. The β_{II} material has a first charge plateau capacity of ~ 150 mAh/g, equivalent to removal of 92% of lithium in a $\text{Li}_2\text{CoSiO}_4$ one electron oxidation process.

The presence of a discharge plateau beginning just below 4.2 V is encouraging as it suggests the presence of a reversible process of lithium insertion/removal, but the plateau capacity is much reduced compared to charging garnering only ~ 40 mAh/g on the plateau (24% of available lithium) and 67 mAh/g over all. Figure 4.3.15 (2) shows the large hysteresis between charge and discharge capacities is repeated through the cycling regime with the capacity generated on charge dropping rapidly until it reaches parity with the discharge capacities, where upon it stabilises and diminishes slowly.

The voltage difference between the charging and discharging plateau could be a purely polarisation artefact caused by poor conductivity or it could be caused by the introduction of a process (structural rearrangement etc.) between charging and discharging that causes a thermodynamic difference between removing and inserting lithium (i.e. the voltage shift).

Subsequent structural refinement at the end of the first and tenth cycle showed no new phases present. The cycling was accompanied by slight volume reduction of the unit cell (primarily along the *b* axis). This volume reduction may be down to lower lithium concentration within the material (something hard to accurately ascertain given the low scattering X-ray cross section of lithium). This may be due to the asymmetric charge and discharge capacities leading to lower lithium concentrations throughout the material (though it should be kept in mind that due to the recovery process of cycled material, good x-ray statistics are hard to achieve with cycled materials and the certainty in refinement values are subject to these limitations).

	Unit Cell parameters /Å			Cell volume/ Å ³
	a	b	c	
<i>Pristine β_{II} material</i>	6.2694(4)	5.3563(4)	4.93844(5)	165.967(2)
<i>β_{II} material after 1 cycle</i>	6.269(3)	5.356(2)	4.938(1)	165.8(1)
<i>β_{II} material after 10 cycles</i>	6.2610(5)	5.3557(4)	4.9358(3)	165.49(1)

Table 4.3.9 Unit cell parameters of pristine β_{II} material (R_{wp} 8%) , and after the first(R_{wp} 4.77%) and second cycle (Rwp 4.72%); space group Pmn2₁.

The slow sweep cyclic voltammetry shown in Figure 4.3.16 shows selected cycles of the β_{II} material at a scan rate of 0.05 mV/s. The first sweep shows a sample free of any impurities with one defined oxidation peak at 4.36 V, assumed to be the removal of lithium from the sample (even at the slow sweep rate, the peak's voltage cannot be taken as absolute, given over-potential effects). Near the voltage cut-off the current begins to increase suggesting a secondary electrochemical process (most likely the same process that causes the sloping voltage rise after the plateau in the galvanostatic load curve); the reduction peak at 4.1 V is attributable to the lithium insertion process.

On subsequent cycles the lithium removal and insertion peaks shift to more oxidising and reducing voltages respectively. The voltage difference is incremental through the cycles and when coupled with the minimal plateau shift in the galvanostatic load curves it is unlikely that the same drastic structural changes that are seen in $\text{Li}_2\text{FeSiO}_4$ on the first cycle²⁵ are at work in β_{II} $\text{Li}_2\text{CoSiO}_4$.

Given the poor capacity retention of the material the peak shift could be due to the reduction of accessible Li^+ in the material on cycling manifesting itself as an increasing over-potential (hence peak shift) required to remove lithium.

From AC resistivity measurements in Figure 4.3.16 (2) we can see that, in the complex impedance plot, the material shows a classic double semi-circle thought to represent both the bulk diffusion process within the material and the grain boundary processes. Equivalent circuit refinements were carried out using the ECLab Zfit program, utilising an equivalent circuit of two Resistor(R)/Constant phase element(CPE) dipoles in series. The pseudo capacity values generated are quoted in Farads per second.

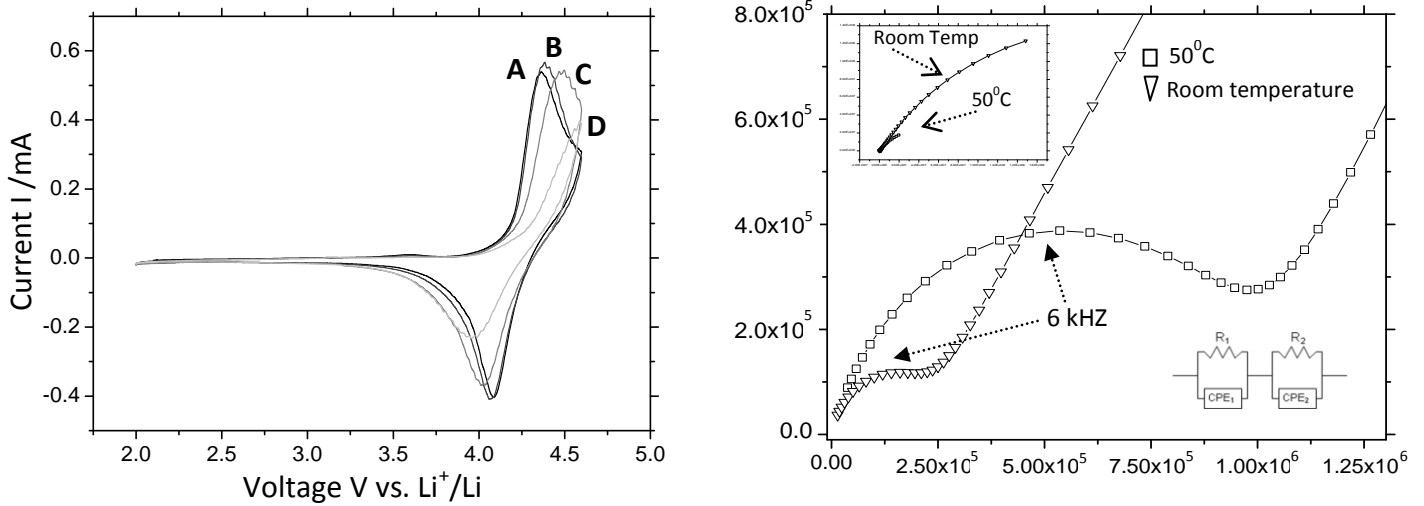


Figure 4.3.16 β_{II} material: (1) Slow sweep cyclic voltammetry plot of selected cycles of the as prepared β_{II} material; A) 1st cycle, B) 2nd Cycle, C) 5th cycle D) 10th cycle. - Electrolyte LP30, sweep rate 0.05mV/s at 50^oC. (2) Nyquist plot of β_{II} material between stainless steel blocking electrodes.

AC Impedance

	Room Temp.		50 ^o C	
	High Freq.	Low Freq.	High Freq.	Low Freq.
Resistivity/ Ωm	2.02×10^7	6.97×10^8	1.07×10^7	5.58×10^9
Capacitance/ Fs^{n-1}	2.41×10^{-10}	1.39×10^{-9}	4.54×10^{-10}	1.22×10^{-9}

DC Resistivity

	Room Temp.	50 ^o C
Resistivity/ Ωm	1.54×10^7	2.05×10^6

Table 4.2.1 AC and DC resistivity details for β_{II} material.

The capacities of the high frequency and low frequency semi-circles are $\sim 10^{-10} \text{Fs}^{n-1}$ and $\sim 10^{-9} \text{Fs}^{n-1}$ respectively, inferring that the high frequency semi-circle is responsible for the bulk process and the low frequency semi-circle due to grain boundary effects^{3,26}. The measurements taken at room temperature and 50^oC display a high frequency semi-circle at 6kHz with conductivities (σ) (1/resistivity) of $\sim 10^{-7} \text{S/cm}$.

This is an improvement on reported values of the bulk contributions for LiFePO_4 ^{27,28} by two orders of magnitude suggesting that the majority of transport

problems in β_{\parallel} $\text{Li}_2\text{CoSiO}_4$ must be ionic in nature. It is also worth noting that the bulk resistivity changes little from 20°C to 50°C. The grain boundary (low frequency) semi-circle gives conductivity values of $\sim 10^{-9}$ and $\sim 10^{-10}$ S/cm for the room temperature and 50°C samples respectively which is similar to other olivine materials²⁷.

From the DC resistivity measurements shown in Table 4.3.10 it's confirmed that the resistivity is mainly electrical in nature and dominated by bulk processes.

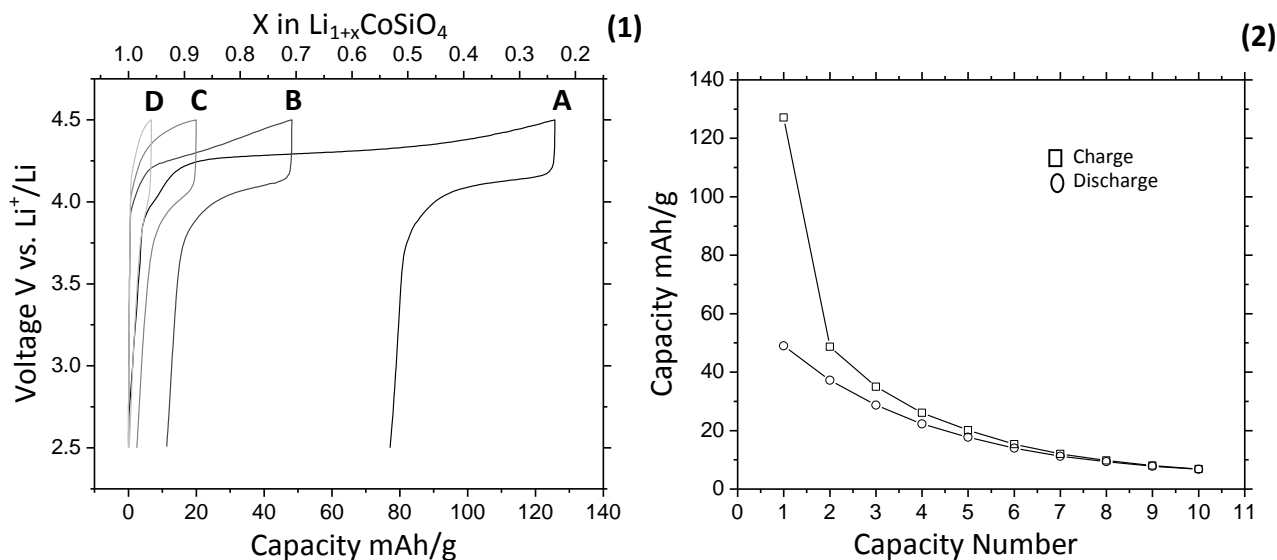
4.2.3.2. $\text{Li}_2\text{CoSiO}_4 \beta_{\text{I}}$ (hydrothermal) material

Figure 4.3.17 β_{I} from hydrothermal material: (1) Galvanostatic load curve, A) 1st cycle, B) 2nd cycle, C) 5th cycle, 4) 10th cycle; (2) Variation of capacity vs. Cycle number; \square Charging, \circ Discharging - Electrolyte LP30, cycling Rate 10 mA/g at 50^oC.

Compared to its β_{II} parent, the β_{I} material, produced from reheating of the hydrothermal product, gives a diminished capacity; achieving a capacity of only ~125mAh/g out of a possible 162mAh/g on the first charge (approximately 80% of theoretical capacity), of which ~100 mAh/g can be ascribed to the plateau process 0. (~0.6 Li per $\text{Li}_2\text{CoSiO}_4$ unit). As before the uninterrupted plateau suggests a two phase reaction. The reduced capacity could be due to the size differences between β_{I} and β_{II} materials.

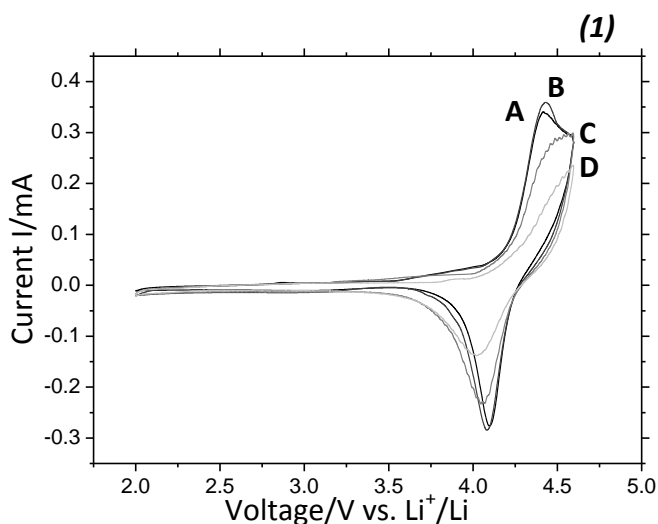
The voltage plateau sits at a slightly higher voltage in β_{I} compared to its β_{II} counterpart (the plateau begins at 4.25V compared to 4.17 V for β_{II} material) and it could be the structural differences between β_{I} and β_{II} LiO_4 polyhedra volume introduce a degree of polarisation resistance forcing the extraction voltage plateau to shift to a higher voltage. Considering the Co-O-Si triplet theory (i.e. a shorter Co-O bond suggests greater orbital overlap between cobalt and oxygen orbitals which in turn

increases the redox band-gap). Within the Co-O-Si triad, the average Co-O bond in β_I is shorter than in β_{II} (1.927 Å vs. 1.9905 Å respectively) which would, qualitatively suggest a higher voltage for the $\beta_I \text{Co}^{3+/2+}$ redox couple. Most likely it is a combination of the greater thermodynamic penalty for removing Li^+ ions (hence greater polarisation of the electrode) coupled with the increased $\text{Co}^{3+/2+}$ redox level.

The discharge process bears similarities to the β_{II} material, initially occurring at a voltage of 4.16V and experiencing a 50 mV voltage drop between charging and discharging plateaus. At 50mAh/g, the gross capacity of the discharge cycle is lower compared to the ~65 mAh/g achieved by the β_{II} material (though the charge to discharge capacity ratio is higher for the β_I vs. the β_{II} , 39% vs. 31% respectively).

The voltage plateau region accounted for the majority of the discharge capacity (approximately 35mAh/g), but as with the β_{II} polymorph there is a large disparity between the charge and discharge capacities. There was no noticeable difference between charge/discharge capacity ratios compared to when both stages were undertaken at a rate of 10 mAh/g, suggesting that the charge/discharge capacity difference was not based on a kinetic effect (or not a kinetic effect that is measurable by this magnitude of rate difference).

On subsequent cycling the charging plateau is less resolved, presumably being lost to polarisation effects as it becomes harder to remove lithium from the material. The discharge plateau is more stable but diminishes gradually as the capacity vs. cycle plot in Figure 4.3.17 (2) highlights.

**DC Resistivity**

	Room Temp.	50°C
Resistivity/ ΩM	1.38×10^7	2.19×10^8

Figure 4.3.18 β_{I} (hydrothermal) material: (1) Slow sweep cyclic voltammetry plot of selected cycles of the as prepared β_{I} material; A) 1st cycle, B) 2nd cycle, C) 5th cycle, D) 10th cycle - Electrolyte LP30, sweep rate 0.05mV/s at 50°C : (2) Table 4.3.11 DC Resistivity measurements of β_{I} (hydrothermal) material at room temperature and 50°C between 2 stainless steel electrodes

The slow sweep cyclic voltammogram of the β_{I} polymorph displayed in Figure 4.3.18 (1) indicate similar behaviour to its β_{II} analogue. There is one large oxidation peak (equivalent to the charging plateau process), albeit at a slightly higher voltage (4.41V) to its β_{II} counterpart (4.37 V). As before there is slight over-potential effect compared to the voltage values from the galvanostatic plateau. The reduction peak gives a maximum current at 4.1V (compared to β_{II} 4.085V) which, as expected, is shifted to a more reducing voltage compared to the mid-plateau voltage from the galvanostatic load curve.

As observed for the β_{II} material there is no pronounced peak shift, only a gradual peak drift to higher voltages, presumably caused by the need for greater over potential, as removal of lithium from the material becomes more laboured (as suggested by the plateau polarisation seen in the load curve).

With structural refinement it was discovered that, after charging, conversion of the β_{I} material (and in subsequent cycles) to the β_{II} phase can be observed. The β_{II} phase fraction (relative to the β_{I} phase) grows with subsequent cycling until it becomes the dominant phase. The slow sweep C.V. shows no evidence of the expected shift in charging peak voltage to the lower value associated with the β_{II} oxidation process (and there is no noticeable galvanostatic voltage plateau shift) but this may be occluded by greater polarisation effects present from factors such as the larger size of particles.

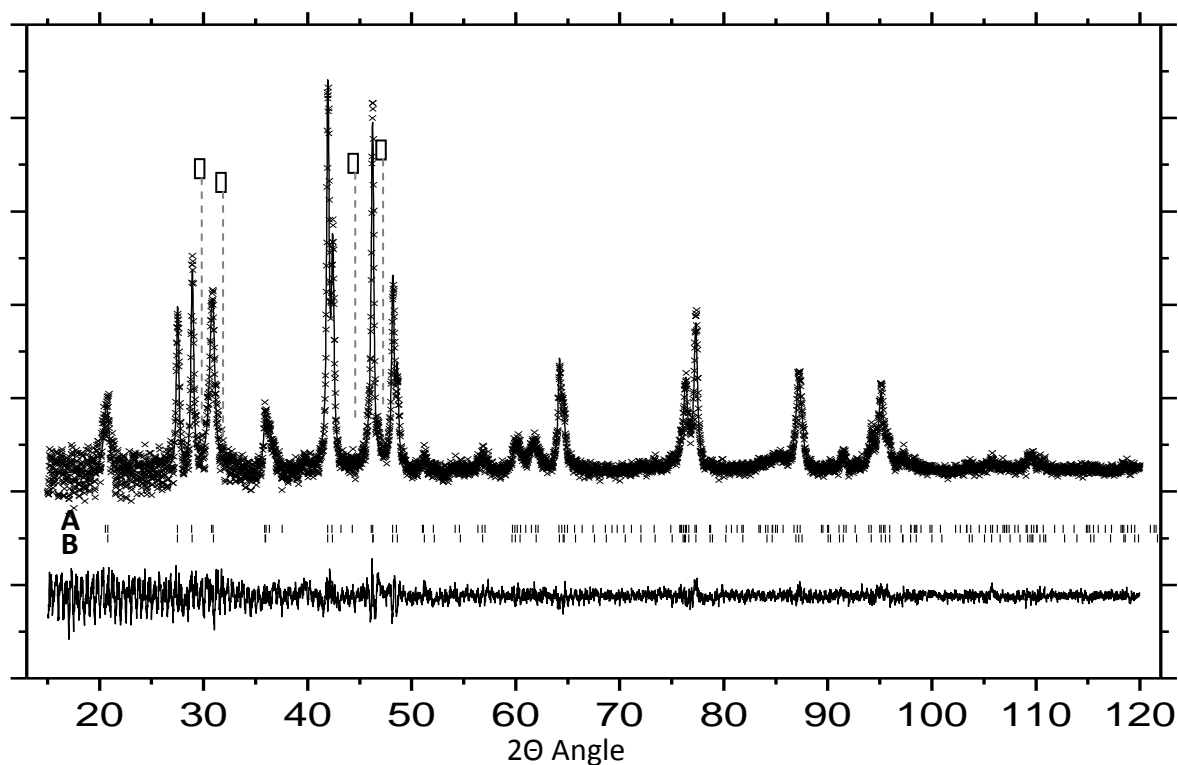


Figure 4.3.19 X-ray diffraction pattern and Rietveld refinement for β_{I} (hydrothermal) material after 9 cycles and 1 charge: A, Peak positions for the β_{I} $\text{Li}_2\text{CoSiO}_4$ phase. B, Peak positions for the β_{II} $\text{Li}_2\text{CoSiO}_4$ phase. \square Unknown impurity phase. $R_{\text{wp}} = 5.63\%$, Phase ratio, $\beta_{\text{I}}:\beta_{\text{II}}$ 0.27:0.73

The absence of β_{II} activity in the electrochemistry is not easy to understand- one possible explanation is, as the β_{II} is only created after the first charge sweep, its presence is harder to observe in the subsequent charging plateaus, due to polarisation effects obscuring the true plateau voltage (the β_{II} and β_{I} discharge voltages are almost

identical, In the β_I case this may be due to an electrochemical contribution from the recently created β_{II} phase).

	Unit Cell parameters /Å			Cell vol. / Å ³	Phase ratio	R _{wp}
	a	b	c			
Pristine β _I material						
β _{II} phase	x	x	x	x	x	17.32%
β _I phase	6.2694(4)	5.3563(4)	4.9384(5)	165.96(2)	1	
1 Charge						
β _{II} phase	6.2733(1)	5.3549(6)	4.9341(5)	165.7(3)	0.28(2)	6.32%
β _I phase	6.264(1)	10.712(2)	4.9377(8)	331.3(9)	0.72	
9 cycles 1charge						
β _{II} phase	6.2610(3)	5.3448(2)	4.9245(2)	164.79(1)	0.73(6)	5.63%
β _I phase	6.255(1)	10.704(1)	4.9341(8)	330.39(8)	0.27	
10 cycles						
β _{II} phase	6.251(2)	5.359(2)	4.961(1)	166.20(9)	0.68(5)	7.36%
β _I phase	6.2673(5)	10.6986(7)	4.9307(3)	330.62(6)	0.32	

Table 4.3.12 Rietveld refinement parameters from cycled β_I (hydrothermal) material : β_{II} phase space group $Pmn2_1$, β_I phase Space group, $Pbn2_1$

There is also an unknown impurity present which appears in the later cycles (indicated in Figure 4.3.19). The impurity is possibly a lithium carbonate derivative which may form as part of the parasitic side reaction occurring in the higher voltage region (seen after the plateau in the galvanostatic load curves, or in the rapidly increasing current as the voltage sweeps towards the voltage cut-off in the cyclic

voltammograms). It may be that this impurity (or its associated side reaction) has an effect on the overall efficiency of the cycling process, causing the poor capacity retention seen in Figure 4.3.18 (during a β_I - β_{II} transition, cobalt sites with a lowered surface activation energy may be exposed to the electrolyte, potential catalysing the dissolution of electrolyte with the transition metal ion, as has been observed in other systems^{29,30}).

It may be of some note that the presence of the β_{II} phase is recorded at the end of the first charge. On later cycles the majority of the material is made up of β_{II} . The β_I/β_{II} ratio seems to vary slightly with charge/discharge, most likely at each subsequent charge process more β_{II} was created adjusting the phase ratio accordingly. This conversion mechanism must occur at similar voltages to lithium removal, given the lack of separate peaks in the cyclic voltammetry.

Attempts to measure the AC impedance of the pristine β_I material provided few clues, with the impedance spectrum resolving to a single point characteristic of a 'shunt'. The DC resistivity measurements show that the conductivity decreased with increased temperature (from $\sim 10^{-8}$ to $\sim 10^{-9}$ s/cm) this may suggest the β_I (hydrothermal) does not fit the simple semi-conductor model (i.e. the presence of strain or more exotic charge carrier effects). The β_I material has a lower DC conductivity compared to β_{II} ($\sim 10^{-7}$ s/cm) which is further evidence of its poor relative electrochemical performance.

4.2.3.3. $\text{Li}_2\text{CoSiO}_4$ β_I (solid state) material

For clarity the electrochemical results for β_I (solid state) are presented here to act as a useful comparison to the β_I (hydrothermal) material

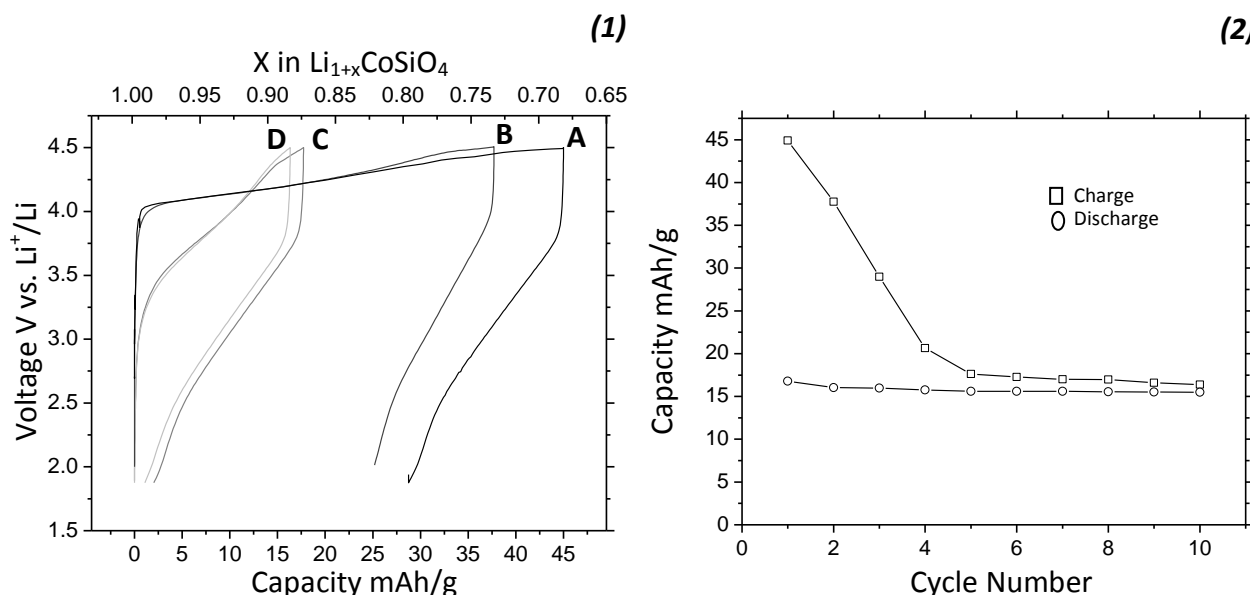


Figure 4.3.20 β_I solid state material: (1) Galvanostatic load curve, A) 1st cycle, B) 2nd cycle, C) 5th cycle, D) 10th cycle; (2) Variation of capacity vs. Cycle number; \square Charging, \circ Discharging - Electrolyte LP30, cycling Rate 10 mA/g at 50^oC.

The composition vs. voltage profile of the β_I material prepared from solid state synthesis is notably different from the β_I material from hydrothermal reheating. Not only is the first charge capacity severely reduced (45 mAh/g vs. 125mAh/g, solid state vs. hydrothermal respectively) but there is no defined plateau; instead there is a gentle slope running from 4.05 V to the 4.5 V cut-off. This starting voltage is significantly lower than β_I (hydrothermal) material (~ 4.25 V) and β_{II} material (~ 4.14 V). The lower voltage for the pseudo-plateau could indicate the presence of another electrochemical process preceding lithium removal, the slight shoulder seen in the voltammogram in Figure 4.3.21 would seem to confirm this. Unlike the previous materials, there is no clear discharge plateau in the β_I (solid state) material, instead a voltage drop (~ 60 mV) is observed, followed by a sharp slope which accounts for almost all of the 16mAh/g

capacity seen in the first discharge. On subsequent cycles the charging capacity quickly drops until it stabilises, in line with the discharge capacity of $\sim 15\text{mAh/g}$ (shown in Figure 4.3.20.). Subsequent cycles show the decreasing starting voltage (and capacity) of the charging pseudo-plateau, insinuating that the pseudo-plateau process is diminishing.

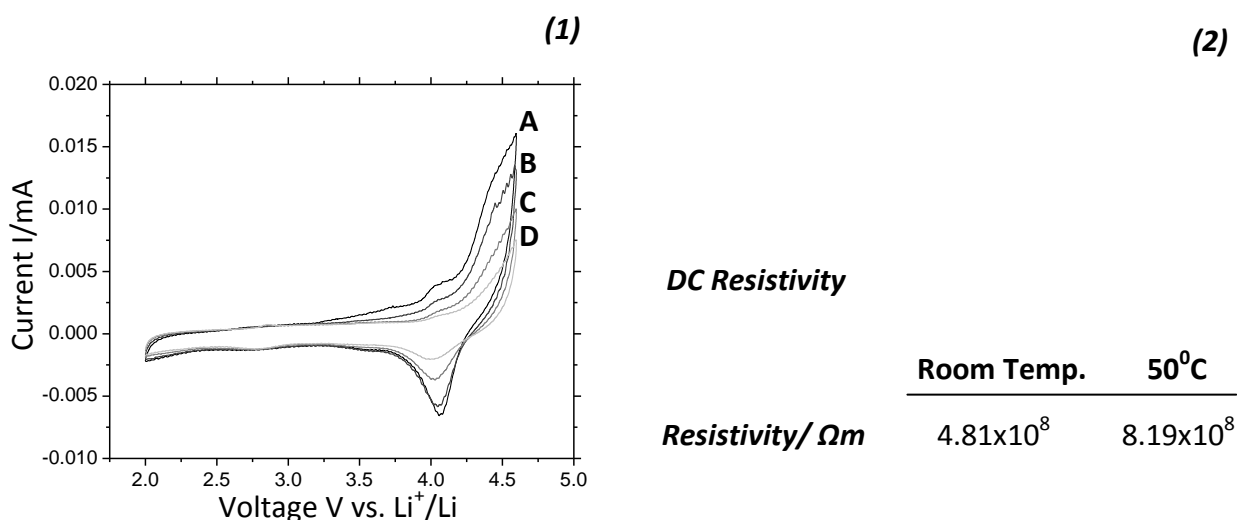


Figure 4.3.21 β_{I} (solid state) material: (1) Slow sweep cyclic voltammetry plot of selected cycles of the as prepared β_{I} solid state material; A) 1st cycle, B) 2nd cycle, C) 5th cycle D) 10th cycle - Electrolyte LP30, sweep rate 0.05mV/s at 50°C: (2) Table 4.3.13 DC Resistivity measurements of β_{I} (solid state) material at room temperature and 50°C between 2 stainless steel electrodes

The cyclic voltammetry of the β_{I} solid state material consists of a small shoulder preceding the current increase to the voltage cut-off, the lack of a major peak is no surprise given the galvanostatic profile (i.e. the lack of a plateau). The shoulder peak at 4.04 V bears a similarity to the larger β_{I} (hydrothermal) and β_{II} major oxidation peaks, in that it slowly fades with cycles, suggesting it could be an lithium insertion process (or an irreversible side-reaction with very slow kinetics). There does appear to be a more consistent reduction peak which doesn't suffer the peak shifts seen in β_{I} (hydrothermal) and β_{II} , but this may be to do with drastically lowered current density not exhausting the kinetic limitations of lithium insertion (and hence doesn't require

an over-potential peak shift to remove lithium, as seen in the more electrochemically active β_{II} and β_I (hydrothermal) phases).

As before, the AC impedance spectrum resolved to a point. The DC conductivity is slightly higher than for the β_I (hydrothermal) material and similarly shows a decrease in conductivity for the increasing temperature (2×10^{-9} S/cm at room temperature vs. 1×10^{-9} S/cm) but the difference is less pronounced. The similarity between conductivities for the two β_I materials suggest that the difference in performance is probably caused by something chemical (the different doping may affect the internal ionic kinetics) or physical (morphological, particle size) rather than electrical state of the solid state material.

The difference in electrochemical behaviour between the β_I polymorphs is fairly pronounced but the structural differences are subtle. As both β_I materials were natively produced with similar morphologies, the most notable difference between the two β_I polymorphs is the change in fractional occupancies. It may be this 'doping' of lithium within the Co1 cobalt site alters the lithium insertion/removal properties of the material (or the lack of doping hinders the β_I (solid state) converting to β_{II}).

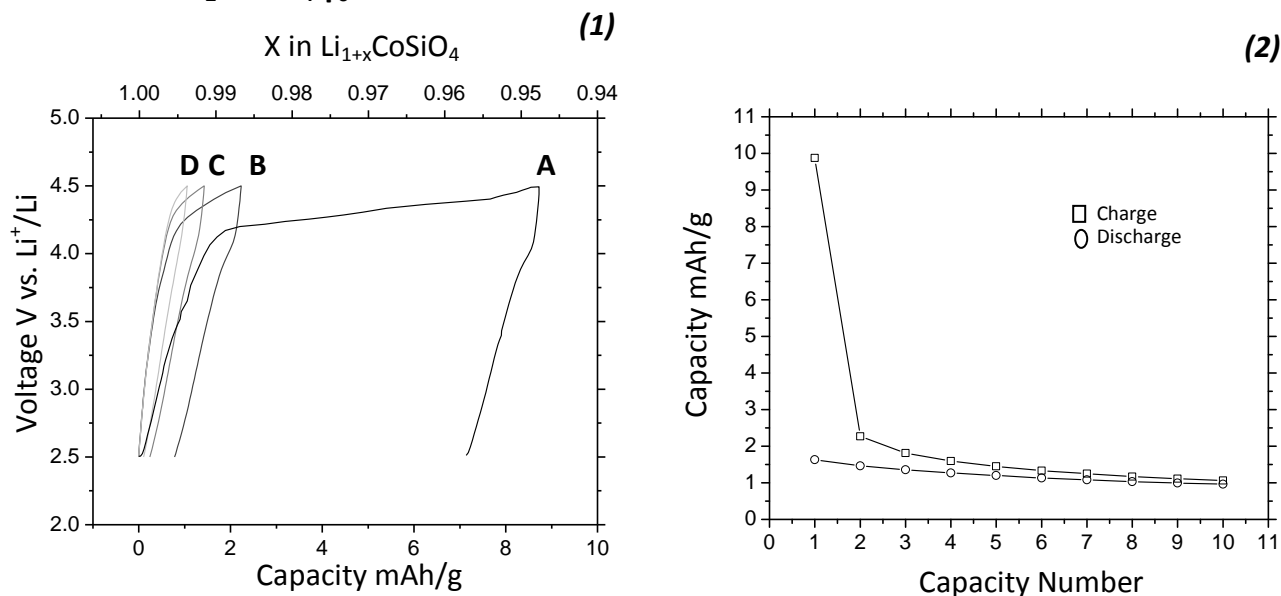
4.2.3.4. $\text{Li}_2\text{CoSiO}_4$ γ_0 material

Figure 4.3.22 γ_0 material (1) Galvanostatic load curve; A) 1st cycle, B) 2nd cycle, C) 5th cycle, D) 10th cycle (2) Variation of capacity vs. Cycle number; \square Charging, \circ Discharging - Electrolyte LP30, cycling Rate 10 mA/g at 50^oC.

The γ_0 polymorph has greatly decreased capacity compared to the three other materials. It shares a similar profile to the solid state β_I , again the particularly low electrochemical activity making it hard to discern what is due to lithium removal/insertion process and what is due to side reaction processes. As with β_I (solid state) the load curve begins with a rapid voltage increase until a sloping charge plateau is reached at 4.2 V. The plateau then gently increases up to 4.5 V voltage cut off. The plateau occupies a marginally higher voltage than the β_I polymorph, though whether this is indicative of an over-potential caused by poor sample conductivity (as highlighted in the DC conductivity measurements in Figure 4.3.23 (2)) or the different structural environment affecting the lithium removal voltage is difficult to tell. The initial plateau is in the correct range for a lithium removal process (at 4.2 V it sits between the initial plateau voltages of β_{II} and β_I (hydrothermal) materials).

The low capacity could be due to several factors; the pristine γ_0 material has relatively large particles causing unfavourable kinetics between the active material and the electrolyte. The γ_0 crystal structure consists of the smallest LiO_4 tetrahedra, theoretically making it harder to remove lithium. The average Co-O bond length in the Co-O-Si bonding triplet sits between the lengths of β_I and β_{II} which may explain the intermediate initial voltage at the start of the charging plateau. It is likely that a combination of these factors ensure that the γ_0 gives poor electrochemical performance, indeed on subsequent cycles the capacity produced is negligible (as is the discharge capacity).

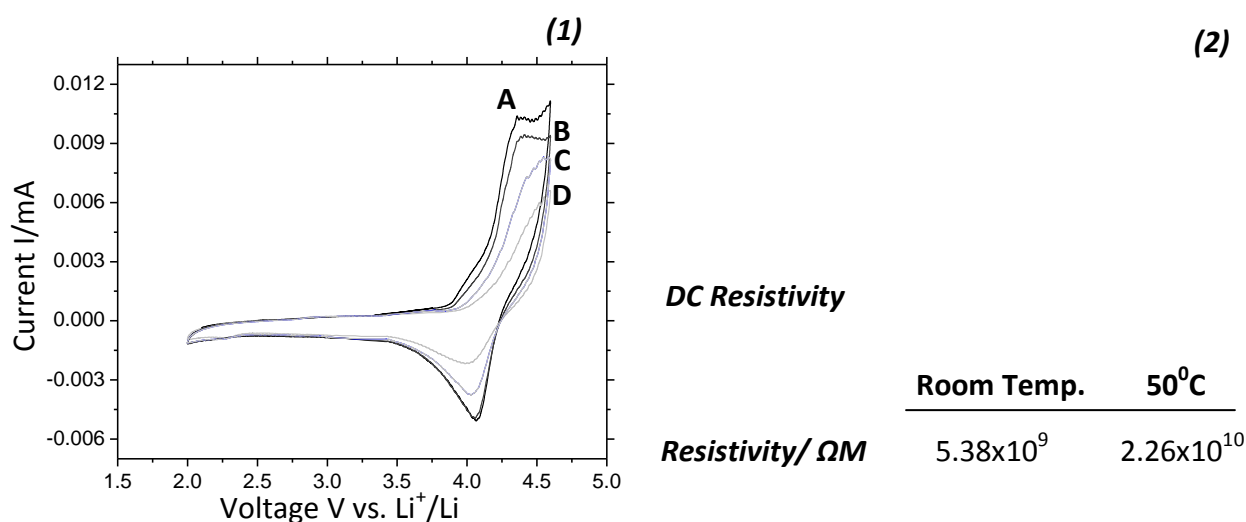


Figure 4.3.23 γ_0 material: (1) Slow sweep cyclic voltammetry plot of selected cycles of the as prepared γ_0 material; A) 1st cycle, B) 2nd cycle, C) 5th cycle D) 10th cycle - Electrolyte LP30, sweep rate 0.05mV/s at 50°C: (2) Table 4.3.14 DC Resistivity measurements of γ_0 material at room temperature and 50°C between 2 stainless steel electrodes

The cyclic voltammogram for the γ_0 polymorph is shown in Figure 4.3.23 and does show that there is a slight oxidation peak at 4.36 V (the same voltage peak as β_{II}) which diminishes on subsequent cycles until there is no obvious peak. The presence of

a reduction peak is encouraging as it suggests that, for what minimal lithium removal/insertion processes are present they appear to be repeatable. There is no voltage shift in the reduction peak. This may differ from previous polymorphs because the insertion of lithium process is not on a scale to be kinetically limited (and hence, force an over-potential).

Like the β_{II} and, different from the β_{I} (hydrothermal) material, the X-ray diffraction pattern after cycling did not show the presence of any new phases, or the presence of any impurities. Both these factors could be accounted for by the incredibly low electrochemical activity seen with the γ_0 phase, ensuring minimal presence of products activated by electrochemical cycling.

	Unit Cell parameters /Å			Cell volume/ Å ³
	a	b	c	
<i>Pristine γ_0 material</i>	6.3067(1)	10.676(1)	5.02342(7)	338.237(8)
<i>γ_0 material after 10th cycle</i>	6.2760(2)	10.7039(5)	5.0222(2)	337.37(4)

Table 4.3.15. Unit cell parameters of pristine γ_0 material (R_{wp} 7.9%) , after the 10th cycle (R_{wp} 6.69%); Obtained from Rietveld refinement, space group $P12_1/n1$.

Table 4.3.15 indicates, as with the β_{II} material, there is a volume cell reduction after cycling, primarily caused by a reduction in the a axis of the unit cell (probably due to the removal of lithium which is not fully replaced by lithium insertion on discharge). There was no evidence of evolution of the β_{II} phase. This may be because the γ_0 phase does not convert to β_{II} under cycling, or more likely the electrochemical activity is so low that it is hard to determine the actual behaviour of γ_0 material under cycling.

As with the β_{I} materials the AC impedance spectrum was resolved to a point, leaving only DC resistivity measurements to provide an insight into the conductivity. As

expected from the γ_0 structure, morphology and galvanostatic behaviour, the γ_0 material has particularly low conductivity ($\sim 10^{-10}$ S/M at room temperature and $\sim 10^{-11}$ s/M at 50°C) which may go some way to explaining the poor cycling performance, as with the β_1 materials the conductivity slightly decreases from room temperature to 50°C .

4.3. Conclusions and Further work

Three polymorphs of $\text{Li}_2\text{CoSiO}_4$ were successfully produced using either a solid state or hydrothermal synthesis approach. The materials were characterised by X-ray diffraction and TEM. As suggested by West *et al.*^{6,7} It was found that the phases follow their Li_3PO_4 analogues with both high temperature γ , and low temperature β phases being preserved at room temperature. The hydrothermal synthesis offered the most convenient (and versatile) method of producing the three phases, allowing access to β_I and γ_0 polymorphs, through reheating of the natively produced β_{II} phase.

The electrochemical behaviour of the materials was characterised by galvanostatic testing in conjunction with slow sweep cyclic voltammetry, AC impedance spectroscopy, DC conductivity measurements as well as *ex situ* X-ray diffraction studies. The relatively superior performance of β_{II} was observed, having a first charge capacity of nearly 210 mAh/g of which 150mAh/g (0.9 Li) which could be accurately described as due to lithium removal. This was ascribed to the previously discussed structural conditions and the low bulk resistivity established through AC impedance. It was shown that β_{II} did not undergo a gross structural rearrangement in the first cycle, as had been reported for different silicate¹⁷. Investigation of the electrochemical behaviour of the hydrothermally produced β_I polymorph revealed a phase change to β_{II} upon charging, a transformation that continued through subsequent cycles.

Both the hydrothermally reheated γ_0 and the β_I phase produced through solid state synthesis showed poor cycling ability to an extent that it was hard to characterise the processes occurring on cycling. This was most likely due to the poor conductivity of

γ_0 and the lack of doping in the β_I phases (present in the hydrothermal β_I material). While the capacity retention for all phases was particularly poor, even over a relatively short number of cycles, the initial first charge performance of both the β_{II} and β_I phases show evidence of electrochemical activity.

This initial investigation into the properties of the $\text{Li}_2\text{CoSiO}_4$ material opened several interesting directions for future work. Further attempts to produce the γ_{II} phase observed by West *et al.* as well as accessing other phases through the solid state synthesis are obvious routes for future research. In order for $\text{Li}_2\text{CoSiO}_4$ to be a useful Li-ion battery cathode the capacity retention would have to be vastly improved and several easy methods exist for the optimisation of electrodes.

An investigation into the cause of different cycling behaviour of the solid state and hydrothermal β_I phases, as well as the exact nature of the β_I to β_{II} conversion observed upon cycling would help to elucidate the nature of some of the processes occurring with cycling. Another area of investigation that may produce interesting insight, both of $\text{Li}_2\text{CoSiO}_4$ and possibly further afield is a quantitative study of the structural properties of the materials and their effects upon the cycling behaviour as well as establishing the exact affect of the Co-O-Si triad has upon the insertion/removal voltage of lithium.

This initial investigation of $\text{Li}_2\text{CoSiO}_4$ has provided an interesting overview of the possibilities offered by cobalt silicate olivines as cathode materials. Much work is still needed to establish the exact nature of the electrochemical processes occurring during battery cycling, but $\text{Li}_2\text{CoSiO}_4$ offers a useful insight into this growing area of cathode research.

4.4. References.

1. A. Yamada, M. Hosoya, S. Chung, Y. Kudo, K. Hinokuma, K. Liu, and Y. Nishi, *Journal of Power Sources*, 2003, **119-121**, 232-238.
2. S. Shi, L. Liu, C. Ouyang, D. Wang, Z. Wang, L. Chen, and X. Huang, *Phys. Rev. B*, 2003, **68**, 195108.
3. R. Amin and J. Maier, *Solid State Ionics*, 2008, **178**, 1831-1836.
4. M. Arroyo-de Dompablo, M. Armand, J. Tarascon, and U. Amador, *Electrochemistry Communications*, 2006, **8**, 1292-1298.
5. K. Ozawa, *Solid State Ionics*, 1994, **69**, 212-221.
6. A. R. West and F. P. Glasser, *Journal of Solid State Chemistry*, 1972, **4**, 20-28.
7. M. E. Villafuerte-Castrejon and A. R. West, *J. Chem. Soc., Faraday Trans. 1.*, 1979, **75**, 374-384.
8. M. E. Villafuerte-Castrejon and A. R. West, *J. Chem. Soc., Faraday Trans. 1.*, 1981, **77**, 2297-2307.
9. A. R. West and P. G. Bruce, *Acta Crystallogr B Struct Crystallogr Cryst Chem*, 1982, **38**, 1891-1896.
10. H. Yamaguchi, K. Akatsuka, and M. Setoguchi, *Acta Crystallogr B Struct Crystallogr Cryst Chem*, 1979, **35**, 2678-2680.
11. A. R. Armstrong, C. Lyness, M. Menetrier, and P. G. Bruce, *Chemistry of Materials*, 2010, **22**, 1892-1900.
12. C. Lyness, B. Delobel, A. R. Armstrong, and P. G. Bruce, *Chem. Commun.*, 2007, 4890-4892.
13. S. Wu, Z. Zhu, Y. Yang, and Z. Hou, *Transactions of Nonferrous Metals Society of China*, 2009, **19**, 182-186.
14. S. Wu, Z. Zhu, Y. Yang, and Z. Hou, *Computational Materials Science*, 2009, **44**, 1243-1251.
15. M. Arroyo y de Dompablo, U. Amador, J. Gallardo-Amores, E. Morán, H. Ehrenberg, L. Dupont, and R. Dominko, *Journal of Power Sources*, 2009, **189**, 638-642.
16. Z. Gong, Y. Li, and Y. Yang, *Journal of Power Sources*, 2007, **174**, 524-527.
17. A. Nytén, A. Abouimrane, M. Armand, T. Gustafsson, and J. O. Thomas, *Electrochemistry Communications*, 2005, **7**, 156-160.
18. P. E. A. de Moor, T. P. M. Beelen, B. U. Komanshek, O. Diat, and R. A. van Santen, *The Journal of Physical Chemistry B*, 1997, **101**, 11077-11086.
19. C. R. A. Catlow, D. S. Coombes, D. W. Lewis, and J. C. G. Pereira, *Chemistry of Materials*, 1998, **10**, 3249-3265.
20. K. Kang and G. Ceder, *Phys. Rev. B*, 2006, **74**, 094105-7.
21. S. Nishimura, G. Kobayashi, K. Ohoyama, R. Kanno, M. Yashima, and A. Yamada, *Nat Mater*, 2008, **7**, 707-711.
22. S. Al-Muhtaseb and J. Ritter, *Advanced Materials*, 2003, **15**, 101-114.
23. I. Belharouak, C. Johnson, and K. Amine, *Electrochemistry Communications*, 2005, **7**, 983-988.
24. P. Larsson, R. Ahuja, A. Nytén, and J. O. Thomas, *Electrochemistry Communications*, 2006, **8**, 797-800.
25. A. Nytén, A. Abouimrane, M. Armand, T. Gustafsson, and J. O. Thomas, *Electrochemistry Communications*, 2005, **7**, 156-160.
26. J. E. Bauerle, *Journal of Physics and Chemistry of Solids*, 1969, **30**, 2657-2670.
27. C. Delacourt, L. Laffont, R. Bouchet, C. Wurm, J. Leriche, M. Morcrette, J. Tarascon, and

- C. Masquelier, *J. Electrochem. Soc.*, 2005, **152**, A913-A921.
28. S. Chung, J. T. Bloking, and Y. Chiang, *Nat Mater*, 2002, **1**, 123-128.
29. J. M. Zheng, Z. R. Zhang, X. B. Wu, Z. X. Dong, Z. Zhu, and Y. Yang, *J. Electrochem. Soc.*, 2008, **155**, A775-A782.
30. G. T. Fey, P. Muralidharan, C. Lu, and Y. Cho, *Solid State Ionics*, 2006, **177**, 877-883.

Chapter 5. $\text{Li}_2\text{CoSiO}_4$ Electrode Optimisation

Chapter 5. $\text{Li}_2\text{CoSiO}_4$ Electrochemical Optimisation

Chapter contents:

5.1. Introduction	120
5.2. Results and Discussion	121
5.2.1. Mechanical Milling	122
5.2.1.1. Structural and Morphological Effects of Mechanical Milling.....	122
5.2.1.2. Electrochemical Effects of Ball-milling.....	125
5.2.2. Carbon Coating of $\text{Li}_2\text{CoSiO}_4$	134
5.2.2.1. Structural Characterisation of Carbon Coated $\text{Li}_2\text{CoSiO}_4$	139
5.2.2.2. Electrochemical Behaviour of Carbon Coated $\text{Li}_2\text{CoSiO}_4$	143
5.3. Conclusions and Further Work.....	150
5.4. References	152

5.1. Introduction

In an attempt to improve the cycling behaviour of $\text{Li}_2\text{CoSiO}_4$ the effect of mechanical milling and carbon coating upon β_{II} , β_{I} and γ_0 materials was investigated. The materials were structurally and electrochemically characterised to determine the various effects of milling and coating.

There is substantial interest in electrode optimisation methods¹⁻⁸ due to the recent effort to commercialise LiFePO_4 materials which, though preferential to the LiCoO_2 , suffer from low conductivity. Though the exact optimisation approach is tailor-made for the individual material, generally, areas such as electrode/electrolyte interface and electrode 'wiring' are sought out for improvement. It is hoped that by targeting the electronic and ionic movement in the bulk and at the interface a significant improvement in the electrochemical performance should occur.

LiFePO_4 type materials are known for their sluggish ionic and electronic conductivity^{4,9-11} (as witnessed by the resistivity values of the three as-prepared polymorphs in the previous chapter), as such olivine optimisation approaches tend to focus upon improving conductivity. Two classic methods to improve the materials electronic properties are through reducing the particle size (thus reducing the ionic diffusion length) and surface coating the particles with a conducting material to improve 'wiring' between the particles and the performance of the material at the interface. Through mechanical milling and carbon coating the effects of these two processes on $\text{Li}_2\text{CoSiO}_4$ materials were investigated to gauge whether the electrochemical performance of $\text{Li}_2\text{CoSiO}_4$ could be easily improved.

5.2. Results and Discussion

The materials were produced hydrothermally (with re-heating to produce the β_1 and γ_0 phases) as described in the experimental section in Chapter 3. It was felt that the hydrothermal method offered a far more convenient (and reproducible) alternative to the solid state method also discussed in Chapter 3 and, thus, was used exclusively to produce the β_{II} , β_I and γ_0 phases for the optimisation investigation.

As witnessed in the slow sweep cyclic voltammetry of the as-prepared material in Chapter 4, section 4.3, there is a noticeable current contribution in the voltage cut off region (near 4.5 V vs. Li^+/Li). There is considerable precedent for this to be the consequence of side-reactions between the electrolyte and the electrode, especially at higher voltages associated with Li^+ removal¹²⁻¹⁵. It is generally thought this is an effect of exposure of the redox active cations (transition metal ions) to the electrolyte, which can catalyse reactions with the electrolyte and cause dissociation, when under increased thermodynamic ‘pressure’ (i.e. elevated voltages or lower activation energies during structural rearrangement from lithium removal/insertion). In theory NASICON type materials and their lithium analogues are better equipped to withstand electrolyte attack, the redox active cations being ensconced within a 3D poly-anion network, unlike their layered transition metal oxide counter-parts⁹. Several different electrolyte systems were tested with the $\text{Li}_2\text{CoSiO}_4$ materials to find the most appropriate (see appendix iv) It was found that the electrolyte used to characterise the pristine material, LP30 (1:1 DMC:EC, 1M LiPF_6) still gave the best results, and so was used.

5.2.1. Mechanical Milling

A convenient method to reduce powder particle size is to mechanically mill materials in a hardened high energy ball milling vessel. The mill is sealed with the active material and two tungsten carbide bearings inside, the whole container is then vigorously mechanically shaken, the time length determining the size of the milled particles. By reducing the particle size and, thus, the Li^+ diffusion length within the particles of the material, the internal Li^+ diffusion kinetics should improve. Any internal benefit is also coupled with the increased electrode/electrolyte interface area due to the greatly increased surface area of the particles. Both effects should combine to give an improved capacity for each polymorph compared to their pristine analogue. While this simple method is easy to implement, its inherently energetic nature and the increase in particle surface area can introduce side-reactions and subsequent impurities during the milling process.

5.2.1.1. Structural and Morphological Effects of Mechanical Milling

In Figure 5.2.1 we can see a typical diffraction pattern of a $\text{Li}_2\text{CoSiO}_4$ polymorph after ball-milling. From the TEM images, displayed in Figure 5.2.2, we see that both β_{I} and γ_0 polymorphs have reduced in size compared to their as-prepared counterparts (in the γ_0 case by an order of magnitude). The β_{II} hydrothermal preparation is the only material without a significant change in particle size on milling, in this case, the ball milling may even be counter-productive, as the high energy milling process may allow some of the smaller particles to sinter together, creating larger, less

desirable, particles. This may well be the case as seen by the larger range in particle sizes observed in the ball milled material ($\phi \sim 20\text{-}150\text{nm}$) compared to the more homogeneous as-prepared material ($\phi \sim 60\text{-}100\text{nm}$ seen in Chapter 4, section 4.3.2).

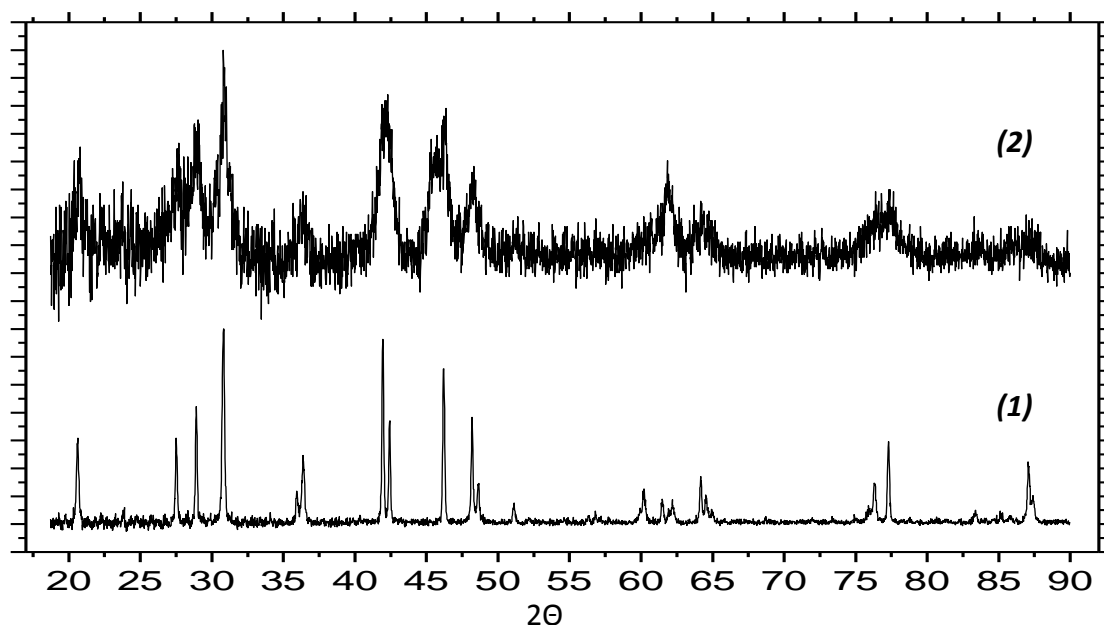


Figure 5.2.1. Comparison of (normalised) X-ray diffraction patterns for $\beta_I \text{Li}_2\text{CoSiO}_4$ material; (1) As prepared material, (2) After 60 minutes ball-milling.

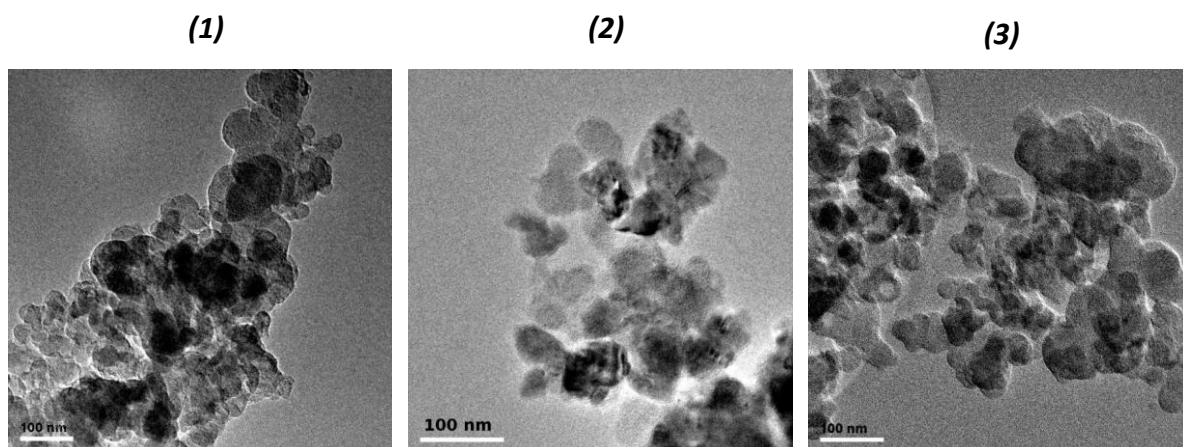


Figure 5.2.2. TEM images of $\text{Li}_2\text{CoSiO}_4$ polymorphs ball-milled for 60 minutes; (1) γ_0 polymorph, (2) β_{II} polymorph, (3) β_I polymorph.

As the T.E.M. images in Figure 5.2.2 highlight, the ball-milling process produces a fairly homogenous particle size across all materials. Both the β_I and γ_0 polymorph

show significant particle size reduction with the majority of the ball-milled material having a diameter of less than 100nm (both β_I and γ_0 materials contained particles with $\varnothing > 500\text{nm}$ prior to ball milling). The β_{II} material only experienced a marginal change in particle size, with the particles seeming to increase diameter after ball-milling (from 60nm \varnothing as-prepared to $>100\text{nm}$ \varnothing after ball-milling).

5.2.1.2. Electrochemical Effects of Ball-milling

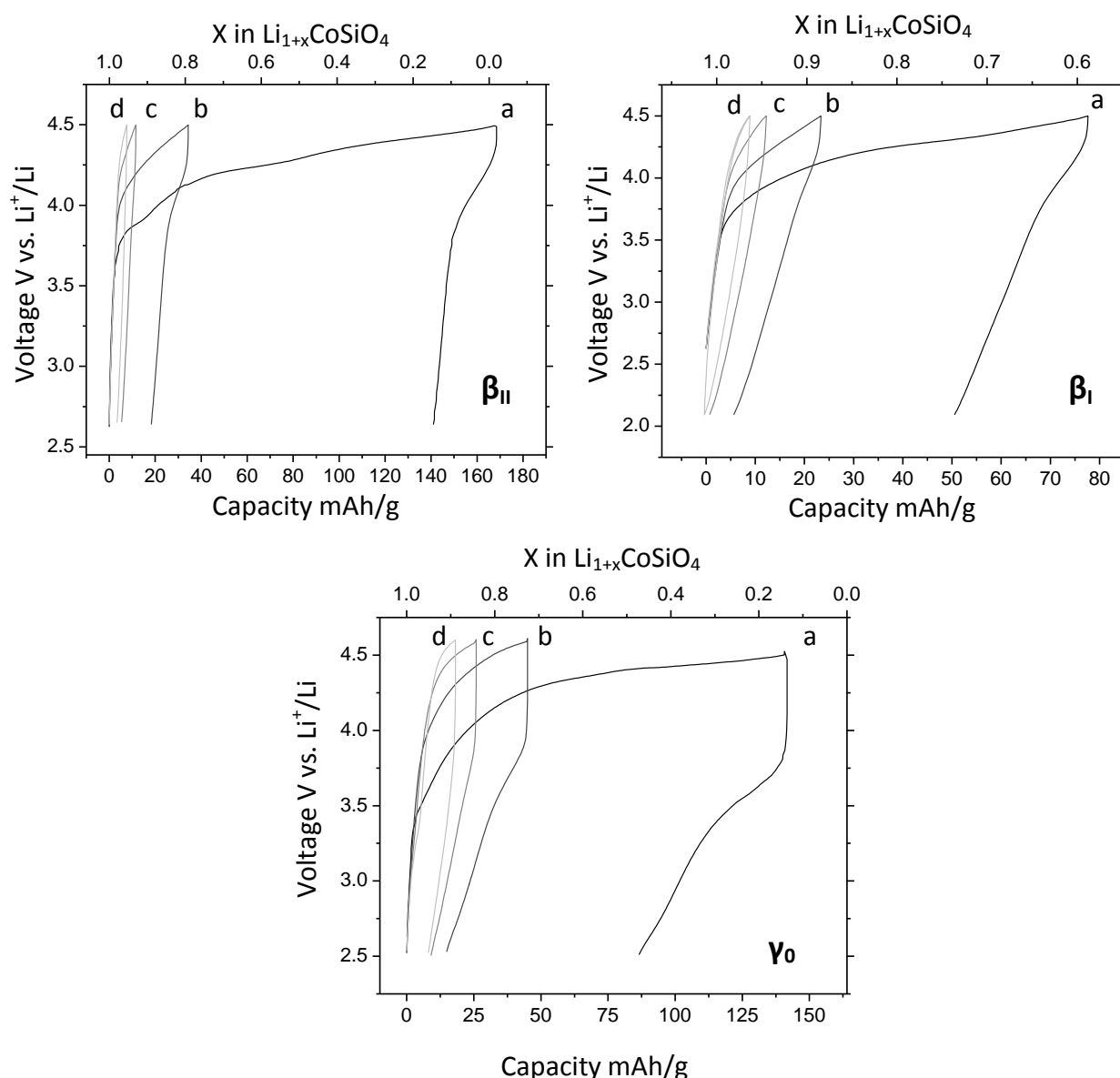


Figure 5.2.3. Galvanostatic load curves of ball-milled $\text{Li}_2\text{CoSiO}_4$ polymorphs; a) first cycle, b) second cycle, c) fifth cycle, d) tenth cycle – Electrolyte LP30, cycle rate 10mA/g at a temperature of 50°C.

It is apparent from Figure 5.2.3 that ball-milling significantly alters the galvanostatic behaviour of the $\text{Li}_2\text{CoSiO}_4$ polymorphs. The γ_0 polymorph is the only material whose electrochemical performance is visibly improved after ball-milling. This is not surprising given that the γ_0 material shows the greatest change in particle size after milling, from particles of over $1\mu\text{m}$ \varnothing to an approximate particle size of less than 100nm \varnothing . The first charge capacity of ~ 130 mAh/g is notably better than the pristine

material ($\sim 8 \text{ mAh/g}$). This improvement could be due to kinetic enhancement brought about by reduction in particle size from milling, in-turn reducing lithium (and electronic) diffusion lengths as well as potentially improving the 'wiring' between particles through energetic sintering of particles during the milling process. There is also a distinct possibility that the large capacity merely represents a side reaction caused by the more reactive smaller particles.

The whole first discharge process develops a capacity of $\sim 50 \text{ mAh/g}$ and, where a discharge pseudo-plateau is identifiable, it comes after significant polarisation ($\sim 600 \text{ mV}$ between charge and discharge process, compared to $\sim 500 \text{ mV}$ for as-prepared β polymorphs). This poor electrochemical performance, despite the, presumably, greatly enhanced surface area, suggests that the structure of γ_0 phase presents considerable obstacles to the efficient insertion and removal of Li^+ ions from the structure.

While the capacity retention upon cycling does show improvement over the as-prepared γ_0 material, this is to be expected given the near negligible electrochemical activity exhibited in the as-prepared material and both charge and discharge capacities of the ball-milled materials quickly dissipate in subsequent cycles (as can be seen in Figure 5.2.4).

Unlike the ball-milled γ_0 phase, the β_{I} and β_{II} phases show significantly reduced electrochemical performance compared to their as-prepared material. For the β_{I} phase this is counter-intuitive given the reduction of particle size post-milling (particles were reduced from up to $500 \text{ nm } \varnothing$ down to particles under $100 \text{ nm } \varnothing$). Structural refinement

was attempted to determine if the ball-milled β_{I} material was structurally different to its as-prepared counterpart.

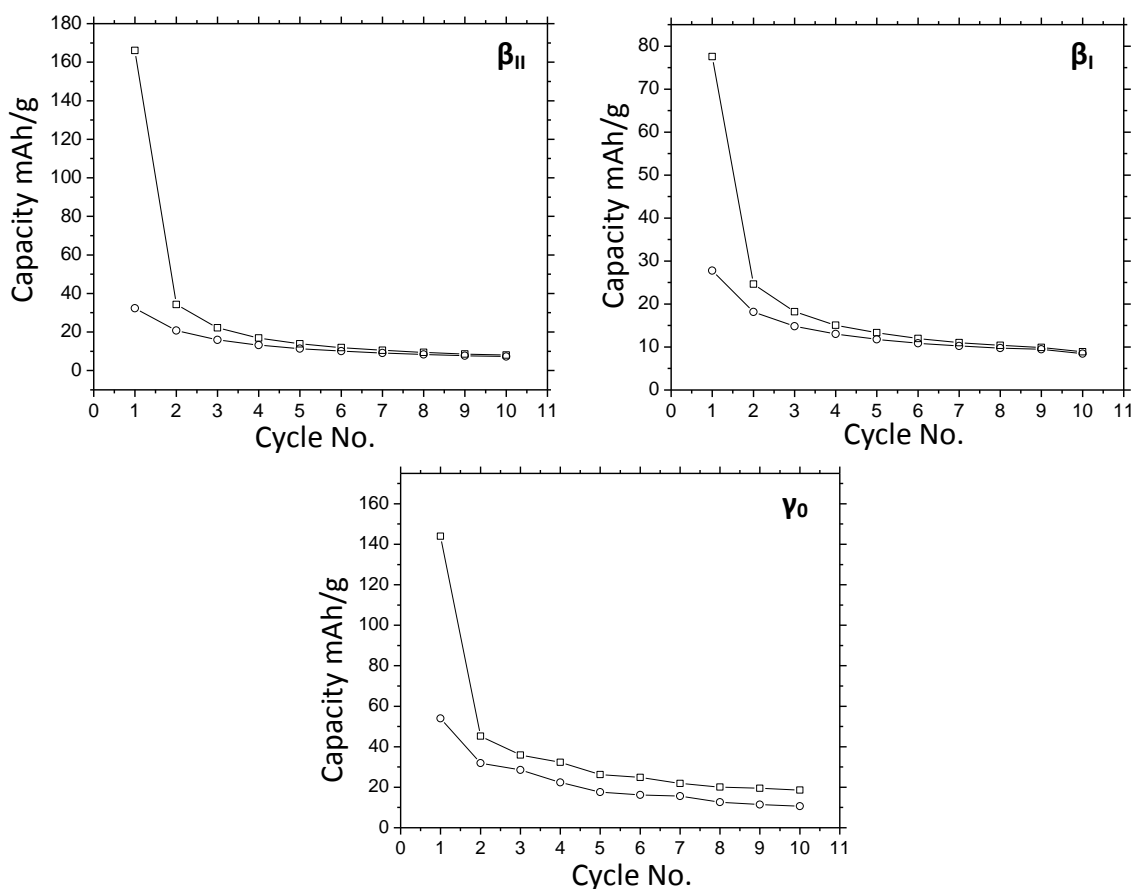


Figure 5.2.4 Capacity Vs. Cycle number for ball-milled $\text{Li}_2\text{CoSiO}_4$ β_{II} , β_{I} and γ_0 materials.-Electrolyte LP30, cycle rate 10mA/g at a temperature of 50°C

The refinement did not provide any clear answers, though it inferred that milling may globally increase disorder in the cobalt and lithium sites. Although given the poor state of the ball-milled diffraction pattern, the refinement results should be treated with a large degree of caution.

The reduction in capacity of ball-milled β_{II} on first charge is perhaps to be expected given the slight increase in particle size post-milling. Looking closer at the profiles of the β polymorph it can be seen that the voltage plateaus seen on charge (and to a certain extent on discharge) in the as-prepared materials have been replaced by sloping pseudo-plateaus for the ball-milled samples. The lack of any single

electrochemical process (i.e. a voltage plateau) suggests that side-reactions are present, and perhaps prevalent, a notion which may explain Figure 5.2.4 which displays the capacity versus cycle number of the ball-milled material over 10 cycles and shows diminished capacity retention compared to the as-prepared material.

As with the pristine material, the charge capacity drops off sharply after the first cycle but capacity loss slows on subsequent cycles. The discharge capacity reduction is not so severe but (as with the pristine material) the discharge capacity continues to significantly lag the charge capacity. As this effect seems to be ubiquitous (i.e. the improvement in the first charge capacity of the γ_0 ball-milled material is not matched in an equally improved discharge capacity) it would seem there is fundamentally a problem with reinserting lithium into the once occupied sites; whether this is a result of structural impediments or parasitic side-reactions is unclear.

The apparent change in cycling behaviour on ball-milling was investigated further using AC impedance and DC resistivity measurements. If the reduction in performance is caused by the loss of lithium or other elements at the surface during milling, this 'delithiated' phase may subsequently form a surface layer, which should become apparent with AC impedance. This process has been witnessed with the more air sensitive iron silicates¹² and under the energetic environment of ball-milling the surface layers may be more susceptible to reaction with the atmosphere^{16,17} (attempts were made to mill the materials under argon but similar electrochemical results were achieved, suggesting that it may not be a surface oxidation layer forming during ball-milling *per se* but a loss of lithium/ions and subsequent reactions in the cell that causes the reduced performance).

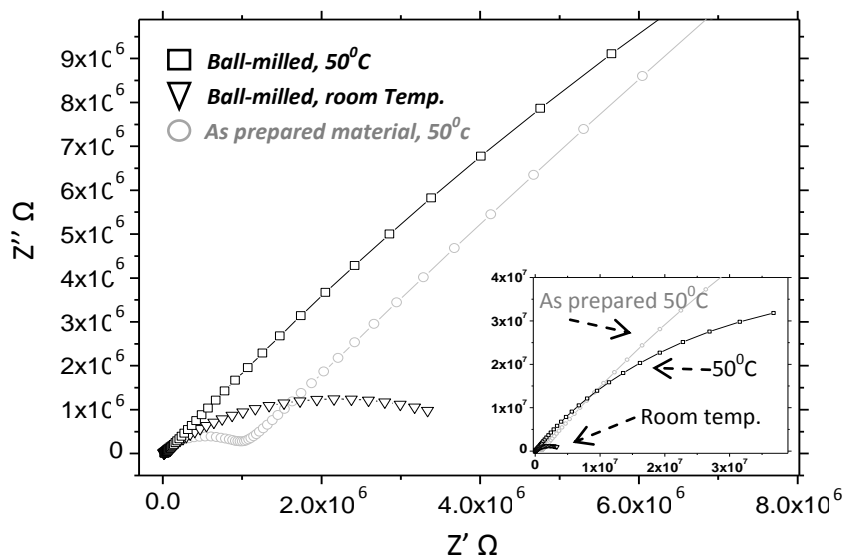


Figure 5.2.5. AC Impedance spectrum of Ball-milled β_{II} material; \square measured at 50°C , ∇ measured at room temperature, \circ As prepared β_{II} material at 50°C (provided as a reference). Inset shows full spectrum. Spectrum taken using two stainless steel blocking electrodes.

As with the pristine materials, the only phase that displays a complex impedance spectrum is the β_{II} material (the other materials resolving to a single point about zero on both impedance axis, i.e. an electrical 'shunt').

An identical equivalent circuit to the one used for the pristine material was employed (-Resistor₁/Constant Phase element₁ + Resistor₂/Constant Phase Element₂-) fitted using a least square refinement. Compared to the as-prepared material, the high frequency semi-circle (traditionally assigned to the bulk processes) is severely depressed relative to the low frequency semi-circle (thought to be produced by particle surface/grain boundary effects). This indicates that the surface/grain boundary effect is the dominating feature.

The values generated from the impedance spectrum are displayed in Table 5.2.1. Traditionally the high frequency (bulk) semi-circle is expected to have a capacitance of hundreds of picoFarads, while the low frequency (surface/grain

boundary) semi-circle is of the order of nanoFarads. The ball-milled β_{II} material is found to have a high frequency capacitance of $\sim 10^{-10}$ Fs⁻¹ suggesting a bulk contribution, but the low frequency capacitance is in the order of $\sim 10^{-7}$ F s⁻¹ which is a considerably lower capacitance than expected for a surface/grain contribution. The low capacitance may be due to oxygen deficiencies or loss of other ions at the surface of the grains or other intricate effects such as increased strain, resulting in a low permittivity.

AC Impedance	Room Temp.		50°C	
	High Freq.	Low Freq.	High Freq.	Low Freq.
Resistivity/Ωm	1.02×10^4	9.45×10^6	5.99×10^4	1.14×10^8
Capacitance/Fs⁻¹	2.41×10^{-10}	1.39×10^{-7}	2.57×10^{-9}	2.42×10^{-6}

DC Resistivity/Ωm	Room temp.	50°C
β_{II} material	4.51×10^6	1.16×10^7
β_I material	1.36×10^9	9.80×10^9
γ_0 material	1.09×10^9	1.74×10^9

Table 5.2.1. Results obtained from AC impedance spectroscopy of ball-milled β_{II} material, using a - $R_1/CPE_1 + R_2/CPE_2$ - equivalent circuit. DC Resistivity data for β_{II} (taken for the 3-4.5 volt region), β_I and γ_0 materials at room temperature and 50°C.

The resistivity and capacity for the bulk process within the ball-milled β_{II} material was $\sim 10^5 \Omega m$ and $\sim 10^{-10}$ Fs⁻¹ respectively, changing to $\sim 10^6 \Omega m$ and $\sim 10^{-9}$ Fs⁻¹ at 50°C. Compared to the as-prepared material, the bulk resistivity is reduced while the grain boundary resistance remains similar.

One possible explanation for the bulk resistivity reduction is the loss of lithium during ball-milling. As the silicate materials are expected to be semi-conductors⁹, the loss of Li⁺ ions could result in P-type doping within the bulk material, this in turn could improve the conductivity (i.e. reduce the resistivity). Ball-milling is known to increase

internal strain within crystallites^{18,19}, due to the presence of lattice distortion at the grain boundary, possible from the accentuation of dislocation density due to prolonged milling. From the DC resistivity measurement it would seem that the electrical resistance is dominated by the grain boundary resistance which may explain why β_{II} and β_I and γ_0 do not show altered performance.

The DC voltage vs. current profile of ball-milled β_{II} , β_I and γ_0 materials showed non-linear behaviour (an example is given with the β_{II} material in appendix v). This may explain why the polymorphs deviate from 'classic' semi-conductor behaviour, i.e. their resistance increases with temperature. The resistivity measurements were calculated for the region 2 - 4.5 V and produced values that were lower than the pristine material for the β_{II} polymorph but higher for β_I and γ_0 materials ($\sim 10^7$, 10^7 and 10^9 Ωm for the as-prepared β_{II} , β_I and γ_0 respectively). The improvement in the DC resistance of the β_{II} material could be explained by particle sintering (seen in the TEM image) improving the 'wiring' between crystallites, an effect that is outweighed by the dominating features of the higher resistance surface/grain boundary layer which is much more ubiquitous in the after milled β_I and γ_0 materials compared to their as-prepared counterparts.

From the electrochemical and structural study it is clear that the γ_0 polymorph initially experiences an improvement in the electrochemical performance either from particle size reduction (by an order of magnitude) or side reactions, but the performance of the γ_0 phase quickly diminishes and (while an improvement on the pristine γ_0 material) overall the ball-milled material does not perform particularly well.

When the change in particle size is less dramatic (i.e. β_I and β_{II}) no apparent improvement in electrochemistry is observed. This is seen in both β_{II} and β_I galvanostatic load curve which show diminished first charge (and discharge) capacities and poor capacity retention over cycling, compared to the pristine material.

The electrochemical behaviour of all materials post-milling is most telling. All materials display a first charge pseudo-plateau which gently slopes upwards to the voltage cut-off. The lack of reversible discharge, or subsequent charging plateaus strongly suggests that the pseudo-plateau is not formed by reversible lithium removal. Instead it would seem that it is the consequence of irreversible side-reactions probably initiated by some lithium removal from the structure (hence the plateau starts around the lithium removal voltage seen in the as prepared material). The side reactions may not be as prevalent on subsequent cycles because their products may be passivating, causing a reduction in electrochemical activity.

Both β_I and β_{II} polymorphs show reduced capacities compared to their non-milled counterparts. With the γ_0 material it is possible that initially a balance is struck, on the first cycle at least, between the benefits of reducing the particle size versus the debilitating effects of side reactions that seem to occur due to the increased particle surface area/electrolyte interaction.

It would seem that ball-milling is not an ideal technique for $\text{Li}_2\text{CoSiO}_4$ electrode optimisation as the reduced particle size does not offer a remedy to the poor capacity retention. This infers that ionic conductivity (in the bulk at least) may not be the determining factor on the capacity retention with cycling, given that, in the β_I and γ_0 materials such a large reduction in bulk diffusion length is not met with an

improvement in the electrochemical behaviour. This is hard to give this as absolute, as negative effects associated with particle size reduction, (i.e. side reactions) may diminish any kinetic benefit gained from reducing particle size. It is clear that the next stage of work on particle size reduction would have to investigate the nature of the side reactions and establish a method to negate them.

5.2.2. Carbon Coating of $\text{Li}_2\text{CoSiO}_4$

Another established approach to improve electrode performance is to coat the particles with a conducting surface to improve electronic connections between particles and electron conduction at the particle surface^{1,8,13,17,20-23}. This method has an advantage over ball-milling as (assuming the coating is near total) the surface covering can act as a barrier against side reactions between the cathode and electrolyte^{13,20,21,24}. The simplest conductive additive to employ (and most favoured from an industrial perspective) is carbon. It is cheap, ubiquitous, non-toxic and offers a wide variety of coating methods. In the case of $\text{Li}_2\text{CoSiO}_4$, due to the pyrolysis temperature of the carbon precursors (to ensure a complete coating regime) and subsequent graphitisation temperatures (to optimise conductivity) special consideration of coating technique is necessary as the coating procedure may involve temperatures in the region of $\text{Li}_2\text{CoSiO}_4$ polymorphic phase change.

Various forms of carbon coating were investigated to determine the optimum carbon precursor, including sucrose (mixed in with the hydrothermal precursors or dispersed in acetone and mixed with the fully formed β_{II} material), citric acid sol-gels and xerogel polymers (added as precursors at the hydrothermal stage, as well as pre-prepared xerogels after hydrothermal synthesis or as pre-prepared $\text{Li}_2\text{CoSiO}_4$ material added during gelation stage of the xerogel). Each coating approach gave a different product, depending greatly on the carbon decomposition process.

As a degree of graphitisation was required to produce a conductively beneficial carbon coating, temperatures near 700°C were necessary during the carbon coating process. It was discovered that, as graphitisation temperatures are approached, the $\text{Li}_2\text{CoSiO}_4$ is highly susceptible to side-reactions with the carbon coating itself or the pyrolysis decomposition products. It may be that as $\text{Li}_2\text{CoSiO}_4$ nears the phase change boundary it forms an intermediate or transitional phase which, given its meta-stable nature, may have significantly lower activation energy than its more thermodynamically stable parent phases. This makes it significantly more reactive to the pyrolysis decomposition products and reduction. Impurities observed from the carbon coating processes tended to be Li_2SiO_3 , other higher order silicates, Li_2CO_3 or cobalt metal, indicative of reductive reactions.

The least disruptive coating process utilised xerogel added to the hydrothermal β_{II} material prior to the final pyrolysis stage of xerogel formation. The xerogel was mixed into β_{II} material in acetone; once the acetone had evaporated the mixture was heated to an appropriate pyrolysis temperature in an oven under flowing argon.

Xerogels are high surface area polymers, consisting of aromatic and extended carbon chains formed through an acid or base catalysed polymerisation of resorcinol and formaldehyde as shown in Figure 5.2.6.

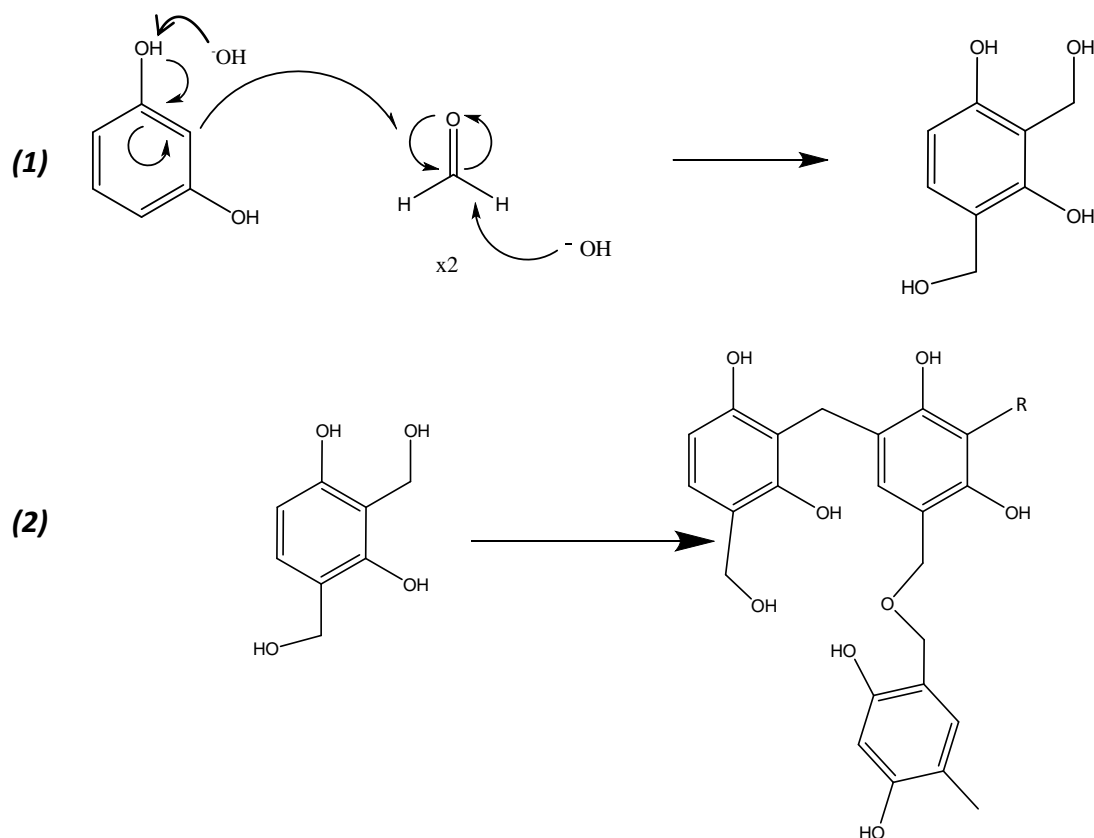


Figure 5.2.6. Xerogel polymerisation reaction scheme: (1) Acid/based catalysed initial condensation, (2) Subsequent polymerisation condensation.

Xerogel has the potential advantage over other types of carbon treatment as it consists of a large network of interconnected high-surface area pores built from a scaffold of conjugated and aromatic bonded carbons, requiring less graphitisation²⁵. Xerogels have previously been successfully employed to improve the electrochemical performance of the iron polyanion silicates²⁶ with impressive results, and thus, were a natural choice for investigation as a conductive additive for cobalt silicate materials.

The Xerogel synthesis involved several stages; the precursors (formaldehyde, resorcinol and lithium carbonate as a catalyst) are mixed together in water then heated to gelation. Subsequent heating removes the water from the polymer matrix

and forms a brittle solid. This is then mixed with the active cathode material and heated under flowing argon to pyrolyse the carbon and coat the active material. At each stage there is the opportunity to alter the conditions and, hence, change the nature of the final xerogel material. By pyrolysing the xerogel with the active material (and thus, choosing a relatively high temperature for xerogel pyrolysis) much of the structural and morphological nature of the material is lost.

The pyrolysis stage of carbon coating involves delicate manipulation of heating and argon flow rates to minimise the effects of the reductive carbothermal pyrolysis. The xerogel undergoes several reactions as it decomposes to carbon, notably water and hydroxide loss below 200°C and subsequent hydrogen gas evolution between $350\text{--}500^\circ\text{C}$, as polymer chains are carbonised²⁵. Hydrogen gas is a strong reducing agent and the management of its evolution within the heated xerogel/ $\text{Li}_2\text{CoSiO}_4$ system became an important factor in producing a (relatively) pure product, with the argon gas flow requiring careful control to ensure that low concentrations of hydrogen gas were produced and could be quickly removed by the flowing argon.

Various approaches were employed to try and produce the 3 previously synthesised $\text{Li}_2\text{CoSiO}_4$ phases, but with limited success. Considerable effort was employed to produce a fast quenching, gas tight apparatus, to form the β_{II} and γ_0 phases. Failure to produce a pure γ_0 material appeared to be caused by a chemical rather than technological obstacle, given that the starting β_{II} phase was always reduced to cobalt metal and lithium silicates at temperatures above 800°C and no remaining $\text{Li}_2\text{CoSiO}_4$ phases were observed. This may suggest that the β to γ

transformation created a reactive intermediate or that the higher temperature produced a more reducing environment (or a combination of the two), hence producing the mentioned impurities, irrespective of the cooling regime. Pure carbon coated β_{II} also proved elusive, as after heating to the $\beta_{\text{II}}/\beta_{\text{I}}$ phase boundary region, carbon coating seemed to introduce considerable hysteresis in the reverse (kinetically dependent) β_{I} to β_{II} transformation, always producing a mixed phase no matter the cooling regime. These effects, combined with the limitations imposed by the graphitisation temperature ($600\text{-}900^\circ\text{C}$) ensured that a mixed phase of $\beta_{\text{I}}/\beta_{\text{II}}$ was universally produced, with heating time having little effect on the relative phase ratios.

To this end it was established that a heating ramp of $3.14^\circ\text{C min}^{-1}$ to an oven temperature of 710°C for 4hrs while incorporating an argon gas flow of two litres a minute and allowing the material to cool with the oven, gave impurity free $\text{Li}_2\text{CoSiO}_4$.

5.2.2.1. Structural Characterisation of Carbon Coated $\text{Li}_2\text{CoSiO}_4$

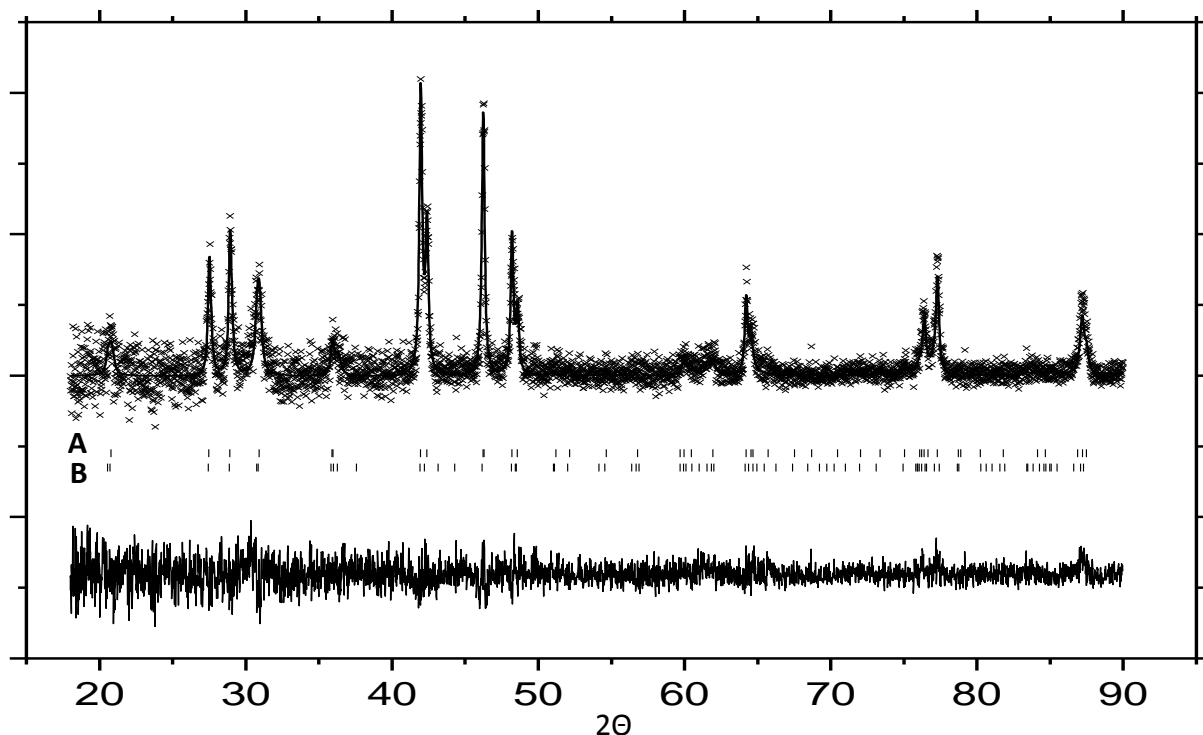


Figure 5.2.7 X-ray diffraction pattern and Rietveld refinement parameters of carbon coated β_I $\text{Li}_2\text{CoSiO}_4$ (10% Xerogel precursor by pre-fired weight): A) $\text{Li}_2\text{CoSiO}_4$ β_{II} polymorph peak positions, B) $\text{Li}_2\text{CoSiO}_4$ β_I polymorph peak positions. R_{wp} 13.64%,

Figure 5.2.7 shows the X-ray diffraction pattern obtained from the carbon coated material. A superficial analysis of the carbon coating diffraction pattern (and in deference to the synthesis conditions) suggested that the β_I polymorph is produced through the coating and subsequent heating process. On closer investigation it was revealed that a phase mixture of β_{II} and β_I gave the best Rietveld fit (the best purely β_I fit gave R_{wp} =22%, when Co/Li mixed sites were allowed to achieve up to 70/30 disorder).

Compared to the pristine β_I material the carbon coated diffraction pattern shows altered relative intensities in the (1,1,1) peak ($2\theta = 30.854$) compared to its

(1,2,0) ($2\theta = 28.43$) and (1,1,0) ($2\theta = 27.54$) neighbours indicative of the presence of the β_{II} phase (using a ' β_{I} only' fit this can be partially accounted for by strongly increasing the disorder in cobalt 4a site).

Table 5.2.2 shows the refinement parameters of the carbon coated $\text{Li}_2\text{CoSiO}_4$ material. The best Rietveld fit was achieved with a relative $\beta_{\text{II}}:\beta_{\text{I}}$ phase ratio of approximately 7:1. This is surprising as the synthesis does not employ the fast cooling supposedly required to produce β_{II} material after heating to relatively high (600-850 $^{\circ}\text{C}$) temperatures²⁷. It is possible this is caused by the initial β_{II} material not undergoing a phase change due to the 'barrier' effects of the carbon coating on the crystallites thus, not allowing the usual conversion of β_{II} to β_{I} at higher temperatures.

The parameters obtained through Rietveld refinement (shown in Table 5.2.2) suggest that there is little difference between the as-prepared β_{II} phase and the β_{II} material present within the carbon coated mixture, apart from a slight change in the overall stoichiometry (from $\text{Li}_{2.06}\text{Co}_{0.94}\text{SiO}_4$ as-prepared to $\text{Li}_{2.1}\text{Co}_{0.9}\text{SiO}_4$ when carbon coated). Though this may have limited significance given the assumed natural variation in stoichiometry between batches.

The β_{I} polymorph present in the carbon coated material is also broadly similar to its as-prepared analogue. The overall stoichiometry is closer to the ideal, at $\text{Li}_{1.99}\text{Co}_{2.01}\text{SiO}_4$ compared to $\text{Li}_{2.02}\text{Co}_{0.98}\text{SiO}_4$ for the as-prepared β_{I} material; this is primarily due to loss of lithium from the mixed cobalt position

β_{II}

Atom	Wyckoff Symbol	x/a	y/b	z/c	B _{iso}	Occupancy
Li1	2a	0.0000	0.15(6)	0.98(5)	0.01(8)	1
Si1	2a	0.5000	0.173(6)	0.946(4)	0.026(3)	1
Li2/Co1	4b	0.25(1)	0.32(1)	0.41(2)	0.019(8)	0.55/0.45(4)
O1	4b	0.279(6)	0.314(7)	0.860(5)	0.06(3)	1
O2	2a	0.0000	0.132(6)	0.367(4)	0.054(7)	1
O3	2a	0.5000	0.17(1)	0.368(6)	0.09(1)	1

$$a = 6.2610(9) \quad b = 5.3448(7) \quad c = 4.9245(7) \quad \text{Space Group: } Pmn2_1$$

$$\text{Cell Volume} = 164.79(5) \text{ \AA}^3,$$

 β_I

Atom	Wyckoff Symbol	x/a	y/b	z/c	B _{iso}	Occupancy
Co1	4a	0.50(1)	0.159(5)	0.157(4)	0.09(4)	Co 0.98/Li 0.02(3)
Si1	4a	0.261(5)	0.421(3)	0.230(2)	0.07(6)	1
Li1	4a	0.88(4)	0.16(1)	0.16(1)	0.09(8)	Li 0.97/Co 0.03(4)
Li2	4a	0.693(8)	0.41(1)	0.231(7)	0.02(7)	1
O1	4a	0.038(5)	0.354(6)	0.154(7)	0.008(9)	1
O2	4a	0.25(1)	0.562(7)	0.151(5)	0.03(1)	1
O3	4a	0.239(4)	0.411(5)	0.594(6)	0.009(7)	1
O4	4a	0.465(5)	0.337(3)	0.158(7)	0.011(4)	1

$$a = 6.251(4) \quad b = 10.731(6) \quad c = 4.931(2) \quad \text{Space Group: } Pbn2_1$$

$$\text{Cell Volume} = 330.8(2) \text{ \AA}^3, \quad R_p = 10.02\% \quad R_{wp} = 13.64\%, \quad \chi^2 = 1.176$$

$$\text{Relative Phase Ratio, } \beta_{II}:\beta_I \text{ 7:1}$$

Table 5.2.2 Refinement parameters achieved from carbon coated Li₂CoSiO₄ : β_{II} Polymorph and β_I polymorph gave $R_{wp} = 13.64\%$ at a relative phase ratio of $\beta_{II}:\beta_I$ 7:1.

TEM images in of the carbon coated material (Figure 5.2.8) show that there is none of the particle growth seen previously when the β_{II} material was heated (i.e. to access the β_I and γ_0 phases). There is also an absence of an obvious thick carbon

surface layer sometimes associated with high degrees of carbon coating²⁰. The lack of particle growth again suggests that the carbon acts to retard crystal growth which may be crucial for the β_{II} to β_{I} transformation.

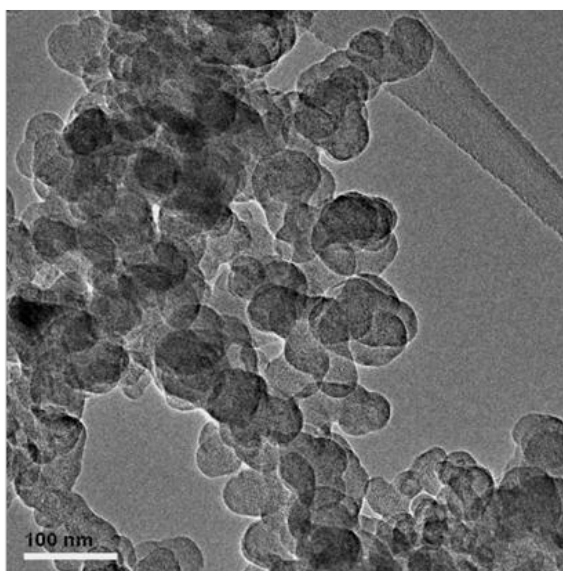


Figure 5.2.8 TEM micrograph image of carbon coated $\text{Li}_2\text{CoSiO}_4$ material.

Further investigation showed that, when purely xerogel underwent an identical heating regime, a large weight loss was observed, the xerogel losing over 70% of its mass. This is to be expected given the transformation of hydrolysed polymer to graphitic carbon thought to occur during heating²⁵. As a rough approximation (using volume and surface area of the particles, and the densities and ratios of involved materials) a starting pre-fired mixture of 90% active material and 10% wt. Xerogel precursor would result in only ~ 1 Å deep universal carbon coating covering the particles which would explain why a clear surface layer isn't observed in the TEM image. It could well be that the carbon only covers patches of the particles.

While the physical presence of the carbon coating may be only slight, it is clear that the xerogel treatment has an effect upon the nature of the material and it is expected that the carbon coating should also have some effect on the electrochemical performance of the material.

5.2.2.2. Electrochemical Behaviour of Carbon Coated $\text{Li}_2\text{CoSiO}_4$

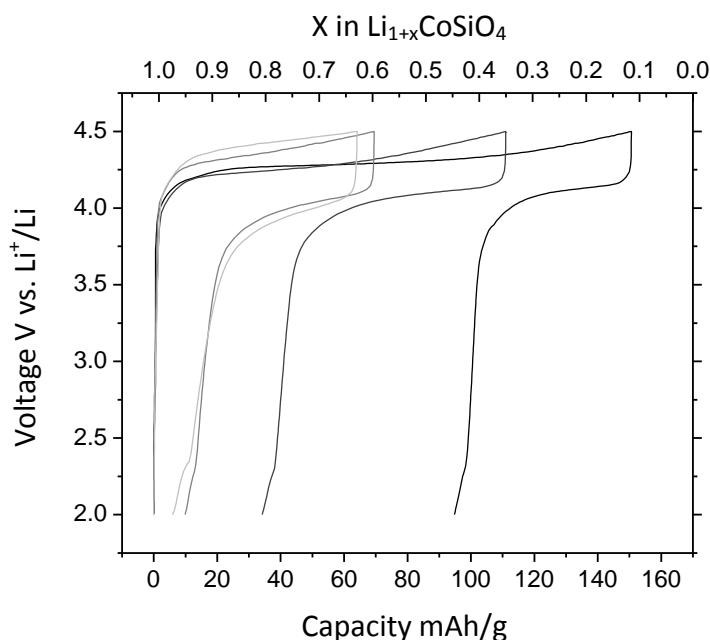


Figure 5.2.9 Galvanostatic load curve for carbon coated $\text{Li}_2\text{CoSiO}_4$ material: - Electrolyte LP30, cycle rate 10 mA/g at a temperature of 50°C

The electrochemical behaviour shown in Figure 5.2.9 is improved compared to the pristine (and ball-milled) β_{I} material (Chapter 3, Section 4.3.3 and Figure 5.2.3 respectively). The first charge shows a defined plateau beginning at 4.21V, slightly higher than the as-prepared β_{II} material but clearly a single plateau (i.e. not 2 separate plateaus for β_{II} and β_{I} phases). This would suggest that the major contribution to the electrochemical behaviour comes from the β_{II} phase. Approximately 150mAh/g capacity passes before the 4.5V cut-off, which is significantly less than the 210 mAh/g capacity observed in the β_{II} as-prepared material. There is a 300mV hysteresis between

charge and discharge plateaus, a reduction of $\sim 200\text{mV}$ compared to the observed charge/discharge polarisation in the pristine β_{II} material. While this polarisation reduction suggests that the carbon coating goes some way to mitigating the ohmic effects between charge and discharge, it either does not fully negate the kinetic impediment, or perhaps, it hints at a process that is not improved by the benefit provided by carbon coating (e.g. a slightly different thermodynamic process between initiating lithium removal and lithium insertion). The first discharge capacity is slightly larger than its un-coated counterpart (110mAh/g vs. 103mAh/g) but it is in the subsequent cycles that a difference in behaviour becomes more noticeable as Figure 5.2.10 shows.

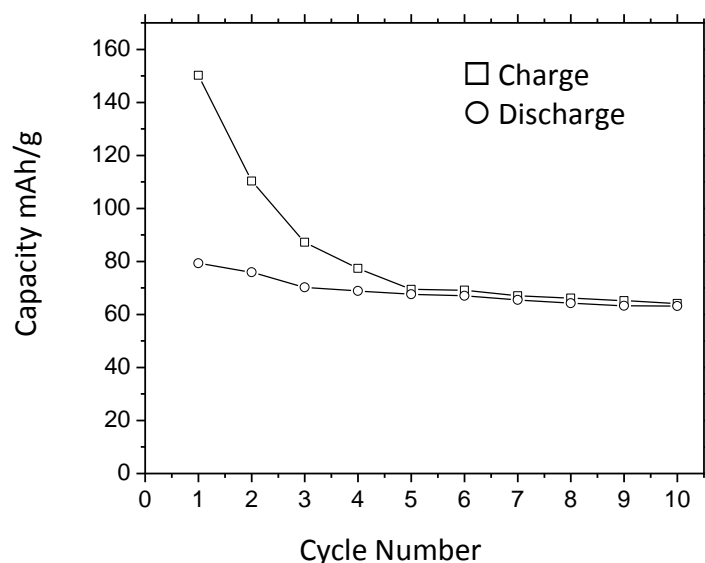


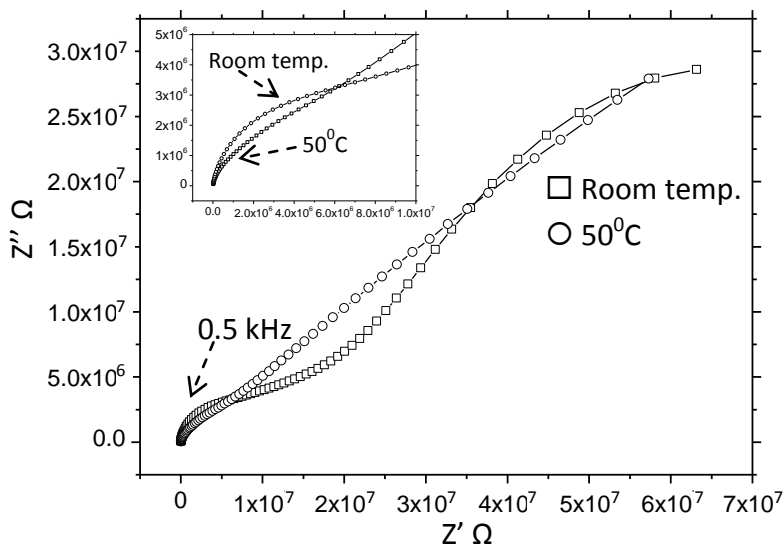
Figure 5.2.10. Capacity Vs. Cycle number for β_{I} carbon coated material: \square Capacity on Charge, \circ Capacity on discharge – Electrolyte LP30, cycle rate 10mA/g at a temperature 50°C

As with the pristine material the carbon coated material shows a diminished second cycle capacity in both charge and discharge ($\sim 60\%$ and 3% reduction respectively, compared to $\sim 62\%$ and 24% drop for the pristine material) and continues

this trend through the following cycles, showing a second to tenth cycle reduction of ~40% for charging capacities and 26% for discharge capacities

The improved capacity retention is indicative that the carbon coated material is able to improve the cycling behaviour of the $\text{Li}_2\text{CoSiO}_4$ material and, as witnessed by the selected galvanostatic cycles in Figure 5.2.9, it reduces the polarisation seen on charging and discharging. It is not clear whether the carbon coating acts solely as a barrier to the side reactions assumed to be present (as identified in the as-prepared and ball-milled materials). There is a chance the carbon coating improves the surface kinetics of the particles, diminishing the ohmic drop between the surface of the particles and the $\text{LiCoSiO}_4/\text{Li}_2\text{CoSiO}_4$ interface (the reduction of charge/discharge polarisation would suggest this). Most likely it is a combination of the two factors.

(1)



(2)

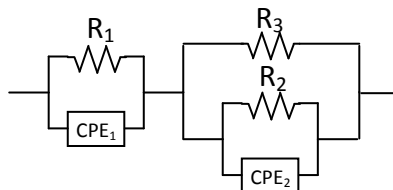


Figure 5.2.11. (1) Nyquist plot of carbon coated $\text{Li}_2\text{CoSiO}_4$ taken between stainless steel blocking electrodes: \square Room temperature, \circ 50°C ; Inset high frequency region. (2) Equivalent circuit used to model carbon coated AC impedance. Spectrum taken using two stainless steel blocking electrodes.

The AC impedance spectrum from the carbon coated material was notably different from the as-prepared (and ball-milled) β_{II} material, suggesting the carbon coating process had changed the electronic nature of the material. Instead of a clear high frequency and low frequency semi-circle, representing the bulk and grain boundary process respectively, there appears to be a more complex system at work. Several equivalent circuits were developed and tested, modelling various different scenarios (e.g. complete coating of particles with carbon, partial covering, and replacement of surface layer with carbon etc.). It was found that the circuit that gave the best fit (i.e. the lowest χ^2 value for the non-linear least squares fit) represented the carbon coating (and possibly the β_I phase electronic contributions) as a single resistor in parallel with the dipole that is assumed to include the surface/grain boundary contribution (equivalent circuit shown in Figure 5.2.11 (2), It has been used previously to model similar situations¹).

AC impedance

	Room Temp.			50°C		
	High Freq.	Low Freq.		High Freq.	Low Freq.	
Resistivity/ ΩM	$1.26 \times 10^8 (R_1)$	$7.59 \times 10^9 (R_2)$	$1.62 \times 10^9 (R_3)$	$2.3 \times 10^8 (R_1)$	$7.59 \times 10^8 (R_2)$	$1.01 \times 10^{10} (R_3)$
Capacity/ Fs^{n-1}	$5.31 \times 10^{-11} (CPE_1)$	$2.57 \times 10^{-6} (CPE_2)$		$1.84 \times 10^{-10} (CPE_1)$	$1.12 \times 10^{-6} (CPE_2)$	

The diagram shows an equivalent circuit with two main parallel branches connected in series. The first branch contains a resistor R_1 in parallel with a constant phase element CPE_1 . The second branch contains a resistor R_3 in parallel with a series combination of a resistor R_2 and a constant phase element CPE_2 .

DC Resistivity

	Room Temp.	50°C
Resistivity/ Ωm	1.39×10^5	2.22×10^6

Table 5.2.3. AC impedance and DC Resistivity details for carbon coated Li₂CoSiO₄.

The capacities of the high frequency and low frequency semi-circles are $\sim 10^{-11}$ F sⁿ⁻¹ and $\sim 10^{-6}$ F sⁿ⁻¹ ($\sim 10^{-10}$ F sⁿ⁻¹ and $\sim 10^{-6}$ F sⁿ⁻¹ for 50°C respectively), inferring that the high frequency semi-circle is again responsible for the bulk process. The low frequency semi-circle is of a lower capacity traditionally associated with purely grain boundary effects (normally quoted as nF)^{2,28}. If the low frequency semi-circle includes the surface/grain boundary effects then the process of carbon coating has intimately affected the electrical properties of the boundary regions. The lower capacity could hint that there could be a distribution of relaxation times within the low frequency semi-circle. This is consistent with the complicated nature of surface coatings and their interactions with grain boundary contributions (pitting effects etc.)²⁹

The measurements taken at room temperature and 50°C display a high frequency semi-circle at 0.5kHz with conductivities (1/resistivity) of $\sim 10^{-7}$ S/cm. This is a lower conductivity than the as-prepared β_{II} material (though in line with olivine materials such as LiFePO₄^{10,30}). Which suggests that the bulk β_{II} phase within the carbon coated material may be subtly (electronically) different to the as-prepared material.

As with pristine material there is little change in the bulk conductivity between the room temperature and 50°C measurements. The grain boundary (low frequency) contribution gives conductivity values of $\sim 10^{-7}$ s/cm for both the room temperature and 50°C samples, while the extra resistance contribution (R_3) develops a resistivity of $\sim 10^9$ and 10^{10} Ω/m respectively. The R_3 resistance is likely to be the sum of a combination of factors, with surface coatings being notoriously complex to analyse, especially if the carbon coating process produced incomplete coverings.

Given that only the as-prepared β_{II} gave quantifiable AC impedance data, the AC data is most likely to represent the β_{II} material, with contributions from the β_{I} material, the carbon coating and other effects represented in the R_3 contribution. The DC resistivity measurements show that the purely electronic (i.e. DC) contributions are lower than the resistivity observed in the individual bulk or surface/grain boundary contributions, suggesting that the AC resistivity has other factors other than purely electronic contributions. The carbon coated $\text{Li}_2\text{CoSiO}_4$ material has DC resistivity values that sit between the values of the β_{I} and β_{II} phases. The increase in DC resistivity (and in R_3) resistance at 50°C again suggests that a simplistic semi-conductor does not fit with the $\text{Li}_2\text{CoSiO}_4$ material, and further work is needed to fully explore the charge carriers present in the silicate materials.

While the carbon-coated cycle retention is greatly improved compared to the as-prepared material it still represents a considerable loss of capacity over a short number of cycles. The effect of different amounts of carbon loading on the electrode performance was investigated. Figure 5.2.12 shows the result of the carbon loading series (5-30% (wt.) of xerogel precursor) on the charging capacity over ten cycles.

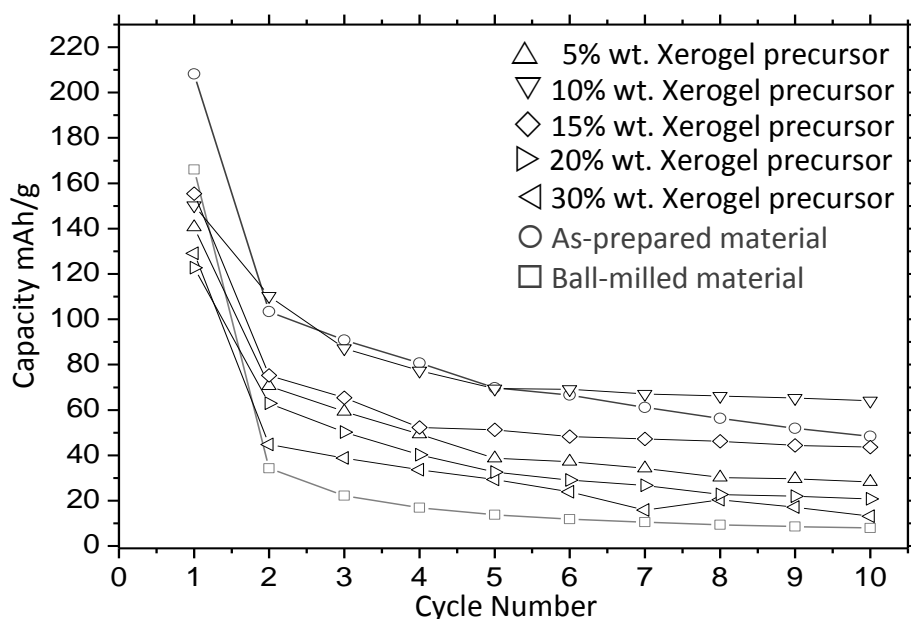


Figure 5.2.12. Capacity Vs. Cycle number for the gross charge capacities of carbon coated $\text{Li}_2\text{CoSiO}_4$: ○ As-prepared, △ Pristine material + 5% (wt.) xerogel precursor, ▽ Pristine material + 10% (wt.) xerogel precursor, ◇ pristine material + 15% xerogel precursor, ▷ Pristine material + 20% (wt.) xerogel precursor, ◁ Pristine material + 30 % xerogel precursor, □ ball-milled(60m) pristine material – Electrolyte LP30, cycling rate 10mA/g at a temperature of 50°C.

While the pristine material has the highest first charge capacity, relatively low carbon loading (5 & 10% loading) perform better over ten cycles. The loss of capacity with subsequent cycles levels off for all carbon coated materials, where the pristine material continues to lose significant capacity with each cycle. It would seem that higher loading of carbon (>15%) had a detrimental effect on the charging capacity of the material. This may be caused by the coating became thick enough to present an obstacle to lithium diffusion at the electrode/electrolyte interface. In the case of higher carbon loading it also became increasingly difficult to produce impurity free material, the prevalence of pyrolysis decomposition side-reactions increasing with increasing carbon loading.

5.3. Conclusions and Further Work

Both ‘classical’ approaches to electrode optimisation provided mixed results. Some benefit was observed with ball-milling $\text{Li}_2\text{CoSiO}_4$ materials (namely the γ_0 phase). This performance improvement is assumed to be due to a large particle size reduction. Any benefit from ball-milling was significantly counter-balanced by the negative effects of ball-milling, such as increased contributions from side reactions, to the extent that materials not known to suffer from chronically low ionic/electronic kinetics (the β_{II} and β_I $\text{Li}_2\text{CoSiO}_4$ polymorphs) performed worse after ball milling due to the presence of these side-reactions.

Carbon coating of the material improved the capacity retention (though some capacity loss with cycling was still observed) but the inability to produce carbon coated β_I or γ_0 polymorphs or phase pure β_{II} materials is disappointing. While it appears that the ‘LP30’ solvent/salt combination was the optimum electrolyte for the relatively high voltage $\text{Li}_2\text{CoSiO}_4$ cathode, the apparent presence of parasitic side-reactions suggests that further investigation into the electrode/electrolyte reactions could improve many of the factors influencing $\text{Li}_2\text{CoSiO}_4$ electrode performance.

Several important factors need to be addressed in order to fully understand the $\text{Li}_2\text{CoSiO}_4$ system namely the role of any side-reactions seemingly enhanced by mechanical-milling which may be studied by *in situ* techniques such as IR or AC impedance. Further investigation into the nature of the effect of carbon coating on the crystal growth may point the way to producing phase pure coated materials, as well as fully establishing the carbon/active material ratio in the coated material. Exploration of

different coating materials (such as metal oxides^{13,17,20,21}) whose favourable coating regimes may allow access to the γ_0 phase and phase pure β_{II} and β_I , in conjunction with improving capacity retention over repeated cycling, are necessary in order for the cobalt silicate materials to be seriously considered as cathode materials.

5.4. References

1. I. Belharouak, C. Johnson, and K. Amine, *Electrochem. Comms.*, 2005, **7**, 983-988.
2. R. Amin and J. Maier, *Solid State Ionics*, 2008, **178**, 1831-1836.
3. S. Shi, L. Liu, C. Ouyang, D. Wang, Z. Wang, L. Chen, and X. Huang, *Phys. Rev. B*, 2003, **68**, 195108.
4. A. Yamada, M. Hosoya, S. Chung, Y. Kudo, K. Hinokuma, K. Liu, and Y. Nishi, *Journal of Power Sources*, 2003, **119-121**, 232-238.
5. R. Amin, C. Lin, J. Peng, K. Weichert, T. Acartürk, U. Starke, and J. Maier, *Advanced Functional Materials*, 2009, **19**, 1697-1704.
6. M. Herstedt, M. Stjerndahl, A. Nyten, T. Gustafsson, H. Rensmo, H. Siegbahn, N. Ravet, M. Armand, J. O. Thomas, and K. Edstrom, *Electrochem. Solid-State Lett.*, 2003, **6**, A202-A206.
7. C. Delacourt, L. Laffont, R. Bouchet, C. Wurm, J. Leriche, M. Morcrette, J. Tarascon, and C. Masquelier, *J. Electrochem. Soc.*, 2005, **152**, A913-A921.
8. J. M. Tarascon, C. Delacourt, A. S. Prakash, M. Morcrette, M. S. Hegde, C. Wurm, and C. Masquelier, *Dalton Trans*, 2004, 2988-2994.
9. M. Arroyo-de Dompablo, M. Armand, J. Tarascon, and U. Amador, *Electrochemistry Communications*, 2006, **8**, 1292-1298.
10. S. Chung, J. T. Bloking, and Y. Chiang, *Nat Mater*, 2002, **1**, 123-128.
11. F. Zhou, M. Cococcioni, C. A. Marianetti, D. Morgan, and G. Ceder, *Phys. Rev. B*, 2004, **70**, 235121.
12. A. Nyten, M. Stjerndahl, H. Rensmo, H. Siegbahn, M. Armand, T. Gustafsson, K. Edstrom, and J. O. Thomas, *J. Mater. Chem.*, 2006, **16**, 3483-3488.
13. G. T. Fey, P. Muralidharan, C. Lu, and Y. Cho, *Solid State Ionics*, 2006, **177**, 877-883.
14. A. Nyten, A. Abouimrane, M. Armand, T. Gustafsson, and J. O. Thomas, *Electrochemistry Communications*, 2005, **7**, 156-160.
15. M. Broussely, P. Biensan, and B. Simon, *Electrochimica Acta*, 1999, **45**, 3-22.
16. J. P. Peres, C. Delmas, A. Rougier, M. Broussely, F. Pertont, P. Biensan, and P. Willmann, *Journal of Physics and Chemistry of Solids*, 1996, **57**, 1057-1060.
17. T. Fang, J. Duh, and S. Sheen, *J. Electrochem. Soc.*, 2005, **152**, A1701-A1706.
18. L. Vijayan and G. Govindaraj, *Physica B: Condensed Matter*, 2009, **404**, 3539-3543.
19. M. N. Obrovac, O. Mao, and J. R. Dahn, *Solid State Ionics*, 1998, **112**, 9-19.
20. C. Li, H. Zhang, L. Fu, H. Liu, Y. Wu, E. Rahm, R. Holze, and H. Wu, *Electrochimica Acta*, 2006, **51**, 3872-3883.
21. S. B. Park, H. C. Shin, W. Lee, W. I. Cho, H. Jang, *J. Power Sources*, 2008, **180**, 597-601.
22. X. Yang, Y. Huang, H. Zhou, J. Chen, X. Zhang, *Frontier of Chem. China*, 2008, **3**, 64-69.
23. R. Amin and J. Maier, *Solid State Ionics*, 2008, **178**, 1831-1836.
24. S. Huang, Z. Wen, X. Yang, Z. Gu, and X. Xu, *Journal of Power Sources*, 2005, **148**, 72-77.
25. S. Al-Muhtaseb and J. Ritter, *Advanced Materials*, 2003, **15**, 101-114.
26. A. Nyten, A. Abouimrane, M. Armand, T. Gustafsson, and J. O. Thomas, *Electrochemistry Communications*, 2005, **7**, 156-160.
27. A. R. West and F. P. Glasser, *Journal of Solid State Chemistry*, 1972, **4**, 20-28.
28. J. E. Bauerle, *Journal of Physics and Chemistry of Solids*, 1969, **30**, 2657-2670.
29. A. S. Hamdy, D. Butt, and A. Ismail, *Electrochimica Acta*, 2007, **52**, 3310-3316.
30. C. Delacourt, L. Laffont, R. Bouchet, C. Wurm, J. Leriche, M. Morcrette, J. Tarascon, and C. Masquelier, *J. Electrochem. Soc.*, 2005, **152**, A913-A921.

Chapter 6. LiVO_2 as a Lithium Intercalation Anode

Chapter 6: LiVO_2 as a Lithium intercalation Anode

Chapter Content:

6.1. Introduction	155
6.2. Results and Discussion	157
6.2.1. Structural Characterisation	157
6.2.2. Electrochemical Behaviour	164
6.2.2.1. Influence of Lithium Doping.....	164
6.2.2.2. Computational studies	169
6.2.2.3. The Discharge Process	172
6.3. Conclusions and Further Work	185
6.4. References.....	187

6.1. Introduction

Layered compounds of the composition Li_xMO_2 are traditionally seen as cathode materials, recent work has shown that the group of compounds may provide a useful alternative to the graphite anode¹⁻⁴. This chapter focuses on the new anode material LiVO_2 and its subsequent characterisation.

Traditionally graphite has been the anode of choice⁵⁻¹². Since the introduction of a lithium ion host as both anode and cathode in the early 1990's graphite has dominated the anode market due to it being cheap, ubiquitous and non-toxic, most importantly graphite has a capacity (370mAh/g) that easily exceeds the capacity of most cathodes; hence the focus of research normally falls on cathodes. Unfortunately the electrochemical process of intercalating lithium into graphite is not ideal. Graphite has an inherently low energy density (0.0372 kWh/kg) as well as the low lithium intercalation voltage (about 0.1V away from the Li/Li^+ equilibrium voltage) which can cause lithium plating when a high over-potential is applied^{7,9-11}; hence, alternatives to graphite are now being actively sought.

Recent investigations into non-graphitic anodes have produced materials that utilise more complex electrochemical behaviour, such as conversion reactions of CoO ¹³, tin based alloy systems¹⁴ and titanate based, zero strain intercalation materials^{8,15}. However, these materials come with their own problems, most notably large voltage hysteresis between charge and discharge process, large volumetric changes and high intercalation voltages respectively.

Research has begun into layered transition metal oxides as anodes. Traditionally seen as cathodes, materials such as LiCoO_2 and $\text{LiMn}_{0.5}\text{Ni}_{0.5}\text{O}_2$ ^{1-3,16-19} have been investigated as potential anodes partly due to the existence of the Li_2MO_2 phase. It is thought that a LiMO_2 to Li_2MO_2 phase conversion can take place during cycling and had been observed to a limited extent with the $\text{LiMn}_{0.5}\text{Ni}_{0.5}\text{O}_2$ materials¹⁹. LiVO_2 offers similar structural characteristics as LiMO_2 materials and is thought to have a low (0.2V) $\text{V}^{(3+/2+)}$ redox couple²⁰ and high material density (4.29g/cm^3), ensuring high power densities, combined with a theoretical specific capacity close to graphite (298 mAh/g). Recent work has found that LiVO_2 will undergo reversible cycling at low voltages²¹⁻²³ but the electrochemical processes and the nature of the LiVO_2 to Li_2VO_2 phase conversion has yet to be fully established.

6.2. Results and Discussion

6.2.1. Structural Characterisation

$\text{Li}_{1+x}\text{V}_{1-x}\text{O}_2$ materials were synthesised using a solid state method as described in the experimental section, special attention was needed prior to calcinations to ensure an argon atmosphere was maintained during ball milling, due to the reactive nature of the V_2O_3 starting material. Various stoichiometries were produced using differing amounts of excess lithium in the starting materials. Doped $\text{Li}_{1+x}\text{V}_{1-x}\text{O}_2$ products with the starting stoichiometries of $x = 0, 0.025, 0.05, 0.07, 0.1$ and 0.2 were produced. The X-ray diffraction patterns of the various doped materials can be seen in the inset of Figure 6.3.1. All materials could be indexed to a $R\bar{3}m$ space group based on the classic $\alpha\text{-NaFeO}_2$ structure. A typical refinement is shown in Figure 6.3.1 where the nominally 5% lithium excess material was refined, giving a good fit of $R_{\text{wp}} = 3.35\%$. A list of refinement parameters is given in Table 6.3.1.

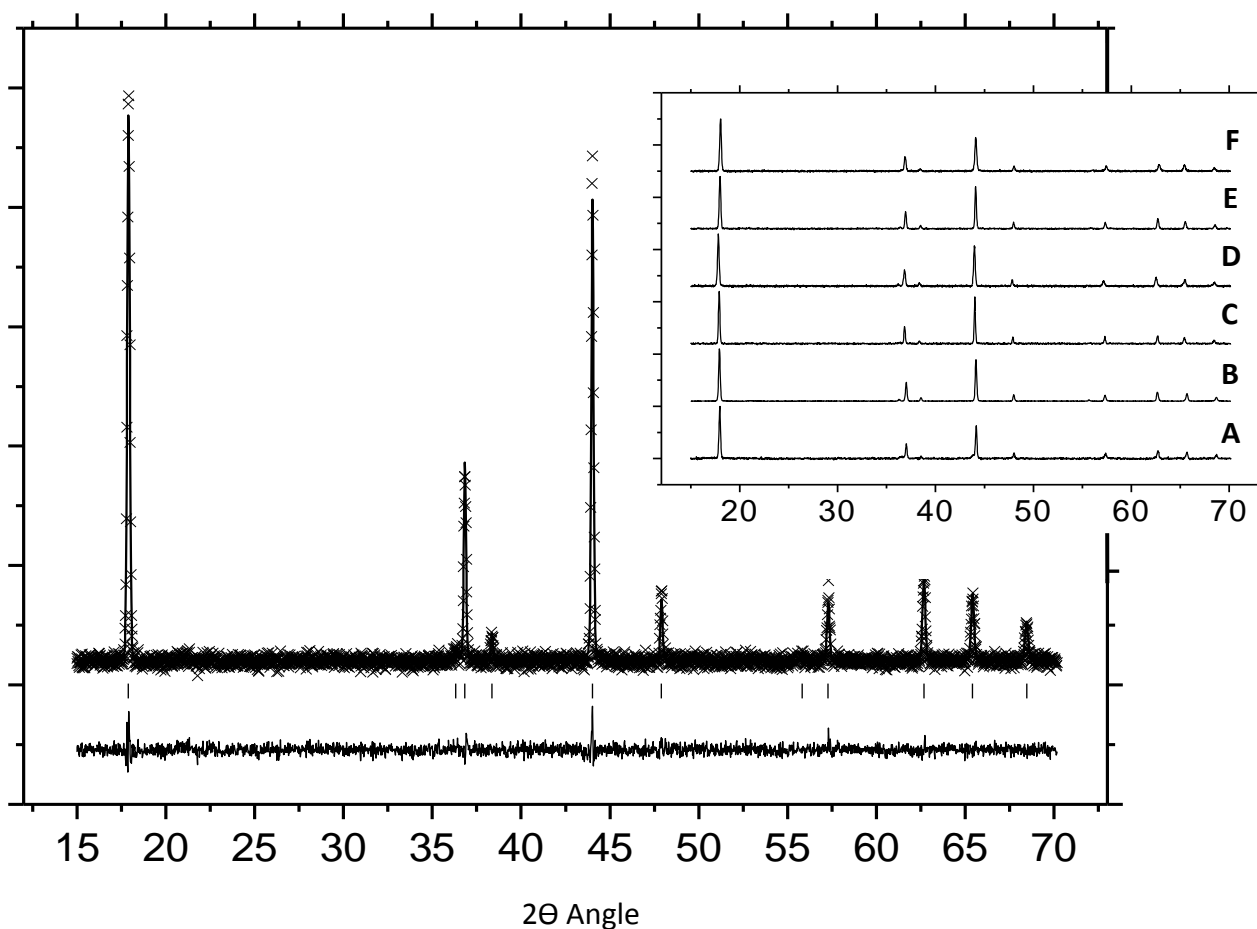


Figure 6.3.1 X-ray diffraction pattern and Rietveld fitting of $\text{Li}_x\text{V}_{1-x}\text{O}_2$ (nominally Li 5% excess). Insert X-ray diffraction patterns of $\text{Li}_x\text{V}_{1-x}\text{O}_2$: A) $x=0$ (nominal Li 0% excess lithium) $R_{wp}=4.65\%$, B) $x=0.01$ (nominally Li 2.5% excess) $R_{wp}=1.35\%$, C) $x=0.08$ (nominally Li 5% excess) $R_{wp}=3.1\%$, D) $x=0.13$ (nominally Li 7% excess) $R_{wp}=3.72\%$, E) $x=0.17$ (nominally Li 10% excess) $R_{wp}=3.52\%$, F) $x=0.21$ (nominally Li 20% excess) $R_{wp}=3.4\%$.

Atom	Wyckoff Symbol	x/a	y/b	z/c	B_{iso}	Occupancy
Li1	3b	0.00	0.00	0.50	0.8(6)	1
V1/Li2	3a	0.00	0.00	0.00	0.030(1)	V0.920/Li0.080(8)
O1	6c	0.00	0.00	0.2560(1)	0.032(1)	1

$$a = 2.8438(4) \quad b = 2.8438(4) \quad c = 14.791(3) \quad \text{Cell Volume} = 103.59(3)$$

$$\text{Space group: } R\bar{3}m \quad R_p = 2.36\% \quad R_{wp} = 2.98\% \quad \chi^2 = 1.023$$

Table 6.3.1 Refined parameters of $\text{Li}_{1.08}\text{V}_{0.92}\text{O}_2$ (nominally 5% excess lithium).

The material is analogous to the well known $\alpha\text{-NaFeO}_2$ structure, or the layered transition metal oxide cathode materials, primarily associated with LiCoO_2 ^{5,24-27}. The structure is based around a scaffold of hexagonally close packed oxygen anions, with

layers of transition metal ions (in this case vanadium) occupying octahedral holes forming VO_6 octahedra, alternating with layers of octahedrally coordinated lithium ions forming a layer of LiO_6 with an ABC.. structure. A schematic representation of the structure is shown in Figure 6.3.2. It is the tetrahedral sites in the LiO_6 'slabs' that the lithium is expected to intercalate into.

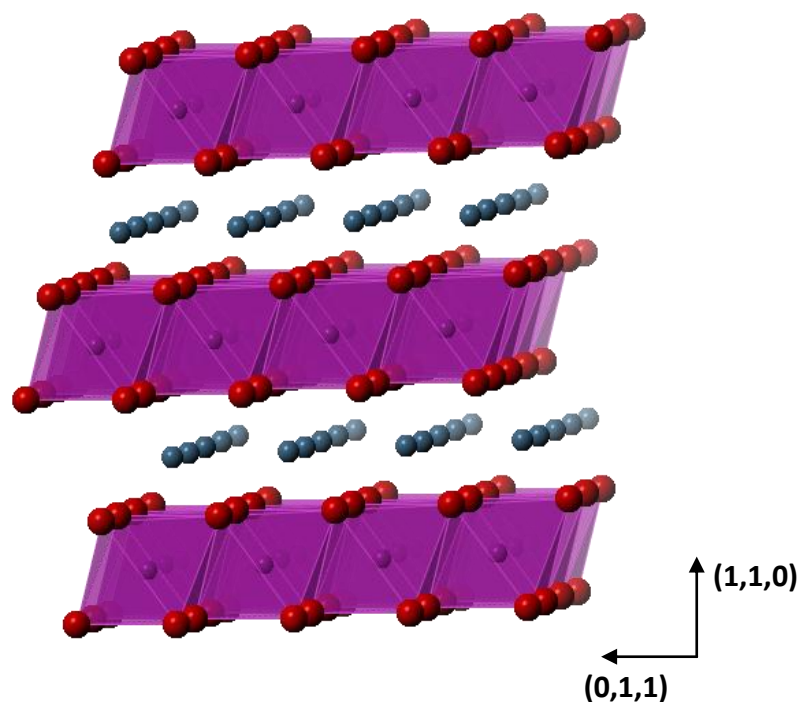


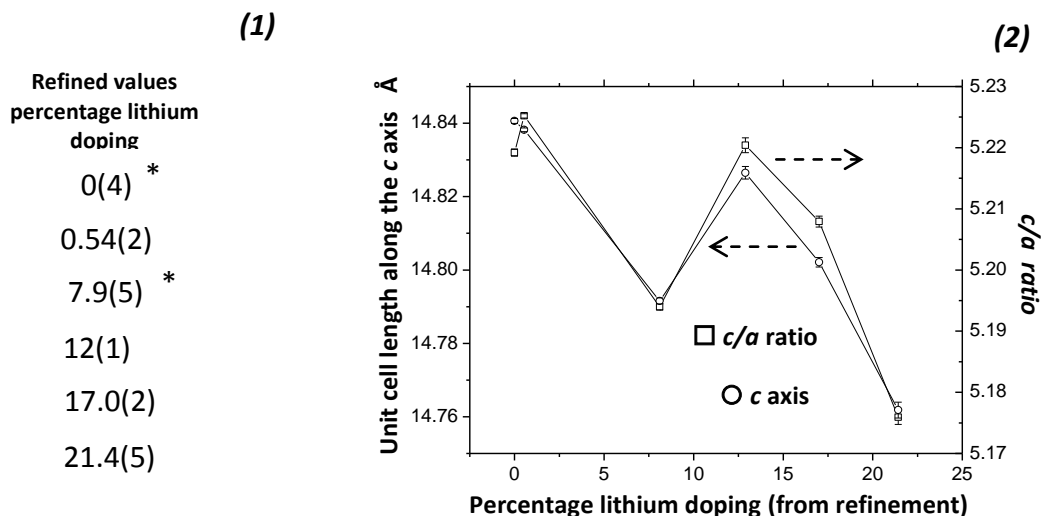
Figure 6.3.2 Schematic representation of the LiVO_2 structure: Purple polyhedra VO_6 , Blue Spheres lithium, Red spheres oxygen.

It was found that the doped lithium could be modelled as lithium within the 3a vanadium site (displacing the vanadium). This was seen to cause a slight expansion along the a (and b) axis and a contraction along the c axis. It should be noted that replacement of lithium by vanadium in lithium 3b sites was also considered, but the refinement model suggested this was unlikely to have occurred in the materials).

With reference to the LiVO_2 structure displayed in Figure 6.3.1, the structural changes upon doping corresponds to the VO_6 slabs getting closer together via

contraction of the LiO_6 layers. This is due to the occupation of some of the octahedral vanadium sites with lithium. The 6 coordinate Li^+ ion has a radius of 90 pm while the V^{3+} ion in octahedral coordination has a radius of 78pm, which causes an expansion of the $\text{V}(\text{Li})\text{O}_6$ slab volume and consequently compressing the LiO_6 slab volume (the structure seemingly pinned by the electrostatic repulsion of the hexagonal oxygen lattices, allowing for the compression of the wider LiO_6 layer). This effect is slightly counter-balanced by the introduction of a small amount of the (smaller) V^{4+} ions in the VO_6 layers, necessary to maintain charge balance due to the replacement of V^{3+} with Li^+ in the VO_6 layer (the presence of V^{4+} was confirmed with double titration oxidation state analysis, mentioned in Figure 6.3.3, and subsequent computer modelling discussed later in this section).

The change in c axis and c/a axis ratio with lithium content is displayed in Figure 6.3.3 (2). It is clear that the nature of lithium doping mechanism and the effect this has upon the unit cell defies a simple explanation. The stoichiometry of lithium in the starting materials compared to the stoichiometry of the final material also bears closer inspection, seemingly increasing the amount of excess lithium during the reaction.



*Confirmed by double titration; 0% lithium doping had a gross vanadium oxidation state of +3.02. The 7.9% lithium doping had a gross vanadium oxidation state of +3.18

Figure 6.3.3 (1) Lithium composition of doped material. (2) Variation in LiVO_2 a (□) and c (○) unit cell axis with lithium content.

The refinements were repeated several times with separately prepared materials to confirm the accuracy of values (Subsequent joint x-ray and neutron refinement work by Dr Armstrong also showed good agreement with the un-doped and 5% excess lithium materials. The difference in the final stoichiometry of the 5% material ($\text{Li}_{1.07}\text{V}_{0.93}\text{O}_2$ by joint neutron/X-ray diffraction, compared to $\text{Li}_{1.08}\text{V}_{0.92}\text{O}_2$ from X-ray only) is within the error margin, see submitted paper in appendix *vii*).

The large contraction in the c axis length with the replacement of $\sim 8\%$ lithium in the octahedral vanadium sites seems out of place with the trend of gradual reduction in c axis length with increasing lithium/vanadium disorder (though not without some precedent²⁸). It would seem (as observed through the change in c/a axis with composition) that the a axis remains largely unperturbed by the inclusion of lithium into the vanadium layer.

The complicated structural behaviour observed with doping may be a consequence of the intricate defect chemistry caused by the inter-play between V^{3+} , Li^+ and V^{4+} ions in the vanadate layer. The exact conformation of Li^+ and V^{4+} ions in a layer of V^{3+} may change drastically with the introduction of a little extra lithium in the layer perhaps incurring a shift to a subtly different solid solution structure shifting the overall unit cell parameters with greater lithium.

It is also notable that Figure 6.3.3 (1) shows the lithium stoichiometry of the product increases over the synthesis compared to the reagents. It is common with solid state reactions containing lithium oxides to observe lithium loss over the course of the heating stage of the reaction because of the relatively high volatility of lithium oxides²⁹⁻³¹ but it would appear (somewhat unusually) that the materials suffer from vanadium loss. The oxidation state of the vanadium was independently confirmed in the ~8% doped material by double titration giving a gross vanadium oxidation state of +3.18 (equivalent to 8.25% lithium doping). The difference between starting and refinement stoichiometry is probably based in the diminished accuracy of weighing the (moisture sensitive) starting materials in a controlled atmosphere. Since the oxidation state and refinement data are in agreement, it is more appropriate to use the refinement data to quote the stoichiometry.

The TEM image, shown in Figure 6.3.4., confirms that the classic solid state synthesis procedure produces uniform particles with particle sizes of 70-200 nm, suggesting that gross kinetic transport issues should not be a problem given the small size of the crystallites.

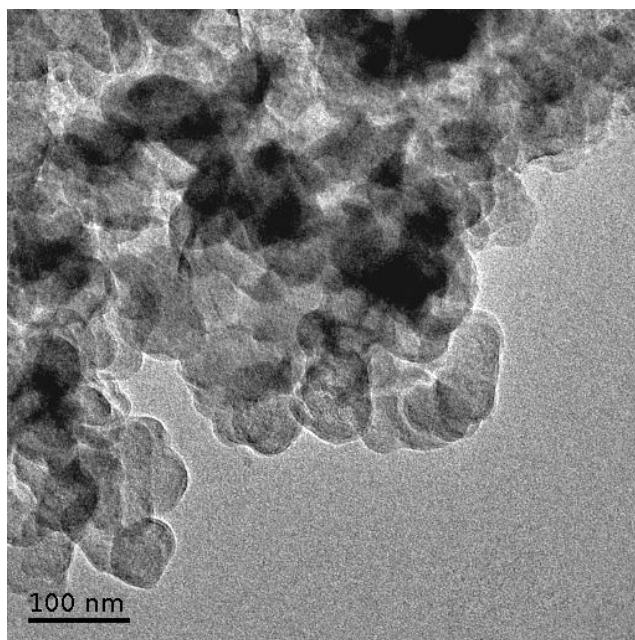


Figure 6.3.4 TEM image of as prepared $\text{Li}_{1.08}\text{V}_{0.92}\text{O}_2$.

6.2.2. Electrochemical Behaviour

6.2.2.1. Influence of Lithium Doping

The electrochemical behaviour displayed a strong dependence upon the amount of doped lithium present in the material. Figure 6.3.5 shows the effect of doping upon the galvanostatic profile of some selected materials.

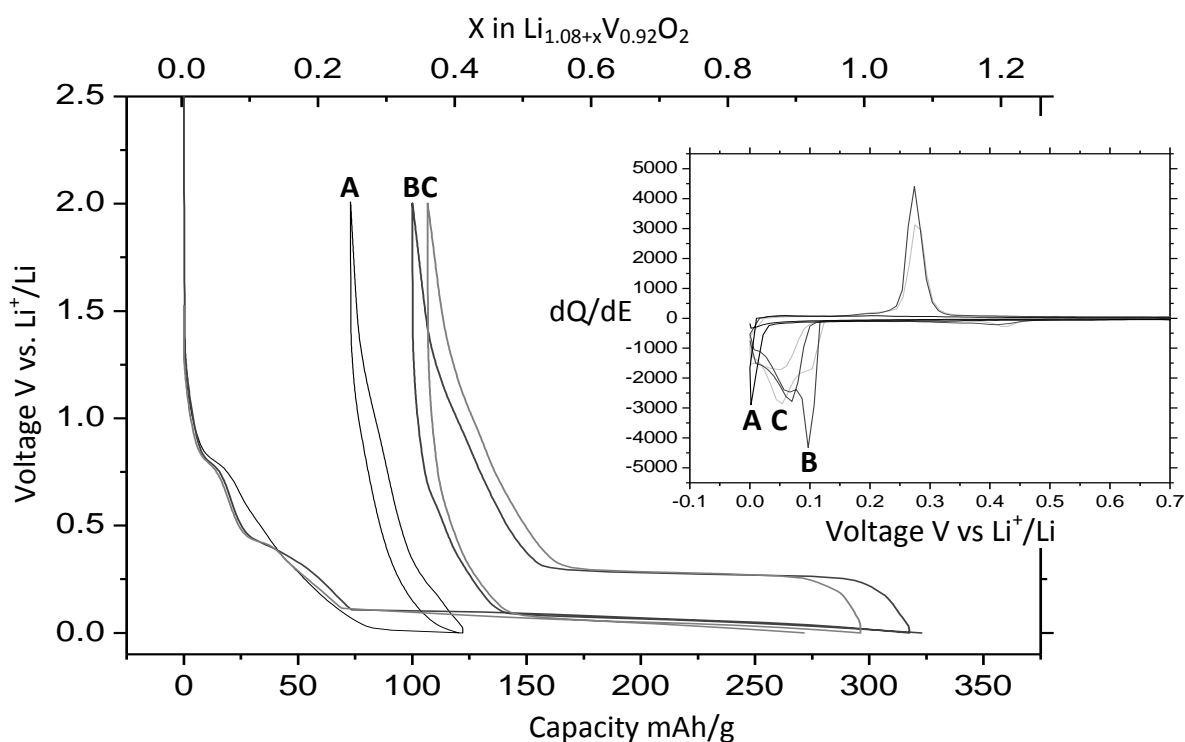


Figure 6.3.5. Voltage change with lithium composition for selected doped $\text{Li}_{1+x}\text{V}_{1-x}\text{O}_2$ materials; A) Un-doped LiVO_2 material, B) $\text{Li}_{1.08}\text{V}_{0.92}\text{O}_2$ C) $\text{Li}_{1.12}\text{V}_{0.88}\text{O}_2$. *Inset:* Incremental capacity plot for A) Un-doped LiVO_2 material, B) $\text{Li}_{1.08}\text{V}_{0.92}\text{O}_2$ C) $\text{Li}_{1.12}\text{V}_{0.88}\text{O}_2$. - Electrolyte LP30, cycling rate 10 mA/g at a temperature of 30°C

All materials display a shoulder at 0.8V, assumed to be part of the SEI formation procedure, given its existence has been observed with other (graphitic) anode systems¹², as expected this shoulder then disappears on subsequent cycles. The voltage composition plots show a heavy doping dependence, with the un-doped

material showing significantly poorer performance than the 8% and 12% doped materials (which display reasonably similar behaviour). The un-doped material has a particularly short 1st discharge plateau of 40 mAh/g near 0V. Although as the majority of this capacity is evolved in the near lithium plating region it is possible that the 40mAh/g is just a consequence of lithium deposition.

The doped materials show ~310 mAh/g and ~300 mAh/g discharge capacity for the 8% and 12% doped materials respectively. Figure 6.3.6 shows that the largest discharge (and charge) capacity from all the doped materials was achieved with the 8% material, which may be a consequence of the subtle structural differences between the doped materials seen in Figure 6.3.3.

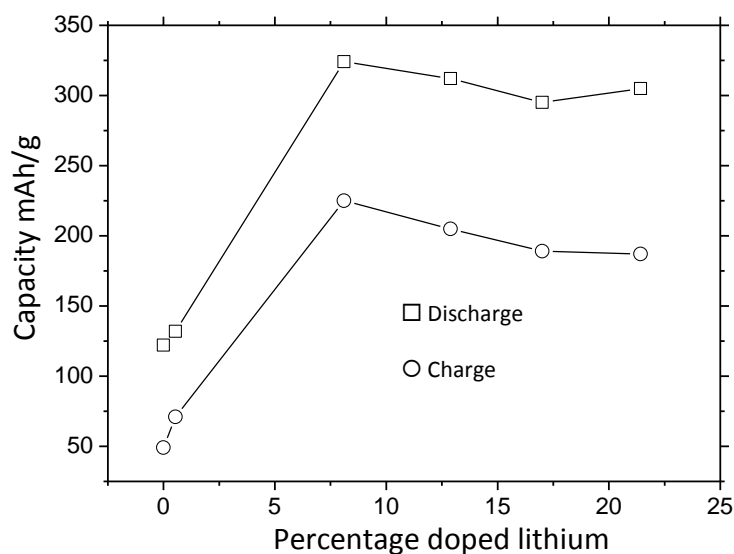


Figure 6.3.6 First discharge and charge capacities of doped $\text{Li}_{1+x}\text{V}_{1-x}\text{O}_2$ materials: \square Discharge capacity, \circ Charge capacity - Electrolyte LP30, cycling rate 10 mA/g at a temperature of 50°C

Both the doped materials in Figure 6.3.5 evolved a second shoulder around 0.4V which is not present in the un-doped material. This suggests that the second shoulder could be a consequence of lithium activity at the anode (absent in the almost inert un-doped material), though it does not look like 'classic' intercalation behaviour (which

would be shown as a flat plateau for a two phase reaction or a constant gradient slope for a solid solution with lithium intercalation). It could be further SEI formation which has been suggested before with $>1\text{Li}$ insertions in LiMO_2 structures^{1,32,33} (incidentally the absence of peaks associated with the shoulder processes in the incremental capacity plots is due to the lack of constant rate of change of capacity with voltage hence not appearing as peaks in the dQ/dE plot). There is a possibility that this 'shoulder' region also represents structural changes occurring within the LiVO_2 material prior to a LiVO_2 to Li_2VO_2 phase conversion associated with the plateau voltage region.

The flat voltage plateau suggests a two phase reaction and is reached after ~ 70 mAh/g capacity has passed. From the incremental capacity plots it can be seen that the first discharge of the 8% doped material (and to a lesser extent the 12% doped material) consists of two electrochemical processes (one of which disappears on repeated cycling) indicated by the two peaks in the incremental capacity plot. The peak at 0.1V disappears after the first cycle as the peak at $\sim 0.05\text{V}$ dominates.

During the charging processes the incremental capacity plot there is only a slight difference in the peak voltages between doped materials (2.99V vs. 2.95V of 8% and 12% doping respectively) more indicative of a polarisation (ohmic drop) difference between the two materials, rather than two distinct electrochemical processes.

The ability of a small amount of lithium doping to ‘switch on’ the intercalation process bears closer inspection. It is unlikely that the doping alters the kinetic behaviour of the LiVO_2 materials, as highlighted in Figure 6.3.7, where there is little difference between the GITT (pseudo-equilibrium) profiles and the galvanostatic profiles (taken at 10mA/g) of the un-doped material and the 8% doped material.

When the material was cycled using a galvanostatic intermittent titration (GITT) regime the ‘equilibrium’ voltage/composition profile (ostensibly a galvanostatic profile at 0 mA) can be used to find the absolute voltage plateau.

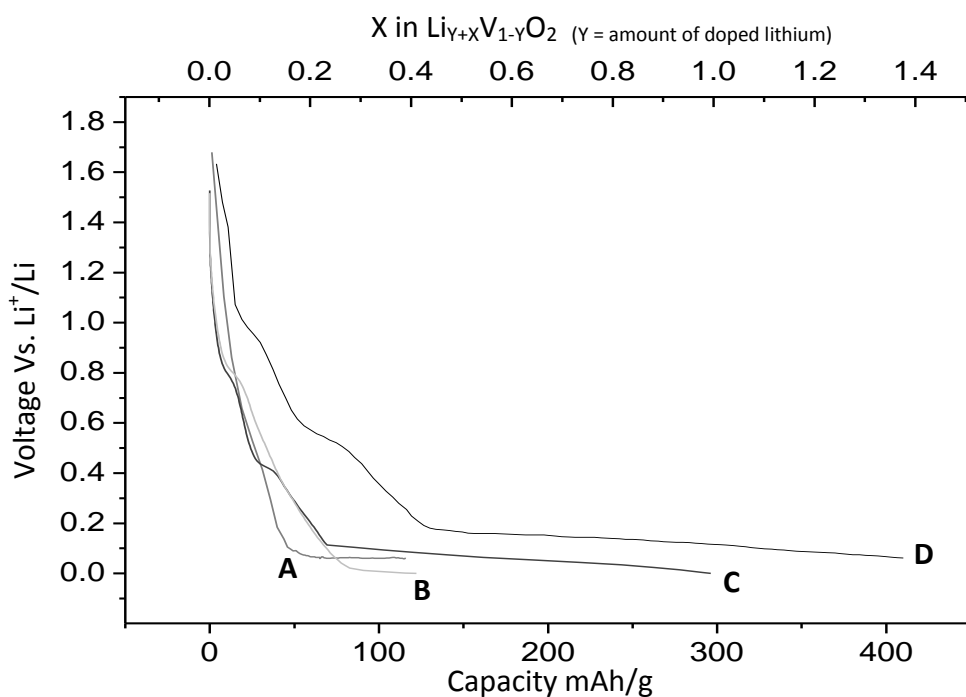


Figure 6.3.7 1st discharge Galvanostatic profiles of un-doped and 8% doped $\text{Li}_{1+x}\text{V}_{1-x}\text{O}_2$: A) Un-doped LiVO_2 galvanostatic profile cycling rate; 10 mA/g, B) Un-doped LiVO_2 GITT, C) $\text{Li}_{1.08}\text{V}_{0.92}\text{O}_2$ Galvanostatic profile cycling rate 10 mA/g cycling rate, D) $\text{Li}_{1.08}\text{V}_{0.92}\text{O}_2$ GITT – Electrolyte LP30, temperature 30°C

As Figure 6.3.7 shows in the un-doped material both the GITT and galvanostatic profile have near identical total capacities suggesting that cycling at 10mA/g does not kinetically hinder the material. The 8% lithium doped material has a larger capacity

when discharged under equilibrium type conditions, suggesting that there is a slight kinetic impediment to be considered when discharging the material, especially in the region above $\sim 0.2\text{V}$, which appears to be kinetically limited, producing more capacity with slower cycling. More importantly there is still a significant difference between the doped and un-doped material, even when transport effects are removed. The un-doped material producing very little capacity until the voltage drops into the lithium plating region. This suggests that the difference between the doped and un-doped material is more intricate, perhaps relying on the subtle structural differences.

From the structural refinement it can be seen that there is no vanadium in the lithium layer in either of the doped and un-doped materials, removing the possibility of vanadium pinning, which may have inhibited shearing on any LiVO_2 to Li_2VO_2 phase conversion.

6.2.2.2. Computational studies

To explore the difference between doped ($\text{Li}_{1.07}\text{V}_{0.93}\text{O}_2$) and un-doped (LiVO_2) materials atomistic modelling was undertaken, although this work was not directly undertaken by C. Lyness. It provides vital insight into the structural affects associated with doping the LiVO_2 structure with excess lithium and so, it is beneficial to discuss the work here. The work was carried out, in collaboration with Professor Peter Bruce and Dr. Rob Armstrong, by Dr. Pooja Panchmatia and Professor M. Saiful Islam of the University of Bath (further technical details can be found in the paper attached in the appendix *vii*).

Atomistic modelling has a history of providing useful insights into defect chemistry³⁴⁻³⁷ and so was an obvious choice to investigate the LiVO_2 materials, providing a perspective which would be hard to obtain from X-ray (or neutron) refinement alone. LiVO_2 , $\text{Li}_{1.07}\text{V}_{0.93}\text{O}_2$ (stoichiometry as per the joint refinement) and Li_2VO_2 were all successfully modelled in good agreement with the joint x-ray and neutron diffraction refinements undertaken by Dr Armstrong (and data presented in this chapter). It was found that a significant 3eV energy penalty existed for introduction of vanadium into a 3b lithium site- further confirming the absence of vanadium pinning in any of the materials. As expected from the double titration information and structural refinements, introducing Li^+ ions into the V^{3+} layer was found to cause charge compensation in the surrounding vanadium sites forcing some local vanadium to a V^{4+} oxidation state. The computer model found that, out of the various conformations considered, the most likely (i.e. most stable) vanadium/lithium ion conformation was two V^{4+} ions edge sharing with the octahedral lithium ion. The free energy of the trimer was suitably lower than isolated defects (though, due to similar energies, the exact conformation of the trimer structure (out of a choice of three) was hard to deduce.

The possibility of larger agglomerations of trimer clusters was also investigated. It was discovered that even the lowest energy cluster (a dodecamer) had a significantly higher energy (by 0.35eV) than the isolated trimer cluster environment, suggesting a prevalence of the trimer conformation throughout the structure.

The nature of the doping effect on lithium intercalation was also investigated. As there are no empty octahedral sites in the $R\bar{3}m$ structure, the intercalating lithium is

expected to insert into a tetrahedral site in the lithium layer. An issue with this insertion mechanism was found when the inserted Li^+ has to face share with an octahedral V^{3+} (inevitable in the LiVO_2 material, while in $\text{Li}_{1.07}\text{V}_{0.83}\text{O}_2$ there is the possibility of face sharing with a doped octahedral Li^+ site). It was discovered that the energetic cost of inserting lithium into a tetrahedral site in the alkali layer is 0.62 eV higher if that site face shares with a V^{3+} ion, compared to a Li^+ ion from the vanadate layer, showing obvious favour to the doped material which contains lithium in the 3a vanadium site.

Due to lack of Li^+ face sharing in the un-doped material, it was determined that un-doped LiVO_2 would require a voltage of 2.98 V to insert lithium into the alkali tetrahedral site, far below the voltage at which lithium would start plating (0V) and consequently occlude any further reactions. In contrast, $\text{Li}_{1.07}\text{V}_{0.93}\text{O}_2$ was found to intercalate lithium into its alkali tetrahedral sites at 0.58V, a voltage that may explain some of the extended voltage shoulders prior to the plateau seen in the galvanostatic profiles (Figure 6.3.5). This suggests that prior to any phase conversion, some lithium intercalation into the tetrahedral sites may be necessary.

Further computational work showed that the lithium inserted into tetrahedral sites in the alkali layer causes large lattice distortions. This was due to the inserted lithium ion being displaced slightly towards the octahedral Li^+ face and the resulting $\text{Li}^+ - \text{Li}^+$ repulsion distorting the octahedral lithium ion causing it to maintain three short Li-O bonds (1.91 Å) and 3 long Li-O bonds (2.45 Å) compared to the ubiquitous Li-O bond length (1.99 Å) prior to tetrahedral lithium insertion. The effects of this distortion are felt throughout the local lattice causing the anionic sub-lattice to distort

(the O-O bond length altering from 2.93 Å to 3.0 Å). These changes could possibly herald the onset of shearing, required if the $\text{LiVO}_2 R\bar{3}m$ structure was to undergo phase change to the $\text{Li}_2\text{VO}_2 P\bar{3}m1$ material.

It is thought that the four Li^+ face sharing environment of the inserted Li^+ ion (three in the alkali layer, one from doped lithium in the vanadate layer) is enough to trigger a shearing event (primarily caused by $\text{Li}^+\text{-Li}^+$ repulsion). The new Li_2VO_2 structure can then adopt all the lithium from the alkali layer in the original LiVO_2 material, and allow one new lithium to be inserted into the empty tetrahedral site now present within the Li_2VO_2 material, allowing for Li_2VO_2 stoichiometry to be adopted.

The new structure is stabilised by the absence of face sharing, with all the tetrahedral sites filled and all octahedral sites empty within the alkali layer. DFT calculations give the phase conversion reaction a voltage of +0.23V, a difference of ~0.1V with the experimentally observed voltage plateau, an incongruity expected from previous DFT work³⁷⁻³⁹ and allowing for the possible need for a slight over-potential for the kinetically inhibited LiVO_2 material.

6.2.2.3. The Discharge Process

To further investigate the nature of the over-lithiated phase of LiVO_2 , X-ray diffraction patterns were collected of the material at different stages of discharge (shown in Figure 6.3.8.). There is a clear phase transition from the previously identified LiVO_2 phase to what has been ascribed the Li_2VO_2 phase refined using a Li_2MnO_2 model⁴⁰ with the space group $P\bar{3}m1$. The refinement of the material after 115mAh/g is given in Figure 6.3.9 as an example, with the associated Li_2VO_2 refinement parameters displayed in Table 6.3.2.

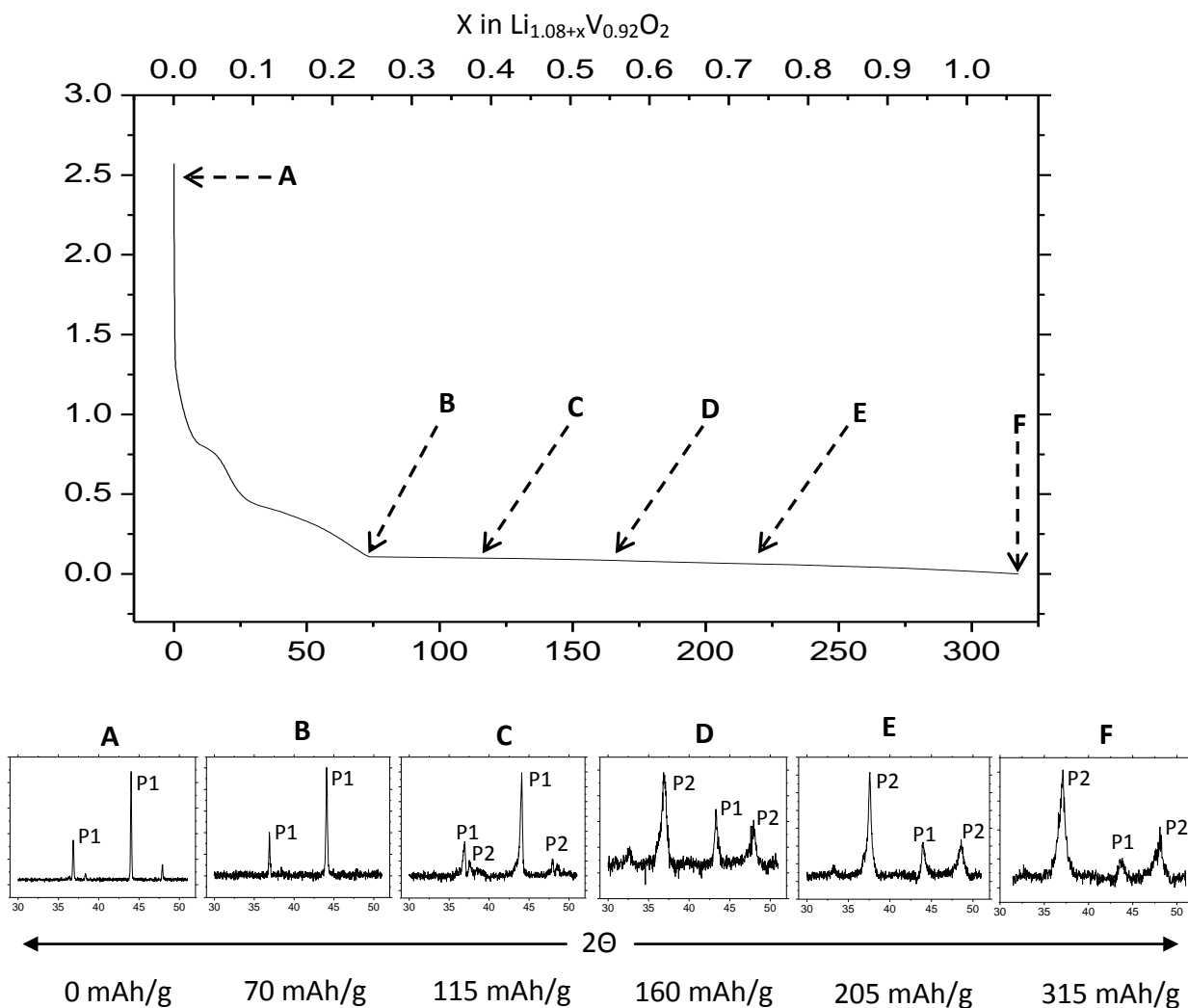


Figure 6.3.8 Selected regions of X-ray diffraction patterns taken at different lithium compositions during cycling: P1 and P2 are selected peaks of Phase 1 (LiVO_2) and Phase 2 (Li_2VO_2) respectively.

The 30-50 2θ regions displayed in the insets in Figure 6.3.8 show that there is no detectable new phase growth during the 'SEI' stage of the cycle (i.e. no 'P2' peaks up to 70mAh/g). As the discharge plateau proceeds, the presence of the Li_2VO_2 phase becomes apparent (observed as minor peaks at 38 and 47 degrees in Figure 6.3.9). This phase comes to dominate by the end of the discharge plateau.

The Li_2VO_2 phase is made up of hexagonally close-packed oxygen scaffold with layers of lithium ions occupying all tetrahedral sites, alternating with layers of vanadium situated in the octahedral sites (a schematic is displayed in Figure 6.3.9). This structure is isostructural with previously documented materials such as Li_2NiO_2 ⁴¹, Li_2MnO_2 ^{42,43} and $\text{Li}_2\text{Mn}_{0.5}\text{Ni}_{0.5}\text{O}_2$ ².

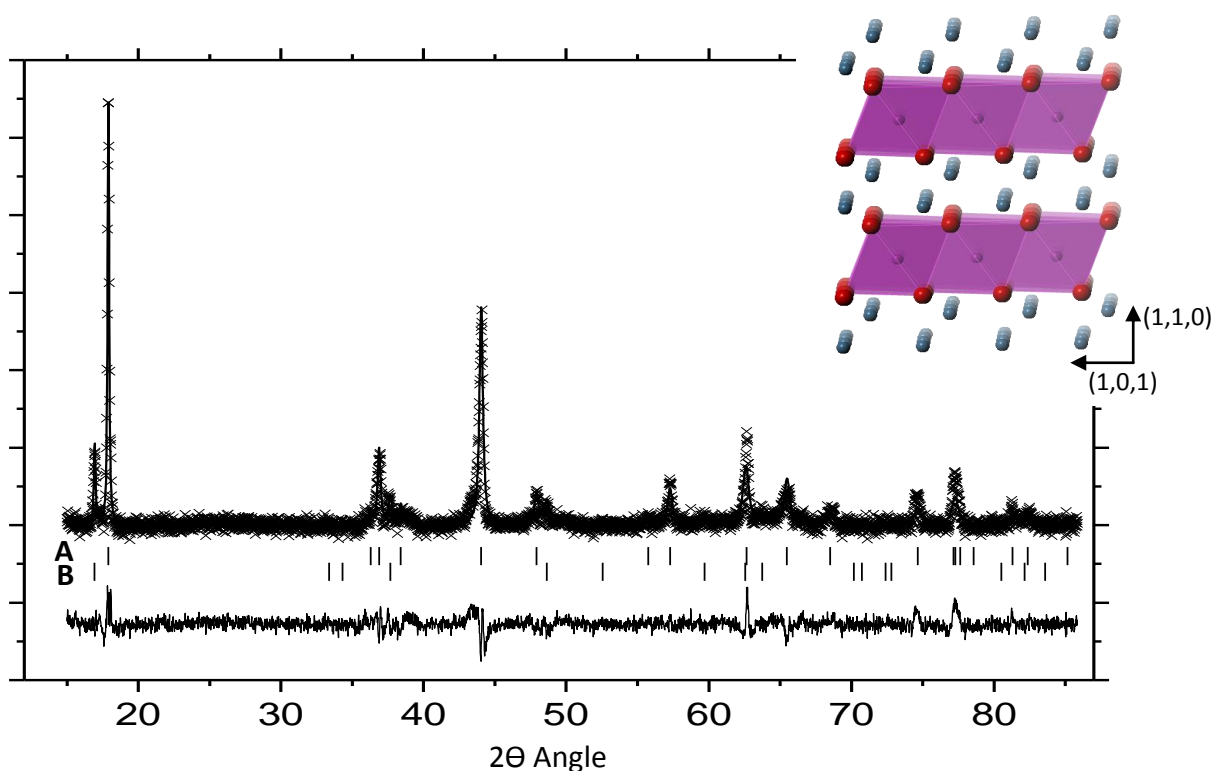


Figure 6.3.9. X-ray diffraction pattern and Rietveld refinement parameters for $\text{Li}_{1.08}\text{V}_{0.92}\text{O}_2$ at 115mAh/g ($\sim 0.3\text{Li}$) discharge capacity, $R_{wp}=4.34\%$: A) LiVO_2 phase peak positions, B) Li_2VO_2 phase peak position. *Inset*: schematic representation of Li_2VO_2 structure along the a direction.

Within the partially cycled material it became particularly hard to (reliably) identify the amount of mixing between the metals in the vanadium/lithium sites (i.e. manually altering the fractional occupancies of the 2d and 1a site did not significantly alter the quality of the fit). This was due in part to the poor quality of the recovered materials (and X-ray diffraction patterns) and not helped by lithium's small X-ray scattering cross-section.

Atom	Wyckoff Symbol	x/a	y/b	z/c	B _{iso}	Occupancy
Li1	2d	0.667	0.333	0.39(2)	0.8(5)	1
V1/Li2	1a	0.00	0.00	0.00	0.09(6)	1
O1	2d	0.333	0.667	0.249(5)	0.054(4)	1

$$a = 3.0998(3) \text{ } b = 3.0998(3) \text{ } c = 5.2207(8) \text{ } \textit{Cell Volume} = 43.351(8)$$

$$\textit{Space group: } P\bar{3}m1 \quad R_p = 3.24\% \quad R_{wp} = 4.34\% \quad \chi^2 = 1.621$$

* Values produced from two phase refinement from material recovered at 115mAh/g

Table 6.3.2. Refinement parameters of (nominally) Li₂VO₂ derived from X-ray diffraction of Li_{1.08}V_{0.92}O₂ materials after 115mAh/g of discharge.

In subsequent work utilising neutron diffraction (see appendix vii) the presence of the Li₂VO₂ phase was further confirmed throughout the cycle. Table 6.3.3 displays some refined parameters of the recovered material collected at different points during discharge. It becomes clear that the processes occurring during cycling are considerable more complicated than the simplistic picture painted by the electrochemical plateau.

Throughout discharge the LiVO₂ unit cell is seen to expand slightly, this can be understood by the reduction of the small amounts of V⁴⁺ in the structure (thought to be present to balance the replacement of some V³⁺ with Li⁺) The reduction to V³⁺ is expected to be accompanied by an increase in the V-O bond lengths, due to the

differing charge densities of V^{4+} and V^{3+} ions. There is also a possibility that the insertion of Li^+ ions into the tetrahedral sites in the LiO_6 layer causes lattice expansion prior to a shearing event. The relationship between the relative phase ratio is harder to understand and suggests that more than one electrochemical process may occur during the plateau region possibly due to the onset of lithium plating near the Li/Li^+ equilibrium voltage.

	Unit Cell Parameters			Cell Vol. Å ³	Phase Ratio	R _{wp} (joint)
	a	b	c			
Pristine Li _{1.08} V _{0.92} O ₂						
LiVO ₂	2.8445(2)	2.8445(2)	14.7981(9)	103.59(2)	1	3.35%
Li ₂ VO ₂	X	X	X	X	X	
70 mAh/g						
LiVO ₂	2.8443(1)	2.8443(1)	14.8124(8)	103.736(7)	1	7.34%
Li ₂ VO ₂	X	X	X	X	X	
115 mAh/g						
LiVO ₂	2.8457(5)	2.8457(5)	14.813(1)	103.87(3)	0.697	4.34%
Li ₂ VO ₂	3.099(7)	3.099(7)	5.21(2)	43.3(1)	0.303	
160 mAh/g						
LiVO ₂	2.8512(5)	2.8512(5)	14.847(3)	104.49(3)	0.253	3.96%
Li ₂ VO ₂	3.107(3)	3.107(3)	5.2217(8)	43.671(8)	0.747	
205 mAh/g						
LiVO ₂	2.866(2)	2.866(2)	14.96(3)	106.4(1)	0.17	19.2%
Li ₂ VO ₂	3.1065(6)	3.1065(6)	5.223(2)	43.65(1)	0.83	
End of Discharge						
LiVO ₂	2.852(3)	2.852(3)	14.85(2)	104.7(3)	0.16	17.93%
Li ₂ VO ₂	3.107(2)	3.107(2)	5.223(3)	43.66(6)	0.84	

Table 6.3.3 Selected Refinement parameters from the X-ray diffraction patterns taken at different points during discharge of $\text{Li}_{1.08}\text{V}_{0.92}\text{O}_2$.

The Li_2VO_2 phase appears to undergo little change in the unit cell parameters during discharge and it is mainly due to the ratio relationship between the two phases that the discharge picture becomes more complicated. It would seem that the majority of the LiVO_2 to Li_2VO_2 phase transformation occurs during the first half of the plateau (primarily between the 45-90 mAh/g region). After 90mAh/g of 'plateau' capacity has passed, little more phase transformations occurs, with the majority of the material consisting of Li_2VO_2 after 205mAh/g (135mAh/g of plateau capacity).

This raises the question of what other reduction process is producing the subsequent capacity and more importantly why does the LiVO_2 stop converting to Li_2VO_2 . The amount of capacity passed during the 'phase change' section of the plateau is similar to the reversible capacity seen in subsequent cycles (Figure 6.3.13) suggesting that the excess capacity (i.e. the capacity produced after Li_2VO_2 was the large majority phase) is due to an irreversible process occurring after the formation of Li_2VO_2 in the first discharge (this may explain the two electrochemical processes seen on discharge in the incremental capacity plot in Figure 6.3.5).

To better understand the results of the first discharge structural study further electrochemical analysis was undertaken. Figure 6.3.10 displays the first discharge of $\text{Li}_{1.08}\text{V}_{0.92}\text{O}_2$ under multiple cycling rate regimes, from this information can be derived about the transport properties of the $\text{Li}_{1.08}\text{V}_{0.92}\text{O}_2$ material.

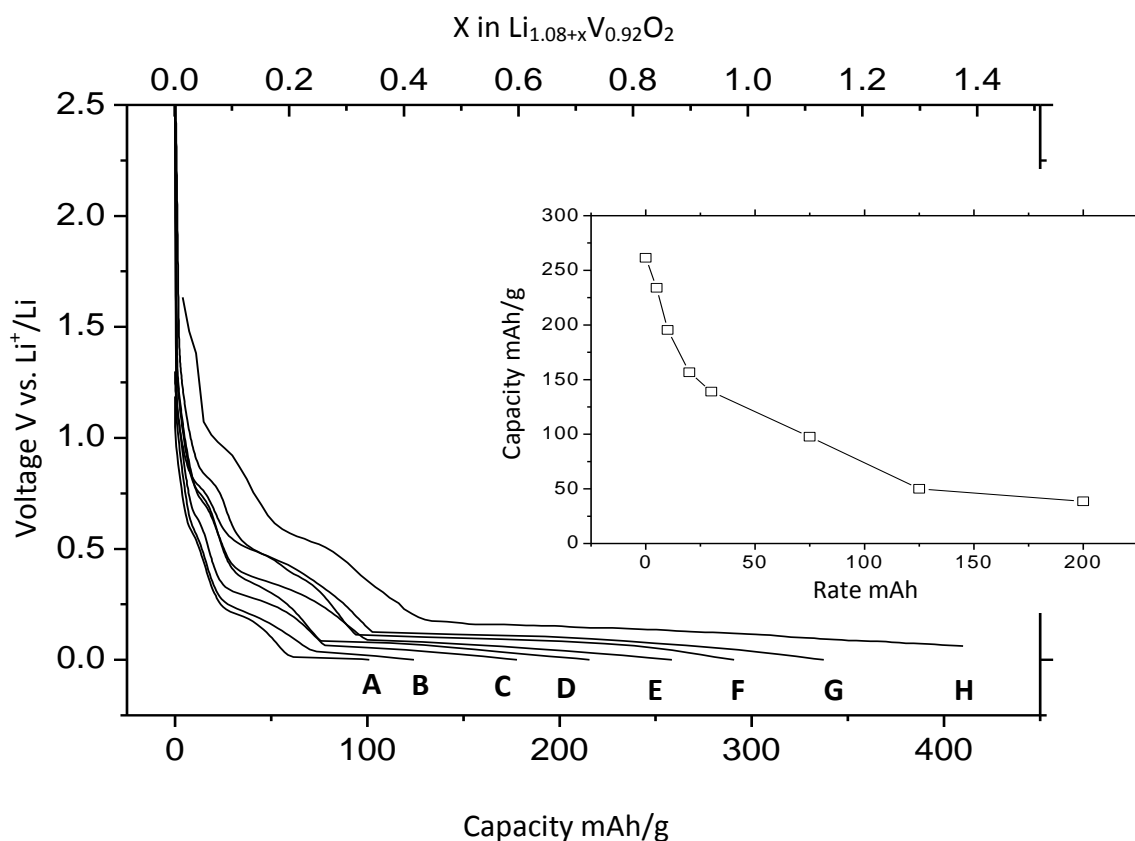


Figure 6.3.10 First discharge voltage vs. composition profiles of $\text{Li}_{1.08}\text{V}_{0.92}\text{O}_2$ at different rates: A) 200 mA/g, B) 125 mA/g, C) 75 mA/g, D) 30 mA/g, E) 20 mA/g, F) 10 mA/g, G) 5 mA/g, H) 0 mA (equilibrium GITT measurement). *Inset:* Plateau capacity vs. rate – Electrolyte LP30 at a temperature 30°C .

The slow decrease in plateau voltage with cycling rate is indicative of an ‘over-potential’ effect, seen in the faster rate regimes because of the increase in polarisation resistance effects (amongst others) upon lithium insertion voltage. The reduction in capacity with rate is due to the inability to completely insert lithium at the faster rate before the voltage cut off. Both the SEI layer formation at $\sim 0.8\text{V}$ and the subsequent shoulder process at $\sim 0.5\text{V}$ are rate dependent (reducing in capacity with faster rate). The ratio of capacity produced by ‘shoulder’ processes to plateau capacity does alter with different cycling rate suggesting that the two have different rate dependencies, and thus are linked to different electrochemical processes. As the

insert shows in Figure 6.3.10, the plateau capacity slowly decreases with rate in a roughly exponential manner.

Combining the information of the different cycling rates we can gain further insight into the processes occurring as the $\text{Li}_{1.08}\text{V}_{0.92}\text{O}_2$ material undergoes discharge. The polarisation resistance at different lithium compositions can be determined by the ohmic drop at a certain lithium composition⁴⁴. This is found by (at a given Li^+ composition) plotting the voltage of the system at different current rates and finding the gradient (i.e. finding $V/I = R$ at different lithium compositions by measuring the voltage response at different current rates). The results are shown in Figure 6.3.11

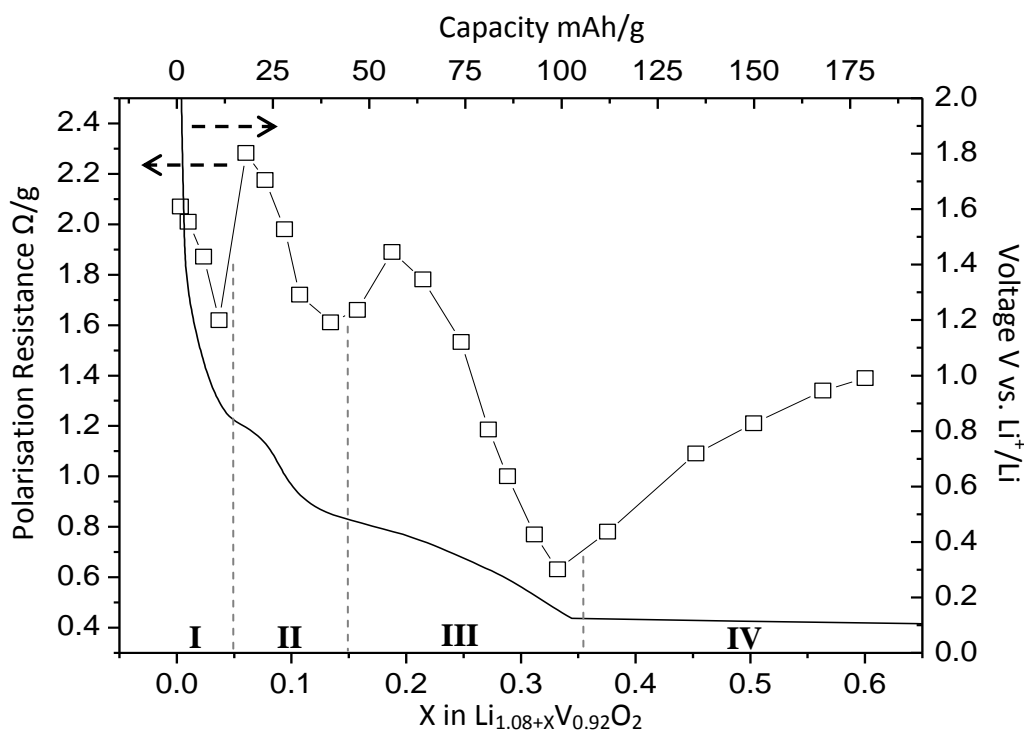


Figure 6.3.11 Polarisation resistance at different lithium compositions for $\text{Li}_{1.08}\text{V}_{0.92}\text{O}_2$

Whenever there is a pronounced change in polarisation, it can be assumed that this is instigated by either a dominating side-reaction or a new structural process. It would seem that there are 4 distinct processes at the start of the doped LiVO_2 discharge; these match up closely with the different processes observed with the

galvanostatic profile. Stages I to III all start as more insulating their resistances then drop. As Stage I and II have been ascribed to SEI formation previously in the literature¹² it might be assumed that stage III, also follows similar resistance behaviour, is part of an SEI formation (or some sort of amorphous electrode/electrolyte surface layer formation). However the computer modelling, discussed previously, would suggest that this region may also account for lithium insertion into empty tetrahedral sites in the alkali layer, prior to possible phase conversion of LiVO_2 to Li_2VO_2 material. The decreasing polarisation resistance may be due to the structure becoming more 'open' prior to shearing, with it reaching a critical concentration of tetrahedrally intercalated lithium at around 0.2V when it is easiest to insert Li^+ into the tetrahedral site (hence lowest resistance) and when it begins to shear (hence proceeding voltage plateau). This ties in well with the expanded structure seen in the unit cell volume increase in the *ex situ* refinement of the LiVO_2 material at 70mAh/g.

Phase IV displays different polarisation resistance behaviour, initially with a low polarisation resistance ($0.7\Omega/\text{g}$) and then slowly increasing as the plateau lengthens. This is behaviour that would be expected during lithium intercalation, with the relative resistance increasing as the LiVO_2 material is over-lithiated and the structure undergoes significant changes to convert to Li_2VO_2 . Both the break-up of contiguous LiVO_2 domains and the gradual filling of the empty tetrahedral sites in the Li_2VO_2 structure may be expected to increase the resistance of the material.

Investigating the AC impedance *in situ* provides a different perspective on the cycling behaviour. Figure 6.3.12(1) displays the AC impedance of the battery system as a whole and how this changes with lithium composition.

The AC modelling of the complete battery system is inherently more complicated than for an individual material, factors such as the system resistance (comprising of the ohmic resistance of the electrolyte, leads, current collectors, various electric fields etc.) as well as the surface film resistance, SEI layer resistance and the charge transfer resistance must be taken in to account along with the effects of semi-infinite diffusion of the lithium ions and various double layer capacitances.

While several models have been proposed for two electrode battery systems^{14,45-48} it is generally accepted that the high frequency intercept is given over to the ohmic resistance (including leads and other system resistance), the high frequency semi-circle (labelled A in Figure 6.3.12) is a consequence of the surface film resistance R_f and the low frequency semi-circle (labelled B) is due to the charge transfer resistance R_{ct} , associated with the solid/electrolyte interface and hence represents the electrochemical behaviour of the system. The low frequency 'tail' is thought to be from the semi-infinite diffusion (Warburg) of lithium ions in bulk processes. The values for R_{ct} match up well with previously reported charge transfer resistances, for example $\text{LiMn}_{0.5}\text{Ni}_{0.5}\text{O}_2$ ⁴⁹

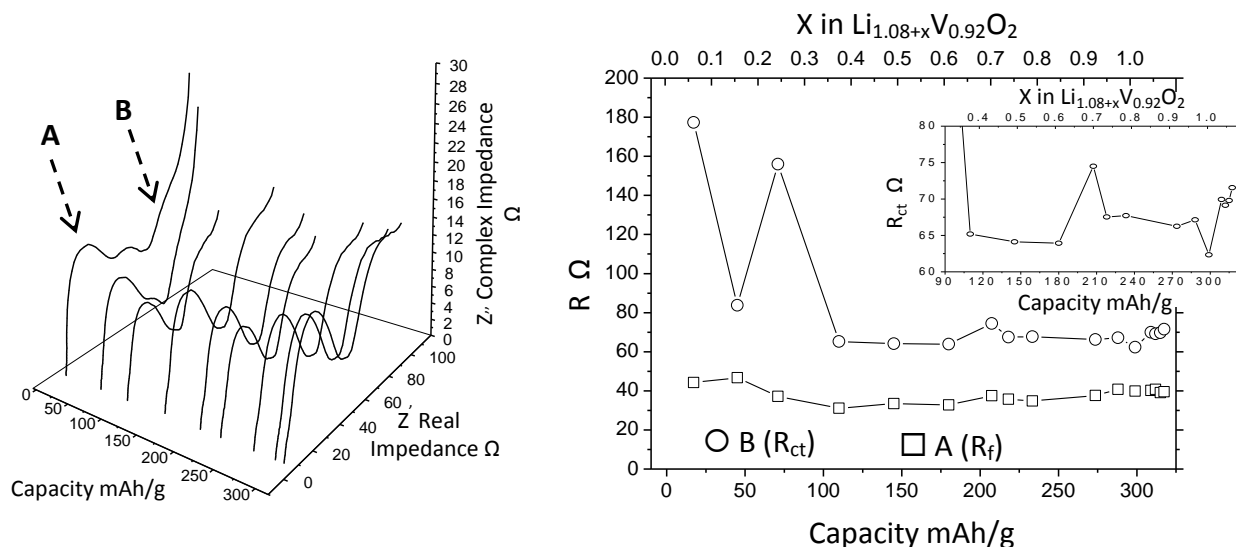


Figure 6.3.12 (1) Nyquist plots of AC impedance spectrum of a 2 electrode $\text{Li}_{1.08}\text{V}_{0.92}\text{O}_2$ | Lithium battery system taken at different states of discharge. (2) Various resistance parameters obtained from the Impedance spectrums at different states of charge. Inset : close up of 90-325 mAh/g region for R_{ct} – Electrolyte LP30, cycling rate 10mA/g at a temperature of 30°C

The *in situ* impedance lines up well with the previously discussed data in both Figure 6.3.11 (*ex situ* X-ray diffraction data) and Figure 6.3.8 (polarisation resistance) comprising of three fairly well defined regions. With reference to Figure 6.3.12(2) we can see that the charge transfer resistance (R_{ct}) undergoes large changes from the 0-100 mAh/g region starting at almost 180 Ω and eventually dropping to $\sim 70\Omega$ with the onset of the plateau region and lithium intercalation at around 70 mAh/g.

This 0-70 mAh/g region consists of SEI formation and the large fluctuations in R_{ct} is commensurate with the observations from the polarisation resistance in Figure 6.3.11 which suggest that there is more than one type of SEI formation. The presence of a third definable semicircle between the ‘high’ and low’ frequency semi-circles is also noted. This exists up until around 70mAh/g and has a resistance value in between

R_f and R_{ct} . It could represent the presence of an insulating layer upon the active material which disappears with the onset of lithium intercalation.

The region from 70 mAh/g up to ~ 175 mAh/g presents relatively little change in the charge transfer resistance, from the x-ray diffraction, this region is associated with the single electrochemical process of LiVO_2 to Li_2VO_2 conversion and is expected to be a monotonic charge transfer process.

After ~ 200 mAh/g the charge transfer resistance begins to alter, settling at the higher resistance of $\sim 70 \Omega$, indicative of a different process compared to the 70-175 mAh/g region. During this process the R_{ct} is relatively unchanging perhaps suggesting that the capacity of this region is generated by a single process. While the charge-transfer resistance only confirms the presence of different process during discharge, it correlates well to the previously observed regions through polarisation resistance and X-ray diffraction, though it does not directly show what causes the change in R_{ct} .

A self-consistent picture begins to emerge between the galvanostatic, X-ray diffraction and AC impedance information. There are 3 distinct stages occurring through discharge. Initially, what is believed to be SEI formation occurs with little change to the LiVO_2 material except with a slight expansion. This is possibly a consequence of intercalation of Li^+ into the tetrahedral sites in the alkali layers of LiVO_2 . This stage is followed by the onset of full lithium intercalation causing LiVO_2 to Li_2VO_2 phase transformations. Finally the LiVO_2 phase transformation slows, to be replaced by a process which does not produce any crystalline products.

While not explicitly showing the processes occurring during LiVO_2 discharge, both the *in situ* AC impedance and polarisation resistance are consistent with the *ex situ* diffraction data (and to a certain extent, the computer modelling). All techniques point to a complicated first discharge process, this does not bode well for the long term cycling of LiVO_2 material with the intercalation seemingly dependent on multiple inter-connected processes.

As Figure 6.3.13 shows, the capacity retention over even a short number of cycles is poor with the discharge capacity diminishing by almost 70% over 10 cycles (though this value is closer to 50% when you consider just the 'reversible' capacity from the plateau of the first discharge). The charging capacity fares a little better losing ~55% of the capacity after ten cycles (due to the lack of irreversible capacity on the first charge). It would seem that the lithium intercalation process is fairly efficient, with similar amounts of lithium being removed as charge is inserted in the previous discharge cycle. The slow reduction in capacities seen in Figure 6.3.13 (2) is monotonic and shows no signs of stabilising after the ten cycles.

It was not clear whether the poor capacity retention is a consequence of side reactions (although any side reactions are probably not electrolyte specific, given that the capacity decline was observed with other electrolytes, see appendix vi). Since altering electrochemical factors made little difference, the poor performance could be rooted in a physical process such as dissolution of the electrode.

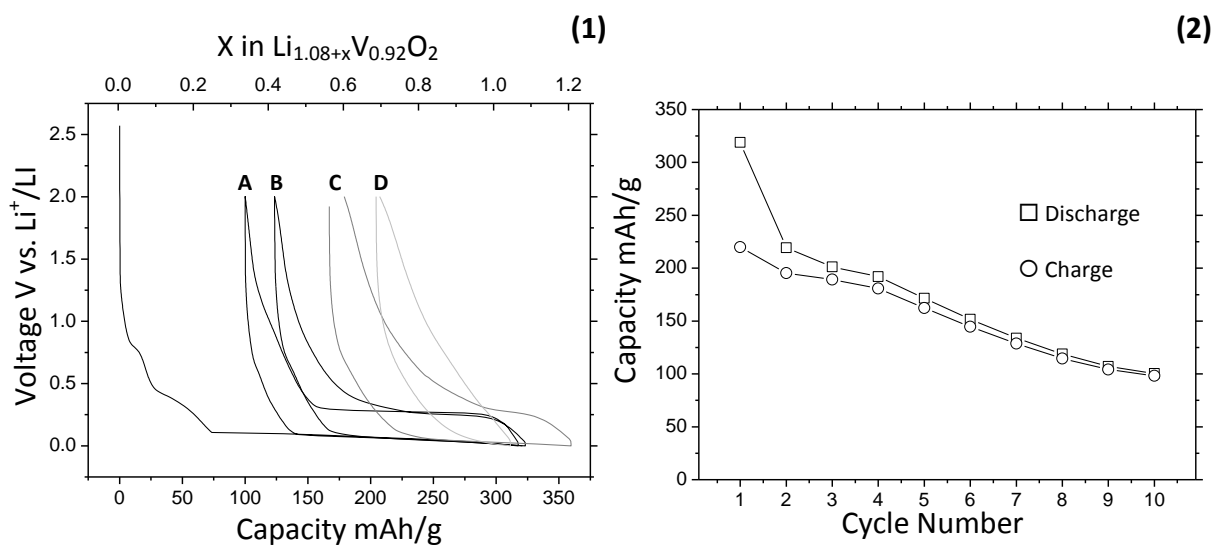


Figure 6.3.13. (1) Selected cycles of Voltage vs. composition plots of $\text{Li}_{1.08}\text{V}_{0.92}\text{O}_2$: A) 1st cycle, B) 2nd cycle, C) 5th Cycle, D) 10th cycle. (2) Capacity vs. cycle number for $\text{Li}_{1.08}\text{V}_{0.92}\text{O}_2$ material. - Electrolyte LP30, cycling rate 10mA/g at a temperature 30°C.

The stoichiometry of the Li_2VO_2 phase (i.e. lack of lithium/vanadium site mixing) may explain the poor capacity retention over repeated cycles. While it is apparent from the atomistic modelling that a small amount of doping is crucial for LiVO_2 to Li_2VO_2 phase conversion the same may not be true for the reverse process; the nature of the LiVO_2 material created from de-lithiation of Li_2VO_2 is of crucial importance. Due to the large structural rearrangement occurring when LiVO_2 shears to Li_2VO_2 it would appear that the doping in the vanadate layer is not retained (at least it is not obvious from the refinement of the recovered material). It is likely that this ‘un-doped’ stoichiometry is maintained when Li_2VO_2 undergoes phase conversion to LiVO_2 , which as the modelling suggests would seriously hamper subsequent intercalation of Li^+ into the LiVO_2 material and may be the cause of the poor capacity retention seen in Figure 6.3.13.

6.3. Conclusions and Further Work

Various doped LiVO_2 materials were produced using a solid state synthesis. Subsequent structural characterisation revealed a complicated relationship between the unit cell dimensions and the amount of lithium doping. The electrochemical behaviour of the LiVO_2 material was found to be closely linked with the amount of doped lithium present with the 8% excess lithium residing in the vanadium layer giving the highest first discharge capacity.

A self consistent picture emerged of the electrochemical processes occurring within the doped LiVO_2 material under galvanostatic cycling. It was ascertained from various observations that from 0-70mAh/g there is a region of sloping voltage shoulders as more charge is inserted into the electrode. There is a gradual reduction in charge transfer resistance and no detectable change in the x-ray diffraction patterns during this stage. In conjunction with previous studies this suggests the growth of various amorphous SEI layers.

After ~70mAh/g there is a period marked by a flat galvanostatic voltage plateau and a gradual increase in polarisation resistance. There is observed growth, and subsequent domination, of a second phase in the X-ray diffraction patterns that can be refined using a $P\bar{3}m1$ Li_2VO_2 model. This region is marked with little change in the charge transfer resistance and thus is ascribed to LiVO_2 to Li_2VO_2 transformation. This lasts until ~180mAh/g of charge has been inserted after which, although little change is seen in the galvanostatic plateau voltage, no new Li_2VO_2 growth (or other phase) is seen in the X-ray diffraction pattern. The charge transfer resistance is seen to increase

from the previous region to stabilise at around 70 Ω which suggests some subtle change has occurred in the electrochemical behaviour. The resilience of the voltage plateau despite the lack of new Li_2VO_2 growth in the diffraction patterns suggest that some lithium insertion (i.e. triggering the $\text{V}^{3+/2+}$ redox couple) is occurring but no crystalline phases are being produced, or the voltage is close enough to the lithium Li^+/Li equilibrium voltage to start depositing lithium metal.

While this work has explored the nature of the electrochemical processes occurring within the LiVO_2 system, further characterisation is needed to fully understand the complicated anodic nature of LiVO_2 . Further *in situ* studies perhaps utilising IR, Raman and NMR techniques may help to investigate the nature of the SEI layer formation (or lithium intercalation) and the subsequent drop off in LiVO_2 to Li_2VO_2 phase conversion. A more in depth *ex situ* analysis of the structures of LiVO_2 and Li_2VO_2 on repeated cycling would help to establish if the doping of the 3a octahedral vanadate site is carried through on phase conversion. Establishing the full nature of the first discharge process may go some way into determining methods to increase the cyclability of the material and would be an important step into establishing LiVO_2 as a viable anode.

6.4. References

1. J. Vaughey, A. M. Geyer, N. Fackler, C. S. Johnson, K. Edstrom, H. Bryngelsson, R. Benedek, and M. M. Thackeray, *Journal of Power Sources*, 2007, **174**, 1052-1056.
2. C. S. Johnson, J. Kim, A. J. Kropf, A. J. Kahaian, J. T. Vaughey, L. M. L. Fransson, K. Edstrom, and M. M. Thackeray, *Chemistry of Materials*, 2003, **15**, 2313-2322.
3. C. S. Johnson, J. Kim, A. J. Kropf, A. J. Kahaian, J. T. Vaughey, and M. M. Thackeray, *Electrochemistry Communications*, 2002, **4**, 492-498.
4. S. Myung, S. Komaba, and N. Kumagai, *Solid State Ionics*, 2004, **170**, 139-144.
5. K. Ozawa, *Solid State Ionics*, 1994, **69**, 212-221.
6. M. Mohri, N. Yanagisawa, Y. Tajima, H. Tanaka, T. Mitate, S. Nakajima, M. Yoshida, Y. Yoshimoto, T. Suzuki, and H. Wada, *Journal of Power Sources*, 1989, **26**, 545-551.
7. D. Aurbach, E. Zinigrad, Y. Cohen, and H. Teller, *Solid State Ionics*, 2002, **148**, 405-416.
8. X. Yao, S. Xie, C. Chen, Q. Wang, J. Sun, Y. Li, and S. Lu, *Electrochimica Acta*, 2005, **50**, 4076-4081.
9. M. Holzapfel, A. Martinet, F. Alloin, B. Le Gorrec, R. Yazami, and C. Montella, *Journal of Electroanalytical Chemistry*, 2003, **546**, 41-50.
10. L. Zou, F. Kang, X. Li, Y. Zheng, W. Shen, and J. Zhang, *Journal of Physics and Chemistry of Solids*, **69**, 1265-1271.
11. N. Kambe, M. Dresselhaus, G. Dresselhaus, S. Basu, A. McGhie, and J. Fischer, *Materials Science and Engineering*, 1979, **40**, 1-4.
12. J. Yamaki, H. Takatsuji, T. Kawamura, and M. Egashira, *Solid State Ionics*, 2002, **148**, 241-245.
13. S. A. Needham, G. X. Wang, K. Konstantinov, Y. Tournayre, Z. Lao, and H. K. Liu, *Electrochem. Solid-State Lett.*, 2006, **9**, A315-A319.
14. H. Li, X. Huang, and L. Chen, *Journal of Power Sources*, 1999, **81-82**, 340-345.
15. P. P. Prosini, R. Mancini, L. Petrucci, V. Contini, and P. Villano, *Solid State Ionics*, 2001, **144**, 185-192.
16. J. Kim, C. S. Johnson, J. T. Vaughey, M. M. Thackeray, S. A. Hackney, W. Yoon, and C. P. Grey, *Chemistry of Materials*, 2004, **16**, 1996-2006.
17. L. Zhang, X. Wang, H. Noguchi, M. Yoshio, K. Takada, and T. Sasaki, *Electrochimica Acta*, 2004, **49**, 3305-3311.
18. S. Myung, S. Komaba, and N. Kumagai, *Solid State Ionics*, 2004, **170**, 139-144.
19. R. Benedek, J. Vaughey, and M. M. Thackeray, *Chemistry of Materials*, 2006, **18**, 1296-1302.
20. F. Zhou, M. Cococcioni, C. A. Marianetti, D. Morgan, and G. Ceder, *Phys. Rev. B*, 2004, **70**, 235121.
21. N. Choi, J. Kim, R. Yin, and S. Kim, *Materials Chemistry and Physics*, 2009, **116**, 603-606.
22. J. H. Song, H. J. Park, K. J. Kim, Y. N. Jo, J. Kim, Y. U. Jeong, and Y. J. Kim, *Journal of Power Sources*, 2010, **195**, 6157-6161.
23. S. Kim, Y. Nitta, N. Tatiana, and J. Lee, Application No. 11/258150, US Patent number 2006/0088766,
24. K. Kang, Y. S. Meng, J. Breger, C. P. Grey, and G. Ceder, *Science*, 2006, **311**, 977-980.
25. N. Imanishi, M. Fujii, A. Hirano, and Y. Takeda, *Journal of Power Sources*, 2001, **97-98**, 287-289.
26. V. Subramanian, K. Karki, and B. Rambabu, *Solid State Ionics*, 2004, **175**, 315-318.

27. M. N. Obrovac, O. Mao, and J. R. Dahn, *Solid State Ionics*, 1998, **112**, 9-19.
28. N. Imanishi, M. Fujii, A. Hirano, Y. Takeda, M. Inaba, and Z. Ogumi, *Solid State Ionics*, 2001, **140**, 45-53.
29. M. M. Thackeray, M. F. Mansuetto, D. W. Dees, and D. R. Vissers, *Materials Research Bulletin*, 1996, **31**, 133-140.
30. R. K. Mishra, O. O. Biest, and G. Thomas, *Journal of the American Ceramic Society*, 1978, **61**, 121-126.
31. P. Quintana and A. R. West, *Journal of Solid State Chemistry*, 1989, **81**, 257-270.
32. P. Poizot, S. Laruelle, S. Grugeon, and J. Tarascon, *J. Electrochem. Soc.*, 2002, **149**, A1212-A1217.
33. P. Poizot, S. Laruelle, S. Grugeon, L. Dupont, and J. Tarascon, *Nature*, 2000, **407**, 496-499.
34. M. S. Islam, D. J. Driscoll, C. A. J. Fisher, and P. R. Slater, *Chemistry of Materials*, 2005, **17**, 5085-5092.
35. E. Kendrick, J. Kendrick, K. S. Knight, M. S. Islam, and P. R. Slater, *Nat Mater*, 2007, **6**, 871-875.
36. C. R. A. Catlow, *Computer modelling in inorganic crystallography*, Academic Press, 1997.
37. F. Zhou, M. Cococcioni, C. A. Marianetti, D. Morgan, and G. Ceder, *Phys. Rev. B*, 2004, **70**, 235121.
38. Y. S. Meng and M. E. A. Dompablo, *Energy Environ. Sci.*, 2009, **2**, 589-609.
39. J. S. Braithwaite, C. R. A. Catlow, J. D. Gale, J. H. Harding, and P. E. Ngoepe, *J. Mater. Chem.*, 2000, **10**, 239-240.
40. W. David, J. Goodenough, M. M. Thackeray, and M. G. S. R. Thomas, *Revue De Chimie Minerale*, 1983, **20**, 636.
41. J. R. Dahn, U. von Sacken, and C. A. Michal, *Solid State Ionics*, 1990, **44**, 87-97.
42. W. I. F. David, J. Goodenough, M. M. Thackeray, and M. G. S. R. Thomas, .
43. P. Strobel, J. Levy, and J. Joubert, *Journal of Crystal Growth*, **66**, 257-261.
44. C. Delacourt, L. Laffont, R. Bouchet, C. Wurm, J. Leriche, M. Morcrette, J. Tarascon, and C. Masquelier, *J. Electrochem. Soc.*, 2005, **152**, A913-A921.
45. N. Ding, J. Xu, Y. Yao, G. Wegner, X. Fang, C. Chen, and I. Lieberwirth, *Solid State Ionics*, 2009, **180**, 222-225.
46. Y. Choi, S. Pyun, J. Bae, and S. Moon, *Journal of Power Sources*, 1995, **56**, 25-30.
47. B. A. Boukamp, *Solid State Ionics*, 2004, **169**, 65-73.
48. M. D. Levi, E. Levi, D. Aurbach, M. Schmidt, R. Oesten, and U. Heider, *Journal of Power Sources*, 2001, **97-98**, 525-528.
49. P. Suresh, A. K. Shukla, and N. Munichandraiah, *J. Electrochem. Soc.*, 2005, **152**, A2273.

Chapter 7. Preliminary Investigation into Layered Transition Metal Oxide Anodes

Chapter 7. Preliminary Investigation into layered transition

Metal Oxide Anodes

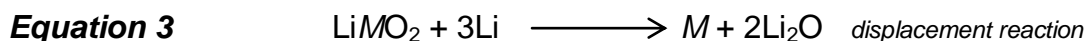
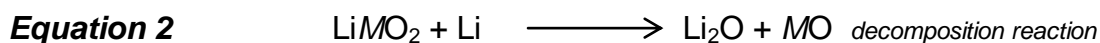
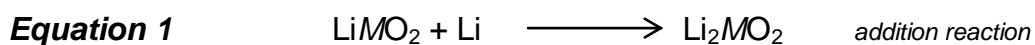
Chapter Contents:

7.1. Introduction	192
7.2. Results and Discussion	194
7.2.1. LiMO_2	194
7.2.2. LiCoO_2	197
7.2.3. $\text{LiMn}_{0.5}\text{Ni}_{0.5}\text{O}_2$	200
7.2.4. $\text{LiNi}_{0.33}\text{Co}_{0.66}\text{O}_2$	206
7.3. Conclusions and Further Work	212
7.4. References	214

7.1. Introduction

Several transition metal oxide (LiMO_2) systems were investigated for their ability to convert to layered Li_2MO_2 materials upon over-lithiation ($> 1\text{Li}^+$ per unit cell). A preliminary investigation concerning the structural nature of the LiCoO_2 , $\text{LiMn}_{0.5}\text{Ni}_{0.5}\text{O}_2$ and $\text{LiNi}_{0.33}\text{Co}_{0.66}\text{O}_2$ systems during electrochemical discharge was undertaken.

Layered oxide anodes remain an undeveloped area of research; although there has been some work (mainly by Thackeray *et al.*) little is understood about which systems can successfully undergo addition of lithium at low voltages. It is thought that layered LiMO_2 (where $M = \text{Co, Ni, Mn, V, Ni}_{0.5}\text{Mn}_{0.5}\dots$) type materials can undergo several types of reaction with $>1\text{Li}^+$ intercalation. Three of the best understood reactions are:



Reaction (1) has been observed in the LiVO_2 system (as discussed in the previous chapter), as well as, tentatively, for the $\text{LiNi}_{0.5}\text{Mn}_{0.5}\text{O}_2$ system¹ which has been the focus of several articles by Thackeray *et al.*¹⁻⁵. Other materials known to form Li_2MO_2 phases (albeit through chemical rather than electrochemical methods) include Li_2MnO_2 ⁶ (which adopts a similar hexagonal structure to Li_2VO_2 and $\text{Li}_2\text{Mn}_{0.5}\text{Ni}_{0.5}\text{O}_2$) and Li_2NiO_2 ^{7,8} (which forms both rhombohedral and orthorhombic structures) and Li_2CuO_2 which is known to adopt an orthorhombic structure^{9,10}.

The electrochemical addition reaction is advantageous because it involves a 'simple' phase conversion rather than a separate electrochemical process which may incur a variety of products and a large thermodynamic (i.e. voltage) difference between the discharging and charging reaction. The conversion of LiMO_2 materials to $P\bar{3}m1$ type Li_2MO_2 materials (i.e. not destroying the rhombohedral symmetry) is an attractive solution to anode design as it would promote higher capacity and longevity given the, presumably, lower energy cost of the phase change process compared to decomposition or displacement type reactions.

Decomposition and displacement reactions represent other types of processes occurring upon $> 1\text{Li}^+$ being added to the system. In the case of equation 2 the ternary oxide decomposes to the monoxide (or potentially, a higher $M_x\text{O}_y$ oxide) and lithium peroxide (Li_2O). In equation 3 the metal is displaced to its elemental form by extrusion from the LiMO_2 structure upon excess lithium insertion. There is a strong possibility that both equations 2 and 3 could happen simultaneously or sequentially leading to multiple products (such as metal monoxide (MO) from equation 2 displacing to give the metal and lithium peroxide (a reaction that has been further investigated for its anodic properties^{11,12}). It is thought that this may explain the behaviour of LiCoO_2 ¹³.

Thackeray *et al* suggest that it is the balance struck between thermodynamic and kinetic factors of the over-lithiation reaction which determine the reaction pathway⁵. The work concluded that the explanation is inherently complex and various physical and structural factors can influence the type of reaction pathway when the system is over-lithiated.

7.2. Results and Discussion

All materials were initially cycled from 3-0V to establish the presence of any plateaus and determine the most appropriate cycling regime.

7.2.1. LiMO_2

Several systems were assessed for possible addition type behaviour (eq. 1) a selection of their voltage composition profiles are displayed in Figure 6.3.1.

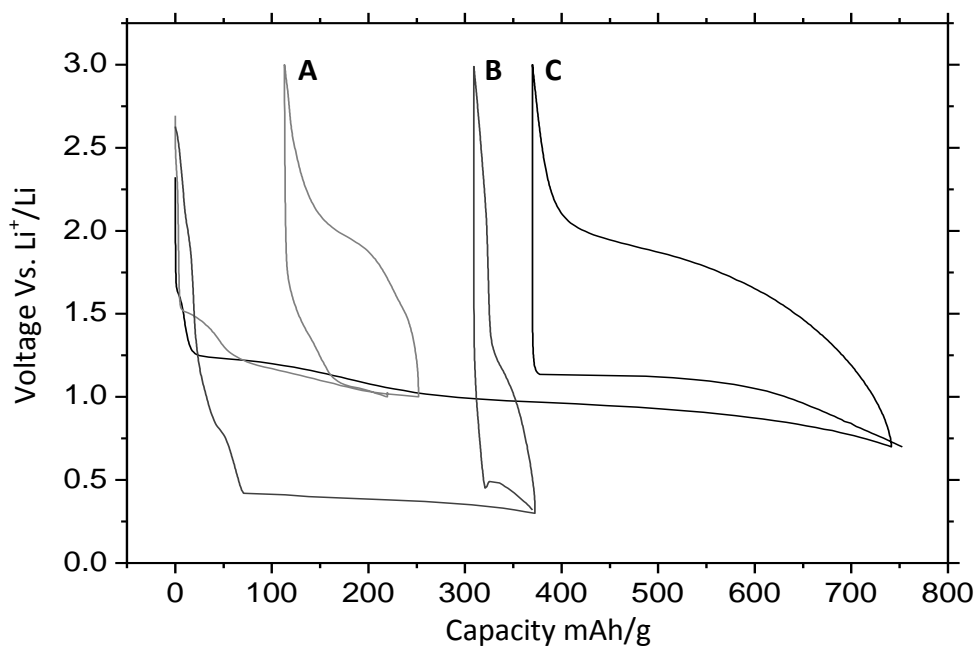


Figure 7.3.1. 1st and 2nd cycles of voltage vs. lithium composition for selected layered transition metal compounds – Electrolyte LP30, cycling rate 10mA/g at a temperature 30°C A) $\text{LiMn}_{0.5}\text{Co}_{0.5}\text{O}_2$, B) LiMnO_2 , C) $\text{LiMn}_{0.33}\text{Co}_{0.33}\text{O}_2$

As can be seen from the galvanostatic profiles in Figure 6.3.1. the layered transition metal oxides display a wide variety of behaviour upon over-lithiation. The different voltages of the first discharge plateaux of the three materials indicate either differing redox couples or discrete thermodynamic processes which occur at different

voltages. It would seem that, given the similar plateau voltages, both the $\text{LiMn}_{0.33}\text{Ni}_{0.33}\text{Co}_{0.33}\text{O}_2$ and $\text{LiMn}_{0.5}\text{Co}_{0.5}\text{O}_2$ materials utilise the same process (at least on the first discharge). The previously reported ability of $\text{LiMn}_{0.5}\text{Ni}_{0.5}\text{O}_2$ to undergo addition of lithium using the Mn ion⁵ would suggest that perhaps the manganese ion is the redox active component of the Ni/Mn system. Indeed Thackeray has proved, theoretically, that $\text{LiMn}_{0.5}\text{Co}_{0.5}\text{O}_2$ would contain a tetravalent Mn ion⁵ (this is especially pertinent as the $\text{LiMn}_{0.5}\text{Ni}_{0.5}\text{O}_2$ to $\text{Li}_2\text{Mn}_{0.5}\text{Ni}_{0.5}\text{O}_2$ transition is thought to occur at a similar voltage to the $\text{LiMn}_{0.5}\text{Co}_{0.5}\text{O}_2$ plateau). Though without further experimental proof of the oxidation states of the transition metal ions it is difficult to ascertain which ions are likely to undergo reduction. The nearly symmetric charge and second discharge profile of the $\text{LiMn}_{0.5}\text{Co}_{0.5}\text{O}_2$ material suggests a reversible reaction, hinting at a possible $\text{LiMn}_{0.5}\text{Co}_{0.5}\text{O}_2$ to $\text{Li}_2\text{Mn}_{0.5}\text{Co}_{0.5}\text{O}_2$ phase change.

The $\text{LiMn}_{0.33}\text{Ni}_{0.33}\text{Co}_{0.33}\text{O}_2$ displays an initial (and 2nd) discharge capacity (~750 mAh/g), far in excess of the theoretical capacity for a lithium addition reaction (~280 mAh/g). The lack of symmetrical charge and discharge profile suggests the plateau reaction is not reversible. Perhaps the Mn is reduced upon discharge, as has been observed in other binary metal systems (hence the similar plateau voltage to $\text{LiMn}_{0.5}\text{Co}_{0.5}\text{O}_2$) on charge another process likely occurs.

The layered LiMnO_2 material shows an entirely different first discharge plateau at ~0.4V, indicative of a distinct process. Given the large difference between initial discharge capacity and subsequent charge and 2nd discharge capacities it is unlikely that LiMnO_2 undergoes a simple addition type reaction to produce Li_2MnO_2 . This hints at the complicated nature of how the addition/decomposition/displacement reactions

are determined, as Li_2MnO_2 is a known, thermodynamically stable, material¹⁴ which would suggest that, thermodynamically at least, a reversible LiMnO_2 to Li_2MnO_2 transition should be possible.

LiCoO_2 and solid solutions of $\text{LiMn}_x\text{Ni}_{1-x}\text{O}_2$ and $\text{LiNi}_x\text{Co}_{1-x}\text{O}_2$ were also investigated and these are explored in further depth, as these materials displayed behaviour exemplifying either addition type reactions or displacement/decomposition reactions.

7.2.2. LiCoO₂

Figure 6.3.2 shows the galvanostatic profile of LiCoO₂ when cycled from 3V-1.1V. Previously it has been suggested that LiCoO₂ cannot undergo an addition type reaction⁵ and when cycled it is clear that the first discharge far exceeds the theoretical capacity (~274mAh/g) for an addition type reaction (as do subsequent discharge plateaus).

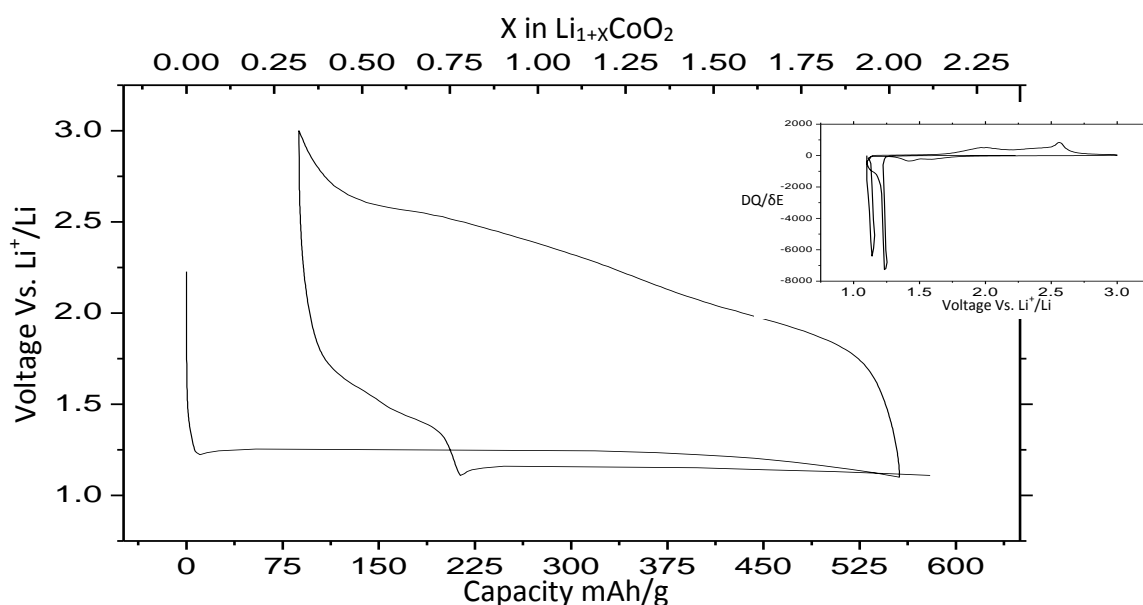


Figure 7.3.2. 1st and 2nd cycle of LiCoO₂ Voltage vs. Lithium composition profile - *Inset:* Incremental capacity plot of 1st and 2nd cycle of LiCoO₂ - Electrolyte LP30, cycling rate 10 mA/g at a temperature 30°C.

The near flat voltage plateau at 1.24V suggests a monotonic reaction (without any of the SEI formation seen in the LiVO₂ system), which undergoes a large hysteresis of approximately 1 V upon charging. From the incremental capacity plot in the inset it can be seen that there is a large difference between the discharge and charging peaks. The discharge is characterised by a single large peak which shifts to a lower voltage on further cycles. This would tend to suggest that simple sequential reactions (i.e. a combination of eq. 2 and 3) are not occurring, as these would be expected to produce different voltage plateaus during discharge. Although the discharge appears to be a

single process, the charging process indicates multiple reaction types at different voltages which may reflect the discharge products reacting on lithium removal to form multiple products. The subsequent second discharge cycle has three identifiable processes, the first two occurring in the region at $\sim 1.5\text{V}$, and may represent reactions between some of the products from the charging reaction and lithium (or indeed a sequential type displacement/decomposition reaction). The third discharge peak process represents the galvanostatic voltage plateau and occurs at a slightly reduced voltage compared to first discharge plateau which may be indicative of a simple over-potential (IR drop) or may hint at a distinctly new process.

From the *ex situ* diffraction patterns in Figure 6.3.3 It can be seen that the LiCoO_2 does not undergo a 'classic' phase change on over-lithiation. After 100mAh/g capacity has passed there is very little change to the diffraction pattern, indeed it is only at the end of discharge that a noticeable change is observed with the introduction of the Li_2O phase. The Li_2O material is thought to be produced through both dissociation and displacement reactions (eq. 2 and 3). The lack of any CoO or Co metal products in the X-ray diffraction pattern is likely due to the nanoscopic and/or amorphous nature of the extruded products^{4,15} which makes them weak coherent scatterers of X-rays.

Without any other obvious crystalline cobalt products in the fully discharged X-ray diffraction pattern it is hard to say whether a dissociation or displacement reaction dominates when over-lithiating of LiCoO_2 and further work using small-angle or non-diffraction based techniques is needed to further elucidate the nature of the $\sim 1\text{V}$ discharge reaction. What is clear is that no LiCoO_2 to Li_2CoO_2 phase conversion occurs.

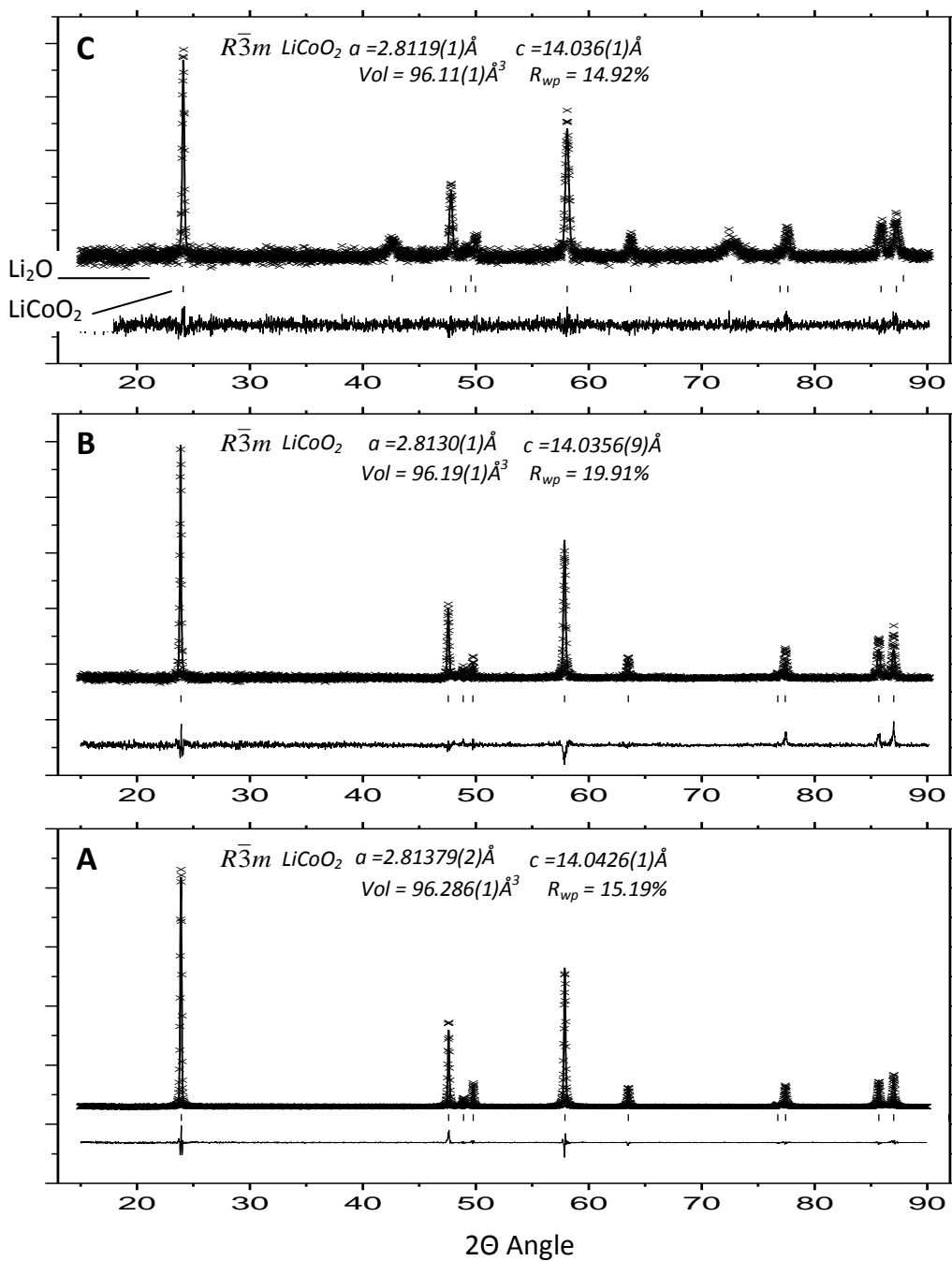


Figure 7.3.3. X-ray diffraction patterns and Rietveld refinement of LiCoO_2 material through discharge to 1.1V : A) Pristine LiCoO_2 material, B) LiCoO_2 after 100 mAh/g capacity, C) LiCoO_2 discharged to 1.1V.

Although not a candidate for a layered oxide ‘addition’ anode, the LiCoO_2 system should not be neglected, as it may offer valuable insight into the mechanisms which favour displacement/ dissociation over addition type reactions.

7.2.3. $\text{LiMn}_{0.5}\text{Ni}_{0.5}\text{O}_2$

An ‘addition’ type phase transformation is expected for $\text{LiMn}_{0.5}\text{Ni}_{0.5}\text{O}_2$ after the presence of $\text{Li}_2\text{Mn}_{0.5}\text{Ni}_{0.5}\text{O}_2$ was experimentally confirmed by Thackeray *et al*³. The galvanostatic profile is displayed in Figure 6.3.4.

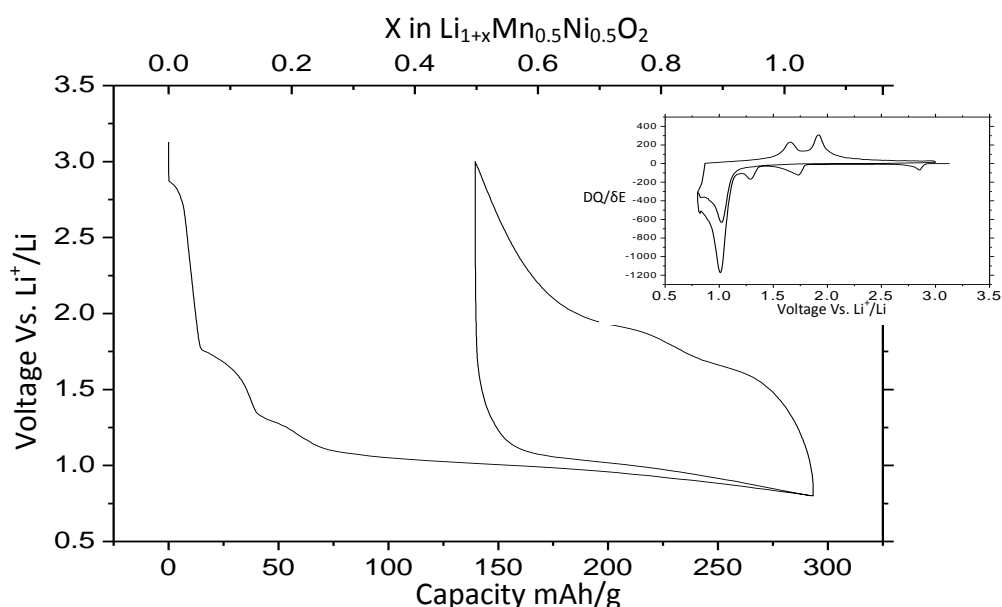


Figure 7.3.4. 1st and 2nd cycle of $\text{LiMn}_{0.5}\text{Ni}_{0.5}\text{O}_2$ Voltage vs. Lithium composition profile - *Inset:* Incremental capacity plot of 1st and 2nd cycle of $\text{LiMn}_{0.5}\text{Ni}_{0.5}\text{O}_2$ – Electrolyte LP30, cycle rate 10mA/g at a temperature of 30°C

This profile is markedly different from LiCoO_2 material, with the first and second discharge voltage plateaus showing gently sloping behaviour at similar voltages (~1V) with no obvious discharge peak shift seen between the first and second cycles (seen in the incremental capacity plot). In many ways the first discharge profile of $\text{LiMn}_{0.5}\text{Ni}_{0.5}\text{O}_2$ is similar to the LiVO_2 material discussed in the previous chapter. It has multiple voltage ‘shoulders’ before reaching the voltage plateau (presumably due to a similar process that occurs within the LiVO_2 system). There is also a large irreversible capacity on the first discharge, with the second discharge only having a capacity of ~150 mAh/g (0.5Li). The $\text{LiMn}_{0.5}\text{Ni}_{0.5}\text{O}_2$ system deviates from the LiVO_2 archetype on

charging, where (from the incremental capacity plot in Figure 6.3.4) it can be seen that there are clearly two processes occurring. It appears that the approximate capacities (derived from area under the peak) for each peak are similar ($\sim 60\text{mAh/g}$ for the peak at 1.6V and $\sim 80\text{mAh/g}$ for the peak at 1.9V). The reason for the two peaks may be down to the more intricate redox chemistry present in the $\text{LiMn}_{0.5}\text{Ni}_{0.5}\text{O}_2$ system.

$\text{LiMn}_{0.5}\text{Ni}_{0.5}\text{O}_2$ represents a slightly more complicated electrochemical system than LiCoO_2 as it contains more than one redox couple ($\text{Mn}^{x+/x}$ and $\text{Ni}^{x+/x}$). It has been previously established theoretically⁵ that the nickel adopts a +2 oxidation state and the manganese shows a +4 oxidation state within the $\text{LiMn}_{0.5}\text{Ni}_{0.5}\text{O}_2$ system. Hence the nickel redox couple is thought to be only active above 2V^{16-18} (i.e. when the material is used as a cathode) utilising the $\text{Ni}^{3+/2+}$ and $\text{Ni}^{3+/4+}$ redox couples either as sequential one electron reactions or a direct $\text{Ni}^{4+/2+}$ reduction/oxidation. Conversely below 2V the manganese redox couple is active, again either through one electron reactions or a direct $\text{Mn}^{4+/2+}$ couple. Depending on the nature of this reaction this can introduce the problematic Jahn-Teller structural distortion associated with the octahedral Mn^{3+} ion- which has a history of debilitating the performance of systems which contain Jahn-Teller active ions¹⁹⁻²⁴.

From the incremental capacity plot it would seem that the single discharge process is a consequence of $\text{Mn}^{4+/2+}$ reduction and the two processes observed on charging are a sequential $\text{Mn}^{4+/3+}$, $\text{Mn}^{3+/2+}$ oxidation (while it could be argued that the 0.5 Li plateau on 2nd discharge may suggest a 1 electron process on discharge, the presence of the 2 charging peaks in the incremental plot insinuates a 2 electron oxidation which could only happen with a full 4+ to 2+ reduction on discharge).

The *ex situ* X-ray diffraction pattern taken after 160mAh/g of discharge (displayed in Figure 6.3.5) confirms the behaviour that was first observed by Thackeray *et al*³ with the apparent growth of the $\text{Li}_2\text{Mn}_{0.5}\text{Ni}_{0.5}\text{O}_2$ phase. The $\text{Li}_2\text{Mn}_{0.5}\text{Ni}_{0.5}\text{O}_2$ phase can be refined to a $P\bar{3}m1$ space group, iso-structural to Li_2NiO_2 ⁷, Li_2VO_2 and Li_2MnO_2 ²⁵ type materials.

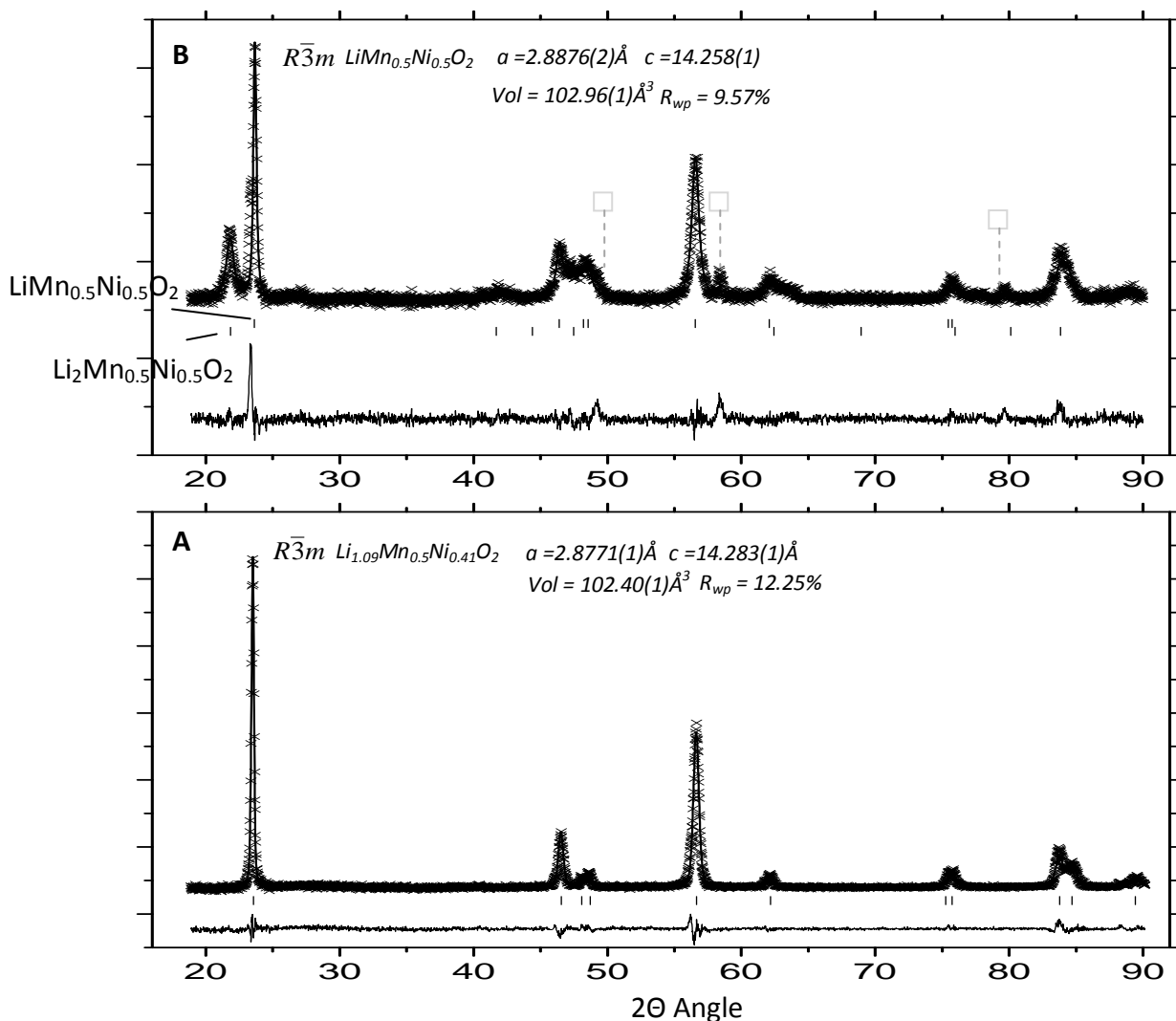


Figure 7.3.5. X-ray diffraction patterns and Rietveld refinements for nominally $\text{LiMn}_{0.5}\text{Ni}_{0.5}\text{O}_2$ materials at different states of discharge: A) Pristine $\text{LiMn}_{0.5}\text{Ni}_{0.5}\text{O}_2$ as received from Fluka, B) $\text{LiMn}_{0.5}\text{Ni}_{0.5}\text{O}_2$ after 160mAh/g of discharge, \square Unknown impurity.

The joint refinement gives a fit of $R_{wp} = 9.57\%$ and a phase ratio of approximately 0.4:0.6 $\text{LiMn}_{0.5}\text{Ni}_{0.5}\text{O}_2$: $\text{Li}_2\text{Mn}_{0.5}\text{Ni}_{0.5}\text{O}_2$. Selected parameters are given below for the $\text{Li}_2\text{Mn}_{0.5}\text{Ni}_{0.5}\text{O}_2$ phase, due to the similar X-ray scattering cross sections of manganese and nickel (combined with the poorer X-ray statistics from the recovered

powder sample) the model showed very little bias for fractional occupancies in the 1a site and thus the ratio was fixed at 1:1.

Atom	Wyckoff Symbol	x/a	y/b	z/c	B _{iso}	Occupancy
Li1	2d	0.667	0.333	0.35(1)	0.8(1)	1
Mn/Ni	1a	0.00	0.00	0.00	0.022(1)	Mn0.51/Ni0.49(1)
O1	2d	0.333	0.667	0.249(5)	0.084(2)	1

$$a = 3.150(1) \quad b = 3.150(1) \quad c = 5.139(2) \quad \text{Cell Volume} = 44.17(4)$$

$$\text{Space group: } P\bar{3}m1 \quad R_p = 7.2\% \quad R_{wp} = 9.57\% \quad \chi^2 = 1.597$$

* Values produced from two phase refinement from material recovered at 115mAh/g

Table 7.3.1. Refinement parameters of (nominally) $\text{Li}_2\text{Mn}_{0.5}\text{Ni}_{0.5}\text{O}_2$ derived from X-ray diffraction of $\text{LiMn}_{0.5}\text{Ni}_{0.5}\text{O}_2$ material after 160mAh/g of discharge.

The refinement gave similar (if slightly reduced) lattice parameters to the material reported by Thackeray *et al.*³ The growth of the new phase can be clearly seen in the selected 2 θ regions throughout the discharge process displayed in Figure 6.3.6. While the majority of the phase conversion occurs by 160mAh/g the $\text{LiMn}_{0.5}\text{Ni}_{0.5}\text{O}_2$ material does not suffer as strongly from the effect seen with the LiVO_2 material which seemingly stopped the LiVO_2 to Li_2VO_2 change half way through the plateau. One clue as to the cause of ‘non phase conversion’ capacity may be the impurity peaks seen in the X-ray diffraction pattern taken at 160mAh/g (and present in the later diffraction patterns).

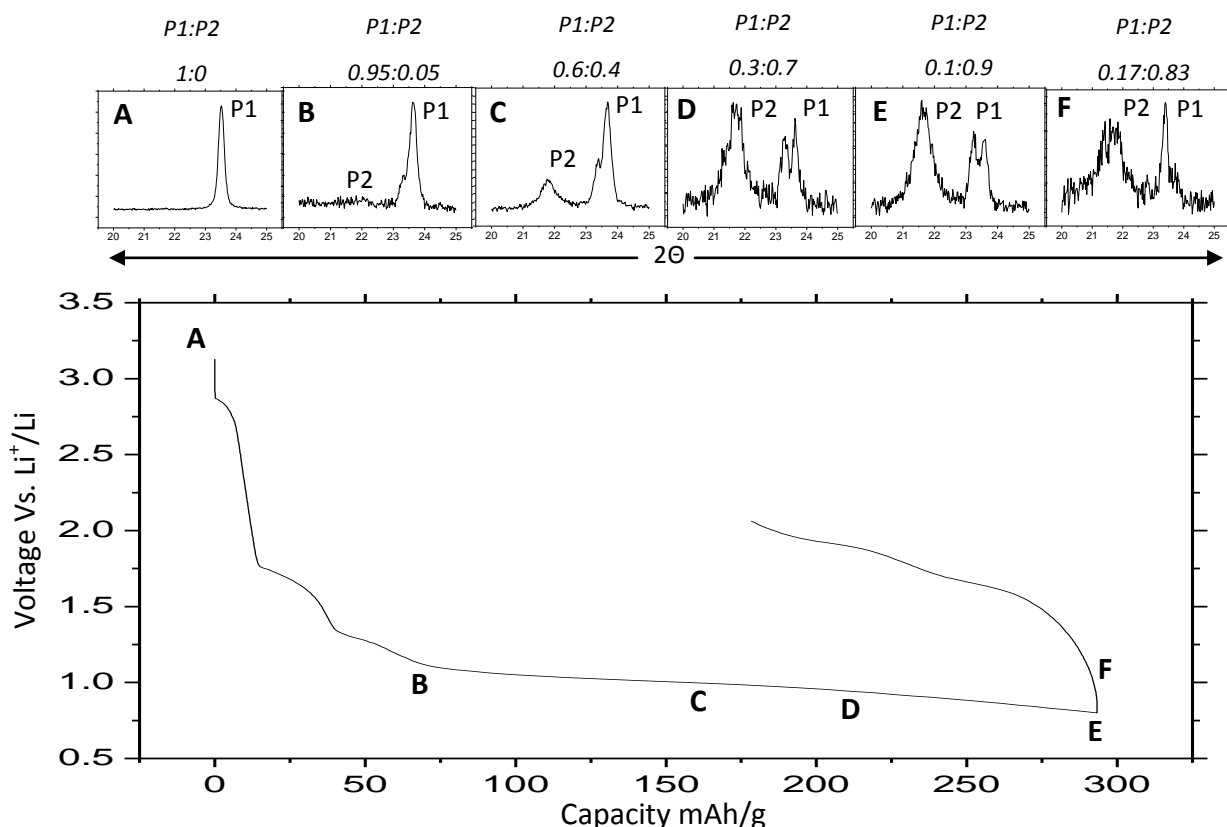


Figure 7.3.6. selected X-ray diffraction peaks through cycling of $\text{LiMn}_{0.5}\text{Ni}_{0.5}\text{O}_2$ material – Electrolyte LP30, cycling rate 10 mA/g at a temperature of 30°C

The nature of this impurity was not discovered after various obvious materials failed to fully account for all the peaks (i.e. NiO and other dissociation/displacement type products). It is likely that the peaks represent various products from side-reactions with the $\text{LiMn}_{0.5}\text{Ni}_{0.5}\text{O}_2$ materials, possibly as a consequence of reactions during phase change or indeed more exotic dissociation reactions occurring from the start of discharge.

One feature highlighted in the diffraction sections shown in Figure 6.3.6 is the splitting of the prominent $\text{LiMn}_{0.5}\text{Ni}_{0.5}\text{O}_2$ peak ($\sim 23.5^\circ$) during discharge (this also explains the slightly diminished fitting around the strong $\text{LiMn}_{0.58}\text{Ni}_{0.5}\text{O}_2$ peaks in the diffraction pattern taken at 160mAh/g). The phase change may induce stacking faults that initially cause widening of the $\text{LiMn}_{0.5}\text{Ni}_{0.5}\text{O}_2$ peak at 23.5° ($h,k,l=0,0,3$) then, eventually, separation into 2 different peaks. Stacking faults are known to cause the

widening of peaks²⁶, in this case possibly brought about by reordering of the $\text{LiMn}_{0.5}\text{Ni}_{0.5}\text{O}_2$ structure (prior to over-lithiation and shearing) into either of its proposed theoretical structures (i.e. the Mn/Ni organised in a striped or zigzag layers⁵).

Interestingly it appears that when the $\text{LiMn}_{0.5}\text{Ni}_{0.5}\text{O}_2$ reforms on charging, the $\text{LiMn}_{0.5}\text{Ni}_{0.5}\text{O}_2$ is dominated by only one peak (seen in the single peak in 0.8V charged X-ray diffraction pattern segment in Figure 6.3.6). The dominant peak seen upon charging appears in the same place as the peak that splits from the pristine material on discharge, suggesting this new 'sub-phase' is more favourable to convert to from $\text{Li}_2\text{Mn}_{0.5}\text{Ni}_{0.5}\text{O}_2$. The peak splitting may offer insight into the nature of the addition process and would be worthy of further study (possibly shedding light on some of the nebulous data produced from LiVO_2 concerning the shearing process – see appendix *vii*).

7.2.4. $\text{LiNi}_{0.33}\text{Co}_{0.66}\text{O}_2$

A further material that displayed promising addition type of behaviour was $\text{LiNi}_x\text{Co}_{1-x}\text{O}_2$ (where $x=0.33, 0.5, 0.66$). Previously un-investigated as an anode, $\text{LiNi}_x\text{Co}_{1-x}\text{O}_2$ has been intensely researched as a possible cathode material²⁷⁻³⁰. In a computational study on mixed metal layered oxide anodes⁵ it was determined that the Ni/Co LiMO_2 system would have the largest change in reaction energy upon lithium insertion between the Ni/Co, Ni/Mn and Mn/Co binary metal LiMO_2 series (suggesting that this would be the most favourable system). The same study suggested that for Ni/Co, Ni/Mn and Mn/Co LiMO_2 systems, a displacement reaction is the most thermodynamically favourable reaction hinting that, when addition does occur, kinetic factors may be dominant in the systems that display Li_2MO_2 conversions). In the study it was suggested that a $\text{LiNi}_{0.5}\text{Co}_{0.5}\text{O}_2$ material would have both Ni^{3+} and Co^{3+} present causing the Ni ion to undergo strong Jahn-Teller distortion which may produce structural strain, inducing instabilities upon cycling.

It was found that the $\text{LiNi}_{0.33}\text{Co}_{0.66}\text{O}_2$ showed marginally better performance thus $\text{LiNi}_{0.33}\text{Co}_{0.66}\text{O}_2$ is used as an example in the following analysis.

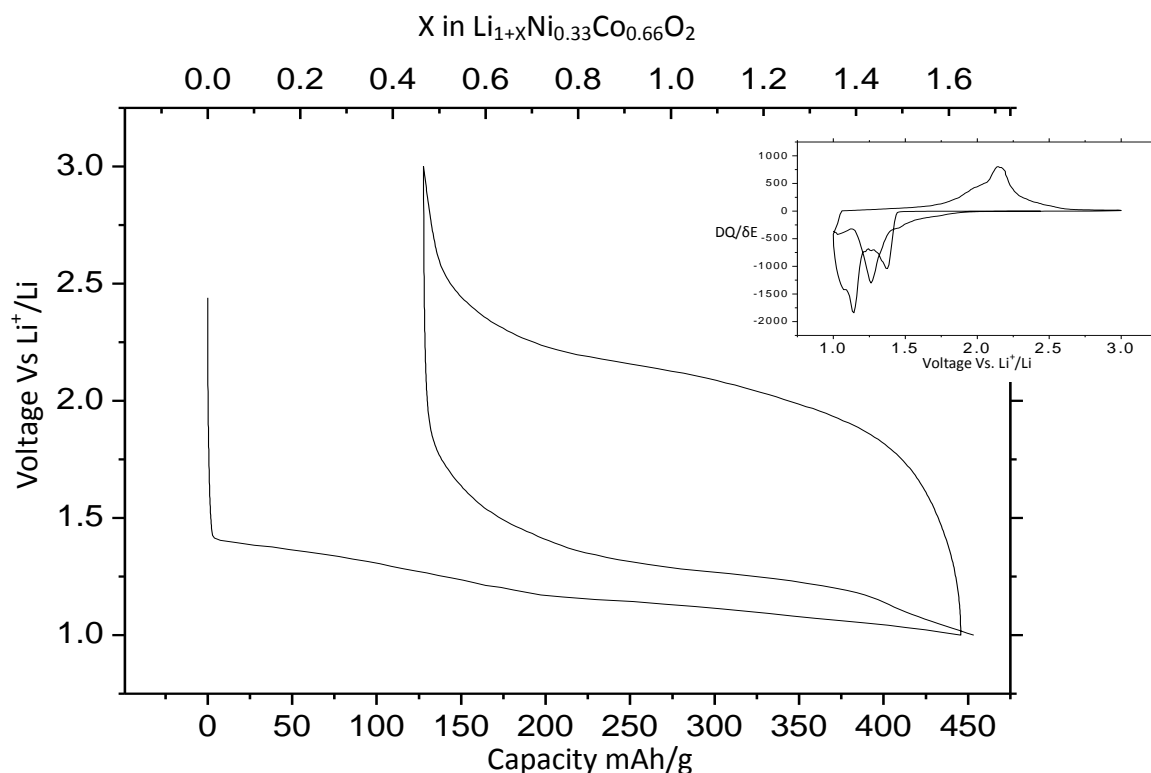


Figure 7.3.7. 1st and 2nd cycle voltage vs. composition profile for $\text{LiNi}_{0.33}\text{Co}_{0.66}\text{O}_2$. Inset: 1st and 2nd incremental capacity plot – Electrolyte LP30, cycling rate 10mA/g at a temperature of 30°C.

The galvanostatic profile of $\text{LiNi}_{0.33}\text{Co}_{0.66}\text{O}_2$ does not show any of the voltage ‘shoulders’ seen with the $\text{LiMn}_{0.5}\text{Ni}_{0.5}\text{O}_2$ material (or the LiVO_2) instead the first discharge is defined by 2 processes (indicated by the 2 peaks in the incremental capacity plot) and can be identified by the steeply or gently sloping regions of the first discharge. Neither process is repeated on the second discharge instead being replaced by a single plateau at a voltage mid-way between both first discharge plateaus. The charge and 2nd discharge processes are almost symmetrical with the plateaus of both producing comparable capacity, suggesting that the charging processes is reversible with the second discharge. The first discharge exceeds the theoretical one Li^+ addition reaction of $\text{LiNi}_{0.33}\text{Co}_{0.66}\text{O}_2$ (as does the second to a lesser extent)(~274mAh/g if both metal ions utilise a one electron redox couple or ~180 mAh/g if just the Co^{3+} is active) but the plateau is dissimilar to the ‘runaway’ plateaus of LiMnO_2 and LiCoO_2 .

Given the sloping nature of the first plateau it is possible that the initial sloping ‘pseudo-plateau’ is a consequence of prolonged SEI formation and the latter plateau represents a $\text{LiNi}_{0.33}\text{Co}_{0.66}\text{O}_2$ to $\text{Li}_2\text{Ni}_{0.33}\text{Co}_{0.66}\text{O}_2$ structural conversion or the two electrochemically distinct voltage plateaus may represent distinct cobalt or nickel clusters known to be present within $\text{LiNi}_x\text{Co}_{1-x}\text{O}_2$ systems^{31,32}.

The charging process appears to be a simple monotonic process with only one prominent peak shown in the incremental capacity plot. The same appears to be true for the second discharge, the altered voltage plateau suggesting a new phase is produced on charging which then undergoes lithiation on the second discharge.

The nature of the first discharge process was further investigated by *ex situ* X-ray diffraction patterns as seen in Figure 6.3.8. The diffraction pattern taken at 200mAh/g of discharge revealed the growth of a second phase. The second phase was refined using a $P\bar{3}m1$ space group initially based on the (theoretical) $\text{Li}_2\text{Ni}_{0.5}\text{Co}_{0.5}\text{O}_2$ model produced by Thackeray *et al.*⁵ The model gave a joint refinement fit of $R_{\text{wp}}=7.68\%$ (the majority of the misfit coming from the $\text{LiNi}_{0.33}\text{Co}_{0.66}\text{O}_2$ phase) suggesting that, for the first time, a $\text{Li}_2\text{Ni}_x\text{Co}_{1-x}\text{O}_2$ material has been experimentally observed.

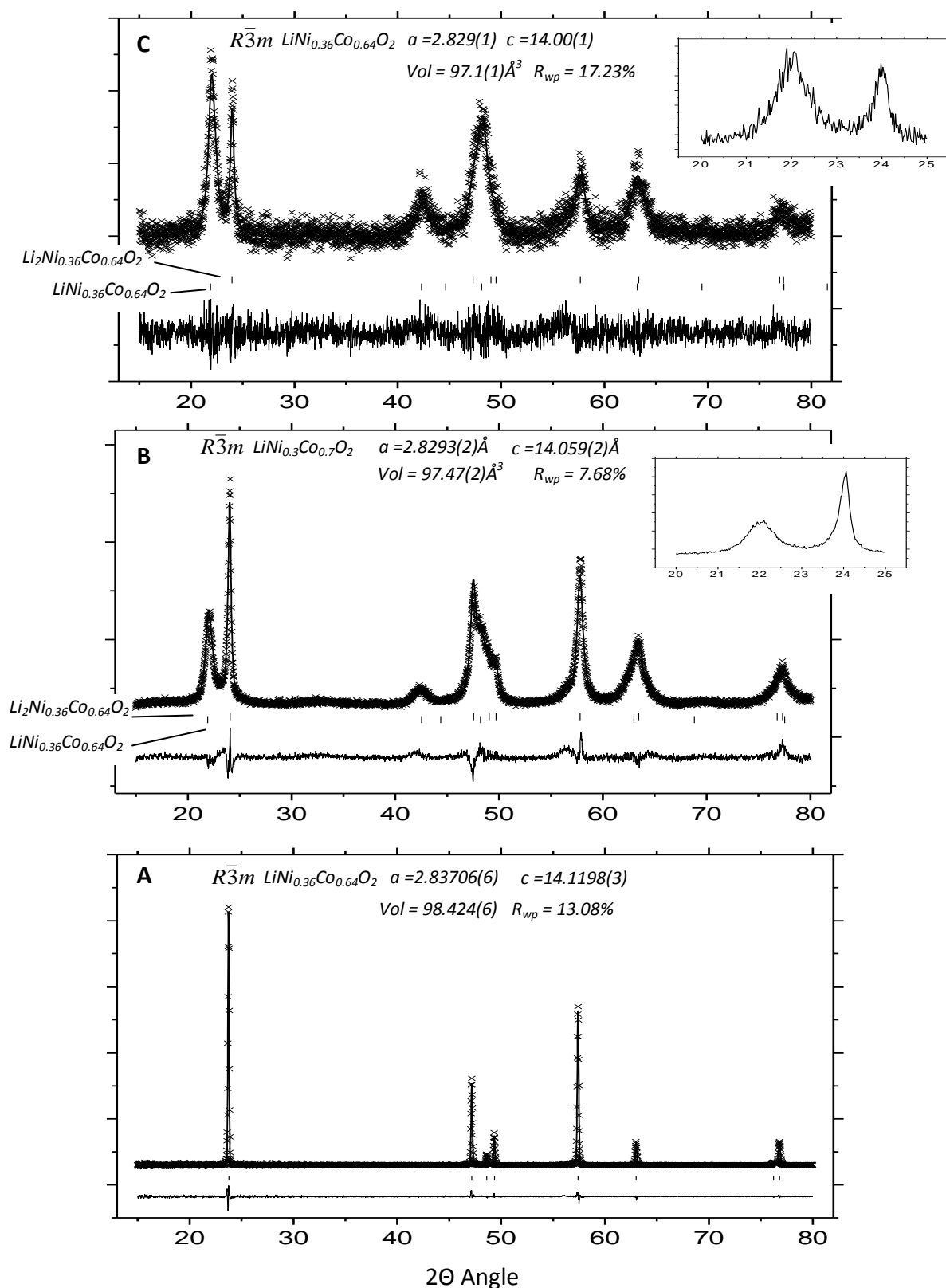


Figure 7.3.8. X-ray diffraction patterns and Rietveld refinement of $\text{LiNi}_{0.5}\text{Co}_{0.5}\text{O}_2$ at different stages of discharge: A) Pristine (nominally) $\text{LiNi}_{0.33}\text{Co}_{0.66}\text{O}_2$ material, B) (nominally) $\text{LiNi}_{0.33}\text{Co}_{0.66}\text{O}_2$ after 200mAh/g of discharge, C) (nominally) $\text{LiNi}_{0.33}\text{Co}_{0.66}\text{O}_2$ material discharged to 1V.

The lattice parameters (displayed in Table 6.3.1) confirm a reasonable unit cell, commensurate with the previous theoretical work on $\text{Li}_2\text{Ni}_{0.5}\text{Co}_{0.5}\text{O}_2$.

Atom	Wyckoff Symbol	x/a	y/b	z/c	B _{iso}	Occupancy
Li1	2d	0.667	0.333	0.351(5)	0.05(1)	1
Co/Ni	1a	0.00	0.00	0.00	0.11(5)	Co0.6/Ni0.4(1)
O1	2d	0.333	0.667	0.243(1)	0.15(3)	1

$$a = 3.1003(6) \text{ } b = 3.1003(6) \text{ } c = 5.1608(9) \text{ } \text{Cell Volume} = 42.96(1)$$

$$\text{Space group: } P\bar{3}m1 \quad R_p = 6.12\% \quad R_{wp} = 7.68\% \quad \chi^2 = 2.202$$

* Values produced from two phase refinement from material recovered at 115mAh/g

$$\begin{array}{c} \text{Phase Ratio} \\ \text{LiNi}_{0.36}\text{Co}_{0.64}\text{O}_2 : \text{Li}_2\text{Ni}_{0.4}\text{Co}_{0.6}\text{O}_2 \\ 0.3 : 0.7 \end{array}$$

Table 7.3.2. Selected Lattice Parameters for $\text{Li}_2\text{Ni}_{0.4}\text{Co}_{0.6}\text{O}_2$.

There is a slight change in transition metal stoichiometry during phase change, possibly due to leaching of the metal ions into the electrolyte as the $R\bar{3}m$ structure shears to form the $P\bar{3}m1$ material- though without more detailed information (from neutron diffraction, for example) it is hard to say whether the change in stoichiometry is a physical property or a refinement artefact.

The refinement taken at the end of discharge (1V) shows that both phases are still present, with a phase ratio of 0.13 ($\text{LiNi}_{0.36}\text{Co}_{0.64}\text{O}_2$):0.87 ($\text{Li}_2\text{Ni}_{0.4}\text{Co}_{0.6}\text{O}_2$) suggesting a continued $\text{LiNi}_{0.64}\text{Co}_{0.36}\text{O}_2$ to $\text{Li}_2\text{Ni}_{0.4}\text{Co}_{0.6}\text{O}_2$ phase change throughout the plateau. The lack of evidence of any other phase (or other material) lends more support to the idea that the first sloping section seen in the galvanostatic profile is SEI formation and the amorphous organo-metallic product is transparent to X-ray diffraction techniques. Indeed it highlights that the preceding voltage ‘shoulders’ are not necessary for

addition type reactions contrary to what the $\text{LiMn}_{0.5}\text{Ni}_{0.5}\text{O}_2$ and LiVO_2 systems may suggest.

As highlighted by the insets in Figure 6.3.8 (2) and (3), $\text{LiNi}_{0.33}\text{Co}_{0.66}\text{O}_2$ material does not undergo the peak splitting (of the (0,0,3) peak) observed in $\text{LiNi}_{0.5}\text{Mn}_{0.5}\text{O}_2$ system which may suggest a subtly different process occurring on over-lithiation, with stacking faults precluded by the different structural chemistries of the $\text{LiMn}_{0.5}\text{Ni}_{0.5}\text{O}_2$ and $\text{LiNi}_{0.33}\text{Co}_{0.66}\text{O}_2$ (it is thought that Jahn-Teller distortion present in $\text{LiNi}_{0.33}\text{Co}_{0.66}\text{O}_2$ means the ‘zigzag’ and ‘striped’ ordering difference theoretical thought to exist in $\text{LiNi}_{0.5}\text{Mn}_{0.5}\text{O}_2$ can’t occur⁵). Unlike the $\text{LiMn}_{0.5}\text{Ni}_{0.5}\text{O}_2$ material there was no impurity observed during $\text{LiNi}_{0.33}\text{Co}_{0.66}\text{O}_2$ discharge suggesting that the nickel/cobalt material may be more stable on longer cycling regimes.

The presence of the previously unreported $\text{Li}_2\text{Ni}_{0.4}\text{Co}_{0.6}\text{O}_2$ phase suggests that the over-lithiation of (nominally) $\text{LiNi}_{0.33}\text{Co}_{0.66}\text{O}_2$ may provide a viable anode system. Certainly the lack of impurities produced on discharge and the more symmetric charge and 2nd discharge galvanostatic profile may make it a more favourable material compared to the nickel/manganese system

A more in-depth study is needed to establish the nature of the charging process and the cause of the change in plateau voltage in the subsequent discharge but the presence of a $\text{Li}_2\text{Ni}_{0.33}\text{Co}_{0.66}\text{O}_2$ phase is an encouraging place to start.

7.3. Conclusions and Further Work

Although only a brief overview, several interesting areas of research have been highlighted for more in-depth study. The effect of over-lithiation of LiCoO_2 was reported using *ex situ* X-ray diffraction. It was found that Li_2O is produced during discharge, strongly suggesting that a dissociation or displacement reaction occurs. The lack of cobalt materials indicated that the extruded cobalt oxide or cobalt metal or transparent to X-rays suggesting either nanoscopic and/or amorphous reaction products. Establishing the nature of the over-lithiation reaction either through small-angle scattering techniques or electron microscopy would go some way towards establishing the nature of the over-lithiation reaction.

The occurrence of the phase change of $\text{LiMn}_{0.5}\text{Ni}_{0.5}\text{O}_2$ to $\text{Li}_2\text{Mn}_{0.5}\text{Ni}_{0.5}\text{O}_2$ was also investigated. It was established that the $\text{LiMn}_{0.5}\text{Ni}_{0.5}\text{O}_2$ systems is similar to the LiVO_2 material in many ways, both consisting of multiple first discharge processes, with the majority of the LiMO_2 to Li_2MO_2 phase change occurring in the first part of the discharge plateau. Unlike LiVO_2 , $\text{LiMn}_{0.5}\text{Ni}_{0.5}\text{O}_2$ undergoes a 2 part charging process, possibly due to the two electron $\text{Mn}^{4+/2+}$ redox couple. The discharge process also indicated that some localised structural rearrangement occurs in the $\text{LiMn}_{0.5}\text{Ni}_{0.5}\text{O}_2$ prior to phase change to $\text{Li}_2\text{Mn}_{0.5}\text{Ni}_{0.5}\text{O}_2$. This may go some-way to explaining the complicated structural conversion from LiMO_2 to Li_2MO_2 . Further study of $\text{LiMn}_{0.5}\text{Ni}_{0.5}\text{O}_2$ may be able to answer several questions applicable to the $\text{LiMO}_2/\text{Li}_2\text{MO}_2$ system as a whole, not least the nature of the lithium insertion process during phase change and the redox environment of the transition metal ion during charge and discharge. To accomplish this, an in-depth neutron diffraction study of materials at different states of discharge/charge (which would also help identify the unknown

impurity) coupled with an *in situ* XPS study would enable better understanding of the system through cycling.

A $\text{LiNi}_x\text{Co}_{1-x}\text{O}_2$ material was shown, for the first time, to undergo an addition type reaction to form a $\text{Li}_2\text{Ni}_x\text{Co}_{1-x}\text{O}_2$ type material at low voltage discharge. The $\text{Li}_2\text{Ni}_{0.4}\text{Co}_{0.6}\text{O}_2$ was identified through *ex situ* X-ray diffraction and found to be structurally analogous to previously reported $\text{Li}_2\text{Ni}_{0.5}\text{Ni}_{0.5}\text{O}_2$ and Li_2VO_2 materials. The nature of the discharge/charge process was found to be subtly different to the $\text{LiMn}_{0.5}\text{Ni}_{0.5}\text{O}_2$ material as there were no voltage ‘shoulders’ upon initial discharge, seemingly replaced by two voltage plateaus, sloping at slightly different gradients.

The incremental capacity plots also showed that charging bore a single electrochemical process, something mimicked by the second discharge process which shifted to a different voltage compared to first discharge. Both factors indicate that the electrochemical nature of the $\text{LiMO}_2/\text{Li}_2\text{MO}_2$ phase change is slightly different for the Ni/Mn and Ni/Co systems. The altered Ni/Co electrochemical behaviour would provide a useful counter-point to the Ni/Mn system and a similarly in-depth structural and redox study of the system would complement the investigation into its $\text{LiNi}_{0.5}\text{Mn}_{0.5}\text{O}_2$ counterpart.

The $\text{LiMO}_2/\text{Li}_2\text{MO}_2$ system may yet provide a useful anode material; certainly the results from this preliminary investigation are promising with several possible Li_2MO_2 systems identified. Much work is needed before a transition metal layered oxide anode would be ready for commercialisation with the most prevalent problem being the understanding of the varied electrochemical behaviour of the LiMO_2 system and the factors that allow it to convert to its Li_2MO_2 analogue.

7.4. References

1. C. S. Johnson, J. Kim, A. Jeremy Kropf, A. J. Kahaian, J. T. Vaughey, and M. M. Thackeray, *Electrochemistry Communications*, 2002, **4**, 492-498.
2. J. Kim, C. S. Johnson, J. T. Vaughey, M. M. Thackeray, S. A. Hackney, W. Yoon, and C. P. Grey, *Chemistry of Materials*, 2004, **16**, 1996-2006.
3. C. S. Johnson, J. Kim, A. J. Kropf, A. J. Kahaian, J. T. Vaughey, L. M. L. Fransson, K. Edstrom, and M. M. Thackeray, *Chemistry of Materials*, 2003, **15**, 2313-2322.
4. J. Vaughey, A. M. Geyer, N. Fackler, C. S. Johnson, K. Edstrom, H. Bryngelsson, R. Benedek, and M. M. Thackeray, *Journal of Power Sources*, 2007, **174**, 1052-1056.
5. R. Benedek, J. Vaughey, and M. M. Thackeray, *Chemistry of Materials*, 2006, **18**, 1296-1302.
6. P. Strobel, J. Levy, and J. Joubert, *Journal of Crystal Growth*, **66**, 257-261.
7. J. R. Dahn, U. von Sacken, and C. A. Michal, *Solid State Ionics*, 1990, **44**, 87-97.
8. I. Davidson, J. Greedan, U. von Sacken, C. Michal, and J. Dahn, *Solid State Ionics*, 1991, **46**, 243-247.
9. G. Vitins, E. A. Raekelboom, M. T. Weller, and J. R. Owen, *Journal of Power Sources*, 2003, **119-121**, 938-942.
10. E. M. L. Chung, G. J. McIntyre, D. M. Paul, G. Balakrishnan, and M. R. Lees, *Phys. Rev. B*, 2003, **68**, 144410.
11. P. Poizot, S. Laruelle, S. Grugeon, and J. Tarascon, *J. Electrochem. Soc.*, 2002, **149**, A1212-A1217.
12. S. A. Needham, G. X. Wang, K. Konstantinov, Y. Tournayre, Z. Lao, and H. K. Liu, *Electrochem. Solid-State Lett.*, 2006, **9**, A315-A319.
13. D. Kramer and G. Ceder, *Chemistry of Materials*, 2009, **21**, 3799-3809.
14. W. David, M. Goodenough, M. Thackeray, and J. Thomas, 1983, **20**.
15. R. Dedryvere, S. Laruelle, S. Grugeon, P. Poizot, D. Gonbeau, and J. Tarascon, *Chemistry of Materials*, 2004, **16**, 1056-1061.
16. M. G. Kim, M. Jo, Y. Hong, and J. Cho, *Chem. Commun. (Camb.)*, 2009, 218-220.
17. H. Arai, S. Okada, Y. Sakurai, and J. Yamaki, *Solid State Ionics*, 1997, **95**, 275-282.
18. H. Ha, K. H. Jeong, and K. Kim, *Journal of Power Sources*, 2006, **161**, 606-611.
19. A. Yamada, M. Tanaka, K. Tanaka, and K. Sekai, *Journal of Power Sources*, 1999, **81-82**, 73-78.
20. M. Thackeray, W. David, P. Bruce, and J. Goodenough, *Materials Research Bulletin*, 1983, **18**, 461-472.
21. I. Nakai, K. Takahashi, Y. Shiraishi, T. Nakagome, and F. Nishikawa, *Journal of Solid State Chemistry*, 1998, **140**, 145-148.
22. Y. Choi, S. Pyun, J. Bae, and S. Moon, *Journal of Power Sources*, 1995, **56**, 25-30.
23. S. B. Park, H. C. Shin, W. Lee, W. I. Cho, and H. Jang, *Journal of Power Sources*, 2008, **180**, 597-601.
24. M. M. Thackeray, M. F. Mansuetto, D. W. Dees, and D. R. Vissers, *Materials Research Bulletin*, 1996, **31**, 133-140.
25. W. David, J. Goodenough, M. M. Thackeray, and M. G. S. R. Thomas, *Revue De Chimie Minerale*, 1983, **20**, 636.
26. J. Kim and H. Chung, *Journal of Power Sources*, 2003, **115**, 125-130.
27. K. M. Kim, J. Kim, N. Park, K. S. Ryu, and S. H. Chang, *Journal of Power Sources*, 2003, **123**, 69-74.
28. T. Ohzuku, A. Ueda, M. Nagayama, Y. Iwakoshi, and H. Komori, *Electrochimica Acta*, 1993, **38**, 1159-1167.
29. Y. Itou and Y. Ukyo, *Journal of Power Sources*, 2005, **146**, 39-44.

30. V. Sethuprakash, W. Basirun, and A. Arof, *Ionics*, 2005, **11**, 406-409.
31. M. Wang and A. Navrotsky, *Solid State Ionics*, 2004, **166**, 167-173.
32. E. Zhecheva, R. Stoyanova, R. Alcántara, P. Lavela, and J. Tirado, *Pure Appl. Chem.*, 2002, **74**, 1885-1894.

Chapter 8. Conclusions and Further Work

Chapter 8: Conclusions and Future Work

Chapter Contents:

8.1. Conclusions.....	218
8.2. $\text{Li}_2\text{CoSiO}_4$.....	218
8.2.1. $\text{Li}_2\text{CoSiO}_4$ Electrode Optimisation	221
8.2.2. $\text{Li}_2\text{CoSiO}_4$ Future Work	223
8.3. LiVO_2.....	224
8.3.1. LiVO_2 Future Work	226
8.4. LiMO_2.....	226
8.4.1. LiMO_2 Future Work	228
8.5. Summary	229
8.6. References	230

8.1. Conclusions.

This thesis has focussed on synthesis and subsequent structural and electrochemical characterisation of novel electrode materials and processes. Three polymorphs of $\text{Li}_2\text{CoSiO}_4$ were produced and a comparison between their structural nature and electrochemical behaviour was undertaken. Further research was initiated in order to improve the electrochemical performance of the material. A novel class of layered LiMO_2 anode was examined, primarily the material LiVO_2 , which, in conjunction with $\text{LiMn}_{0.5}\text{Ni}_{0.5}\text{O}_2$ and $\text{LiNi}_{0.5}\text{Co}_{0.5}\text{O}_2$, was found to undergo lithium addition upon discharge, causing a phase change to a layered Li_2MO_2 structure.

8.2. $\text{Li}_2\text{CoSiO}_4$

The compound $\text{Li}_2\text{CoSiO}_4$ was found to have three easily synthesised phases produced either through solid state or hydrothermal methods, denoted β_I , β_{II} and γ_0 as described previously by West and Glasser¹ (a fourth phase, γ_{II} , reported by West and Glasser could not be realised). The phase was dependent on the synthesis conditions, primarily the final heating stage and it was found that the hydrothermal synthesis produced the most consistent material. Depending on the heating conditions, reheating of the hydrothermally produced β_{II} phase allowed access to phase pure β_I and γ_0 materials.

The phases were structurally characterised via x-ray diffraction and refined using the Rietveld method (the results have subsequently been corroborated with neutron diffraction and a ^7Li NMR study^{2,3}). It was found that, as suggested by previous studies^{1,4,5}, the $\text{Li}_2\text{CoSiO}_4$ polymorphs form structures based around distorted forms of

the classic Li_3PO_4 structure. The hydrothermally produced β_{II} material could be indexed to a $Pmn2_1$ space group. The structure takes the form of rows of offset LiO_4 , $\text{CoO}_4/\text{LiO}_4$ and SiO_4 tetrahedron with mixing in the cobalt/lithium 4a site approximately 50/50. All polyhedra within β_{II} are arranged so that the vertices of the corner sharing tetrahedra point along the c axis. With the disordered lithium/cobalt tetrahedra translating along the a axis and alternating chains of LiO_4 and SiO_4 tetrahedra running in parallel. TEM imaging showed that the hydrothermal synthesis produced roughly spherical particles of β_{II} material, with a diameter of 30 - 100nm.

Electrochemically, it was found that the β_{II} material has a first charge capacity of nearly 210 mAh/g, of which 150mAh/g (0.9 Li) could be assigned to the voltage plateau at 4.2V. The first discharge plateau had a significantly smaller capacity of 40 mAh/g occurring at a voltage of 4.15V. The material suffering a 50mV polarisation between the start of charge and discharge plateaus. Although subsequent *ex situ* Rietveld refinement showed little structural changes after 10 cycles, the performance of the cathode diminished quickly, producing approximately 18mAh/g and 15mAh/g on charge and discharge respectively by the 10th cycle. Unlike what has been reported for the $\text{Li}_2\text{FeSiO}_4$ material⁶⁻⁸ there was no obvious phase change or plateau voltage shift during first discharge.

The β_{I} structure was indexed to a $Pbn2_1$ space group, consisting of alternating layers of polyhedra with their vertices aligned along the c axis. Each layer consists of lines of alternating LiO_4 and SiO_4 , interspaced with lines of the two mixed metal oxide tetrahedra (LiO_4 or CoO_4), propagating along the a axis. There was some cation mixing in the cobalt and one of the lithium sites, with approximately 7% lithium in the cobalt

site and 5% cobalt in the lithium site. The TEM imaging revealed that with reheating of the hydrothermal β_{II} material to form the β_I polymorph large particles were formed with diameters up to $1\mu\text{m}$. The difference between the particulate dimensions of hydrothermally produced parent material is presumably a consequence of crystallite growth during the subsequent heating.

Electrochemically, the β_I material had an initial charging plateau around 4.25V vs. Li^+/Li which produced a capacity of approximately 100 mAh/g. The discharge plateau had an initial voltage of 4.16V and produced a capacity of around 35mAh/g. It was found that the structure underwent a phase change upon cycling, with the initial β_I phase changing to a β_{II} structure during charging. This complicated electrochemical behaviour is perhaps reflected in the cycling performance of the β_I material, as the capacity diminished over a relatively small number of cycles and by the tenth cycle produced only 10mAh/g for both charge and discharge. It is difficult to tell the electrochemical contribution solely from the β_I phase, especially as in later cycles the contributions from both β_I and β_{II} were occluded by polarisation effects.

The γ_0 material was indexed to a $P2_1/n$ space group and consisted of layers along the a,b, plane of LiO_4 , CoO_4 and SiO_4 tetrahedra with their vertices pointing in opposing directions. The structure consists of clusters of 3 edge sharing tetrahedra, with a central tetrahedron accompanied by two tetrahedra facing the opposite direction. Unlike the two β polymorphs there is no site sharing or disorder between the lithium and cobalt ions. As with the β_I material, TEM images showed the particles, formed by reheating of β_{II} material to be up to $1\mu\text{m}$ in diameter.

Electrochemically, the γ_0 phase appeared to be almost inert, producing a total first charge capacity of only 8mAh/g without a distinct voltage plateau. On first discharge there was negligible capacity produced, a situation that did not improve on subsequent cycling. Unsurprisingly, there was no structural change on cycling, presumably due to the limited electrochemistry of the material.

The only polymorph successfully produced through solid state synthesis was the β_I phase, this material had subtle differences compared to its hydrothermally based β_I counterpart. While cation disorder was observed in both the cobalt and one of the lithium sites for β_I material made from reheating hydrothermally prepared material, the solid state β_I polymorph showed cation disorder only within the cobalt site, with approximately 7% lithium occupancy. TEM imaging showed that the solid state material was made up of particles with approximately the same dimensions as the hydrothermally prepared β_I analogue (particle diameters up to 1 μ m).

The electrochemistry of the solid state β_I polymorph was poorer than its hydrothermally based counterpart, producing a first charge capacity of only 40 mAh/g and a first discharge capacity of around 17 mAh/g, both of which diminished with subsequent cycling. Apparently the subtle structural differences between the two polymorphs were enough to instigate the difference in electrochemical behaviour.

8.2.1. $\text{Li}_2\text{CoSiO}_4$ Electrode Optimisation

In an attempt to improve the cycling behaviour of $\text{Li}_2\text{CoSiO}_4$ the effect of mechanical milling and carbon coating upon hydrothermally produced β_{II} , β_I and γ_0

materials was investigated. The materials were structurally and electrochemically characterised to determine the various effects of milling and coating. It was found that, in general, mechanical milling had a negative effect on the cycling performance of the materials, seemingly encouraging spurious side-reactions. The γ_0 material was the only phase that had a noticeable improvement (showing a first charge capacity of 140 mAh/g) but it was unclear whether this was due to the large particle size reduction (1 μ m to 100nm before and after ball-milling respectively) or side reactions enhanced by the increased surface area of the electrode/electrolyte interface. The capacity of the first charge was not maintained on discharge or on subsequent cycles and any benefit was significantly offset by reduction in capacity retention on multiple cycles. This was a problem ubiquitous through all polymorphs, highlighted by the poor performance of the β_{II} and β_I materials.

Carbon coating was successfully undertaken using a procedure that had been employed previously with $\text{Li}_2\text{FeSiO}_4$ materials⁹. The β_{II} polymorph and a formaldehyde/resorcinol xerogel were mixed together, to complete the xerogel graphitisation process, the mixture was then heated and the produced material was a mixture of the β_{II}/β_I material in a 7:1 phase ratio, with approximately 3% carbon by weight. The carbon coated material did not show significant first charge improvement on the previously observed pristine β_{II} material but the electrochemical performance was seen to improve over a limited number of cycles, with approximately 45% of the charging capacity being retained after 10 cycles (compared to around 25% for the pristine material).

8.2.2. $\text{Li}_2\text{CoSiO}_4$ Future Work

While the initial investigation into $\text{Li}_2\text{CoSiO}_4$ materials and subsequent electrode optimisation opened several interesting avenues of potential research, it is crucial that fundamental questions are answered, namely the nature of the disparity between charging and discharging regimes, the poor cycling lifetime of the material and the phase change observed on inserting lithium into the β_1 structure. Numerous techniques could be employed: *in situ* analysis would be possibly the most useful with X-ray/neutron diffraction providing the most precise information of the structural changes occurring with cycling. If this was undertaken in conjunction with *in situ* AC impedance and Infra-red spectroscopy a far more intricate picture would appear of the processes occurring with cycling. Further computational studies of the nature of the structural effects on the Co-O-Si triplet system and this effect on the lithium insertion and removal voltage would provide valuable information about the behaviour of the different phases under cycling. This may point to suitable adjustments to the structures or electronic nature of the materials that could be made with doping of the silicon site or indeed introducing solid solutions of cobalt, iron and manganese materials, which would add a useful versatility to the silicate polyanion class of cathodes. Investigation of further optimisation techniques such as utilising different conductive coating techniques which do not require such vigorous preparation conditions may allow the preservation of the pure β_{11} , β_1 and γ_0 phases after coating as well as potentially further improving the long term cycle performance of the materials.

Much work is needed to develop the $\text{Li}_2\text{CoSiO}_4$ materials, but the versatile polyanion structure and the varied electrochemistry they exhibit ensure that it would be a worthwhile venture, allowing greater understanding of the burgeoning class of

lithium silicate polyanion cathode materials and perhaps producing useful, viable cathode materials in the future.

8.3. LiVO_2

Various $\text{Li}_{1+x}\text{V}_{1-x}\text{O}_2$ materials (where $x=0$ to 0.2) were produced through solid state synthesis and were structurally characterised using X-ray diffraction and subsequent Rietveld refinement. The electrochemical behaviour of the system was studied through galvanostatic methods as well as *in situ* AC impedance and X-ray diffraction patterns taken at different lithium compositions during discharge.

The electrochemical behaviour of LiVO_2 was found to be heavily dependent on the amount of doped lithium present. The stoichiometric material had a very poor discharge capacity and showed no evidence of a plateau, whereas the lithium doped material showed a voltage plateau at approximately 0.1V vs. Li^+/Li . The capacity varied with doping amount, highlighting a complicated relationship between discharge capacity and amount of lithium doping. It was found that the 8% lithium doped material showing the highest capacity of around 310mAh/g for the initial discharge. This was in excess of the theoretical capacity (298mAh/g) but a large irreversible capacity was observed on the first discharge which was not present on subsequent charge and discharge cycles.

Combining the structural and electrochemical analysis taken throughout the discharge of $\text{Li}_{1.08}\text{V}_{0.92}\text{O}_2$ a self consistent picture begins to emerge. There were three

clear stages during discharge; from 0-70mAh/g of capacity, from 70-180mAh/g and from 180-310mAh/g.

The region from 0-70mAh/g is characterised by sloping voltage shoulders in the galvanostatic profile. The *ex situ* X-ray diffraction study showed little structural changes during this region and combined with the *in situ* AC impedance and polarisation resistance data (and previous studies) it is suggested that this represents a region of extended SEI growth. Between 70-180mAh/g a new Li_2VO_2 phase was observed in the X-ray diffraction patterns, and a voltage plateau was observed in the galvanostatic profile. Relatively little change was observed in the charge transfer resistance seen in the AC impedance measurements.

After 180mAh/g of capacity had passed the X-ray diffraction patterns showed relatively little new growth of the Li_2VO_2 material, which contrasts with the galvanostatic profile which displays little change to the voltage plateau (the process responsible for the plateau assumed to be the LiVO_2 to Li_2VO_2 phase change). The charge transfer resistance was seen to undergo a change corresponding to the altered structural behaviour, which suggests the presence of a distinct electrochemical process after 180mAh/g, the nature of which could be from the $\text{LiVO}_2/\text{Li}_2\text{VO}_2$ material itself or an external process, possibly lithium deposition.

Extensive computer modelling, undertaken by the Islam group at Bath University in conjunction with the work of this thesis suggested that the doping dependence of $\text{Li}_{1+x}\text{V}_{1-x}\text{O}_2$ was a consequence of the extra lithium presence in the vanadium layer in LiVO_2 . Due to the presence of a small amount of octahedral lithium in the vanadium layer the energy penalty of tetrahedral lithium insertion in the

adjacent lithium layer (required to convert to Li_2VO_2 structure) was considerably reduced allowing lithium to be inserted at a voltage that is high enough to avoid the dominating effects of lithium deposition (i.e. greater than 0V vs. Li^+/Li).

8.3.1. LiVO_2 Future Work

Further characterisation is required in order to fully understand the complicated processes present with lithium insertion into LiVO_2 materials, especially with respect to the SEI formation process at the beginning of discharge and the drop off in LiVO_2 to Li_2VO_2 phase conversion mid way through the voltage plateau. The incorporation of further *in situ* techniques such as Raman and NMR may help to answer some of the questions raised by the discharge behaviour. The poor capacity retention on repeated cycling should also be investigated and research into the nature of lithium doping in the 3a vanadium site upon repeated discharge and charge cycles may suggest useful avenues to follow when trying to improve the cycle lifetime.

8.4. LiMO_2

Several transition metal oxide (LiMO_2) systems were investigated for their ability to convert to layered Li_2MO_2 materials upon over-lithiation ($> 1\text{Li}^+$ per unit cell). A preliminary investigation concerning the structural nature of the LiCoO_2 , $\text{LiMn}_{0.5}\text{Ni}_{0.5}\text{O}_2$ and $\text{LiNi}_{0.33}\text{Co}_{0.66}\text{O}_2$ systems during electrochemical discharge was undertaken.

The voltage plateau for the over-lithiation process of LiCoO_2 occurred at 1.25V and had a first discharge capacity of almost 550mAh/g the charging process showed no

corresponding voltage plateau. On subsequent discharge a similar voltage plateau evolved at around 1.2V but only produced around 300 mAh/g of capacity. Through ex situ X-ray diffraction it was established that LiCoO_2 did not convert to Li_2CoO_2 when cycled. The presence of Li_2O , seen in x-ray diffraction patterns of cycled material strongly suggested a 'dissociation' or 'displacement' type reaction, most likely producing a combination of amorphous cobalt metal and cobalt oxide products along with Li_2O .

$\text{LiMn}_{0.5}\text{Ni}_{0.5}\text{O}_2$ underwent a Li 'addition' type reaction to form $\text{Li}_2\text{Mn}_{0.5}\text{Ni}_{0.5}\text{O}_2$, as suggested by the previous work of Thackeray¹⁰⁻¹³. Upon initial discharge $\text{LiMn}_{0.5}\text{Ni}_{0.5}\text{O}_2$ was seen to undergo a similar process to LiVO_2 with multiple sloping voltage shoulders until a voltage plateau was reached around 1V with the initial discharge producing around 300mAh/g capacity. On charge it was observed that there were two distinct electrochemical processes compared to the monotonous discharge process. It is possible that this reflects multiple redox couples active at different states of charge. X-ray diffraction confirmed the presence of $\text{Li}_2\text{Mn}_{0.5}\text{Ni}_{0.5}\text{O}_2$ on discharge, which was seen to be the dominant phase by the end of discharge. Local structural rearrangement was also observed for the $\text{LiMn}_{0.5}\text{Ni}_{0.5}\text{O}_2$ material during first discharge.

For the first time a $\text{Li}_2\text{Ni}_x\text{Co}_{1-x}\text{O}_2$ ($0 < x < 1$) material was been observed. It was found that on over-lithiation the material $\text{LiNi}_{0.33}\text{Co}_{0.66}\text{O}_2$ was seen to convert to $\text{Li}_2\text{Ni}_{0.4}\text{Co}_{0.6}\text{O}_2$. The $\text{LiNi}_{0.33}\text{Co}_{0.66}\text{O}_2$ material had different first discharge behaviour to its LiVO_2 and $\text{LiMn}_{0.5}\text{Ni}_{0.5}\text{O}_2$ counter parts, with no sloping voltage shoulders observed. Instead a sloping voltage pseudo-plateau was observed beginning at 1.4V and finishing after approximately 450mAh/g of capacity had passed near 1V. There was still the

familiar irreversible capacity of first discharge, with the subsequent discharge achieving approximately 300mAh/g of capacity. Unlike its Mn/Ni counterpart, the $\text{LiNi}_{0.33}\text{Co}_{0.66}\text{O}_2$ seemingly utilised the same redox couple during both discharge and charge. The *ex situ* X-ray diffraction study showed the presence of a $\text{Li}_2\text{Ni}_{0.4}\text{Co}_{0.6}\text{O}_2$ phase during discharge, and the material was seen not to undergo the peak splitting seen previously in the $\text{LiMn}_{0.5}\text{Ni}_{0.5}\text{O}_2$ material on conversion to $\text{Li}_2\text{Mn}_{0.5}\text{Ni}_{0.5}\text{O}_2$.

8.4.1. LiMO_2 Future Work

The variation in electrochemical and structural behaviour of the LiMO_2 materials certainly merits closer inspection. Further identification of similar systems that will and will not undergo ‘addition’ type reactions would better inform about the complicated processes that determine the reactions of layered transition metal oxides on over lithiation. The structural changes that occur during LiMO_2 to Li_2MO_2 phase conversion require further research and an in-depth investigation, akin to the LiVO_2 research, into the behaviour of the $\text{LiMn}_x\text{Ni}_{1-x}\text{O}_2$ and $\text{LiCo}_x\text{Ni}_{1-x}\text{O}_2$ system would answer questions about the process of over lithiation. It may also be pertinent to investigate the lithium doping effect on the layered transition metal oxide anodes and whether this has an effect on the addition/displacement/dissociation reaction pathway selection.

8.5. Summary

The aim of this thesis was to undertake original research into novel lithium host materials. This investigation centred around two areas, namely the cathode material $\text{Li}_2\text{CoSiO}_4$ and the LiMO_2 class of anode. The behaviour of both types of material upon electrochemical lithium insertion and removal were explored, using structural and electrochemical characterisation to understand the nature of the processes occurring within the materials undergoing electrochemical cycling. The research successfully highlighted several viable materials for lithium host electrodes that could be utilised in lithium-ion battery systems and identified numerous interesting avenues for further investigation.

Energy storage technology is constantly evolving to meet new social, economic and environmental pressures facing modern society. There is an urgent need to provide innovative, novel and versatile solutions to the problem of on demand power production. Much research is still needed, even at a fundamental level, to bring energy storage technology to maturity and it is hoped that the work of this thesis can be used to inform future research of lithium host materials and eventually be used to help bring about an improvement in the increasingly vital field of energy storage.

8.6. References

1. A. R. West and F. P. Glasser, *Journal of Solid State Chemistry*, 1972, **4**, 20-28.
2. , and P. G. Bruce, *Chemistry of Materials*, 2010, **22**, 1892-1900.
3. C. Lyness, B. Delobel, A. R. Armstrong, and P. G. Bruce, *Chem. Commun.*, 2007, 4890-4892.
4. M. E. Villafuerte-Castrejon and A. R. West, *J. Chem. Soc., Faraday Trans. 1:*, 1979, **75**, 374-384.
5. M. E. Villafuerte-Castrejon and A. R. West, *J. Chem. Soc., Faraday Trans. 1:*, 1981, **77**, 2297-2307.
6. A. Nytén, A. Abouimrane, M. Armand, T. Gustafsson, and J. O. Thomas, *Electrochemistry Communications*, 2005, **7**, 156-160.
7. A. Nyten, M. Stjerndahl, H. Rensmo, H. Siegbahn, M. Armand, T. Gustafsson, K. Edstrom, and J. O. Thomas, *J. Mater. Chem.*, 2006, **16**, 3483-3488.
8. P. Larsson, R. Ahuja, A. Nytén, and J. O. Thomas, *Electrochemistry Communications*, 2006, **8**, 797-800.
9. A. Nytén, A. Abouimrane, M. Armand, T. Gustafsson, and J. O. Thomas, *Electrochemistry Communications*, 2005, **7**, 156-160.
10. C. S. Johnson, J. Kim, A. J. Kropf, A. J. Kahaian, J. T. Vaughey, L. M. L. Fransson, K. Edstrom, and M. M. Thackeray, *Chemistry of Materials*, 2003, **15**, 2313-2322.
11. J. Vaughey, A. M. Geyer, N. Fackler, C. S. Johnson, K. Edstrom, H. Bryngelsson, R. Benedek, and M. M. Thackeray, *Journal of Power Sources*, 2007, **174**, 1052-1056.
12. C. S. Johnson, J. Kim, A. Jeremy Kropf, A. J. Kahaian, J. T. Vaughey, and M. M. Thackeray, *Electrochemistry Communications*, 2002, **4**, 492-498.
13. R. Benedek, J. Vaughey, and M. M. Thackeray, *Chemistry of Materials*, 2006, **18**, 1296-1302.

Appendix i

Published Paper:

The Lithium Intercalation Compound $\text{Li}_2\text{CoSiO}_4$ and Its Behaviour as a Positive Electrode for
Lithium Batteries.

C Lyness, B Delobel, AR Armstrong, PG Bruce - Chemical Communications, 2007, 4892

The lithium intercalation compound $\text{Li}_2\text{CoSiO}_4$ and its behaviour as a positive electrode for lithium batteries†

Christopher Lyness, Bruno Delobel,‡ A. Robert Armstrong and Peter G. Bruce*

Received (in Cambridge, UK) 30th July 2007, Accepted 11th September 2007

First published as an Advance Article on the web 24th September 2007

DOI: 10.1039/b711552k

The electrochemical behaviour of 3 polymorphs of the lithium intercalation compound $\text{Li}_2\text{CoSiO}_4$, β_{I} , β_{II} and γ_0 , as positive electrodes in rechargeable lithium batteries is investigated for the first time.

The layered Li intercalation compound, LiCoO_2 , is used as the cathode in the majority of commercial rechargeable lithium-ion batteries.^{1,2} Alternative compounds, such as LiNiO_2 or LiMnO_2 have also been considered; their solid solutions, e.g. $\text{Li}(\text{Co}_{1/3}\text{Mn}_{1/3}\text{Ni}_{1/3})\text{O}_2$ are used in the latest commercial products.^{3–5} Recognition that compounds based on the phosphate anion, such as the olivine LiFePO_4 , could act as lithium intercalation hosts, and could operate as cathodes in rechargeable lithium batteries, represented a significant breakthrough.⁶ Bonding of the oxygen to the phosphorus stabilises the former with respect to evolution from the structure, an important problem on charging simple transition metal oxides. Recently, an entirely new class of lithium intercalation compounds based on silicates, Li_2MSiO_4 , where $\text{M} = \text{Fe}, \text{Mn}$, has been described.⁷ Of these the most studied is $\text{Li}_2\text{FeSiO}_4$, it has been shown that at 60 °C 165 mA h g^{−1} of charge may be extracted, corresponding to one lithium per formula unit; with reversible lithium cycling over the range $\text{Li}_x\text{FeSiO}_4$, $1.15 < x < 2$, corresponding to 140 mA h g^{−1} when suitably carbon coated and with a particle size of 150 nm.^{7a} Si doped LiCoO_2 gave $\text{Li}_2\text{CoSiO}_4$ as an impurity with enhanced electrochemical properties but behaviour of the pure phase was not reported.⁸ Here we present the first preliminary report on the electrochemistry of three polymorphs of the compound $\text{Li}_2\text{CoSiO}_4$.§

The Li_2MSiO_4 compounds ($\text{M} = \text{Fe}, \text{Mn}, \text{Co}$) belong to a family of materials known as the tetrahedral structures.⁹ They are composed of tetragonally packed oxide ions (a distorted form of hexagonal close packing) within which half the tetrahedral sites are occupied by cations such that face sharing between the pairs of tetrahedral sites is avoided.¹⁰ The tetrahedral structures exhibit a rich polymorphism, with more than eight polymorphs known. They may be divided into two families, designated β and γ . In the case of the former all the tetrahedra point in the same direction, perpendicular to the close-packed planes, and share only corners with each other, whereas, in the case of the γ polymorphs, the

tetrahedra are arranged in groups of three with the central tetrahedron pointing in the opposite direction to the outer two, with which it shares edges, Fig. 1. Where both β and γ polymorphs exist for a given compound the latter is stable at higher temperatures, with the β to γ transformation involving inversion of half the tetrahedral sites.¹¹ Several variants of both β and γ exist, involving either ordering or distortions of the parent structures, they are designated β_{I} , γ_0 , γ_{II} , etc. In many cases these phases may be quenched to room temperature, where they exhibit long-term stability. Originally the different polymorphs were distinguished only on the basis of differences in their powder X-ray diffraction patterns.^{9a} More recently, the complete crystal structures of a few isolated examples have been solved.¹²

$\text{Li}_2\text{CoSiO}_4$ compounds were synthesised by initial hydrothermal reaction which produces the β_{II} polymorph. The β_{I} form was obtained by heating the β_{II} phase in air to 700 °C for 2 h. The γ_0 phase was formed by heating the β_{II} polymorph to 1100 °C for 2 h, then lowering the temperature to 850 °C whereupon the material was quenched to room temperature. Powder X-ray diffraction patterns of as-prepared $\text{Li}_2\text{CoSiO}_4$, and those heated to 700 and 1100 °C are presented in Fig. 2 (Stoe STADI/P diffractometer, $\text{Fe-K}\alpha_1$). They correspond to the three polymorphs β_{II} , β_{I} and γ_0 , respectively. Their structures have been refined by the Rietveld method (TOPAS).¹³ Full details are beyond the scope of this communication but will be reported later. The structures of β_{II} , β_{I} and γ_0 are shown in Fig. 1.

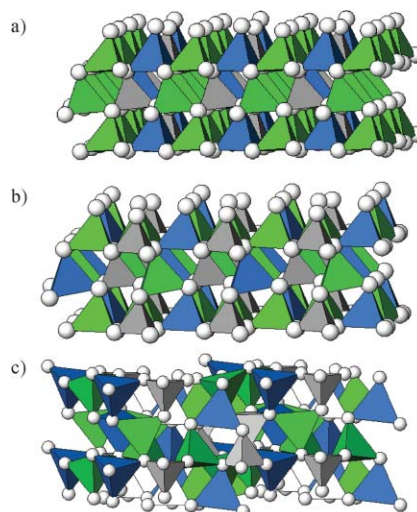


Fig. 1 Crystal structures of three tetrahedral polymorphs of Li_2MXO_4 : (a) β_{II} , (b) β_{I} , (c) γ_0 . Grey tetrahedra: XO_4 , blue: MO_4 , green: LiO_4 .

EaStChem, School of Chemistry, University of St. Andrews, North Haugh, St. Andrews, Fife, UK KY16 9ST.

E-mail: p.g.bruce@st-andrews.ac.uk; Fax: +44 1334 463808; Tel: +44 1334 463825

† Electronic supplementary information (ESI) available: TEM images of composite cathodes. Comparison of powder X-ray diffraction patterns for as-prepared and ball-milled β_{I} , β_{II} and γ_0 $\text{Li}_2\text{CoSiO}_4$. See DOI: 10.1039/b711552k

‡ Present address: LRCS, Université Picardie Jules Verne, 33 Rue Saint-Leu, 80039 Amiens, France.

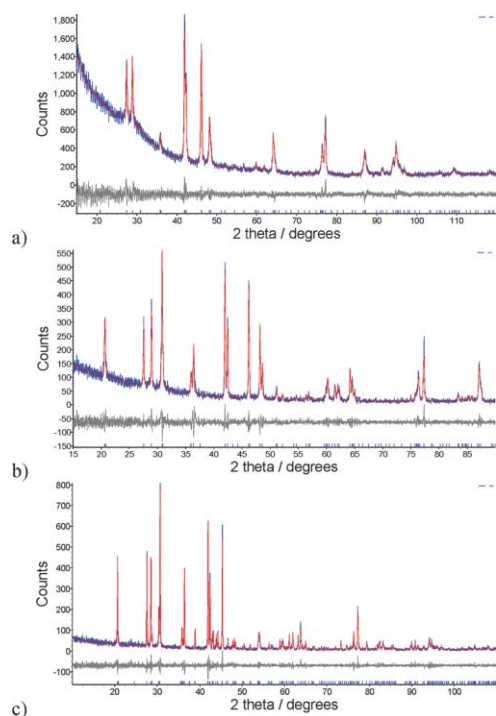


Fig. 2 Fitted powder X-ray diffraction data for the three $\text{Li}_2\text{CoSiO}_4$ polymorphs: (a) β_{II} , (b) β_{I} , (c) γ_0 .

The electrochemistry of all three polymorphs was investigated by forming composite electrodes as described in the notes. The capacity to extract lithium from the three polymorphs, even when charged slowly to 4.6 V, was very low. Each polymorph was mixed with Super P carbon in the ratio 8 : 2 and ball-milled (SPEX Centri-Prep 8000 M mixer/mill) for 1 h. TEM data collected after ball-milling (Jeol JEM-2011) indicated particle sizes of 50–100 nm for all three polymorphs and powder X-ray diffraction data showed peak-broadening compared with the as-prepared materials (see ESI†). Analysis of the peak widths using the Scherrer formula revealed domain sizes of 10–40 nm. These are smaller than the particle sizes observed by TEM demonstrating that ball-milling introduces a domain structure/strain within the grains.

Ball-milling significantly improves the electrochemical response. Cells fabricated from the ball-milled polymorphs were subjected to charge and discharge at 50 °C, a typical temperature used for other Li_2MSiO_4 materials, Fig. 3.⁷ The ball-milled β_{II} phase exhibits a gentle increase in potential on the first charge, corresponding to extraction of 180 mA h g^{-1} (equivalent to 1.1 Li per formula unit). Lithium removal is accompanied by oxidation of the tetrahedral Co^{2+} to Co^{3+} . The first discharge capacity is much smaller at

around 30 mA h g^{-1} . Subsequent cycling leads to further capacity fade, such that after 10 cycles the cell capacity is negligible. Turning to the β_{I} polymorph, cycled under the same conditions, the shape of the first charge curve is similar, although with some additional structure evident. The first charge capacity is significantly lower at only 80 mA h g^{-1} . The discharge capacity on the first cycle was again around 30 mA h g^{-1} , although by virtue of the lower charge capacity the efficiency had improved from 14% for β_{II} to 38% for β_{I} . Again after 10 cycles the capacity of the β_{I} polymorph was negligible, Fig. 3(b). The γ_0 polymorph also exhibits a slow potential rise on the first charge corresponding to a capacity of 100 mA h g^{-1} and around 30 mA h g^{-1} on discharge, again with negligible capacity after 10 cycles.

Although the load curves in Fig. 3, despite a low rate of 10 mA g^{-1} , may still be somewhat influenced by kinetics, it is interesting to note that the charge and discharge potentials are all similar, suggesting that the structural differences in the three polymorphs are not sufficient to induce major changes in the Li^+ and e^- chemical potentials. Also the values are in broad agreement with those predicted by DFT + U calculations for $\text{Li}_2\text{CoSiO}_4$ (4.4 V).^{7,de} They are higher than $\text{Li}_2\text{FeSiO}_4$ (~3 V) and $\text{Li}_2\text{MnSiO}_4$ (~4.2 V).

Although ball-milling aids the distribution of carbon within the composite electrode, carbon coating the particles would further improve the efficiency of the “wiring”, as has been demonstrated for LiFePO_4 .¹⁴ It is necessary to pyrolyse the carbon precursors above 650 °C to form sufficient sp^2 linkages to promote good electron transport. All our attempts to carbon coat the ball-milled polymorphs using a variety of precursors *e.g.* sucrose, resulted in reduction of $\text{Li}_2\text{CoSiO}_4$ and the production of Co metal and Li_2SiO_3 , as demonstrated by powder XRD. However, in the case of the β_{I} polymorph, we were able to coat the as-prepared particles with carbon without such reduction occurring. The difference may reflect the greater reactivity of the particle surfaces formed during ball-milling, making them more susceptible to reduction. Success so far has been restricted to the β_{I} polymorph because heating the β_{II} polymorph at high enough temperatures to induce a conductive carbon coat results in conversion to β_{I} . In the case of the γ_0 phase, to date it has proved impossible to quench the sample sufficiently rapidly in an inert atmosphere to form a single γ_0 phase.

The “wiring” of $\beta_{\text{I}}\text{-Li}_2\text{CoSiO}_4$ was achieved using the resorcinol-formaldehyde approach.¹⁵ Hydrothermally prepared $\text{Li}_2\text{CoSiO}_4$ was mixed with 15 wt% of dried carbon-gel (pre-pyrolysis xerogel) and heated to 700 °C under flowing argon for 2 h. Electrochemical results for composite electrodes fabricated using the β_{I} /carbon composite are shown in Fig. 4. A well defined plateau is observed at around 4.25 V on the first charge. Despite the higher polarisation at the start of charging compared with the ball-milled material, a

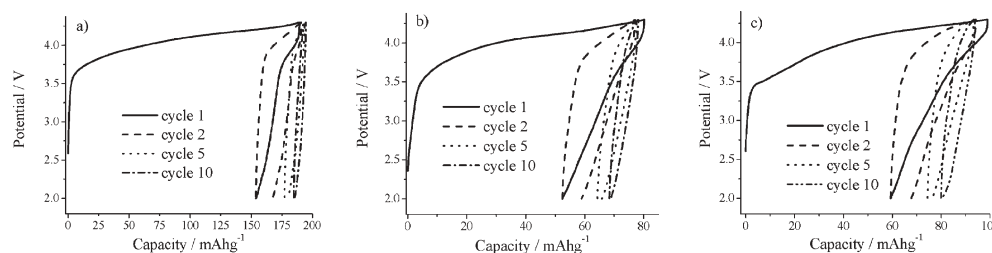


Fig. 3 Variation of voltage with state of charge (Li content) on cycling the three $\text{Li}_2\text{CoSiO}_4$ polymorphs at a rate of 10 mA g^{-1} : (a) β_{II} , (b) β_{I} , (c) γ_0 .

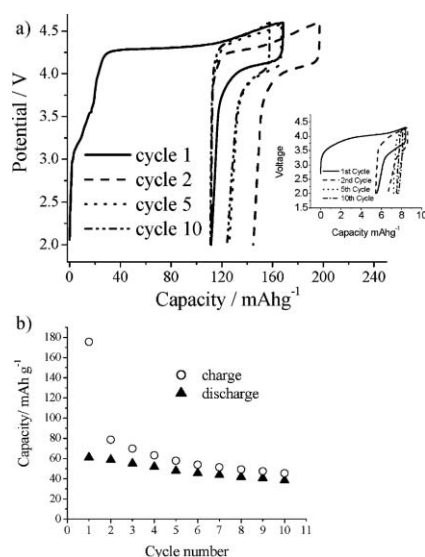


Fig. 4 (a) Variation of voltage with state of charge (Li content) on cycling the β_I $\text{Li}_2\text{CoSiO}_4$ polymorph carbon coated by the xerogel process at a rate of 10 mA g^{-1} . Inset shows performance of uncoated material. (b) Variation of discharge capacity with cycle number for the carbon-coated β_I $\text{Li}_2\text{CoSiO}_4$ polymorph cycled between 2.0 and 4.6 V at 10 mA g^{-1} .

higher capacity of 95 mA h g^{-1} is obtained to the same 4.3 V cut-off, compared with 80 mA h g^{-1} for the ball-milled material. This highlights the effectiveness of the carbon coat in “wiring” the electrode and hence the crucial role of electron transport to the particles on the electrochemical performance. This is reinforced on recalling that the bulk particles, without carbon “wiring” demonstrated almost no electrochemical activity (see inset, Fig. 4). By extending the voltage cut-off to 4.6 V, 170 mA h g^{-1} , corresponding to 1.1 Li per formula unit, could be extracted. The first discharge capacity was also improved (60 mA h g^{-1}) compared with the as-prepared or the ball-milled materials. As is evident in Fig. 4(b) capacity retention is better than for any of the as-prepared or ball-milled materials, with a capacity of 40 mA h g^{-1} observed after 10 cycles. The previous theoretical study suggested extraction of the second Li (associated with the $\text{Co}^{3+/4+}$ couple) would occur at $\sim 5 \text{ V}$, above the stability of the electrolyte and in agreement with the results here (*i.e.* only 1 Li extracted to 4.6 V).^{7d}

In conclusion, the first preliminary results concerning the electrochemical performance of any $\text{Li}_2\text{CoSiO}_4$ materials with, attention focusing on the β_I , β_{II} and γ_0 polymorphs, have all been presented. three exhibit electrochemical activity when ball-milled, although with severe capacity fading after a few cycles. In the case of the β_I polymorph coating the as-prepared material with carbon switches on electrochemistry without the need for ball-milling and gives superior charge capacity ($170 \text{ mA h g}^{-1} \equiv 1.1 \text{ Li per formula unit}$) and cyclability, compared with the same phase when ball-milled with carbon. Only one Li could be extracted up to 4.6 V in agreement with theoretical predictions. For all polymorphs there is a significant difference between the first charge and subsequent cycling. Usually this is indicative of structural changes. Further work on these materials is underway, including investigating any such structural changes. This study has concentrated on the pure $\text{Li}_2\text{CoSiO}_4$ polymorphs, a necessary prelude to studying solid solutions of Li_2MSiO_4 , $M = \text{Fe, Mn, Co}$. It will be interesting to

see whether the performance of such solid solutions proves superior to the pure phases as observed in the case of the LiMO_2 cathodes *e.g.* $\text{Li}(\text{Co}_{1/3}\text{Mn}_{1/3}\text{Ni}_{1/3})\text{O}_2$ and therefore of technological significance.

P. G. B. is indebted to the EPSRC and the EU for financial support

Notes and references

§ *Hydrothermal synthesis of $\text{Li}_2\text{CoSiO}_4$* : 0.05 mol. $\text{LiOH}\cdot\text{H}_2\text{O}$ (Aldrich), was added to 0.0125 mol SiO_2 (Aldrich) in 20 ml of distilled water and stirred. 0.0125 mol CoCl_2 (Aldrich) was added to 10 ml of ethylene glycol and stirred under gentle heat until dissolution occurred. The two solutions were then mixed with stirring and the slurry transferred to a 40 ml Teflon-lined autoclave. The remaining volume was topped up with distilled water. The sealed autoclave was heated at 150°C for 72 h. The product was filtered off and dried at 60°C overnight.

Composite electrodes consisted of the active material, super P carbon and Kynar Flex 2801 (a co-polymer based on PVDF) binder in the ratio 75 : 18 : 7. Electrochemical cells consisted of the $\text{Li}_2\text{CoSiO}_4$ composite electrode, a lithium metal counter electrode and the electrolyte, a 1 molal solution of LiPF_6 in ethylene carbonate–dimethyl carbonate 1 : 1 (v/v) (Merck). All cells were constructed and handled in an Ar filled MBraun glovebox. Electrochemical measurements were carried out at 30°C using a Maccor Series 4200 battery cyclor.

- K. Mizushima, P. C. Jones, P. J. Wiseman and J. B. Goodenough, *Mater. Res. Bull.*, 1980, **15**, 783.
- T. Nagaura, Paper presented at 4th Int. Rechargeable Battery Seminar, Deerfield Beach, FL, 1990; T. Nagaura and K. Tozawa, *Prog. Batteries Sol. Cells*, 1990, **9**, 209.
- (a) W. Li, J. N. Reimers and J. R. Dahn, *Solid State Ionics*, 1993, **67**, 123; (b) A. Rougier, P. Gravereau and C. Delmas, *J. Electrochem. Soc.*, 1996, **143**, 1168.
- A. R. Armstrong and P. G. Bruce, *Nature*, 1996, **381**, 499.
- (a) N. Yabuuchi and T. Ohzuku, *J. Power Sources*, 2003, **119–121**, 171; (b) S. Jouanneau, K. W. Eberman, L. J. Krause and J. R. Dahn, *J. Electrochem. Soc.*, 2005, **150**, A1637.
- (a) A. K. Padhi, K. S. Nanjundaswamy and J. B. Goodenough, *J. Electrochem. Soc.*, 1997, **144**, 1188; (b) A. K. Padhi, K. S. Nanjundaswamy, C. Masquelier, S. Okada and J. B. Goodenough, *J. Electrochem. Soc.*, 1997, **144**, 1609; (c) A. Yamada, S. C. Chung and K. Hinokuma, *J. Electrochem. Soc.*, 2001, **148**, A224; (d) S. Y. Chung, J. T. Bloking and Y. M. Chiang, *Nat. Mater.*, 2002, **1**, 123; (e) P. S. Herle, B. Ellis, N. Coombs and L. F. Nazar, *Nat. Mater.*, 2004, **3**, 147.
- (a) A. Nytén, A. Abouimrane, M. Armand, T. Gustafsson and J. O. Thomas, *Electrochem. Commun.*, 2005, **7**, 156; (b) R. Dominko, M. Bele, M. Gaberscek, A. Meden, M. Remskar and J. Jamnik, *Electrochem. Commun.*, 2006, **8**, 217; (c) Z. L. Gong, Y. X. Li and Y. Yang, *Electrochem. Solid-State Lett.*, 2006, **9**, A542; (d) M. E. Arroyo de Dompablo, M. Armand, J. M. Tarascon and U. Amador, *Electrochem. Commun.*, 2006, **8**, 1292; (e) S. Q. Wu, J. H. Zhang, Z. Z. Zhu and Y. Yang, *Curr. Appl. Phys.*, 2007, **7**, 611; (f) C. Masquelier, G. Quoirin, L. Dupont and F. Taulelle, *Proceedings of International Meeting on Lithium Batteries*, Biarritz, 2006.
- (a) Y. Jin, P. Lin and C. H. Chen, *Solid State Ionics*, 2006, **177**, 317; (b) Y. Yu, J. L. Shui, Y. Jin and C. H. Chen, *Electrochim. Acta*, 2006, **51**, 3292.
- (a) A. R. West and F. P. Glasser, *J. Solid State Chem.*, 1972, **4**, 20; (b) P. Tarte and R. Cahay, *C. R. Acad. Sci. Paris C*, 1970, **271**, 777.
- P. G. Bruce and A. R. West, *Acta Crystallogr., Sect. B*, 1982, **38**, 1891.
- A. R. West, *Z. Kristallogr.*, 1975, **111**, 422.
- (a) H. Yamaguchi, K. Akatsuka, M. Setoguchi and Y. Takaki, *Acta Crystallogr., Sect. B*, 1979, **35**, 2680; (b) V. V. Politaev, A. A. Petrenko, V. B. Nalbandyan, B. S. Medvedev and E. S. Shvetsova, *J. Solid State Chem.*, 2007, **180**, 1045; (c) C. Jousseau, A. Kahn-Harari, D. Vivien, J. Derouet, F. Ribot and F. Villain, *J. Mater. Chem.*, 2002, **12**, 1525; (d) C. Riekel, *Acta Crystallogr., Sect. B*, 1977, **33**, 2656.
- A. A. Coelho, *J. Appl. Crystallogr.*, 2000, **33**, 899.
- (a) N. Ravet, Y. Chouinard, J. F. Magnan, S. Besner, M. Gauthier and M. Armand, *J. Power Sources*, 2001, **97–98**, 503; (b) H. Huang, S. C. Yin and L. F. Nazar, *Electrochem. Solid-State Lett.*, 2001, **4**, A170.
- S. A. Al-Muhtaseb and J. A. Ritter, *Adv. Mater.*, 2003, **15**, 101.

Appendix ii

Published Paper:

Structural Polymorphism in $\text{Li}_2\text{CoSiO}_4$ Intercalation Electrodes: A Combined Diffraction and
NMR Study

AR Armstrong, C Lyness, M Menetrier, PG Bruce – Chemistry of Materials, 2010, 22 (5), 1892

Structural Polymorphism in $\text{Li}_2\text{CoSiO}_4$ Intercalation Electrodes: A Combined Diffraction and NMR Study

A. Robert Armstrong,^{†,§} Christopher Lyness,^{†,§} Michel Ménétrier,^{‡,§} and Peter G. Bruce^{*,†,§}

[†]*EaStCHEM, School of Chemistry, University of St. Andrews, St. Andrews, Fife KY16 9ST, U.K.,*
[‡]*ICMCB-CNRS, 87 Av. Schweitzer, 33608 Pessac, France, and* [§]*Alistore European Research Institute,*
33 Rue Saint Leu, 80039 Amiens Cedex, France

Received November 11, 2009. Revised Manuscript Received January 7, 2010

$\text{Li}_2\text{CoSiO}_4$ was prepared in three polymorphic forms. The β_{II} ($Pmn2_1$) polymorph was obtained by hydrothermal synthesis (150 °C), and subsequent heat treatments yielded the β_{I} ($Pbn2_1$) form (700 °C) and the γ_0 ($P2_1/n$) form (1100° then quenching from 850 °C). Rietveld refinement of X-ray and neutron powder diffraction patterns reveal considerable Li/Co mixing for β_{II} , very moderate mixing for β_{I} , and no mixing for γ_0 . ^7Li MAS NMR spectra have been recorded for the three forms. The mechanism of the Fermi contact interaction that leads to negatively shifted signals is as yet unexplained, but the nature and the number of signals were analyzed in relation to the site occupancies for each compound. The agreement is good for β_{II} , although the extent of disorder leads to very poorly defined NMR signals; it is reasonable (although not fully quantitative) for β_{I} , where well-defined NMR signals can be assigned to definite environments; finally, the γ_0 sample surprisingly leads to a single rather broad NMR signal, whereas two well-defined and rather different environments are present in the structure deduced from diffraction.

Introduction

New batteries are needed urgently to meet the demands of modern technology and to address the challenge of Global Warming. The layered Li intercalation compound, LiCoO_2 , is used as the cathode in the majority of commercial rechargeable lithium-ion batteries.^{1,2} A number of alternative layered compounds, such as LiNiO_2 or LiMnO_2 , have also been considered: their solid solutions, such as $\text{Li}(\text{Co}_{1/3}\text{Mn}_{1/3}\text{Ni}_{1/3})\text{O}_2$, are used in the latest commercial products.^{3–5} Retention of some Co is important in achieving good cathode performance. The recognition that compounds containing the phosphate anion, such as the olivine LiFePO_4 , could act as lithium intercalation hosts and thus operate as cathodes in rechargeable lithium batteries, represented a significant breakthrough.⁶ Bonding of the oxygen to the phosphorus

stabilizes the former with respect to evolution from the structure, an important problem on charging simple transition metal oxides. Recently, an entirely new class of lithium intercalation compounds based on silicates, Li_2MSiO_4 , where $\text{M} = \text{Fe}, \text{Mn}, \text{Co}$, has been described.⁷ Of these the most studied is $\text{Li}_2\text{FeSiO}_4$; it has been shown that at 60 °C, 165 mAhg^{-1} of charge may be extracted, equivalent to 1 lithium per formula unit; with reversible lithium cycling over the range $\text{Li}_x\text{FeSiO}_4$, $1.15 < x < 2$, corresponding to 140 mAhg^{-1} when suitably carbon coated and with a particle size of $< 150 \text{ nm}$.^{7a} In this paper we focus on $\text{Li}_2\text{CoSiO}_4$.

The Li_2MSiO_4 compounds ($\text{M} = \text{Fe}, \text{Mn}, \text{Co}$) belong to a large family of materials known as the tetrahedral structures.⁸ Generally the tetrahedral structures are composed of tetragonally packed oxide ions (a distorted form of hexagonal close packing) within which half the tetrahedral sites are occupied by cations, such that face sharing between the pairs of tetrahedral sites is avoided.⁹ These

*Corresponding author e-mail: pgb1@st-and.ac.uk.

- (1) Mizushima, K.; Jones, P. C.; Wiseman, P. J.; Goodenough, J. B. *Mater. Res. Bull.* **1980**, *15*, 783.
- (2) Nagaura, T. Paper presented at 4th Int. Rechargeable Battery Seminar, Deerfield Beach, FL, 1990. Nagaura, T.; Tazawa, K. *Prog. Batteries Col. Cells* **1990**, *9*, 20.
- (3) (a) Li, W.; Reimers, J. N.; Dahn, J. R. *Solid State Ionics* **1993**, *67*, 123. (b) Rougier, A.; Gravereau, P.; Delmas, C. *J. Electrochem. Soc.* **1996**, *143*, 1168.
- (4) Armstrong, A. R.; Bruce, P. G. *Nature* **1996**, *381*, 499.
- (5) (a) Yabuuchi, N.; Ohzuku, T. *J. Power Sources* **2003**, *119–121*, 171. (b) Jouanneau, S.; Eberman, K. W.; Krause, L. J.; Dahn, J. R. *J. Electrochem. Soc.* **2005**, *150*, A1637.
- (6) (a) Padhi, A. K.; Nanjundaswamy, K. S.; Goodenough, J. B. *J. Electrochem. Soc.* **1997**, *144*, 1188. (b) Padhi, A. K.; Nanjundaswamy, K. S.; Masquelier, C.; Okada, S.; Goodenough, J. B. *J. Electrochem. Soc.* **1997**, *144*, 1609. (c) Yamada, A.; Chung, S. C.; Hinokuma, K. *J. Electrochem. Soc.* **2001**, *148*, A224. (d) Chung, S. Y.; Bloking, J. T.; Chiang, Y. M. *Nat. Mater.* **2002**, *1*, 123. (e) Herle, P. S.; Ellis, B.; Coombs, N.; Nazar, L. F. *Nat. Mater.* **2004**, *3*, 147.

- (7) (a) Nyttén, A.; Abouimrane, A.; Armand, M.; Gustafsson, T.; Thomas, J. O. *Electrochem. Commun.* **2005**, *7*, 156. (b) Dominko, R.; Bele, M.; Gaberscek, M.; Meden, A.; Remskar, M.; Jamnik, J. *Electrochem. Commun.* **2006**, *8*, 217. (c) Gong, Z. L.; Li, Y. X.; Yang, Y. *Electrochem. Solid-State Lett.* **2006**, *9*, A542. (d) Arroyo de Dompablo, M. E.; Armand, M.; Tarascon, J. M.; Amador, U. *Electrochem. Commun.* **2006**, *8*, 1292. (e) Wu, S. Q.; Zhang, J. H.; Zhu, Z. Z.; Yang, Y. *Curr. Appl. Phys.* **2007**, *7*, 611. (f) Masquelier, C.; Quoirin, G.; Dupont, L.; Taulelle, F. Proceedings of International Meeting on Lithium Batteries, Biarritz, **2006**. (g) Lyness, C.; Delobel, B.; Armstrong, A. R.; Bruce, P. G. *J. Chem. Soc., Chem. Commun.* **2007**, 4890.
- (8) (a) West, A. R.; Glasser, F. P. *J. Solid State Chem.* **1972**, *4*, 20. (b) Tarte, P.; Cahay, R. *C. R. Acad. Sci. Paris C* **1970**, *271*, 777.
- (9) Bruce, P. G.; West, A. R. *Acta Crystallogr., Sect. B: Struct. Crystallogr. Cryst. Chem.* **1982**, *38*, 1891.

tetrahedral structures exhibit a rich polymorphism, with more than 8 different polymorphs known. They may be divided into two families, designated β and γ . In the case of the former all the tetrahedra point in the same direction, perpendicular to the close-packed planes, and share only corners with each other. In the case of the γ polymorphs, the tetrahedra are arranged in groups of three with the central tetrahedron pointing in the opposite direction to the outer two, with which it shares edges. Where both β and γ polymorphs exist for a given compound the latter is stable at higher temperatures, with the β to γ transformation involving inversion of half the tetrahedral sites.¹⁰ Several variants of both β and γ exist, involving either ordering or distortions of the parent structures; they are designated β_I , γ_0 , γ_{II} , etc. In many instances these phases may be quenched to room temperature, where they exhibit long-term stability. Originally the different polymorphs were distinguished only on the basis of differences in their powder X-ray diffraction patterns.^{8a} More recently, the complete crystal structures of a few isolated examples have been solved.¹¹

As a result of the complex polymorphism exhibited by the tetrahedral structures it is beneficial, when studying the structures of these materials to employ techniques that probe both short- and long-range structure. Magic angle spinning NMR was chosen as a probe of the local structure since it was shown to be very powerful in assessing the purity of high-pressure treated $\text{Li}_2\text{MnSiO}_4$ ($Pmn2_1$), characterized by a well-defined single type of Li.¹² Since Li is a weak scatterer of X-rays, neutron powder diffraction was chosen to investigate the long-range structure in three polymorphs of $\text{Li}_2\text{CoSiO}_4$.

Experimental Section

The β_{II} polymorph was prepared by hydrothermal synthesis. $\text{LiOH} \cdot \text{H}_2\text{O}$ (0.05 mol) (Aldrich) was added to 0.0125 mol of SiO_2 (Aldrich) in 20 mL of distilled water and stirred. CoCl_2 (0.0125 mol) (Aldrich) was added to 10 mL of ethylene glycol and stirred under gentle heat until dissolution occurred. The two solutions were then mixed with stirring, and the slurry was transferred to a 40 mL Teflon-lined autoclave. The remaining volume was topped up with distilled water. The sealed autoclave was heated at 150 °C for 72 h. The product was filtered and dried at 60 °C overnight.

The β_I form was obtained by heating the β_{II} phase in air to 700 °C for 2 h. The γ_0 phase was formed by heating the β_{II} polymorph to 1100 °C for 2 h and then lowering the temperature to 850 °C whereupon the material was quenched to room temperature.

Powder X-ray diffraction data were collected on a Stoe STADI/P diffractometer operating in transmission mode with $\text{FeK}\alpha_1$ radiation ($\lambda = 1.936 \text{ \AA}$) to eliminate Co fluorescence.

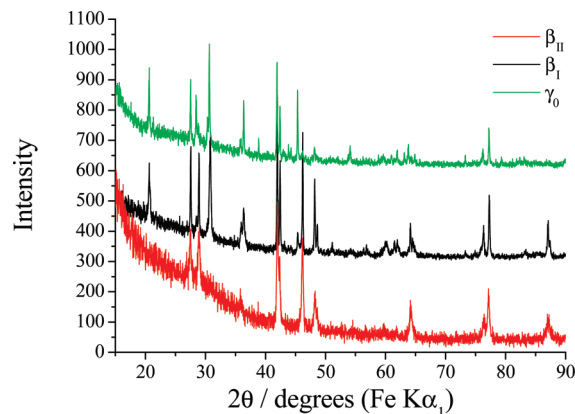


Figure 1. Powder X-ray diffraction patterns for 3 polymorphs of $\text{Li}_2\text{CoSiO}_4$.

Time-of-flight powder neutron diffraction data were obtained on the Polaris high-intensity, medium resolution instrument at ISIS at the Rutherford Appleton Laboratory. Since both lithium and, to a lesser extent, cobalt are neutron absorbers, the data were corrected for absorption. The structures were refined by the Rietveld method using the program TOPAS Academic.¹³

The three polymorphs were characterized by ^7Li MAS NMR at ICMCB, using a Bruker Avance 300 MHz spectrometer with 2.5 mm rotors spinning at 30 kHz. A combination of single pulse and Hahn echo experiments was used with a 90° pulse duration of 1.2 μs . The recycle time was varied to allow full relaxation.

Results

Powder X-ray diffraction patterns of the three $\text{Li}_2\text{CoSiO}_4$ polymorphs β_{II} , β_I and γ_0 , prepared as described in the Experimental Section are presented in Figure 1.

Neutron Diffraction. Powder diffraction data for the as-prepared product of hydrothermal synthesis could be indexed on the basis of a primitive orthorhombic unit cell, space group $Pmn2_1$. According to the notation of West and Glasser this represents the β_{II} polymorph.^{8a} Rietveld refinement of the powder neutron diffraction data using this space group gave an excellent fit with R_{wp} of 1.63%. However, instead of the ideal β_{II} cation arrangement with all the Co in the 2a tetrahedral sites and Li in 4b sites, pronounced disorder was observed. The transition metal 2a site is effectively exclusively occupied by lithium, while the 4b site is approximately equally occupied by lithium and cobalt. This gives a site in which the average neutron scattering length is close to zero, giving poor definition of the cation position. Accordingly, a combined X-ray and neutron refinement was carried out to give better characterization of this 4b site. Final refined parameters are shown in Table 1, and the fit to the neutron data is shown in Figure 2a. The final refined composition corresponds to $\text{Li}_{1.96}\text{Co}_{1.04}\text{SiO}_4$, within 2 e.s.d.s of the ideal stoichiometry. As indicated above the β polymorphs all exhibit corner shared tetrahedra, aligned such that the vertices point along the c direction. In β_{II} $\text{Li}_2\text{CoSiO}_4$ chains of the Li/Co tetrahedra run along the a direction parallel to chains of alternating

(10) West, A. R. Z. *Kristallogr.* **1975**, *111*, 422.

(11) (a) Yamaguchi, H.; Akatsuka, K.; Setoguchi, M.; Takaki, Y. *Acta Crystallogr., Sect. B: Struct. Crystallogr. Cryst. Chem.* **1979**, *35*, 2680. (b) Politaev, V. V.; Petrenko, A. A.; Nalbandyan, V. B.; Medvedev, B. S.; Shvetsova, E. S. *J. Solid State Chem.* **2007**, *180*, 1045. (c) Jousseau, C.; Kahn-Harari, A.; Vivien, D.; Derouet, J.; Ribot, F.; Villain, F. *J. Mater. Chem.* **2002**, *12*, 1525. (d) Riekel, C. *Acta Crystallogr., Sect. B: Struct. Crystallogr. Cryst. Chem.* **1977**, *33*, 2656.

(12) Arroyo-de Dompablo, M. E.; Dominko, R.; Gallardo-Amores, J. M.; Dupont, L.; Mali, G.; Ehrenberg, H.; Jamnik, J.; Moran, E. *Chem. Mater.* **2008**, *20*, 5574.

(13) Coelho, A. A. *J. Appl. Crystallogr.* **2000**, *33*, 899.

Table 1. Refined Crystallographic Parameters for β_{II} $\text{Li}_2\text{CoSiO}_4$, Space Group $Pmn2_1$ ^a

atom	Wyckoff symbol	x/a	y/b	z/c	B_{iso}	occupancy
Li1	2a	0	0.1515(18)	-0.0121(19)	0.94(19)	1
Si1	2a	0.5	0.1743(7)	0	0.50(3)	1
Li2/Co1	4b	0.264(4)	0.293(4)	0.442(6)	0.3(-)	0.48/0.52(1)
O1	4b	0.2839(3)	0.3180(4)	0.9070(8)	0.60(2)	1
O2	2a	0	0.1164(4)	0.4004(11)	0.47(3)	1
O3	2a	0.5	0.1789(6)	0.3362(8)	0.74(3)	1

^a $R_c = 1.46\%$, $R_{wp} = 1.63\%$, $R_p = 2.70\%$, $a = 6.2558(2)$ Å, $b = 5.3584(2)$ Å, $c = 4.9357(2)$ Å.

LiO_4 and SiO_4 tetrahedra. Bond lengths and angles are shown in Table 4.

By heating the as-prepared material to 700 °C for 2 h a polymorph with double the lattice parameter along the b direction is obtained. Powder diffraction data for this phase could be indexed in space group $Pbn2_1$. A $\text{Li}_2\text{CoSiO}_4$ phase adopting this space group was previously reported by Yamaguchi et al., who described it as the β_{II} polymorph.^{11a} However, using the notation of West and Glasser, this should more properly be designated β_1 . Rietveld refinement of the powder neutron diffraction data, using starting coordinates from Yamaguchi et al., gave an excellent fit with R_{wp} of 1.77%. A small degree of site disorder was observed with 2.4(16) % Li on the Co site and 8.6(14) % Co on one of the two Li sites. Final refined parameters are shown in Table 2, and the fit to the data is shown in Figure 2b. Again the final refined composition corresponds to $\text{Li}_{1.94}\text{Co}_{1.06}\text{SiO}_4$, within 2 e. s.d.s of the ideal stoichiometry. While the tetrahedra are again all aligned along the c direction, they are ordered in a different manner. There are chains of alternating LiO_4 and CoO_4 tetrahedra along a , parallel to chains of alternating LiO_4 and SiO_4 tetrahedra. Bond lengths and angles are given in Table 5.

The product of heating the β_{II} polymorph to 1100 °C with quenching from 850 °C generated a third polymorph (γ_0). This is also characterized by a lattice doubling along the b direction and can be indexed in the monoclinic space group $P2_1/n$. Once more Rietveld refinement of the powder neutron diffraction data gave an excellent fit with R_{wp} of 1.62%. No site disorder was observed for this polymorph. Final refined parameters are shown in Table 3, and the fit to the data is shown in Figure 2c. In the γ polymorphs the tetrahedra are arranged in groups of 3 with the central tetrahedron pointing in the opposite direction to the outer 2, with which it shares edges. In γ_0 $\text{Li}_2\text{CoSiO}_4$ this group of 3 edge-sharing tetrahedra consists of Li–Li–Co. Bond lengths and angles are given in Table 6.

Figure 3 shows schematic representations of the structures of the 3 polymorphs revealing the different connectivity.

NMR. The full ^7Li MAS NMR spectra for the three polymorphs are shown in Figure 4. Integration of the whole signal (including the spinning sidebands) leads to very similar amounts of Li per mass of sample for the three polymorphs. Although one cannot exclude the possibility that the T2 relaxation time could be different for the three polymorphs, this suggests that all the Li are observed in the three cases. Most isotropic signals are strongly negatively

shifted due to Fermi contact interaction from the paramagnetic Co^{2+} ions present in the structure.

NMR Shifts – Background. ^7Li NMR Fermi contact shifts are due to the transfer of some density of electron spins to the site of the Li nucleus from the orbitals of a neighboring ion carrying unpaired electrons. Based on earlier Li NMR characterization of Li-transition metal oxides and DFT modeling of the electron spin distribution, the transfer mechanisms elucidated so far can be described as follows.¹⁴

If a d orbital carries an unpaired electron spin, it aligns with the applied field. If this orbital can overlap with the 2s orbital of Li, either directly 2s-nd (like a spin in a t_{2g} orbital of an octahedral transition metal ion with a Li in an edge-sharing octahedron) or via p orbitals of O 2s-O2p-nd (like a spin in an e_g orbital of an octahedral transition metal ion with a Li in a corner-sharing octahedron), a delocalization mechanism operates, and Li receives a density of unpaired spin with the same polarization. This leads to a positive Fermi contact shift.

A fully occupied d orbital (therefore carrying no unpaired spin) can be polarized by unpaired spins in another (higher energy) d orbital of the same transition metal ion that carries unpaired spins (parallel to the applied field). This polarization consists in a separation (in space and in energy) of the two otherwise paired spins. The spin (from the pair) with the same orientation as that of the unpaired spin in the other orbital is attracted by this unpaired spin. Therefore, the spin (from the pair) with the opposite orientation is more spread out in the orbital. If this polarized orbital overlaps with the 2s of Li, again either directly or via oxygen, Li receives a density of spin with opposite orientation to the applied field. This leads to a negative Fermi contact shift. One such case is e_g spins for an octahedral transition metal ion that polarize full t_{2g} orbitals; the latter can overlap with an edge sharing octahedral Li. Another case is electron spins in a (nonbonding) t_{2g} orbital that polarize the bonding counterpart of an empty antibonding e_g (that should actually be called e_g^*). This polarized bonding e_g orbital can overlap via O with a Li in a corner-sharing octahedron.

This is relatively straightforward in octahedral coordination where the e_g orbitals point to the oxygens and the t_{2g} orbitals point to the edges, and the Li in edge or corner sharing octahedra are ideally placed to interact with these

(14) (a) Carlier, D.; Ménétrier, M.; Grey, C. P.; Delmas, C.; Ceder, G. *Phys. Rev. B* **2003**, 67, 174103. (b) Chazal, C.; Ménétrier, M.; Carlier, D.; Croguennec, L.; Delmas, C. *Chem. Mater.* **2007**, 19, 4166.

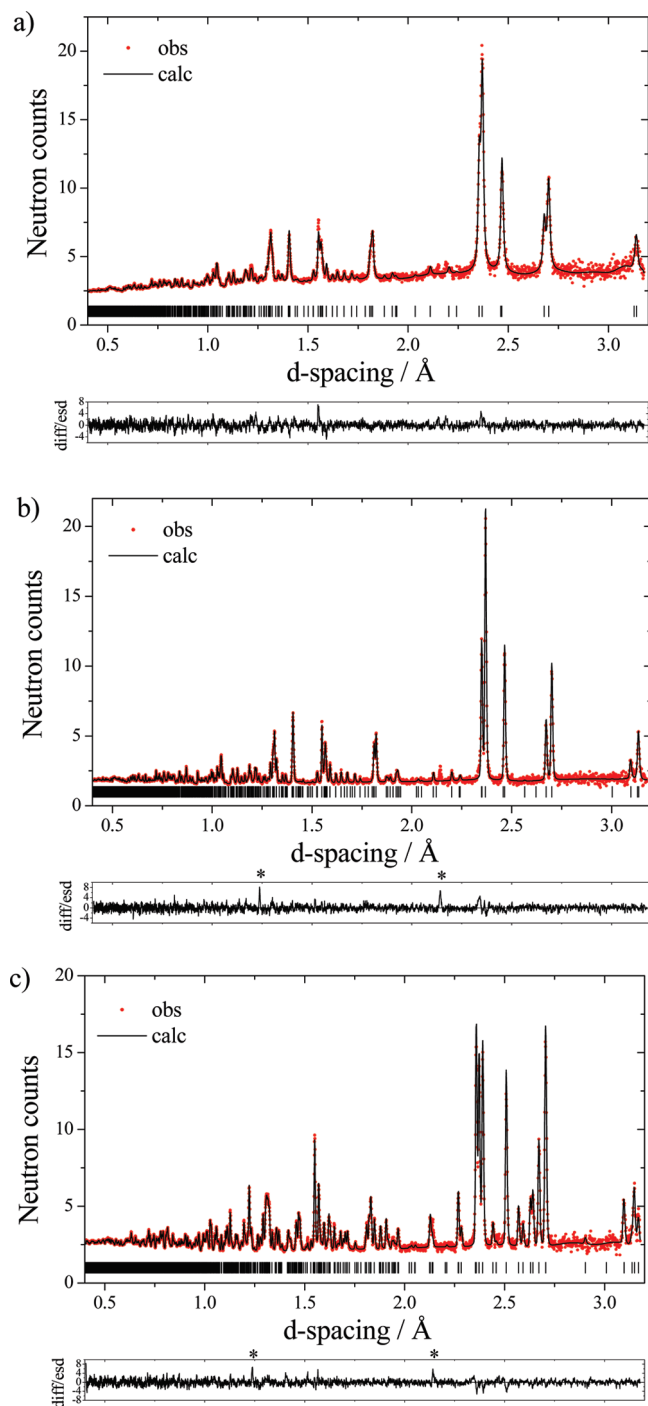


Figure 2. a) Refined powder neutron diffraction pattern for as-synthesized β_{II} $\text{Li}_2\text{CoSiO}_4$, space group $Pmn2_1$. b) Refined powder neutron diffraction pattern for as-synthesized β_I $\text{Li}_2\text{CoSiO}_4$, space group $Pbn2_1$. c) Refined powder neutron diffraction pattern for as-synthesized γ_0 $\text{Li}_2\text{CoSiO}_4$, space group $P2_1/n$. Dots represent observed data and solid line the calculated pattern. The lower line is the difference/esd. The misfit in a) arises from stacking faults, while asterisks in b) and c) denote reflections from the vanadium sample holder.

orbitals. However, in tetrahedral coordination for the transition metal ion and for Li, the e and t_2 orbitals point, respectively, toward the edges (perpendicularly) and to the faces (not perpendicular to a face but parallel to two of the opposite edges) of the tetrahedron, and the Li in adjacent tetrahedra are not in obvious positions to overlap with these orbitals.

Following these rules of thumb, the shifts expected for the $\text{Li}_2\text{CoSiO}_4$ polymorphs can nevertheless be tentatively discussed as follows.

Cobalt has an oxidation state +2 in these compounds, and its electronic configuration in a tetrahedron is therefore $e^4 t_2^3$ (the e orbitals are fully occupied, while each t_2 orbital contains one unpaired spin).

In the β polymorphs, the nature of the connection of any tetrahedral Li site with the surrounding ones containing Co is represented in Figure 5. The Co tetrahedra present either face-to-face, face-to-edge, or edge-to-face connection relative to the Li tetrahedron. Following the rules just expressed, a Co^{2+} ion with a face-to-face connection would have t_2 orbital lobes pointing toward this Li through the facing faces of the tetrahedra (face-to-face geometry); and one would expect the transfer of an electron spin density aligned with the applied field, leading to a positive Fermi contact shift. A similar situation arises for the face-to-edge connection (the orbital exiting from the face now points to Li through the edge of its tetrahedron). Finally, for the edge-to-face connection the fully occupied but polarized e orbital points from the edge but perpendicularly, in such a way that it is not directed toward the Li tetrahedron, and the latter should not receive significant electron spin density with polarization opposite to the applied field.

The experimental shifts in these polymorphs are however clearly negative (Figure 4). There is therefore a polarization mechanism not taken into account in our discussion. This most probably operates via the oxygens, through bonding counterparts of the e and t_2 orbitals discussed so far. If these bonding (mostly of O character) orbitals are polarized by the spin-carrying t_2 orbital, they must transfer an electron spin density leading to a negative Fermi contact shift via the O, superseding the direct overlap of the t_2 orbital through the faces. The precise interplay and respective geometries of the t_2 orbital and of the bonding ones remains to be studied in detail in a tetrahedral coordination.

As concerns the γ_0 polymorph, the same type of connection between the tetrahedra occurs (although with considerable distortion in the alignment of the tetrahedral) (Figure 6), but edge-sharing also occurs in addition, as discussed in the Introduction and shown in Figure 6. In this configuration, a polarized e orbital from Co should point directly to Li through the common edge, contributing a negative Fermi contact shift that could explain the negative shift for one of the Li sites.

Despite this lack of global understanding of the spin transfer mechanism, we can still analyze the NMR signals in terms of number of signals with respect to the possible local environments due to the actual Li/Co site distribution deduced from the Rietveld analyses.

β_{II} Polymorph. The Li (2a) site (Figure 6) is surrounded by 4 (0.52Co/0.48Li) tetrahedra with a face-to-face geometry; this should lead to a distribution of 5 resonances, out of which 3 have significant magnitudes ((1:2:3 Co) with probabilities (0.23:0.37:0.27)). The remaining two have probabilities much lower than 0.10. In addition, the

Table 2. Refined Crystallographic Parameters for β_1 Li₂CoSiO₄, Space Group $Pbn2_1$ ^a

atom	Wyckoff symbol	<i>x/a</i>	<i>y/b</i>	<i>z/c</i>	<i>B</i> _{iso}	occupancy
Co1	4a	0.5005(17)	0.1652(9)	0.253(3)	0.61(11)	Co/Li 0.976/0.024(16)
Si1	4a	0.2494(13)	0.4130(3)	0.25(-)	0.33(3)	1
Li1	4a	-0.019(3)	0.1638(13)	0.251(4)	0.4(2)	Li/Co 0.914/0.086(14)
Li2	4a	0.741(3)	0.4217(7)	0.2402(13)	0.77(9)	1
O1	4a	0.0337(6)	0.3425(4)	0.1478(9)	0.33(6)	1
O2	4a	0.2542(10)	0.55780(14)	0.1459(6)	0.39(2)	1
O3	4a	0.2451(10)	0.4106(2)	0.5811(5)	0.30(2)	1
O4	4a	0.4660(6)	0.3417(5)	0.1396(7)	0.39(5)	1

^a *R*_c = 1.61%, *R*_{wp} = 1.77%, *R*_p = 3.00%, *a* = 6.25990(10) Å, *b* = 10.6892(2) Å, *c* = 4.92866(8) Å.

Table 3. Refined Crystallographic Parameters for γ_0 Li₂CoSiO₄, Space Group $P2_1/n$ ^a

atom	Wyckoff symbol	<i>x/a</i>	<i>y/b</i>	<i>z/c</i>	<i>B</i> _{iso}	occupancy
Co1	4e	0.4968(8)	0.1656(4)	0.3074(7)	0.37(4)	1
Si1	4e	0.2480(4)	0.41233(14)	0.3135(4)	0.13(2)	1
Li1	4e	-0.0047(10)	0.1631(6)	0.3072(10)	0.51(6)	1
Li2	4e	0.2385(11)	0.0760(4)	0.7145(10)	0.86(6)	1
O1	4a	0.2475(3)	0.40939(14)	0.6381(3)	0.350(14)	1
O2	4a	0.2539(3)	0.55630(12)	0.2071(3)	0.41(2)	1
O3	4a	0.0334(3)	0.3409(2)	0.2081(3)	0.36(2)	1
O4	4a	0.4604(3)	0.3400(2)	0.2079(3)	0.34(2)	1

^a *R*_c = 1.33%, *R*_{wp} = 1.62%, *R*_p = 2.89%, *a* = 6.27433(10) Å, *b* = 10.6854(2) Å, *c* = 5.01631(9) Å, β = 90.600°(2).

Table 4. Refined Bond Lengths and Angles for β_{II} Li₂CoSiO₄, Space Group $Pmn2_1$

Li1O4	O1	O1	O2	O3
O1	2.028(5)	122.4(5)	103.7(3)	109.2(3)
O1		2.028(5)	103.7(3)	109.2(3)
O2			2.044(11)	107.7(5)
O3				1.922(10)
SiO4	O1	O1	O2	O3
O1	1.622(3)	112.9(3)	111.6(2)	106.0(2)
O1		1.622(3)	111.6(2)	106.0(2)
O2			1.633(5)	108.4(3)
O3				1.660(4)
(Li/Co)O4	O1	O1	O2	O3
O1	2.113(2)	91.8(9)	111.0(11)	117.2(13)
O1		2.305(3)	100.5(11)	106.3(12)
O2			1.912(2)	123.1(13)
O3				1.682(2)

same Li is also surrounded (Figure 7) by two (0.52Co/0.48Li) tetrahedra with a face-to-edge-geometry and two with an edge-to-face geometry. This should lead to a further splitting of each of the resonance just mentioned into 9 resonances with rather similar magnitudes (probabilities ranging from 0.05 to 0.19).

The Li/Co site (0.48Li/0.52Co) (Figure 8) is surrounded by 4 (0.52Co/0.48Li) tetrahedra (2 face-to-face, 1 face-to-edge, 1 edge-to-face). This should lead to a distribution of 12 resonances with rather similar magnitudes (probabilities from 0.05 to 0.13). Altogether, the distribution of resonances for the two crystallographic types of Li is therefore expected to be very broad.

The experimental pattern (Figure 9) is in good agreement with this. It shows a set of at least two broad resonances, but, not knowing the value of the shift caused by each Co in each possible environment, one cannot infer that these two apparent signals correspond to the two crystallographic sites. It is more likely that for a given

crystallographic site the very broad distribution in the possible number of Co leads to a set of signals contributing within the whole ppm range. For both types of Li, among all the possibilities is the one having zero adjacent Co; such a configuration occurs statistically for 5% of the Li in 2a and for 5% of the 0.48 Li in Li/Co site. It is reasonable to assume that these environments lead to the contribution observed around 0 ppm in the spectrum. Besides, it is interesting to note that contributions with positive shifts are also present in the overall spectrum. These may correspond to cases where the delocalization mechanisms mentioned above are not overtaken by a polarization via O. Improvement of the modeling of these interaction mechanisms is clearly needed in this respect.

β_1 Polymorph. The Li site (containing 0.91Li) is surrounded as in Figure 4 by four tetrahedra containing 0.98 Co: two with a face-to-face geometry, one with a face-to-edge geometry, and one with an edge-to-face geometry. This should lead to a distribution of 12 signals

Table 5. Refined Bond Lengths and Angles for β_1 Li₂CoSiO₄, Space Group *Pbn*2₁

CoO4	O1	O2	O3	O4
O1	1.957(16)	108.5(6)	109.7(6)	109.4(6)
O2		2.036(12)	105.7(6)	112.2(6)
O3			1.928(13)	111.3(6)
O4				1.980(11)
SiO4	O1	O2	O3	O4
O1	1.625(8)	111.0(4)	106.9(4)	111.5(3)
O2		1.631(3)	109.2(2)	108.6(4)
O3			1.632(2)	109.6(4)
O4				1.650(8)
Li1O4	O1	O2	O3	O4
O1	2.004(16)	109.0(8)	114.8(9)	107.0(8)
O2		2.074(16)	106.6(8)	105.9(8)
O3			1.876(18)	113.3(9)
O4				1.916(22)
Li2O4	O1	O2	O3	O4
O1	2.062(17)	104.8(7)	104.6(7)	122.5(4)
O2		2.012(7)	107.3(3)	107.7(7)
O3			1.958(7)	109.2(7)
O4				1.992(17)

Table 6. Refined Bond Lengths and Angles for γ_0 Li₂CoSiO₄, Space Group *P2*₁/*n*

CoO4	O1	O2	O3	O4
O1	1.965(5)	112.8(2)	109.4(2)	111.9(2)
O2		1.960(5)	95.7(2)	118.0(2)
O3			2.022(4)	107.5(2)
O4				1.942(5)
SiO4	O1	O2	O3	O4
O1	1.629(2)	110.25(12)	107.72(14)	108.98(14)
O2		1.629(2)	110.94(16)	108.61(16)
O3			1.631(3)	110.31(13)
O4				1.633(3)
Li1O4	O1	O2	O3	O4
O1	1.926(6)	113.4(3)	112.0(3)	109.6(3)
O2		1.946(6)	117.0(3)	97.1(3)
O3			1.979(7)	106.3(3)
O4				2.025(6)
Li2O4	O1	O2	O3	O4
O1	1.930(5)	106.8(2)	111.6(3)	117.7(3)
O2		1.946(6)	89.9(2)	93.3(23)
O3			2.053(6)	127.1(2)
O4				1.962(7)

corresponding to Li with different numbers of Co neighbors in different positions, but one signal (the one with 4 Co) should dominate (92% of total magnitude, the others representing less than 4%).

The Li2 site, with a Li occupancy of 1, is similarly surrounded by 0.98 Co sites, leading to a similar distribution of signals. In addition, this Li2 site also is similarly surrounded by 0.09 Co (Li1) sites that further splits each of these 12 resonances into a distribution of 12, of which the major one is 0 Co and corresponds to 69% of the total (the rest less than 14%).

The 0.02 Li present in the 0.98 Co site do not have any connection with a Co-rich site. However, again they have the same type of surrounding as shown in Figure 4 with the 0.09 Co tetrahedra. This again leads to a distribution

of 12 resonances for this 0.02 Li, the major one being the one with 0 Co corresponding to 69% of the total (the others are less than 14%). These 0.02×0.69 Li should resonate at 0 ppm since they do not have any connection to a Co tetrahedron.

The NMR spectrum of the β_1 polymorph (Figure 10) exhibits three well-defined signals; following the analysis described above, they can tentatively be assigned as shown in the figure. The other resonances would be too distributed to be identified, although they should account for 25% of the total amount of Li. In addition, a very weak narrow signal close to -1.5 ppm most probably corresponds to an unidentified diamagnetic impurity. Integration of the spectra over all the spinning sidebands, compared to the relative magnitudes expected from this

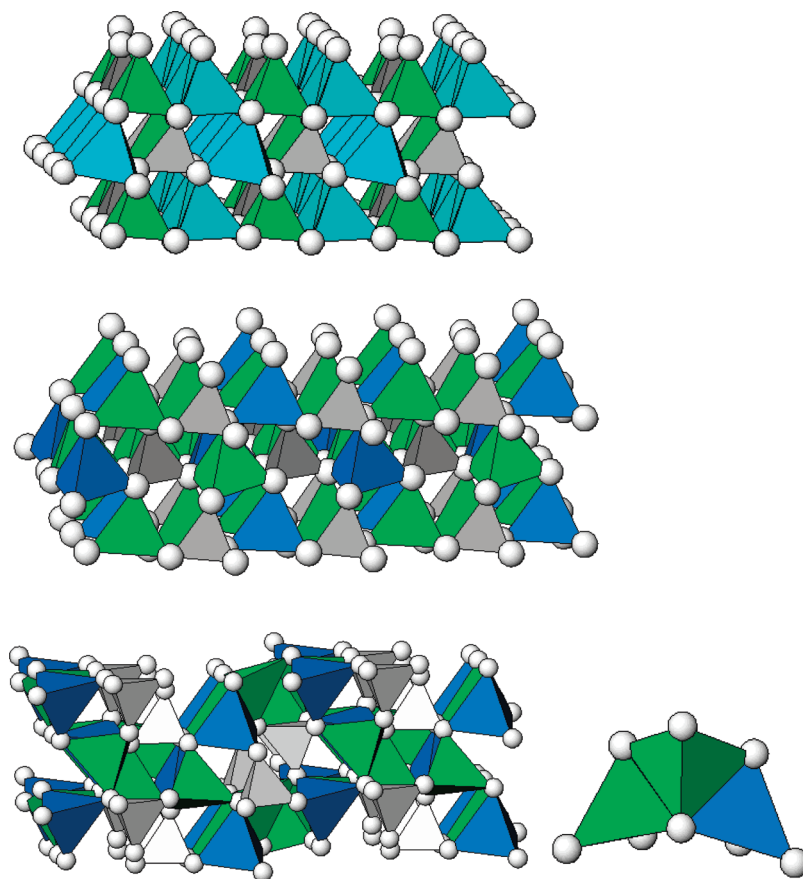


Figure 3. Schematic representations of the three $\text{Li}_2\text{CoSiO}_4$ polymorphs. a) β_{II} , b) β_{I} , and c) γ_0 , with the inset showing edge sharing tetrahedra. Gray tetrahedra represent SiO_4 , green LiO_4 , blue CoO_4 , and cyan $(\text{Li,Co})\text{O}_4$.

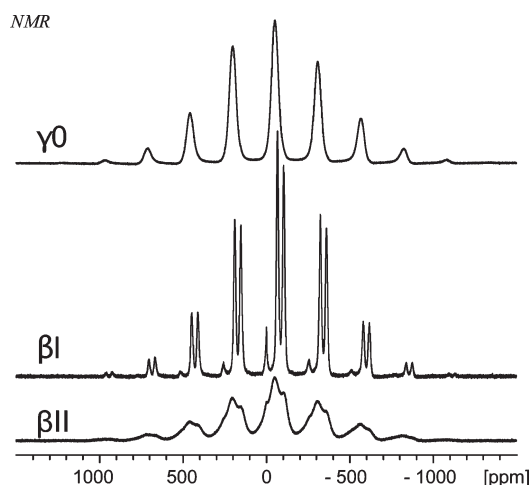


Figure 4. ^7Li MAS NMR spectrum of the three polymorphs of $\text{Li}_2\text{CoSiO}_4$ (116 MHz, 30 kHz spinning, Hahn echo). The absolute magnitude scale referred to the mass of the samples.

assignment, is shown in Table 7. The 0 ppm signal is clearly too intense for this assignment, which would imply more Li in the Co site (or less Co in the adjacent 0.91Li/0.09Co site). This might however also partly be due to difficulties in subtracting the narrow additional component in the spectral decomposition for integration and to the influence of the additional unresolved distribution of signals representing 25% of the total amount of Li.

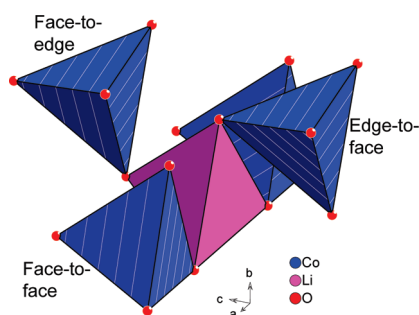


Figure 5. Schematic representation of the surrounding of Li by Co in the beta polymorphs.

γ_0 Polymorph. In the γ_0 polymorph there is no Li/Co mixing according to the Rietveld results reported in this paper, so that only one resonance is expected for each Li site.

The Li in the Li1 site (Figure 6) is connected to four Co tetrahedra with globally the same geometry as in the other two polymorphs (2 face-to-face, 1 face-to-edge, 1 edge-to-face). However, the arrangement of the tetrahedra is so distorted that one can hardly expect the t_2 or the polarized e orbitals of Co to point toward this Li.

The Li in the Li2 site (Figure 6) has a quite different environment, since, in addition to “face-to-face” connection with two Co tetrahedra, it also shares one edge with a Co tetrahedron. Following the mechanisms discussed in this paper, this is an ideal situation

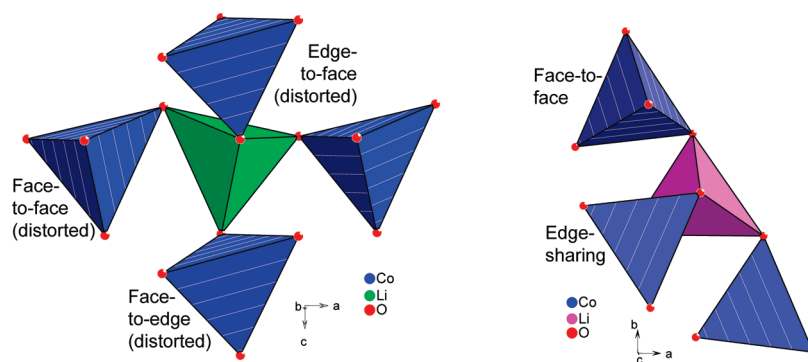


Figure 6. Schematic representation of the surrounding of the two types of Li by Co in the γ_0 polymorph.

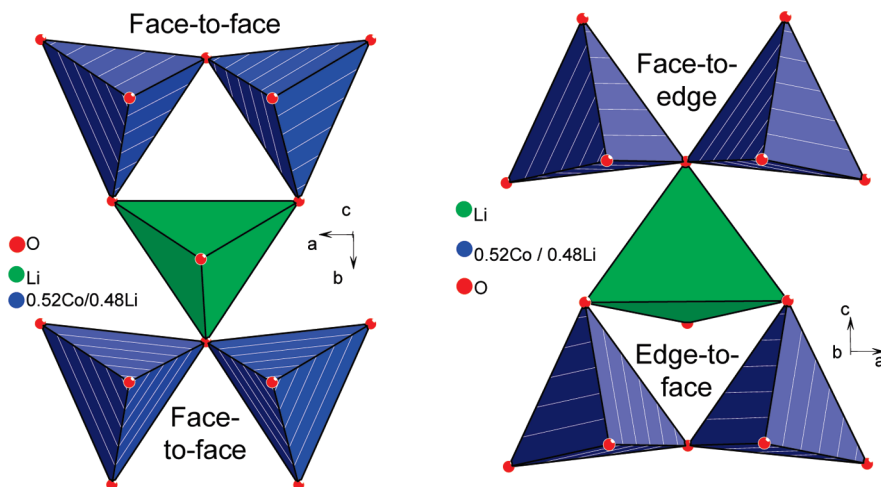


Figure 7. Surrounding of one type of Li (2a site) by Co in the β_{II} polymorph.

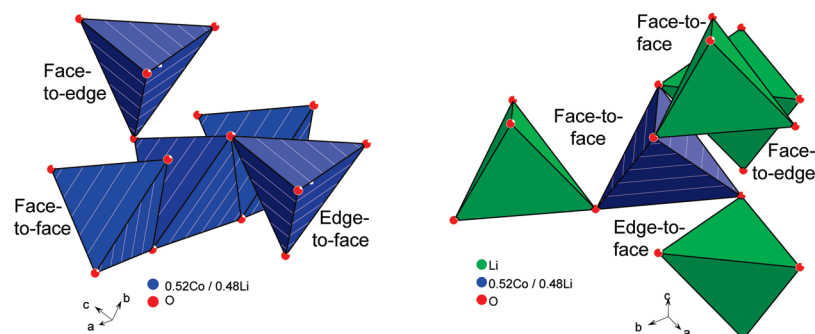


Figure 8. Surrounding of the Li/Co(4b) sites in the β_{II} polymorph.

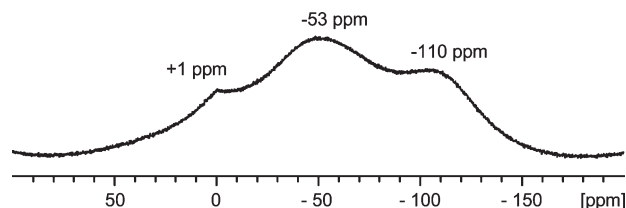


Figure 9. ^7Li MAS NMR spectrum (isotropic signals) of the β_{II} polymorph (116 MHz, 30 kHz spinning, Hahn echo).

for a negative shift due to transfer of electron spin density from the polarized e orbital, although Li2 appears quite off-centered in its tetrahedron (Figure 11).

The ^7Li NMR spectrum of the γ_0 polymorph (Figure 12) however shows a single resonance with a 58% Gaussian – 42% Lorentzian line shape. Variable temperature (cooling to about 250 K), ^6Li resonance at 44.2 MHz, or ^7Li resonance at 38.9 MHz with a 30 kHz spinning did not lead to any sign of splitting of this signal. Not knowing the shift mechanisms in this system, we cannot exclude the possibility that the shifts for the two types of Li happen to coincide, although this appears somewhat unlikely for such different environments. Besides, the width of the line (as compared to the other 2 polymorphs) would rather suggest a distribution of signals that should result from some kind of Li/Co exchange.

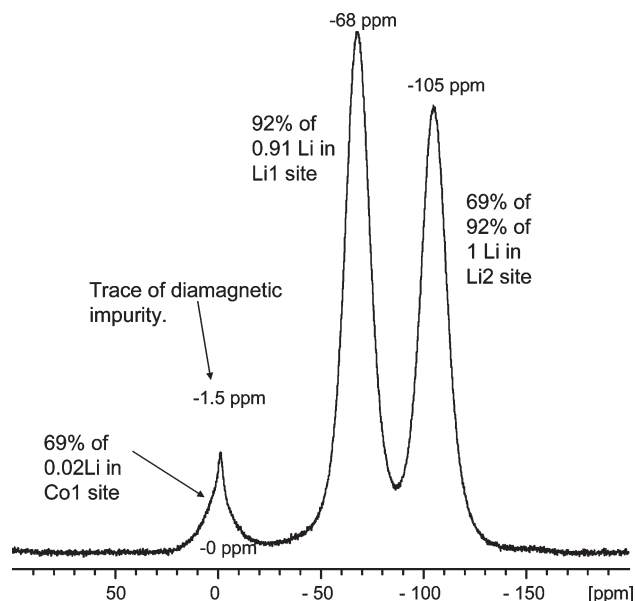


Figure 10. ^7Li MAS NMR spectrum (isotropic signals) of the β_1 polymorph (116 MHz, 30 kHz spinning, Hahn echo).

Table 7. Relative Magnitude of the ^7Li NMR Signals in the β_1 Polymorph Compared to the Values Expected Based on the Analysis Described in the Text

signal	0 ppm	-68 ppm	-105 ppm
expected magnitude %	0.9	56.3	42.7
integration %	5.8	48.43	45.53

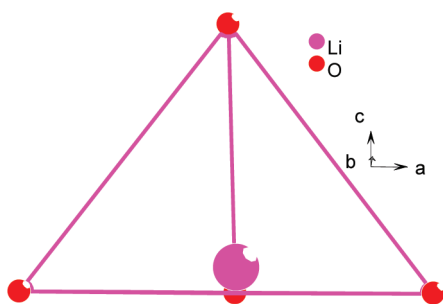


Figure 11. Open view of the $\text{Li}(2)\text{O}_4$ tetrahedron.

Conclusion

$\text{Li}_2\text{CoSiO}_4$ was prepared in three pure polymorphic forms (β_{II} , β_1 , and γ_0) as described previously.^{7g} Rietveld

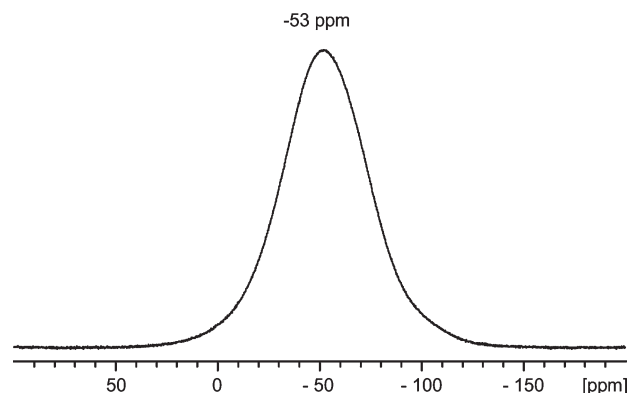
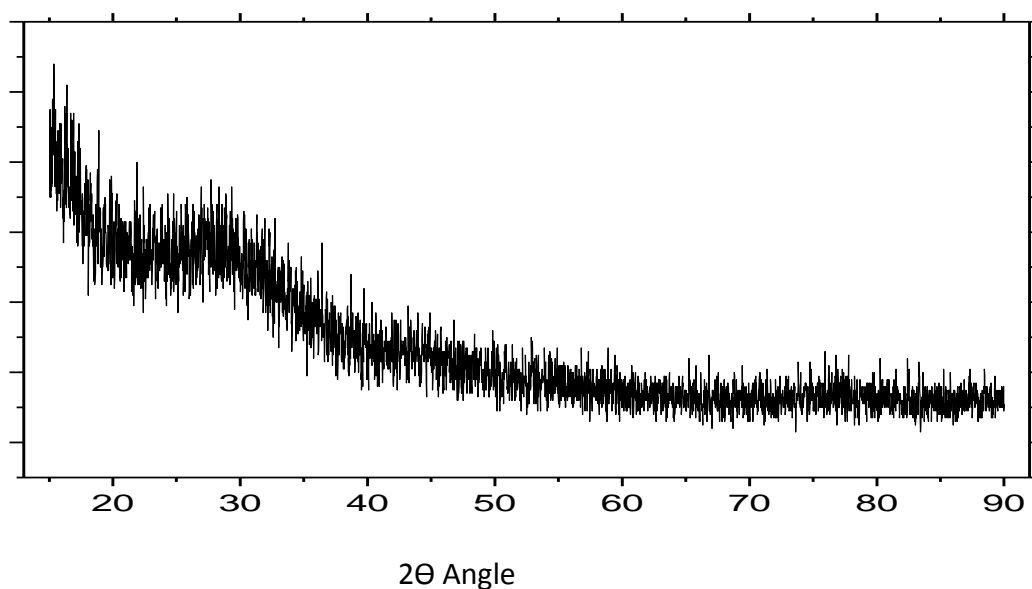
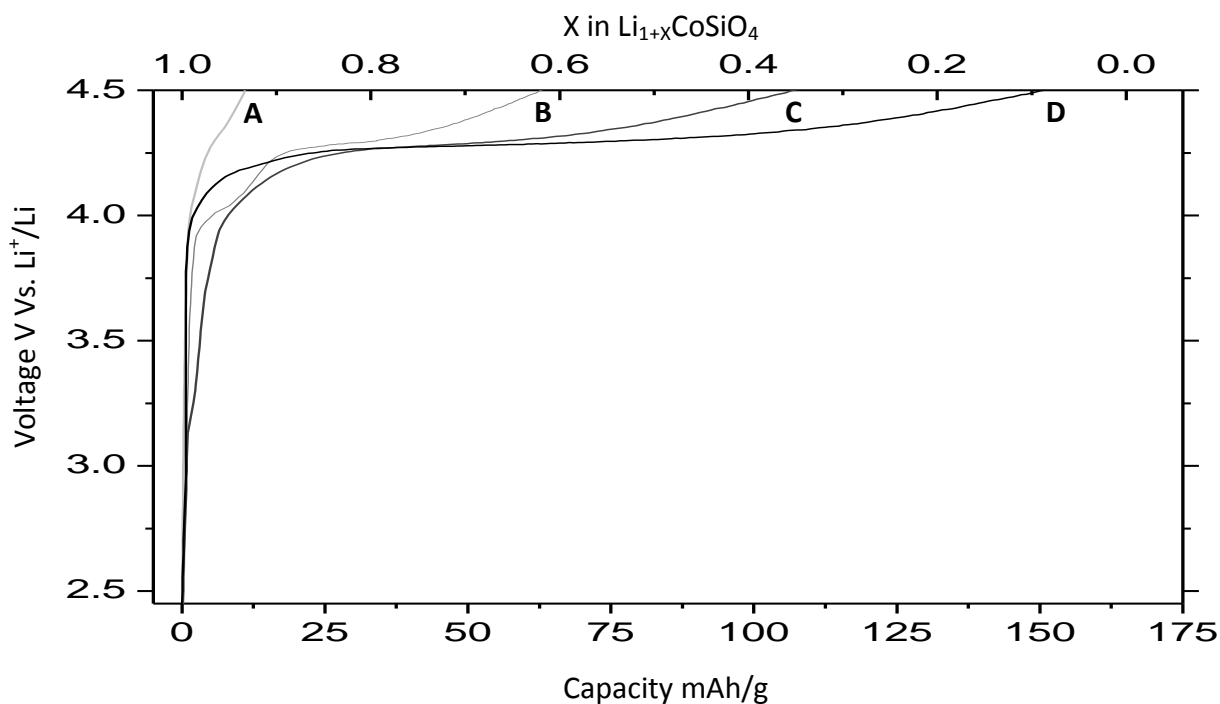


Figure 12. ^7Li MAS NMR spectrum (isotropic signal) of the γ_0 polymorph (116 MHz, 30 kHz spinning, Hahn echo).

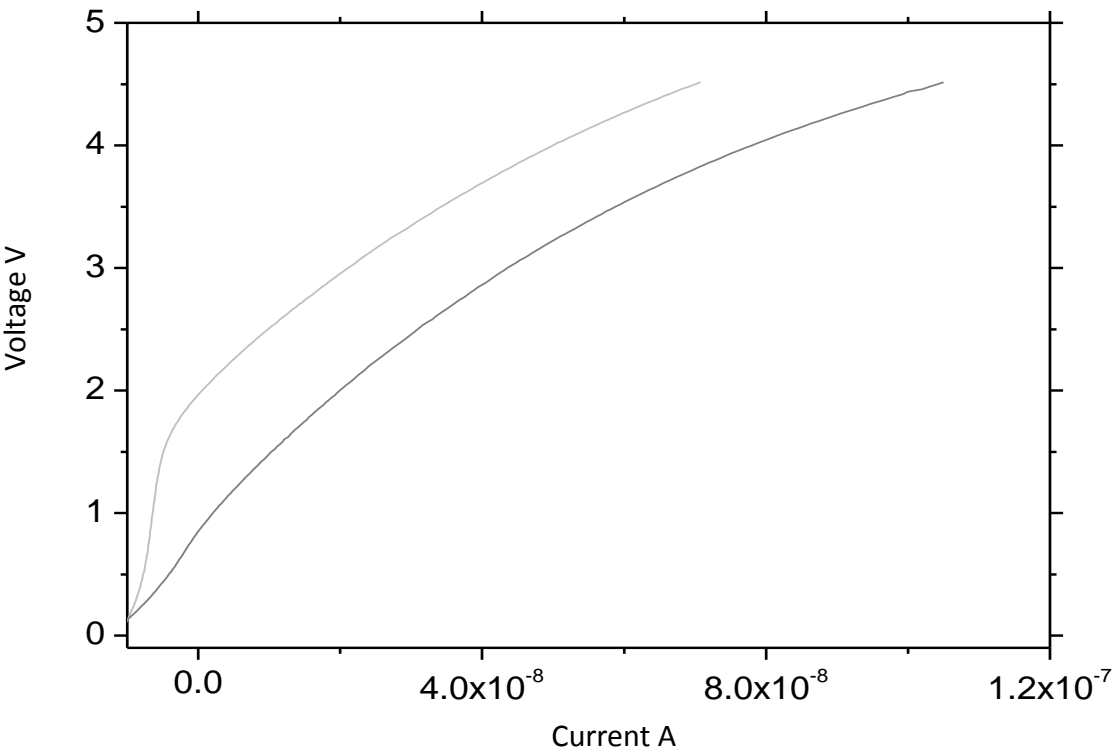
refinement of X-ray and neutron powder diffraction patterns demonstrated a considerable Li/Co mixing for β_{II} with close to 50/50 occupation in the 4b site. Very moderate mixing in the Co site (2.4% Li) and one of the Li sites (8.6% Co) was observed for the β_1 polymorph, and no mixing was found for γ_0 . ^7Li MAS NMR spectra were recorded for all 3 polymorphs. The mechanism of the Fermi contact interaction that leads to the observed negatively shifted signals cannot be explained based on our present understanding. A polarization-type mechanism involving bonding orbitals with O character seems to overwhelm the expected delocalization mechanism from the t_2 orbitals of tetrahedral Co^{2+} ions that carry the unpaired spins. However, the nature and the number of signals were analyzed in relation with the site occupancies for each compound. Very poorly defined signals are obtained for β_{II} , in good agreement with the considerable extent of disorder expected from the diffraction results. For β_1 , well-defined NMR signals can be assigned to definite environments, in reasonable (although not fully quantitative) agreement with the expected structure and site occupancies. Finally, the γ_0 sample surprisingly leads to a single rather broad NMR signal, whereas two well-defined and rather different environments are present in the structure deduced from diffraction.

Acknowledgment. We thank Dany Carlier for fruitful discussions. Peter G. Bruce is indebted to EPSRC for financial support.

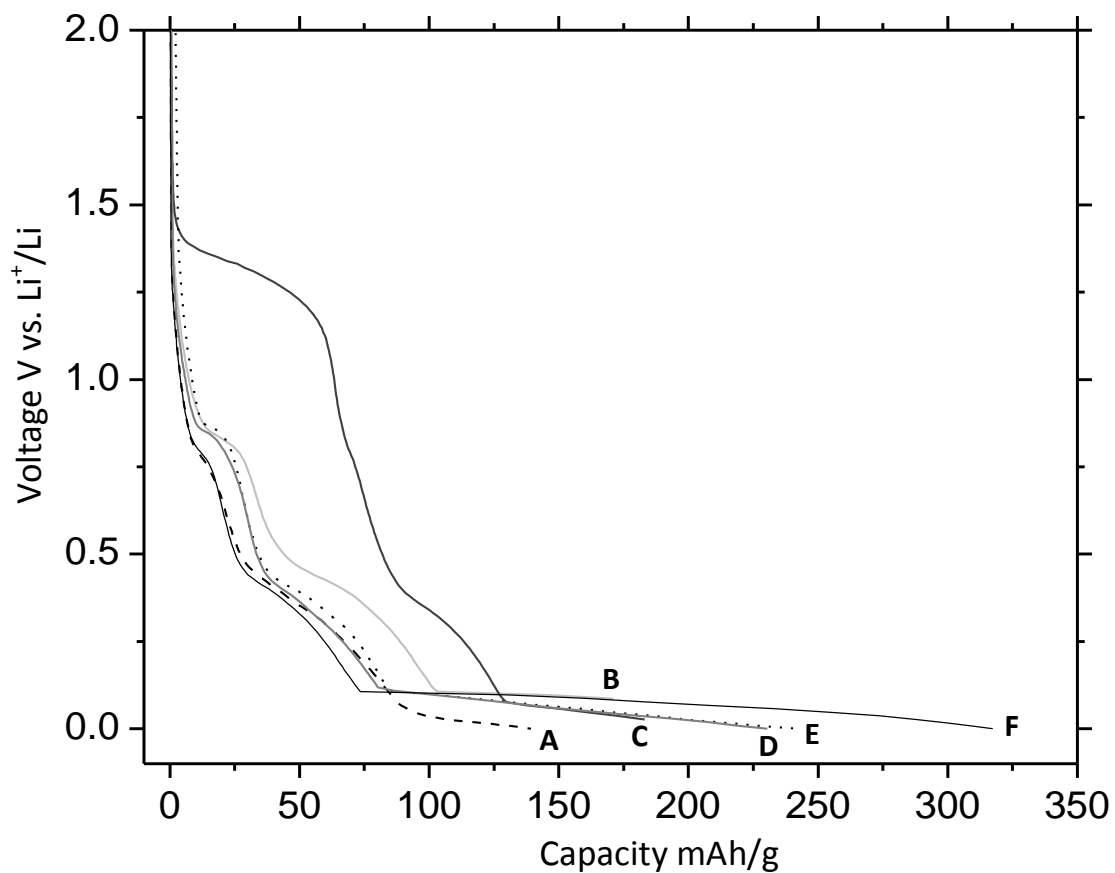
Appendix iii and iv

Appendix iii: X-ray diffraction pattern of the $\text{Li}_2\text{CoSiO}_4$ solid state precursorAppendix iv: Galvanostatic profile of 1st charge of $\beta_1 \text{Li}_2\text{CoSiO}_4$ with different electrolytes. A) 1M Lithium bis(oxalate)borate (LiBOB) in polycarbonate(PC), B) 1M Sulfane in polycarbonate(PC), C) LP31, 1M LiPF_6 in 2:1 ethylene carbonate(EC):dimethyl carbonate(DMC), D) LP30, 1M LiPF_6 1:1 ethylene carbonate(EC): dimethyl carbonate(DMC)

Appendix v



Appendix v: DC voltage vs. Current plot for ball-milled β_{II} $\text{Li}_2\text{CoSiO}_4$ material



Appendix vi: Galvanostatic profile of 1st discharge of $\text{Li}_{1.08}\text{V}_{0.92}\text{O}_2$ with different electrolytes. A) 1M LiPF_6 ethylene carbonate(EC):polycarbonate(PC), B) 1M LiClO_4 in polycarbonate(PC), C) 1M LiASF_6 in polycarbonate, D) LP31 LP31, 1M LiPF_6 in 2:1 ethylene carbonate(EC):dimethyl carbonate(DMC), E) LP30, 1M LiPF_6 1:1 ethylene carbonate(EC): dimethyl carbonate(DMC)

Published Paper:

The lithium intercalation process in $\text{Li}_{1+x}\text{V}_{1-x}\text{O}_2$: a low voltage anode for lithium batteries

AR Armstrong, C Lyness, P Panchmatia, MS Islam, PG Bruce – Nature Materials

The lithium intercalation process in the low-voltage lithium battery anode $\text{Li}_{1+x}\text{V}_{1-x}\text{O}_2$

A. Robert Armstrong¹, Christopher Lyness¹, Pooja M. Panchmatia², M. Saiful Islam^{2*} and Peter G. Bruce^{1*}

Lithium can be reversibly intercalated into layered $\text{Li}_{1+x}\text{V}_{1-x}\text{O}_2$ (LiCoO_2 structure) at ~ 0.1 V, but only if $x > 0$. The low voltage combined with a higher density than graphite results in a higher theoretical volumetric energy density; important for future applications in portable electronics and electric vehicles. Here we investigate the crucial question, why Li cannot intercalate into LiVO_2 but Li-rich compositions switch on intercalation at an unprecedented low voltage for an oxide? We show that Li^+ intercalated into tetrahedral sites are energetically more stable for Li-rich compositions, as they share a face with Li^+ on the V site in the transition metal layers. Li incorporation triggers shearing of the oxide layers from cubic to hexagonal packing because the Li_2VO_2 structure can accommodate two Li per formula unit in tetrahedral sites without face sharing. Such understanding is important for the future design and optimization of low-voltage intercalation anodes for lithium batteries.

Recent reports that Li can be reversibly intercalated into the layered compound $\text{Li}_{1+x}\text{V}_{1-x}\text{O}_2$ (with the LiCoO_2 structure) at a potential of ~ 0.1 V versus Li^+/Li represent an important milestone in lithium-ion battery research^{1–4}. For almost twenty years graphite has remained the dominant anode in rechargeable lithium-ion batteries; operating by intercalation of Li between the graphene sheets. Efforts to improve on the energy storage of graphite have concentrated on reactions other than intercalation, including silicon and tin anodes that form alloys with Li, conversion/displacement reactions such as $\text{Li} + \text{CoO}$ and extrusion reactions^{5–26}. Although work on these alternatives to intercalation has made important progress, and Sn–Co–C alloys are in use, in general, problems of large volume expansion or large voltage hysteresis remain to be solved. As a result, intercalation remains an attractive mechanism for lithium-ion batteries.

Oxide intercalation hosts are attractive because their density is twice that of graphite, leading to double the volumetric energy density, something that is crucial for future applications in electronics and electric vehicles. The lowest voltage oxide intercalation hosts have been the titanates, but their potential is still relatively high at ~ 1.6 V versus Li^+/Li , compared with graphite at ~ 0.1 V, thus halving the overall cell voltage and negating the benefits of using a dense oxide. This is why recent reports that Li can be intercalated into the layered transition metal oxide $\text{Li}_{1+x}\text{V}_{1-x}\text{O}_2$, at ~ 0.1 V and with a theoretical volumetric capacity of $1,360 \text{ mA h cm}^{-3}$ compared to graphite at 790 mA h cm^{-3} , are so significant^{1–4}. Also, intercalation into an oxide at such a low voltage is unprecedented as usually conversion/displacement reactions dominate in this voltage region^{20,21}.

Given the significance of Li intercalation into $\text{Li}_{1+x}\text{V}_{1-x}\text{O}_2$, an important question that arises is why Li can only be intercalated into lithium-rich $\text{Li}_{1+x}\text{V}_{1-x}\text{O}_2$, that is for $x > 0$ (refs 1,2). Here we investigate the intercalation process for $\text{Li}_{1+x}\text{V}_{1-x}\text{O}_2$ and in particular the key role of non-stoichiometry in switching on intercalation, using a combination of powder X-ray and neutron diffraction along with advanced computational methods.

Initial characterization

$\text{Li}_{1+x}\text{V}_{1-x}\text{O}_2$ was prepared by solid state reaction as described in the Methods section. Powder X-ray diffraction patterns for $x = 0$, 0.03 and 0.07 are shown in Fig. 1a. All peaks may be indexed on the basis of the α - NaFeO_2 (LiCoO_2) crystal structure, space group $R\bar{3}m$. The materials are highly crystalline, exhibiting sharp diffraction peaks (FWHM = 0.11° in 2θ for the (104) reflection of $x = 0.07$). These results are consistent with the particle sizes observed by electron microscopy, Fig. 1b, which are typically 100–200 nm and with Brunauer–Emmett–Teller (BET) surface areas of $1\text{--}5 \text{ m}^2 \text{ g}^{-1}$. Compositions were confirmed by structure refinement, inductively coupled plasma (ICP) and vanadium oxidation state analysis, as discussed later.

Structures of the as-prepared materials

To understand the intercalation process, and in particular why extra Li in the structure is necessary to facilitate intercalation, it is first necessary to establish the structures of the as-prepared materials. Rietveld refinement, employing combined X-ray and neutron diffraction data, because Li is insensitive to X-rays and V is insensitive to neutrons, was carried out on LiVO_2 and $\text{Li}_{1.07}\text{V}_{0.93}\text{O}_2$, based on a structural model derived from LiCoO_2 (α - NaFeO_2) in which Co was replaced by V. The only positional parameter not constrained by symmetry is the z coordinate of O; this was allowed to vary freely. In view of the insensitivity of V to neutrons the temperature factor for the transition metal site was fixed in the course of the refinements; those of all other sites were varied independently. The cation distribution was investigated by refining Li and V on the transition metal, 3a, and alkali metal, 3b, sites of the $R\bar{3}m$ space group. In the case of the stoichiometric material, no occupancy of V on the alkali metal sites was observed; therefore, in the final refinements only Li was located on the alkali metal sites. The occupancy of the transition metal sites was 0.99/0.01(1) V/Li. The final refined composition was LiVO_2 within one standard deviation. For $\text{Li}_{1.07}\text{V}_{0.93}\text{O}_2$, again no occupancy of the alkali metal sites by V was detected, only Li. The Li and V

¹EaStCHEM, School of Chemistry, University of St Andrews, St. Andrews, Fife, KY16 9ST, UK, ²Department of Chemistry, University of Bath, Bath, BA2 7AY, UK. *e-mail: m.s.islam@bath.ac.uk; p.g.bruce@st-and.ac.uk.

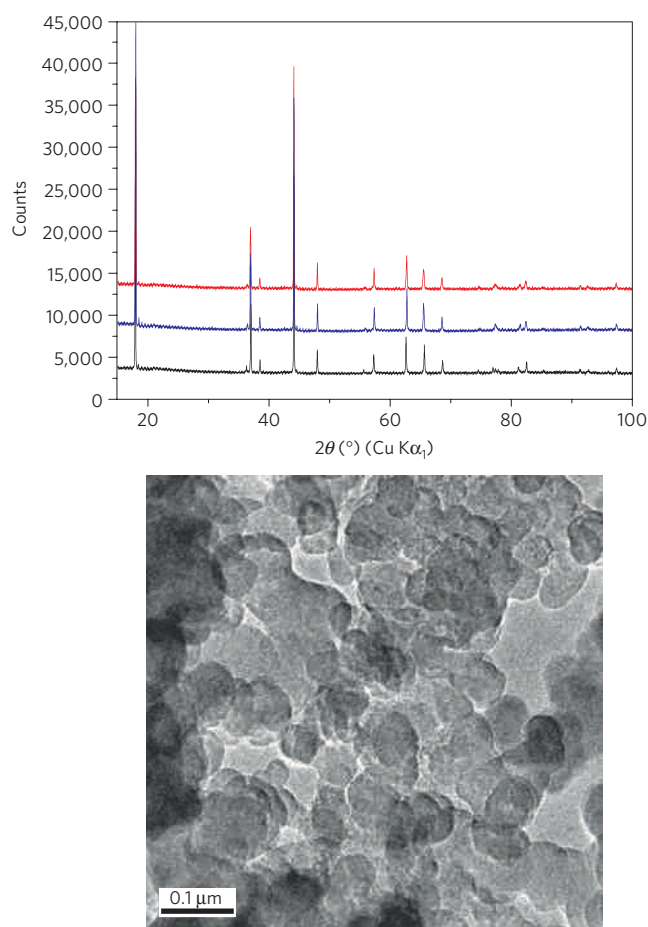


Figure 1 | Structural characterization of as-prepared $\text{Li}_{1+x}\text{V}_{1-x}\text{O}_2$.

a, Powder X-ray diffraction patterns of as-prepared $\text{Li}_{1+x}\text{V}_{1-x}\text{O}_2$. Black, red and blue lines correspond to $x = 0$, $x = 0.03$ and $x = 0.07$ respectively. **b**, Transmission electron micrograph for as-prepared $\text{Li}_{1.07}\text{V}_{0.93}\text{O}_2$.

occupancy on the transition metal sites were varied independently, giving values of 0.92(1) and 0.08(1) and a composition $\text{Li}_{1.08}\text{V}_{0.92}\text{O}_2$. The final parameters are presented in Supplementary Table S1 along with the corresponding R-factors, which indicate excellent fits. The fitted profiles are available as Supplementary Fig. S1. Chemical analysis was carried out by ICP, following the procedure described in the Methods section. Compositions of $\text{Li}_{1.01}\text{V}_{0.99}\text{O}_2$ and $\text{Li}_{1.07}\text{V}_{0.93}\text{O}_2$, ± 0.02 were obtained. Oxidation state analysis by redox titration, also described in the Methods section, gave values of +3.03 and $+3.16 \pm 0.05$ respectively. The compositions derived from the ICP and oxidation state analyses are, within errors, in accord with those derived from the refined data, Supplementary Table S1.

The intercalation process

Considering first stoichiometric LiVO_2 , the load curve, Fig. 2, exhibits a short plateau at 0.8 V corresponding to the potential of electrolyte reduction observed previously for graphite and other low voltage anodes^{27–29}. The low voltage plateau is very short ($\sim 40 \text{ mA h g}^{-1}$), occurs at 0 V; there is no corresponding plateau on charge and no cycling. No change in the X-ray or neutron diffraction patterns was observed up to the end of discharge, consistent with the absence of intercalation into the stoichiometric material. There was no evidence of reduced vanadium phases, such as V or VO , or of Li_2O that might have indicated a conversion reaction. This was also the case for the non-stoichiometric material, confirming the absence of conversion/displacement reactions.

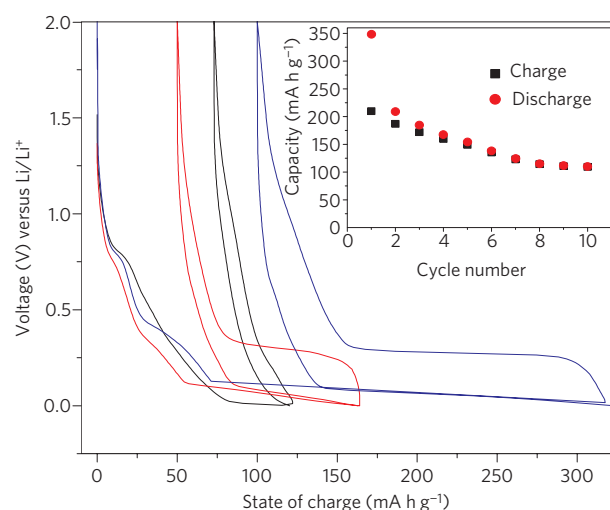


Figure 2 | Variation of potential (versus $\text{Li}^+[\text{1 M}]/\text{Li}$) with state of charge for $\text{Li}_{1+x}\text{V}_{1-x}\text{O}_2$. Rate 10 mA g^{-1} ; black, red and blue lines correspond to $x = 0$, $x = 0.03$ and $x = 0.07$ respectively. Inset shows variation of capacity with cycle number for $x = 0.07$.

Turning to $\text{Li}_{1.07}\text{V}_{0.93}\text{O}_2$, it also exhibits a short plateau at 0.8 V, Fig. 2. However, in contrast to LiVO_2 , the low voltage plateau is extensive, commences at $\sim 0.1 \text{ V}$ with a slight downward slope, possesses a corresponding plateau on charge (lithium extraction) and the material can be cycled (inset Fig. 2). The observed fading of capacity on cycling may be due to the volume change ($\sim 25\%$) and to the two-phase nature of the intercalation reaction; the combination of which leads to strain at the interface between the two phases. However, the composite electrode structure (for example distribution of conducting matrix) may also play a role. Better capacity retention has been reported³⁰. The extent of the low voltage plateau increases markedly with increasing lithium content up to $x = 0.07$, more lithium-rich compositions do not exhibit higher discharge capacities. The load curves are similar to previous reports^{1–4}.

Powder neutron diffraction patterns collected at various points along the charge/discharge curve for $x = 0.07$ are shown in Fig. 3. Commencing with discharge, the powder neutron diffraction pattern after the passage of 25 mA h g^{-1} , that is just after the 0.8 V plateau, is identical to that of the as-prepared material, in accord with the 0.8 V process being associated with reduction of the electrolyte, as described above. The sloping region of the load curve from 35 to 70 mA h g^{-1} has been attributed previously to further solid electrolyte interphase (SEI) layer formation/electrolyte reduction on the surfaces of the composite electrode materials^{1,2}. This may be so to some extent, but neutron diffraction data collected at the end of the sloping region, Fig. 3, show evidence of a new phase, co-existing with the as-prepared phase, and with a similar structure, but with the extra Li in tetrahedral sites in the ccp structure is predicted by the modelling studies discussed later. Further detailed studies are required to fully explore and hence understand the process taking place in these early stages of the load curve, whereas the focus of the present paper is the low voltage plateau.

The diffraction data at 160 mA h g^{-1} and at the end of discharge both exhibit the presence of two phases, with the proportions of these phases varying as expected for a two-phase intercalation reaction. One phase possesses the structure of the as-prepared material and the diffraction data for the other corresponds to Li_2VO_2 . This second phase is isostructural with previously reported materials, including Li_2NiO_2 , Li_2MnO_2 and $\text{Li}_2\text{Mn}_{0.5}\text{Ni}_{0.5}\text{O}_2$, which

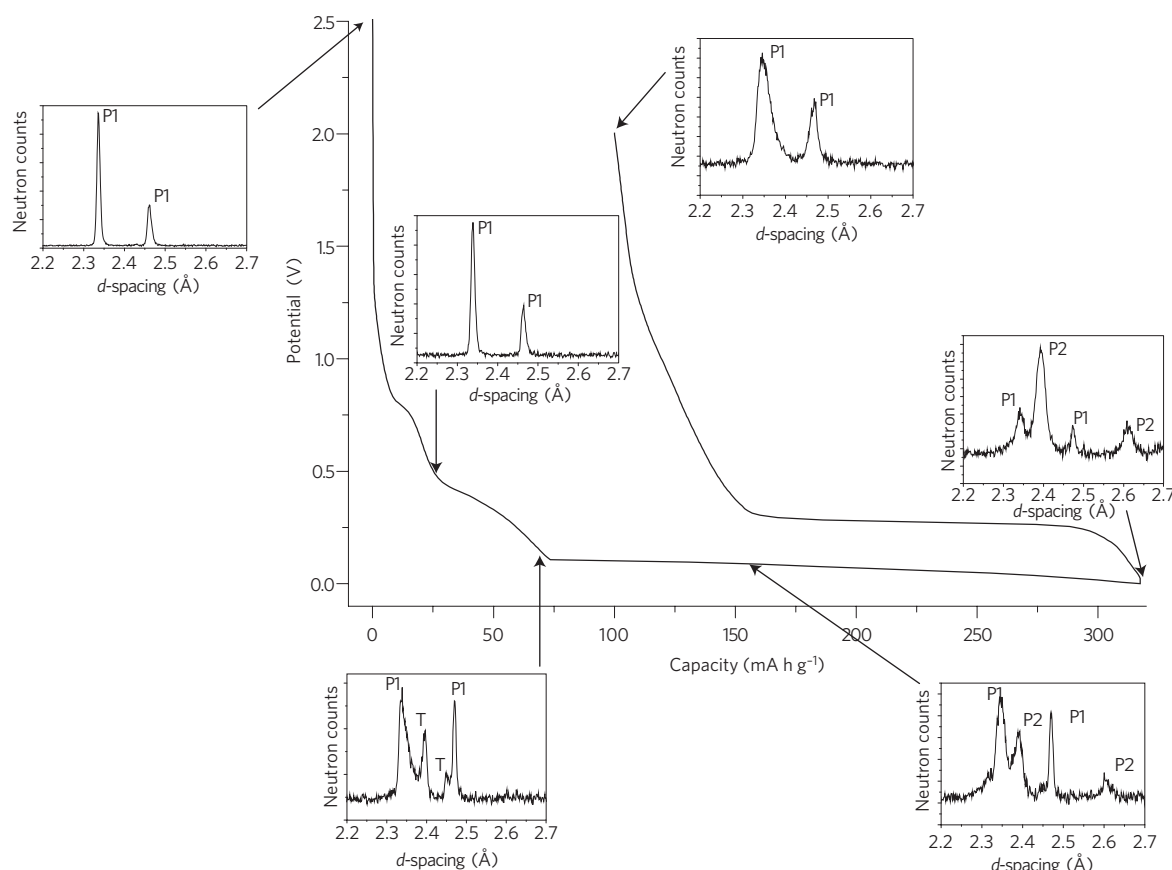


Figure 3 | Expanded regions of the powder neutron diffraction patterns collected at various states of charge for $\text{Li}_{1.07}\text{V}_{0.93}\text{O}_2$. P1 and P2 are prominent peaks of the host structure and Li_2VO_2 respectively whilst T represents an intermediate phase containing tetrahedral lithium ions. The asymmetry of the peak at 2.4 Å in the charged material may be due to a small amount of residual Li_2VO_2 phase. Note that neutron counts are in arbitrary units.

are also derived by intercalation into the corresponding layered LiMO_2 phases but with the crucial difference that the voltage is > 1 V in these cases^{31–35}. Note that even at the end of discharge, 0 V cut-off, two phases remain, as shown in Fig. 3.

Two phase refinements were carried out using combined powder X-ray and neutron diffraction data collected on the $x = 0.07$ material at 160 mA h g⁻¹ and full discharge. The fitted profiles are available as supplementary data, Supplementary Fig. S2, and demonstrate that the fit is good. Crystallographic parameters for the new, Li_2VO_2 , phase are presented in Supplementary Table S2. The structure of Li_2VO_2 is composed of hexagonal close packed oxide ions with vanadium ions occupying alternate sheets of octahedral sites between the oxide ion layers and lithium ions occupying all of the tetrahedral sites in the intervening layers, Fig. 4. On charging the cell to 2 V, the Li_2VO_2 phase converts back to the original structure. High-resolution transmission electron microscopy data collected on samples discharged to 160 mA h g⁻¹, Supplementary Fig S3, are consistent with the presence of two phases in the material. Overall the combined X-ray and neutron refinements confirm that Li intercalation occurs via a 2-phase mechanism between LiVO_2 and Li_2VO_2 (refs 1,2).

On the basis of the ratios of the two phases extracted from fitting the powder diffraction data at 160 mA h g⁻¹ and at the end of discharge, the amount of lithium intercalated as the discharge proceeds along the plateau has been calculated. The analysis indicates that the amount of intercalated lithium corresponds to charges of 65 and 166 mA h g⁻¹ respectively, compared with the actual charges passed along the plateau of 90 and 240 mA h g⁻¹. Clearly, the charge passed on progressing along the discharge plateau exceeds the amount of lithium inserted into the structure,

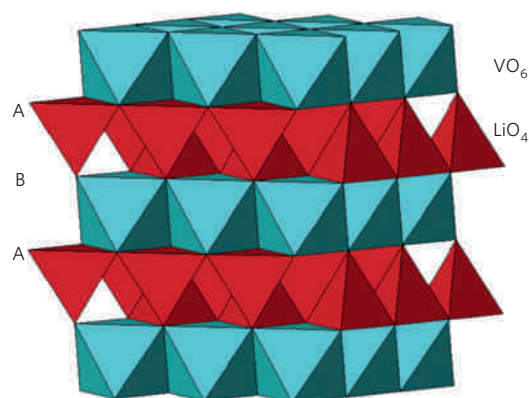


Figure 4 | Schematic representation of the structure of Li_2VO_2 . LiO_4 tetrahedra (red), VO_6 octahedra (blue).

and this discrepancy increases with increasing depth of discharge, the difference being 25 mA h g⁻¹ and 74 mA h g⁻¹ respectively.

A reduction process in addition to Li intercalation is taking place along the plateau. This may involve more SEI layer formation or the formation of soluble products from electrolyte reduction. The difference between the lengths of the charge and discharge plateaux for the $x = 0.07$ composition is similar to the discrepancy between the lithium content and charge passed along the first discharge plateau. This is consistent with the excess capacity on the first discharge plateau being associated with an irreversible process, such that the magnitude of the subsequent charging plateau is less than discharge. It is noteworthy that the efficiency on subsequent cycles is

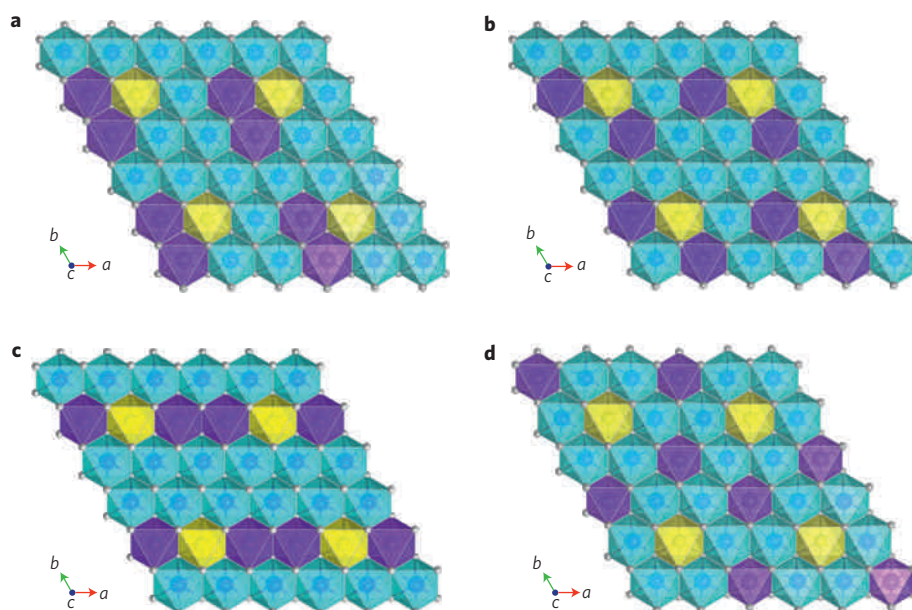


Figure 5 | Configurations of $2V_V^{4+}$ and Li_V^+ in the vanadium layer of $Li_{1.07}V_{0.93}O_2$. Configurations **a–c** are trimer clusters of nearest-neighbour ions, and configuration **d** shows isolated species (yellow: Li_V^+ ; blue: V_V^{3+} ; purple: V_V^{4+}).

much closer to 100%, further indicating that the irreversible process occurs mainly on the first discharge. The incomplete conversion of ccp to hcp on the first discharge may be due to polarization; the greater the polarization the earlier the low voltage cut-off will be reached. We have observed small variations in the polarization between cells, with conversions of up to 70%. Detailed work on optimizing the composite electrode structure should help to maximize the conversion. In the case of $x = 0.03$ material, the discharge plateau is shorter than that for $x = 0.07$ and the difference between the charge and discharge plateaux is correspondingly less.

The role of non-stoichiometry

Why is it that Li cannot intercalate into stoichiometric $LiVO_2$, yet a relatively small amount of excess lithium can switch on a large capacity to intercalate lithium at low voltages? Given the low rate used in Fig. 2, it is unlikely to be the result of differences in transport properties between the stoichiometric and lithium-rich compositions, that is to differences in ionic or electronic transport. This view is supported by galvanostatic intermittent titration technique (GITT) pseudo-equilibrium measurements, which show the same behaviour as in Fig. 2. The 2-phase intercalation process involves shearing of the close packed oxide ion layers from cubic to hexagonal stacking. The structure of stoichiometric $LiVO_2$ shows no evidence of V in the Li layers (site exchange), so the inability to intercalate Li into stoichiometric $LiVO_2$ is not due to V pinning the alkali metal layers together and inhibiting shearing.

To investigate the difference between stoichiometric and non-stoichiometric materials further, atomistic modelling methods were employed, being well-established tools in the study of defect structures in complex oxides^{36–38}. First, the crystal structures of $LiVO_2$, $Li_{1.07}V_{0.93}O_2$ and Li_2VO_2 were reproduced and exhibit good agreement with the experimental structures (see Supplementary Table S3). Simulations of intrinsic defects in stoichiometric $LiVO_2$ find an unfavourable formation energy of more than 3 eV for Li/V site exchange (comprised of isolated Li^+ on the V sites, Li_V^+ , and isolated V^{3+} on the Li^+ sites, V_{Li}^{3+}); this is clearly in accord with the above observation from Rietveld refinement that there is no V in the Li layers.

Formation of the solid solution $Li_{1+x}V_{1-x}O_2$ involves the mechanism $3V_V^{3+} + Li^+ = 2V_V^{4+} + Li_V^+$, that is substitution of V^{3+} by Li^+ on

the octahedral V site and charge compensation by oxidation of two other V^{3+} to V^{4+} . Effective charges are expected to favour the two V^{4+} occupying the nearest neighbour (nn) sites that each share an edge with the Li_V^+ site. Modelling studies have investigated the energetics of several configurations of the $2V_V^{4+}$ and Li_V^+ in the V layer of $Li_{1.07}V_{0.93}O_2$ (shown in Fig. 5); the energies listed in Supplementary Table S4 confirm the stability of the $(2V_V^{4+}/Li_V^+)$ trimer cluster compared with isolated defects. Although the small energy differences do not allow us to distinguish between the three trimer configurations, Fig. 5a–c (the energy differences are small compared with kT at the temperature of synthesis, 850 °C), the results clearly indicate a non-random distribution of V_V^{4+} and Li_V^+ in the vanadium layers.

There is scope for the trimer clusters to coalesce into larger clusters. Each Li_V^+ site is surrounded by six edge sharing V sites. We therefore explored how the V^{4+} could be distributed around the Li_V^+ to form larger clusters, which included a dodecamer (or ‘flower-like’) arrangement in which all six of the edge sharing sites surrounding Li_V^+ are V^{4+} . However, the most stable configurations (shown in Supplementary Figs S4 and S5) are still less favourable than the trimer clusters by more than 350 meV. In general, the calculations on the $Li_{1.07}V_{0.93}O_2$ composition indicate that the $(2V_V^{4+}/Li_V^+)$ trimer is the most favourable arrangement compared to larger, more complex, clusters.

Turning to the intercalation of Li into $LiVO_2$ and $Li_{1.07}V_{0.93}O_2$, Li^+ must first be inserted into a tetrahedral site, as all the octahedral sites are already occupied. In the case of $LiVO_2$ the most favourable empty tetrahedral site is located in the alkali metal layers, and shares one face with a V^{3+} ion in an octahedral site in the transition metal layers, Fig. 6a. In contrast, in $Li_{1+x}V_{1-x}O_2$ the intercalated Li^+ can occupy a tetrahedral site in the alkali metal layer that shares a face with the Li_V^+ in the Li_V^+ site, Fig. 6b. Atomistic modelling calculations have probed the energies for lithium ion occupancy at these two sites (Table 1); note that the lowest energy trimer structure was used for the calculations on $Li_{1.07}V_{0.93}O_2$. The relative energies clearly indicate that the intercalated Li^+ at the site sharing a face with Li_V^+ in $Li_{1.07}V_{0.93}O_2$ is about 620 meV lower in energy than for Li^+ in $LiVO_2$, rendering the intercalation of Li into the lithium-rich $Li_{1.07}V_{0.93}O_2$ much more favourable.

Previous density functional theory (DFT) studies^{39–44} on a variety of oxide electrode materials have shown that such methods

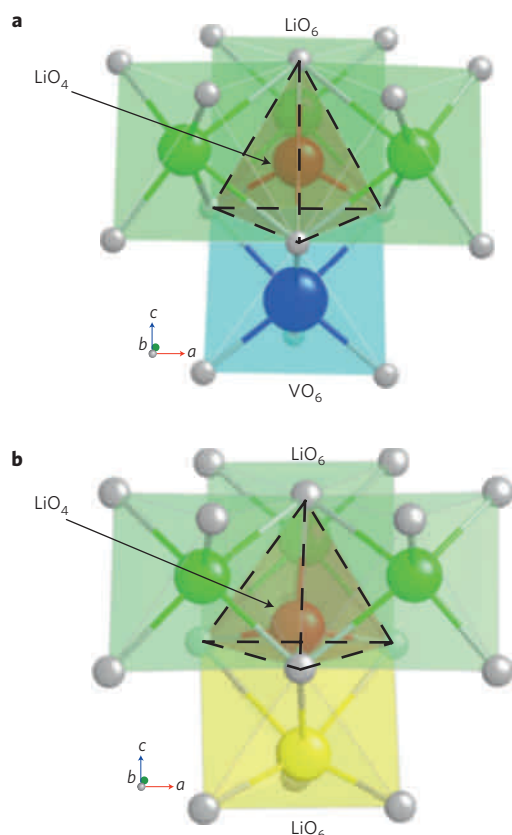


Figure 6 | Calculated local structures around an inserted Li^+ ion in LiVO_2 and $\text{Li}_{1.07}\text{V}_{0.93}\text{O}_2$. Dotted lines highlight its local coordination: **a**, Li^+ at a tetrahedral site in an alkali metal layer of the LiVO_2 structure and sharing a face with a V ion in an octahedral site in the layer below (the other three faces of the tetrahedron are shared with Li in octahedral sites in the alkali metal layers); **b**, Li^+ at a tetrahedral site in an alkali metal layer of the $\text{Li}_{1.07}\text{V}_{0.93}\text{O}_2$ structure and sharing a face with a Li ion in an octahedral site in the layer below (the other three faces of the tetrahedron are shared with Li in octahedral sites in the alkali metal layers). The inserted Li^+ in $\text{Li}_{1.07}\text{V}_{0.93}\text{O}_2$ is displaced by $\sim 0.3 \text{ \AA}$ from the centre of the tetrahedron towards the shared face with Li^+ . The adjacent Li_V^+ ion is also displaced away by $\sim 0.6 \text{ \AA}$ from the inserted lithium leading to a distorted coordination environment.

are well suited to probing lithium insertion properties and to predicting precise trends in cell voltages. Here we derived cell voltages for lithium intercalation into the stoichiometric LiVO_2 and the Li-rich $\text{Li}_{1+x}\text{V}_{1-x}\text{O}_2$ systems using the total energies from a series of structural optimizations. Table 1 indicates a negative cell voltage of -2.98 V for $\text{Li}_{1+y}\text{VO}_2$, confirming that the intercalation of lithium into the stoichiometric oxide is unfavourable; lithium plating would occur, at 0 V , before the voltage for intercalation was reached. This result is consistent with the above experimental data, which show no evidence of intercalation into stoichiometric LiVO_2 , and with previous reports^{1,2}. In contrast, for Li intercalation into $\text{Li}_{1.07}\text{V}_{0.93}\text{O}_2$ a cell voltage of $+0.58 \text{ V}$ is derived, indicating intercalation into this phase is possible. This is consistent with the neutron diffraction data, discussed above, where evidence for Li intercalation into the tetrahedral sites in the ccp structure was observed; although the calculated voltage is somewhat greater than the average for the sloping region of the discharge curve.

The simulations also produce valuable local structural information, which can be difficult to extract from diffraction experiments alone. Figure 6 indicates that the inserted Li^+ in $\text{Li}_{1.07}\text{V}_{0.93}\text{O}_2$ is displaced slightly from the centre of the tetrahedron towards the

Table 1 | Calculated energies for intercalated Li^+ and cell voltages for stoichiometric and Li-rich structures.

Energies of intercalated Li^+ at sites shown in Fig. 6.

Compound	Insertion site	$E(\text{Li}^+)$ (meV)	ΔE^* (meV)
Stoichiometric LiVO_2	Li^+ adjacent to V_V^{3+}	-3552	$+618$
Li-rich $\text{Li}_{1.07}\text{V}_{0.93}\text{O}_2$	Li^+ adjacent to Li_V^+	-4170	0

Average cell voltages

Composition/range	Cell voltage (V)
Stoichiometric $\text{Li}_{1+y}\text{VO}_2$ ($0.0 < y < 0.07$)	-2.98
Li-rich $\text{Li}_{1.07+y}\text{V}_{0.93}\text{O}_2$ ($0.0 < y < 0.07$)	$+0.58$
Li-rich $\text{Li}_{1.07+y}\text{V}_{0.93}\text{O}_2$ ($0.0 < y < 0.93$)	$+0.23$

*Energy difference between these sites with reference to the most stable site.

shared face with Li_V^+ , leading to three $\text{Li}^+\text{--O}$ distances of 1.8 \AA and one of 2.1 \AA . Owing to $\text{Li}^+\text{--Li}^+$ repulsions the adjacent Li_V^+ ion is also displaced away from the inserted lithium, leading to a separation of 2.1 \AA between the two lithium ions. Interestingly, the Li_V^+ ion now sits in a distorted coordination environment of three short $\text{Li}_\text{V}^+\text{--O}$ and three long $\text{Li}_\text{V}^+\text{--O}$ distances of about 1.91 \AA and 2.45 \AA respectively (compared to the initial octahedral coordination of $6 \times 1.99 \text{ \AA}$). Li insertion has also perturbed the local anion sublattice with lengthening of several O–O distances from 2.93 \AA to more than 3.0 \AA . The inserted lithium therefore causes large distortions to the local structure of $\text{Li}_{1.07}\text{V}_{0.93}\text{O}_2$, which could be viewed as precursors to the shearing of oxide layers for cubic to hexagonal packing.

Although the tetrahedral site in the Li layer of $\text{Li}_{1.07}\text{V}_{0.93}\text{O}_2$ is more stable than in LiVO_2 it does share all four faces with Li^+ ions in octahedral sites (3 in the alkali metal layers and the V site substituted by Li, Li_V^+). The resultant $\text{Li}^+\text{--Li}^+$ repulsions trigger the shearing of the close packed oxide ion layers from ABC to the AB stacking of the hexagonal close packed Li_2VO_2 structure. AB stacking can accommodate all of the original Li plus one extra Li per formula unit in the tetrahedral sites of the alkali metal layers (there are twice the number of tetrahedral sites to octahedral sites per alkali metal layer), Fig. 4. The tetrahedral sites share faces with empty tetrahedral sites in the transition metal layers and empty octahedral sites in the alkali metal layers, that is there is no face sharing of occupied sites, leading to a stable structure. By this mechanism it is possible to understand why a small degree of vanadium substitution by lithium can trigger a marked capacity to insert lithium via a 2-phase mechanism.

DFT studies have been extended to calculate the voltage expected for the 2-phase reaction, and give a value of $+0.23 \text{ V}$, Table 1, in good accord with the low voltage plateau commencing at $\sim 0.1 \text{ V}$. As with previous DFT studies^{39–41}, there are small quantitative differences with experimental values, which have been attributed largely to the overestimation of the calculated binding energy for lithium metal. In any case, our calculated trend in cell voltages as a function of structure and stoichiometry confirms the important role that the lithium-rich composition plays in initiating lithium intercalation, and accords well with the electrochemical measurements.

It is interesting to consider the implications of the present work for other layered LiMO_2 compounds. The results presented here indicate that the presence of Li on the transition metal sites should favour Li intercalation and transformation of ccp to hcp in layered compounds. It is noteworthy that compounds such as $\text{Li}(\text{Li}_{0.02}\text{Mn}_{0.46}\text{Ni}_{0.46}\text{Ti}_{0.05})\text{O}_2$, with Li on the transition metal sites, can readily intercalate Li with a marked capacity associated with the ccp to hcp transformation^{34,35}. In contrast, Li cannot be

intercalated into LiCoO_2 . However, further work is required to corroborate this trend.

In conclusion, the process of lithium intercalation into $\text{Li}_{1+x}\text{V}_{1-x}\text{O}_2$ has been investigated by a combination of computational methods along with powder X-ray and neutron diffraction, focussing in particular on the role that excess lithium plays on switching on intercalation. Whereas Li cannot be intercalated into stoichiometric LiVO_2 , substituting as little as 3% of the V on the transition metal sites by Li is sufficient to promote a 2-phase intercalation process between cubic close packed LiVO_2 and hexagonal close packed Li_2VO_2 at potentials of ~ 0.1 V. The process may be reversed on charging (Li extraction). The results show that the inability to intercalate into stoichiometric LiVO_2 is not due to the presence of site-exchange disorder involving V ions in the alkali metal layers pinning them together, as might have been thought. Instead, we show that substitution of Li for V on the octahedral transition metal sites renders tetrahedral sites in the alkali metal layers energetically accessible by Li, which in turn triggers the shearing of the cubic close-packed oxide ion layers to hexagonal close packing such that two Li per formula unit can be accommodated without face sharing.

Given the importance that Li intercalation into $\text{Li}_{1+x}\text{V}_{1-x}\text{O}_2$ at ~ 0.1 V has for lithium battery anodes, and that this occurs only for the Li-rich compositions, the results presented in this paper provide a framework not only for understanding the intercalation process but also for the future design and optimization of low voltage intercalation oxides as anodes for rechargeable lithium batteries.

Methods

$\text{Li}_{1+x}\text{V}_{1-x}\text{O}_2$ was synthesized from lithium carbonate and vanadium oxide using a solid state method. Appropriate ratios of dried V_2O_5 (Aldrich, 99%) and Li_2CO_3 (Aldrich, 99 + %) powders were mixed together, placed in a gas-tight container and subsequently ball-milled for 60 min (SPEX Centri-Prep 8,000 M mixer/mill). The mixture was then placed in an alumina crucible, covered with a lid and heated at 800°C for 10 h under flowing argon. The compound was allowed to cool to room temperature, then heated to 850°C for 12 h under a flowing gas mixture of 95% argon/5% hydrogen to complete the reaction and obtain a single phase product.

Chemical analysis was carried out by ICP using a Perkin-Elmer Optima 7300DV ICP-OES. The samples of lithium vanadium oxide were carefully weighed out, dissolved in hot aqua regia and then diluted before analysis for Li and V. ICP analysis was carried out by an external company (Butterworths Ltd.). Vanadium oxidation state analysis was performed by double titration following the method described in ref. 45. After dissolution in H_2SO_4 , the V^{3+} and V^{4+} content in the sample was determined by titration (V1) with aqueous KMnO_4 (0.01 M). An aqueous solution of $\text{FeSO}_4(\text{NH}_4)_2\text{SO}_4 \cdot 6\text{H}_2\text{O}$ was then added to reduce all the V^{5+} to V^{4+} . The solution was cooled in an ice bath and an excess of $(\text{NH}_4)_2\text{S}_2\text{O}_8$ was added to oxidize Fe^{2+} to Fe^{3+} . Finally, V^{4+} was titrated (V2) with KMnO_4 (0.01 M) to measure the total vanadium content of the sample. The average oxidation state of vanadium was given by $5 - (\text{V1})/(\text{V2})$. Errors, based on the above volumetric analysis are estimated to be $\pm 5\%$.

Composite electrodes were fabricated using the active material, super S carbon and Kynar Flex 2801 (a co-polymer based on PVDF) binder in a mass ratio of 75:18:7. Electrochemical cells consisting of a $\text{Li}_{1+x}\text{V}_{1-x}\text{O}_2$ composite electrode, a lithium metal counter electrode and the electrolyte, a 1 molar solution of LiPF_6 in ethylene carbonate–dimethyl carbonate 1:1 (v/v) (Merck), were constructed and handled in an Ar-filled MBraun glovebox. Electrochemical measurements were conducted using a Biologic Macpile II multichannel instrument. Samples for neutron diffraction were prepared electrochemically. After cycling, cells were transferred to an argon-filled glove box before opening and active material removed. The electrodes were then rinsed with a small amount of dry solvent to remove residual electrolyte. They were left under dynamic vacuum overnight to ensure all solvent had evaporated. The samples were then transferred to 2 mm quartz capillaries.

BET surface areas were determined using a Hiden IGA porosimeter. Powder X-ray diffraction patterns were obtained on pristine material using a Stoe STADI/P diffractometer employing $\text{Cu K}\alpha_1$ radiation operating in transmission mode. Data from cycled materials were obtained on a similar diffractometer with the samples sealed in capillaries. Time-of-flight powder neutron diffraction data were collected on the POLARIS high-intensity, medium resolution instrument at ISIS, Rutherford Appleton Laboratory (UK). The structures were refined by the Rietveld method using TOPAS Academic⁴⁶. TEM studies were carried out using a JEOL JEM-2011 with an accelerating voltage of 200 keV. TEM images were recorded by a Gatan CCD camera in a digital format.

The two principal computational methods employed were atomistic defect modelling and DFT, which have been applied successfully to other complex oxides^{36–44}. Atomistic defect simulations were performed using the GULP code⁴⁷ based on effective interatomic potentials (Supplementary Table S5), and the shell model to describe electronic polarizability. An important feature is the modelling of lattice relaxation around the point defect, treated by the Mott–Littleton approach³⁸. Solid state DFT calculations were performed using the VASP (ref. 48) code, within which the core electrons were represented by ultra-soft pseudopotentials⁴⁹, and the Perdew–Wang (PW91) density functional⁵⁰ was used for exchange–correlation. Introduction of Coulombic on-site correlations through GGA + U is now a well-established approach for transition metal compounds, for which we have used U values of 4 eV and 6.75 eV for V(III) and V(II) phases respectively. We note that previous first-principles calculations find strong V(3d)–O(2p) mixing in $\text{Li}_{1.1}\text{V}_{0.9}\text{O}_2$ (ref. 51). Integration over the Brillouin zone was carried out with $4 \times 4 \times 4$ Monkhorst–Pack grids for geometry optimization calculations on $2 \times 2 \times 1$ supercells of LiVO_2 , $\text{Li}_{1.07}\text{V}_{0.93}\text{O}_2$ and Li_2VO_2 . A large cut-off energy of 600 eV was used to ensure effective convergence. The initial unit cells for the geometry optimizations were taken from our experimental structural data (Supplementary Tables S1 and S2).

Received 6 July 2010; accepted 18 January 2011; published online 13 February 2011

References

- Choi, N. S., Kim, J. S., Yin, R. Z. & Kim, S. S. Electrochemical properties of lithium vanadium oxide as an anode material for lithium-ion battery. *Mater. Chem. Phys.* **116**, 603–606 (2009).
- Song, J. H. *et al.* Electrochemical characteristics of lithium vanadate, $\text{Li}_{1+x}\text{VO}_2$, new anode materials for lithium ion batteries. *J. Power Sources* **195**, 6157–6161 (2010).
- Kim, S.-S., Kim, J., Koike, M. & Kobayashi, N. *14th International Meeting on Lithium Batteries*, Tianjin, China, Abstr. #20 (2008).
- Kim, S.-S., Nitta, Y., Nedoseykina, T. I. & Lee, J.-C. US Patent Application US 2006/0088766 (2006).
- Armand, M. & Tarascon, J.-M. Building better batteries. *Nature* **451**, 652–657 (2008).
- Nazri, G.-A. & Pistoia, G. (eds) *Lithium Batteries Science and Technology* (Kluwer Academic/Plenum, 2004).
- Arico, A. S., Bruce, P. G., Scrosati, B., Tarascon, J. M. & Van Schalkwijk, W. Nanostructured materials for advanced energy conversion and storage devices. *Nature Mater.* **4**, 366–377 (2005).
- Bruce, P. G., Scrosati, B. & Tarascon, J. M. Nanomaterials for rechargeable lithium batteries. *Angew. Chem. Int. Ed.* **47**, 2930–2946 (2008).
- Huggins, R. A. in *Handbook of Battery Materials* (ed. Besenhard, J. O.) (Wiley-VCH, 1999) Part III, Chapter 4.
- Winter, M. & Besenhard, J. O. Electrochemical lithiation of tin and tin-based intermetallic and composites. *Electrochim. Acta* **45**, 31–50 (1999).
- Mao, O. & Dahn, J. R. Mechanically alloyed Sn–Fe(–C) powders as anode materials for Li ion batteries. III. $\text{Sn}_2\text{Fe}/\text{SnFe}_3\text{C}$ active/inactive composites. *J. Electrochem. Soc.* **146**, 423–427 (1999).
- Beaulieu, L. Y. & Dahn, J. R. The reaction of lithium with Sn–Mn–C intermetallics prepared by mechanical alloying. *J. Electrochem. Soc.* **147**, 3237–3241 (2000).
- Magasinski, A. *et al.* High-performance lithium-ion anodes using a hierarchical bottom-up approach. *Nature Mater.* **9**, 353–358 (2010).
- Amadei, I., Panero, S., Scrosati, B., Cocco, G. & Schiffrini, L. The Ni_3Sn_4 intermetallic as a novel electrode in lithium cells. *J. Power Sources* **143**, 227–230 (2005).
- Graetz, J., Ahn, C. C., Yazami, R. & Fuetz, B. Highly reversible lithium storage in nanostructured silicon. *Electrochem. Solid-State Lett.* **6**, A194–A197 (2003).
- Yang, J. *et al.* Si/C composites for high capacity lithium storage materials. *Electrochem. Solid-State Lett.* **6**, A154–A156 (2003).
- Chan, C. K. *et al.* High-performance lithium battery anodes using silicon nanowires. *Nature Nanotech.* **3**, 31–35 (2008).
- Kepler, K. D., Vaughney, J. T. & Thackeray, M. M. $\text{Li}_x\text{Cu}_6\text{Sn}_5$ ($0 < x < 13$): An intermetallic insertion electrode for rechargeable lithium batteries. *Electrochem. Solid-State Lett.* **2**, 307–309 (1999).
- Fransson, L. M. L. *et al.* Phase transitions in lithiated Cu_2Sb anodes for lithium batteries: An *in situ* X-ray diffraction study. *Electrochem. Commun.* **3**, 317–323 (2001).
- Poizot, P., Laruelle, S., Grugeon, S., Dupont, L. & Tarascon, J.-M. Nano-sized transition metal oxides as negative electrode material for lithium-ion batteries. *Nature* **407**, 496–499 (2000).
- Leroux, F., Coward, G. R., Power, W. P. & Nazar, L. F. Understanding the nature of low-potential Li uptake into high volumetric capacity molybdenum oxides. *Electrochem. Solid-State Lett.* **1**, 255–258 (1998).
- Taberna, P. L., Mitra, S., Poizot, P., Simon, P. & Tarascon, J. M. High rate capabilities Fe_3O_4 -based Cu nano-architected electrodes for lithium-ion battery applications. *Nature Mater.* **7**, 567–573 (2006).

23. Pereira, N., Dupont, L., Tarascon, J. M., Klein, L. C. & Amatucci, G. G. Electrochemistry of Cu_3N with lithium — A complex system with parallel processes. *J. Electrochem. Soc.* **150**, A1273–A1280 (2003).
24. Li, H., Ritcher, G. & Maier, J. Reversible formation and decomposition of LiF clusters using transition metal fluorides as precursors and their application in rechargeable Li batteries. *Adv. Mater.* **15**, 736–739 (2003).
25. Badway, F., Cosandey, F., Pereira, N. & Amatucci, G. G. Carbon metal fluoride nanocomposites: High capacity reversible metal fluoride conversion materials as rechargeable positive electrodes for Li batteries. *J. Electrochem. Soc.* **150**, A1318–A1327 (2003).
26. Pralong, V., Souza, D. C. S., Leung, K. T. & Nazar, L. Reversible lithium uptake by CoP_3 at low potential: Role of the anion. *Electrochem. Commun.* **4**, 516–520 (2002).
27. Peled, E. The electrochemical-behaviour of alkali and alkaline-earth metals in non-aqueous battery systems—the solid electrolyte interphase model. *J. Electrochem. Soc.* **126**, 2047–2051 (1979).
28. Fong, R., von Sacken, U. & Dahn, J. R. Studies of lithium intercalation into carbons using nonaqueous electrochemical-cells. *J. Electrochem. Soc.* **137**, 2009–2013 (1990).
29. Besenhard, J. O., Winter, M., Yang, J. & Biberacher, W. Filming mechanism of lithium-carbon anodes in organic and inorganic electrolytes. *J. Power Sources* **54**, 228–231 (1995).
30. Park, S.-Y., Choi, N.-S., Yew, K.-H., Lee, D.-K. & Kim, S.-S. US Patent Application US 2009/0068566 (2009).
31. David, W. I. F., Goodenough, J. B., Thackeray, M. M. & Thomas, M. G. S. R. The crystal-structure of Li_2MnO_2 . *Rev. Chim. Miner.* **20**, 636–642 (1983).
32. Dahn, J. R., Von Sacken, U. & Michal, C. A. Structure and electrochemistry of $\text{Li}_{1+y}\text{NiO}_2$ and a new Li_2NiO_2 phase with the $\text{Ni}(\text{OH})_2$ structure. *Solid State Ion.* **44**, 87–97 (1990).
33. Davidson, I., Greedan, J. E., Von Sacken, U., Michal, C. A. & Dahn, J. R. Structure of $1\text{T-Li}_2\text{NiO}_2$ from powder neutron-diffraction. *Solid State Ion.* **46**, 243–247 (1991).
34. Johnson, C. S. *et al.* The role of Li_2MO_2 structures ($\text{M} = \text{metal ion}$) in the electrochemistry of $(x)\text{LiMn}_{0.5}\text{Ni}_{0.5}\text{O}_2 \cdot (1-x)\text{Li}_2\text{TiO}_3$ electrodes for lithium-ion batteries. *Electrochem. Commun.* **4**, 492–498 (2002).
35. Johnson, C. S. *et al.* Structural characterization of layered $\text{Li}_x\text{Ni}_{0.5}\text{Mn}_{0.5}\text{O}_2$ ($0 < x \leq 2$) oxide electrodes for Li batteries. *Chem. Mater.* **15**, 2313–2322 (2003).
36. Islam, M. S., Driscoll, D. J., Fisher, C. A. J. & Slater, P. R. Atomic-scale investigation of defects, dopants and lithium transport in the LiFePO_4 olivine-type battery material. *Chem. Mater.* **17**, 5085–5092 (2005).
37. Kendrick, E., Kendrick, J., Knight, K. S., Islam, M. S. & Slater, P. R. Cooperative mechanisms of fast-ion conduction in gallium-based oxides with tetrahedral moieties. *Nature Mater.* **6**, 871–874 (2007).
38. Catlow, C. R. A. (ed.) *Computer Modelling in Inorganic Crystallography* (Academic, 1997).
39. Zhou, F., Cococcioni, M., Marianetti, C. A., Morgan, D. & Ceder, G. First principles prediction of redox potentials in transition-metal compounds with LDA + U. *Phys. Rev. B* **70**, 235121 (2004).
40. Kang, K. S., Meng, Y. S., Breger, J., Grey, C. P. & Ceder, G. Electrodes with high power and high capacity for rechargeable lithium batteries. *Science* **311**, 977–980 (2006).
41. Arrouvel, C., Parker, S. C. & Islam, M. S. Lithium insertion and transport in the TiO_2 -B anode material: A computational study. *Chem. Mater.* **21**, 4778–4783 (2009).
42. Braithwaite, J. S., Catlow, C. R. A., Gale, J. D., Harding, J. H. & Ngoepe, P. E. Calculated cell discharge curve for lithium batteries with a V_2O_5 cathode. *J. Mater. Chem.* **10**, 239–240 (2000).
43. Scanlon, D. O., Walsh, A., Morgan, B. J. & Watson, G. W. An *ab initio* study of reduction of V_2O_5 through the formation of oxygen vacancies and Li intercalation. *J. Phys. Chem. C* **112**, 9903–9911 (2008).
44. Meng, Y. S. & Arroyo-de Dompablo, M. E. First principles computational materials design for energy storage materials in lithium ion batteries. *Energy Environ. Sci.* **2**, 589–609 (2009).
45. Hodnett, B. K., Permann, Ph. & Delmon, B. Influence of p/v ratio on the phase composition and catalytic activity of vanadium phosphate based catalysts. *Appl. Catalys.* **6**, 231–244 (1983).
46. Coelho, A. A. Whole-profile structure solution from powder diffraction data using simulated annealing. *J. Appl. Crystallogr.* **33**, 899–908 (2000).
47. Gale, J. D. & Rohl, A. L. The general utility lattice program. *Mol. Simul.* **29**, 291–341 (2003).
48. Kresse, G. & Furthmüller, J. Efficient iterative schemes for *ab initio* total-energy calculations using a plane-wave basis set. *Phys. Rev. B* **54**, 11169 (1996).
49. Vanderbilt, D. Soft self-consistent pseudopotentials in a generalized eigenvalue formalism. *Phys. Rev. B* **41**, 7892–7895 (1990).
50. Burke, K., Perdew, J. P. & Wang, Y. in *Electronic Density Functional Theory: Recent Progress and New Directions* (eds Dobson, J. F. & Vignale, G.) (Plenum, 1998).
51. Yin, R. Z., Kim, Y. S., Choi, W. U., Kim, S. S. & Kim, H. J. Structural analysis and first-principles calculation of lithium vanadium oxide for advanced Li-ion batteries. *Adv. Quantum Chem.* **54**, 23–33 (2008).

Acknowledgements

P.G.B. and M.S.I. are indebted to the European Union and EPSRC for financial support. The computations were run on the HECToR facilities via the Materials Chemistry Consortium.

Author contributions

A.R.A. and C.L. carried out the experimental work and data analysis, P.M.P. the modelling, M.S.I. and P.G.B. conceived and directed the project.

Additional information

The authors declare no competing financial interests. Supplementary information accompanies this paper on www.nature.com/naturematerials. Reprints and permissions information is available online at <http://npg.nature.com/reprintsandpermissions>. Correspondence and requests for materials should be addressed to M.S.I. or P.G.B.